Correlative Microscopy of α' Precipitation in Neutron-Irradiated Fe-Cr-Al Alloys

by

Samuel A. Briggs

A dissertation submitted in partial fulfillment of
the requirements for the degree of

Doctor of Philosophy

(Nuclear Engineering & Engineering Physics)

at the

UNIVERSITY OF WISCONSIN–MADISON

2016

Date of oral examination: 12/08/2016

The dissertation is presented to the following members of the Examining Committee:

Todd R. Allen, Professor, Engineering Physics
James P. Blanchard, Professor, Engineering Physics
Michael L. Corradini, Wisconsin Distinguished Professor, Engineering Physics
Dane D. Morgan, Associate Professor, Materials Science & Engineering
Kumar Sridharan, Distinguished Research Professor, Engineering Physics
Kevin G. Field, R&D Associate, Weinberg Fellow, Oak Ridge National Laboratory

© Copyright by Samuel A. Briggs 2016
All Rights Reserved

To my family.

ACKNOWLEDGMENTS

Primary research funding was sponsored by the DOE's Office of Nuclear Energy, Advanced Fuels Campaign of the Fuel Cycle R&D Program. Neutron irradiation of FeCrAl alloys at ORNL's HFIR user facility was sponsored by the Scientific User Facilities Division, Office of Basic Energy Sciences, DOE. Atom probe tomography was conducted at the Center for Nanophase Materials Science, which is a DOE Office of Science User Facility; and the MaCS Laboratory at the Center for Advanced Energy Studies at Idaho National Laboratory, funded by the Nuclear Science User Facilities. A portion of this work was supported by the US Department of Energy, Office of Nuclear Energy under DOE Idaho Operations Office Contract DE-AC07-051D14517 as part of a Nuclear Science User Facilities experiment. The FEI Talos F200X TEM is provided by the Department of Energy, Office of Nuclear Energy, Fuel Cycle R&D Program and the Nuclear Science User Facilities. A portion of funding for myself was provided by the DOE Office of Nuclear Energy's Nuclear Energy University Programs.

This dissertation would not have been made possible without the help and support of numerous individuals. First, I would like to thank my academic advisers Todd Allen and Kumar Sridharan for taking me on in their research group and for all the guidance they've provided. Additionally, I would like to extend a special thank you to Kevin Field for involving me in this project and for his mentorship and oversight. I would also like to thank Philip Edmondson and Kenneth Littrell for their assistance in developing the analysis techniques used in this work, Yukinori Yamamoto for providing the materials for irradiation and analysis, and Richard Howard for leading irradiation capsule design efforts. Finally, I'd like to acknowledge all the supporting staff of the CAES, IMET, LAMDA and GP-SANS facilities in addition to the Thermal Hydraulics and Irradiation Engineering Group (THIEG) at ORNL for their support.

I would like to thank all of my colleagues, past and present, at the University of Wisconsin. Thanks to Janne Pakarinen, Clarissa Yablinsky, Alex Mairov, and Kim Kriewaldt for assisting me with various experiments and techniques, in addition to Billy Nollet, Tyler

Gerczak, & Matt Gidden for their scientific insight and continuing friendship. I would also like to thank all the other friends I am lucky to have made over the years who have helped keep me sane during my studies — Matt Hendrix and the VeX crew, Madicken Munk, Mr. and Mrs. St. John, Rachel Seibert and all the rest of you wonderful OR and WI folks.

Last and certainly not least, I would also like to thank my family. Without their continuous and unconditional love and support, I never would have made it this far.

To all those I have mentioned and also those that I didn't, *thank you!*

CONTENTS

List of Tables **v**

List of Figures **vi**

Nomenclature **vii**

Abstract **x**

1 Introduction **1**

2 Background **5**

2.1 Overview of Fe-Cr-Al Alloy Properties & Metallurgy 5

2.2 Radiation Damage in Materials 10

2.2.1 Radiation Damage Mechanism and Kinetics 10

2.2.2 Radiation-Induced Microstructural Features 14

2.3 Precipitation in Metals 15

2.3.1 Thermodynamics of Precipitation 15

2.3.2 α' Precipitation in High-Cr Ferritics 18

2.4 Introduction to Atom Probe Tomography 22

2.4.1 Principles of Atom Probe Tomography 22

2.4.2 Quantification of Precipitate Morphology & Chemistry 26

2.4.3 Artifacts and Limitations of Atom Probe Tomography 27

2.5 Introduction to Small-Angle Neutron Scattering 28

2.5.1 Principles of Small-Angle Neutron Scattering 28

2.5.2 Small-Angle Neutron Scattering for Precipitation Investigation . . 30

2.5.3 Artifacts and Limitations of Small-Angle Neutron Scattering . . . 31

2.6 Introduction to Transmission Electron Microscopy 32

2.6.1 Principles of Transmission Electron Microscopy 32

2.6.2 STEM/EDS for Microchemical Analysis 33

3 Methods Development for Correlative Microscopy **34**

3.1 Correlation of APT, SANS & STEM Data 34

3.1.1 Sensitivity of SANS Results to Scattering Length Density 35

3.1.2 Interpretation of Phase Compositions in Fe-Cr-Al APT Data . . . 37
3.2 Correcting for Peak Overlap in the APT TOF Spectrum 38
3.2.1 TOF Peak Decomposition for Neutron-Irradiated Materials 38
3.2.2 Application to Irradiated Fe-Cr-Al alloys 39
3.3 Methods to Correct for Trajectory Aberrations in APT Data 41
3.3.1 The APT POS File Format 42
3.3.2 Cubic Binning Methodology 43
3.3.2.1 Sensitivity to Bin Size & Thresholding Treatment 45
3.3.3 Delaunay Triangulation Methodology 46
3.3.3.1 Applications of Tessellation Algorithms for APT Analysis 46
3.3.3.2 Delaunay Triangulation for Trajectory Aberration Correction 48
3.3.4 Application of Trajectory Aberration Correction Methods to Experimental Data 55
3.4 Model Fittings & Interpretation of SANS Data 59
3.4.1 SANS Diffractogram Reduction 60
3.4.2 Monodisperse SANS Model 61
3.4.3 Polydisperse SANS Model 63
3.4.4 Model Comparison 64
3.5 Discussion 65

4 Experimental **69**
4.1 Materials Investigated 69
4.1.1 Sample Fabrication 69
4.1.2 Irradiation Campaign 69
4.2 Mechanical Testing 75
4.3 APT Data Collection & Analysis Methods 76
4.3.1 APT Sample Preparation 76
4.3.2 APT Data Acquisition 77
4.3.3 APT Data Analysis 78
4.4 SANS Data Collection & Analysis Methods 78
4.4.1 SANS Data Acquisition 78
4.4.2 SANS Data Analysis 79
4.5 STEM/EDS Data Collection & Analysis Methods 79

4.5.1 STEM/EDS Sample Preparation 79
4.5.2 STEM/EDS Data Acquisition 80
4.6 Results 81
4.6.1 APT Results 81
4.6.2 SANS Results 88
4.6.3 STEM/EDS Results 89
4.7 Discussion 90
4.7.1 Comparing SANS & APT Data 90
4.7.2 Trends and Significance of Observed Precipitate Microstructures 94
4.7.3 Comparison of Precipitation Kinetics to LSW/UOKV Model Behavior 97
4.7.4 Impact of Findings on Fe-Cr-Al In-Reactor Performance 101

5 Conclusions **103**
5.1 Summary 103
5.2 Contribution to the State of the Art 105
5.3 Future Work 106

Appendix A **109**

Appendix B **122**

Appendix C **132**

Appendix D **136**

Appendix E **160**

Appendix F **168**

References **184**

LIST OF TABLES

3.1 An example of the change in isotopic abundances for the primary constituent elements of a Fe-18Cr-5.8Al specimen following irradiation in HFIR to 7 dpa at 320 °C and decay for approximately 1 yr, corresponding to the time between specimen discharge and data collection. Predicted by the ORIGEN-2.2 Isotope Generation and Depletion Code. 40
3.2 Comparison of reported α' precipitate compositions resulting from using the standard maximum separation method and the two aberration correction techniques detailed in this chapter for a Fe-18Cr-5.8Al specimen following neutron irradiation to 7 dpa at 320°C. 57
3.3 Comparison of reported Ni-Mn-Si precipitate compositions resulting from using the standard maximum separation method and the two aberration correction techniques detailed in this chapter for an irradiated Ringhals RPV surveillance material specimen. 58
3.4 Comparison of reported Cr-rich precipitate compositions and average radius resulting from using the standard maximum separation method and the Delaunay triangulation aberration correction technique to the known value for a simulated Fe-Cr data set resulting from the Cameca TipSim software. "Expected" column illustrates that reported composition and radius values do approach the known composition for a given densification factor. 60

4.1 Fe-Cr-Al alloy compositions in both at.% and wt.% [16, 95]. 71
4.2 Summary of calculated specimen temperatures according to results of the finite element model developed using the ANSYS Workbench software. The minimum and maximum temperatures listed indicate a 95% temperature span by area. 73
4.3 Summary of irradiation conditions for each target capsule exposed in HFIR. 74
4.4 Summary of results of APT analysis of α' precipitates for all compositions and dose conditions studied. Compositions are given in at.% 83
4.5 Summary of results of SANS analysis of α' clustering for all composition and dose conditions studied. Scattering contrast was determined using matrix and precipitate compositions determined through APT analyses. 89

LIST OF FIGURES

2.1 Schaeffler-Schneider diagram for predicting phase in Fe-based alloys. Adapted from [29]. 6
2.2 Fe-Cr binary phase diagram. Reproduced from [35]. 7
2.3 Effect of Cr and Al additions on the workability of Fe-based alloys. Reproduced from [33]. 8
2.4 Effects of Cr and Al on the passivation and survivability of several model and commercial Fe-Cr-Al alloys following exposure at 1200°C in either Ar-50%H_2O or 100%H_2O. Open symbols represent Ar-50%H_2O tests, while closed symbols represent 100%H_2O, with half colored symbols indicated that it was tested in both environments, but only passivated in Ar-50%H_2O. Reproduced from [37]. 9
2.5 Schematic of a radiation damage event, in which incident energetic particle (a) displaces a lattice atom, resulting in a vacancy (b) and an interstitial (c), also known as Frenkel pair. 11
2.6 Comparison of damage cascade morphologies for different types of incident particles of the same energy. $\bar{T}$ is the average energy transferred to the PKA and ε is the percentage of defects produced that are freely migrating. Reproduced from [39]. 13
2.7 Free energy vs. Composition Curve at temperature T_1 (top) for the phase diagram demonstrating a miscibility gap (bottom). Reproduced from [43]. . 18
2.8 Proposed ternary phase diagram for Fe-Cr-Al alloys. Adapted from [26]. . . 20
2.9 Comparison of miscibility and spinodal gaps for pure Fe-Cr and Fe-Cr-11at.%Al-0.5at.%Ti, as calculated by Capdevila et al. using the CALPHAD software [55]. 21
2.10 Field ion image of $\langle 110 \rangle$ zone axis of tungsten. Reproduced from [65]. 23
2.11 Diagram depicting internal configuration of (a) a straight flight path local electrode atom probe, and (b) a reflectron-equipped local electrode atom probe. Reproduced from [66]. 24
2.12 Comparison of TOF spectra obtained on a 304 stainless steel analyzed using (a) a straight flight path LEAP 3000X Si atom probe, and (b) a reflectron-equipped LEAP 3000 HR atom probe in the voltage-pulsed mode. Reproduced from [66]. 25

2.13 Illustration of how trajectory aberrations affect the atomic density of a reconstruction in the viscinity of precipitates. Reproduced from [66]. 28

3.1 Demonstration of the acute sensitivity of the reported precipitate number density and volume fraction as determine by SANS on the assumed matrix and precipitate phase compositions. Other inputs acquired from SANS measurement of a Fe-18Cr-5.8Al specimen irradiated to 7 dpa at 320°C. . . . 36
3.2 Example proximity histogram, averaged over 5 α' precipitates in an irradiated Fe-18Cr-5.8Al specimen from the current work. Reproduced from [95]. . . . 42
3.3 Example of computational methodology for evaluating matrix and cluster densities using the cubic binning methodology in a sample Fe-Cr-Al data set. A step-by-step description of the process is provided in the text. 44
3.4 Summarized sensitivity analysis for the effects of user-defined inputs (bin size and threshold density) on the densification factor determined by the cubic-binning methodology. 47
3.5 Comparison of cells resulting from Voronoi tessellation (left) and Delaunay triangulation (right) performed on the same two-dimensional data set. . . . 48
3.6 Three-dimensional cells resulting from a Delaunay triangulation of sample precipitate. Black circles represent precipitate atoms, red arrows highlight concave volumes filled by the tessellation algorithm. 50
3.7 (a) Representative Delaunay cell volume distribution for precipitates in a sample Fe-Cr-Al data set. (b) Sensitivity of calculated densification factor to the assigned maximum cell volume threshold. 51
3.8 Three-dimensional cells resulting from a Delaunay triangulation of sample precipitate following maximum volume thresholding step. 52
3.9 (a) Representative Delaunay circumsphere radius distribution for precipitates in a sample Fe-Cr-Al data set. (b) Sensitivity of calculated densification factor to the assigned maximum Delaunay circumsphere radius. 53
3.10 Comparison of Delaunay circumsphere radius distributions for the precipitate volumes (orange), the total reconstruction volume (light blue), and the matrix volume (dark blue, determined by difference). Fits of the theoretical distributions according to Eq. 3.4 are given by the red and green curves for the precipitate and matrix volumes, respectively. 54

3.11 Raw, 2-dimensional SANS diffractogram from the Fe-18Cr-5.8Al specimen following irradiation to 1.8 dpa at 382°C, collected using the medium-length detector configuration. 61
3.12 1-dimensional SANS intensity curve following data reduction of the 2-dimensional diffractogram in Figure 3.11 and diffractograms from short- and long-length detector configurations. Model fit assuming a monodisperse distribution of spherical precipitates is shown for comparison. 62
3.13 Comparison of (a) the assumed ion trajectory behavior responsible for the observed artifacts and (b) what is perhaps more representative behavior of the physics involved in field evaporation in the vicinity of different phases. . 66

4.1 Optical micrographs for the four Fe-Cr-Al model alloys investigated demonstrating initial grain structure. Images courtesy of Y. Yamamoto (ORNL). . . 70
4.2 SS-J2 subsized tensile specimen geometry used in the HFIR irradiation. Reproduced from [16]. 70
4.3 (a) Diagram of experimental positions in the HFIR core. (b) Image of a full-scale model of the HFIR core assembly. 72
4.4 Diagram of irradiated target capsule design, capable of housing 36 SS-J2 subsized tensile specimens. Reproduced from [107]. 72
4.5 Temperature contour plots in °C for (a) inner most tensile specimens (TENSILE 1), (b) middle layer tensile specimens (TENSILE 2), (c) outer most tensile specimens (TENSILE 3), and (d) SiC thermometry specimens. Full design analysis and calculation (DAC) document is found in Appendix D. 73
4.6 Result of dilatometric analysis of a SiC thermometry bar from the FCAY-04 irradiation capsule. 75
4.7 SEM micrograph of a representative sharpened microtip prepared for APT analysis. 77
4.8 SEM micrograph of a representative specimen lamella prepared for STEM/EDS analysis. 80
4.9 Representative APT reconstructions for the various compositions of Fe-Cr-Al irradiated to 7 dpa at 320 °C, in which a unique color is assigned to each α' precipitate detected using the maximum-separation method cluster finding algorithm native to IVAS. Figures are cropped to $50 \times 50 \times 100$ nm volumes to allow for direct comparison. 84

4.10 Representative Cr atom maps show evidence of clustering in all Fe-Cr-Al compositions studied when irradiated to 7 dpa at 320 °C. Maps represent a thickness of 20 nm. 85
4.11 Representative APT reconstructions for the various irradiation conditions studied for Fe(18)CrAl, in which a unique color is assigned to each α' precipitate detected using the maximum-separation method cluster finding algorithm native to IVAS. Figures are cropped to $50 \times 50 \times 100$ nm volumes. 86
4.12 Representative Cr atom maps illustrate the progression of α' clustering in Fe(18)CrAl as radiation dose is increased up to 7 dpa. 87
4.13 Scattering intensities of model Fe-Cr-Al specimens obtained by SANS analysis after irradiation, (a) for varying alloy contents irradiated to 7 dpa at 320 °C, and (b) for varied irradiation conditions for the Fe-18Cr-5.8Al alloy composition. 88
4.14 (a) STEM-ADF image, acquired on the [100] zone axis. (b) STEM/EDS map for Cr-K_α x-rays. (c) Color overlay of ADF image and EDS map. All images from the Fe-18Cr-5.8Al alloy irradiated to 7.0 dpa at 320°C. 91
4.15 High-angle annular dark-field STEM image and x-ray maps derived from EDS spectrum images showing both α' precipitates (green clusters) and RIS at a grain boundary for the Fe-12Cr-8.7Al model alloy following irradiation to 7 dpa at 320°C. Denuded zones on the order of 10-20 nm in width are seen on either side of the boundary. 92
4.16 Comparison of SANS data from the current study with results published in literature for various aged and irradiated Fe-Cr and Fe-Cr-Al alloys [19–22, 25, 49, 50, 53, 118–120]. Data points are color-coded by source and were determined through SANS investigations unless otherwise indicated. 96
4.17 Comparison of precipitate coarsening trends with behavior predicted by the LSW/UOKV models. Reasonable fits to the SANS results are achieved, with the plot shown in (a) demonstrating $\overline{R}_{\alpha'} \propto t^{1/3}$ and (b) demonstrating $N_{\alpha'} \propto t^{-1}$ for the irradiated Fe-Cr-Al alloys. Dashed lines indicate least squares fit of present data to predicted model trends for each Fe-Cr-Al composition studied. 100

E.1 Representative reconstructions of individual major alloying elements for the as-received Fe-18Cr-5.8Al specimen. Reconstruction dimensions are approximately 74.0 nm $\times$ 72.8 nm $\times$ 91.5 nm. 161

E.2 15 nm-thick slices of representative reconstructions of individual major alloying elements for a Fe-18Cr-5.8Al specimen following irradiation to 0.8 dpa at 355 °C. Reconstruction dimensions are approximately 74.0 nm × 75.1 nm × 171.3 nm. 162
E.3 15 nm-thick slices of representative reconstructions of individual major alloying elements for a Fe-18Cr-5.8Al specimen following irradiation to 1.8 dpa at 382 °C. Reconstruction dimensions are approximately 74.1 nm × 73.6 nm × 299.6 nm. 163
E.4 15 nm-thick slices of representative reconstructions of individual major alloying elements for a Fe-18Cr-5.8Al specimen following irradiation to 7.0 dpa at 320 °C. Reconstruction dimensions are approximately 58.5 nm × 59.4 nm × 175.3 nm. 164
E.5 15 nm-thick slices of representative reconstructions of individual major alloying elements for a Fe-15Cr-7.7Al specimen following irradiation to 7.0 dpa at 320 °C. Reconstruction dimensions are approximately 54.9 nm × 57.8 nm × 386.1 nm. 165
E.6 15 nm-thick slices of representative reconstructions of individual major alloying elements for a Fe-12Cr-8.7Al specimen following irradiation to 7.0 dpa at 320 °C. Reconstruction dimensions are approximately 98.3 nm × 99.8 nm × 588.4 nm. 166
E.7 15 nm-thick slices of representative reconstructions of individual major alloying elements for a Fe-10Cr-9.3Al specimen following irradiation to 7.0 dpa at 320 °C. Reconstruction dimensions are approximately 83.6 nm × 83.9 nm × 182.6 nm. 167

NOMENCLATURE

ADF	annular dark field
APT	atom probe tomography
ATF	accident-tolerant fuels
BCC	body-centered cubic
BF	bright field
CAES	Center for Advanced Energy Studies
CALPHAD	Computer Coupling of Phase Diagrams and Thermochemistry
CNMS	Center for Nanophase Materials Science
CSL	coincidence site lattice
DAC	design analysis and calculation
DBH	dispersed-barrier hardening
DF	dark field
DFT	density functional theory
DOE	Department of Energy
dpa	displacements per atom
EDS	energy-dispersive x-ray spectroscopy
FCC	face-centered cubic
FEG	field emission gun
FIB	focused ion beam
FIM	field ion microscope

GP	general purpose
HAADF	high-angle annular dark field
HFIR	High Flux Isotope Reactor
IASCC	irradiation-assisted stress corrosion cracking
ICP-OES	inductively coupled plasma optical emission spectroscopy
IMET	Irradiated Materials Examination and Testing
IVAS	Integrated Visualization & Analysis Software
LAMDA	Low Activation Materials Development & Analysis
LEAP	local electrode atom probe
LOCA	loss-of-coolant accident
LSW	Lifshitz-Slyozov-Wagner
LWR	light water reactor
MaCS	Microscopy & Characterization Suite
MVSA	multivariate statistical analysis
NMS	Ni-Mn-Si-rich
ODS	oxide dispersion-strengthened
ORNL	Oak Ridge National Laboratory
PIE	post-irradiated examination
PKA	primary knock-on atom
R&D	research and development
RIS	radiation-induced segregation
RPV	reactor pressure vessel

SANS	small-angle neutron scattering
SEM	scanning electron microscope/microscopy
STEM	scanning transmission electron microscope/microscopy
TEM	transmission electron microscope/microscopy
THEIG	Thermal Hydraulics and Irradiation Engineering Group
TOF	time-of-flight
UOKV	Umantsev-Olson-Kuehmann-Voorhees

ABSTRACT

Fe-Cr-Al alloys are currently being considered for accident tolerant light water reactor fuel cladding applications due to their superior high temperature oxidation and corrosion resistance compared to Zr-based alloys. However, precipitation of the Cr-rich α' phase during exposure to LWR operational environments can result in application-limiting hardening and embrittlement. To study this effect, four Fe-Cr-Al model alloys with compositions between 10–18 at.% Cr and 5.8–9.3 at.% Al have been neutron-irradiated in the High Flux Isotope Reactor at a target temperature of 320°C to nominal damage doses of up to 7 dpa in order to emulate typical LWR exposure conditions. A correlative microscopy approach involving atom probe tomography, small-angle neutron scattering, and scanning transmission electron microscopy coupled with energy dispersive x-ray spectroscopy was employed to study the resulting precipitate microstructure. This approach necessitated the development of various analysis techniques to allow for cross-comparison between experimental techniques, including a novel method for correcting for trajectory aberration artifacts in atom probe data sets through phase density comparison. Successful correlation of results from these techniques allows for the individual limitations of each to be overcome and enables the detailed microstructural information gleaned from highly localized atom probe tomography analyses to be extrapolated to bulk alloy behavior. Precipitation response was found to increase with Cr content, while Al additions appeared to partially destabilized the α' phase, resulting in precipitate compositions with reduced Cr content compared to binary Fe-Cr systems. Observed precipitate evolution with radiation dose indicates a diffusion-limited coarsening mechanism that is similar to what is observed in the thermally aged system. This work represents the current state-of-the-art on both techniques for analysis of α' precipitate microstructures and the processes and mechanisms governing its formation in neutron-irradiated Fe-Cr-Al alloys.

1 INTRODUCTION

Nuclear power is currently an integral part of the United States' energy economy, accounting for 20% of total domestic electricity generation over the past two decades [1]. With a vast majority of the remaining energy generation coming from fossil fuels, nuclear power also contributes the most carbon-free energy to the U.S. energy grid. Due to greenhouse gas emissions and instabilities in the markets associated with fossil fuels, nuclear power and other clean renewable energy sources are expected to play a key role in addressing rising energy demand in the coming decades while attempting to curb environmental pollution and climate change. Meeting these goals will require the development and construction of modern advanced commercial reactor designs in addition to upkeep and lifetime extensions for the current fleet of operating commercial light water reactors (LWRs).

Materials research and development is a central component for advancing nuclear power, as both the existing and next-generation reactor designs face unique materials challenges. LWRs are demanding environments for materials performance due to the combined effects of long-term exposure to high neutron fluences and high temperature aqueous environments. Furthermore, most of the proposed advanced designs operate at even greater temperatures (> 288 °C) and utilize corrosive coolants, such as molten salt or liquid sodium metal [2]. Construction of these systems require materials that can withstand these harsh environmental conditions while maintaining structural integrity over 60+ year operating lifetimes. As such, developing advanced, radiation-tolerant materials that are tailored to these environments is crucial for maintaining existing LWRs and for deployment of next-generation nuclear technologies.

A key materials vulnerability in existing LWRs was highlighted during the events at the Fukushima Daiichi Nuclear Power Plant in early 2011. A magnitude 9.0 earthquake followed by a 12 m tall tsunami initiated a loss-of-coolant accident (LOCA), causing nuclear reactor core temperature to rise [3]. In the resulting high-temperature steam environment the Zr-based cladding material, typically inert under normal operating conditions, oxidized exothermically, adding additional heat to the reactor core while producing hydrogen gas, which would later vent and cause explosions in the reactor containment buildings. These events prompted the United States Department of Energy (U.S. DOE) to launch a national research initiative with the goal of designing new, accident-tolerant fuels (ATF) and fuel cladding materials to deploy in place of the traditional Zr/UO_2 fuel form that tends to exacerbate accident scenarios [4]. Several different ATF concepts are being developed concurrently. These concepts seek to enhance accident tolerance by replacing Zr-based claddings with advanced steels or ceramics, coating the current Zr-based alloys with corrosion/oxidation barrier materials, and replacing UO_2 with high density/high thermal conductivity fuels such as UN and U_3Si_2.

Of these alternative cladding concepts, Fe-Cr-Al alloys have shown great promise for ATF cladding applications and have the potential to be utilized for other in-core components. This is primarily due to their excellent high temperature oxidation and corrosion resistance due in part to the formation of a protective alumina (α-Al_2O_3) scale, extending alloy survivability to temperatures of at least 1300 °C [5–7]. Additionally, it shares the resistance to radiation-induced void swelling characteristic of high-Cr ferritic alloys [8, 9]. Current research efforts are focused on developing an optimized candidate Fe-Cr-Al alloy that maximizes high-temperature aqueous corrosion resistance [10] while maintaining adequate performance with respect to mechanical properties [11–13], processability

[11, 14], radiation tolerance [8, 15, 16], and reactor core neutronics [17].

Historically, high-Cr ferritic alloys have not been employed in nuclear applications due to a perceived susceptibility to radiation-induced hardening and embrittlement. The primary mechanism for this phenomenon is the precipitation of the low-temperature stable (< 475 °C), Cr-rich α' phase [18]. Long-term exposure to such temperatures results in the decomposition of body-centered cubic (BCC) high-Cr ferritics into an Fe-rich α matrix phase populated with Cr-rich α' precipitates [18, 19]. This process has been extensively characterized in the Fe-Cr binary system [18–24] and has been shown to form in the Fe-Cr-Al ternary alloy system as well [25–27]. While the kinetics of this precipitation process are typically slow, irradiation has been shown to accelerate this process though the production of freely-migrating defects and enhanced diffusion [18, 20, 22].

This dissertation seeks to detail a systematic study of α' precipitation in a series of neutron-irradiated Fe-Cr-Al model alloys with the goal of elucidating the dose evolution of precipitate morphology and determining the composition dependence of the precipitation response. This was accomplished through a rigorous post-irradiation examination (PIE) campaign utilizing multiple microstructural characterization techniques including atom probe tomography (APT), small-angle neutron scattering (SANS), and scanning transmission electron microscopy coupled with energy dispersive x-ray spectroscopy (STEM/EDS). Examination of data collected from each of these complementary techniques side-by-side allows for a portion of their individual limitations to be overcome, resulting in a more wholistic and robust analysis of the α' precipitation phenomena in Fe-Cr-Al alloys. The advantages and limitations of these techniques are discussed in

more detail in Chapter 2.

The organization of this document is as follows: Chapter 2 provides an overview of Fe-Cr-Al alloys properties and metallurgy, precipitation phenomena in metals, the mechanisms of radiation damage in materials, and the individual techniques used to study material microstructure following irradiation. Chapter 3 highlights how correlative microscopy can result in improved characterization and understanding of the observed precipitate microstructure and discusses the technique development required to do so. Chapter 4 details the experimental work performed, including Fe-Cr-Al alloy sample fabrication and preparation, irradiation treatment, and post-irradiation examination, concluding with a presentation and discussion of findings. Finally, Chapter 5 concludes with closing statements and a discussion of suggested future work.

2 BACKGROUND

2.1 Overview of Fe-Cr-Al Alloy Properties & Metallurgy

Fe-Cr-Al alloys have historically been employed as electrical-resistance heating elements owing to the combined high electrical resistivity, high melting point, high-temperature oxidation resistance, and suitable mechanical properties exhibited by these materials [28]. The Schaeffler-Schneider diagram (Fig. 2.1) for predicting the phase of steels based on composition demonstrates that high-Cr Fe-based alloys often have some martensitic structure [29]. However, Al is a ferrite stabilizer and contributes heavily to the Cr equivalent, resulting in the Fe-Cr-Al alloys considered being fully ferritic in nature [30]. While the body-centered cubic structure of Fe-Cr-Al alloys is the primary reason for its perceived radiation tolerance and radiation-induced swelling resistance [31, 32], it also results in poor high-temperature strength [32, 33], though this can be improved through both solid solution- or oxide dispersion-strengthening.

High-Cr ferritic steels have a well-known susceptibility to hardening and embrittlement even in unirradiated materials due to precipitation of both the low-temperature stable α' phase investigated herein, in addition to the σ intermetallic compound at intermediate temperatures [33, 34]. The compositions and temperatures vulnerable to these transformations are identified for the binary Fe-Cr system in the phase diagram (Fig. 2.2). While higher Cr contents are typically more desirable for improved oxidation and corrosion resistance, the degradation of mechanical properties associated with both the α' and σ phase transformations tends to limit the amount of Cr added to these alloys for applications involving exposure to the susceptible temperatures.

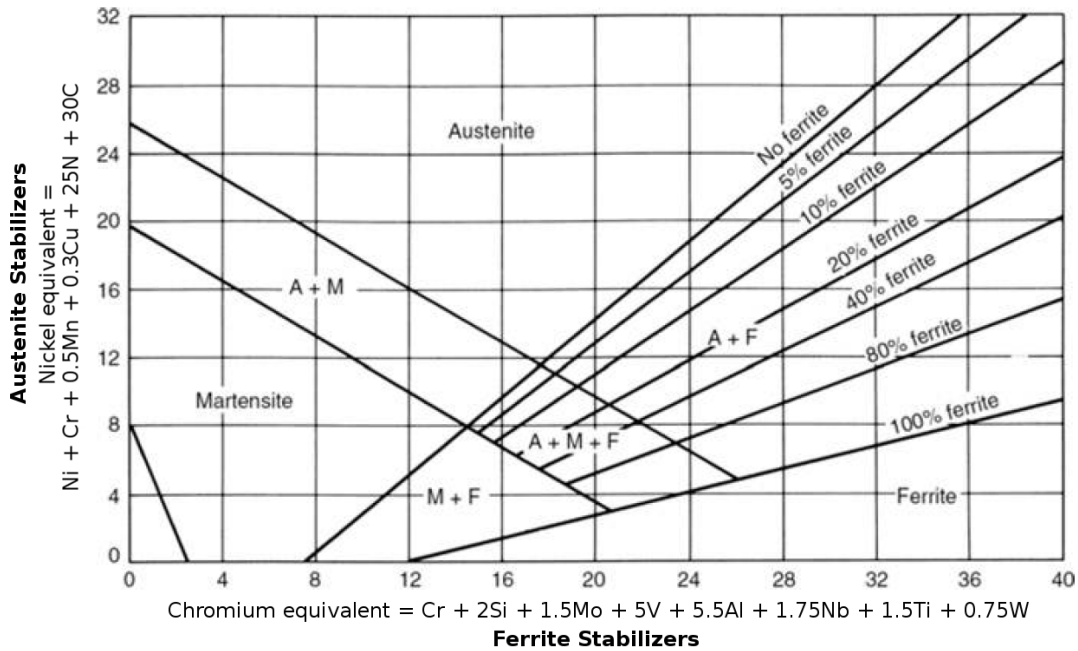

Figure 2.1: Schaeffler-Schneider diagram for predicting phase in Fe-based alloys. Adapted from [29].

As mentioned previously, Al is added to these materials to encourage passivation at high temperatures through the formation of Al_2O_3 scale on the alloy surface. As demonstrated by Wukusick and Collins, a minimum of 2 wt.% Al is necessary to achieve the desired protective behavior in a Fe-25Cr base alloy, with some small amount of yttrium (< 1 wt.%) required to increase oxide scale adhesion and prevent flaking and spallation [36]. However, Al additions in excess of 5 wt.% lead to embrittlement and decreased alloy workability. A large-scope study of physical metallurgy of Fe-Cr-Al alloys performed by Chubb et al. demonstrates the effect of Cr and Al additions on workability of Fe-based alloys, the results of which are shown in Figure 2.3.

For the purpose of alloy oxidation and corrosion performance, especially in high-temperature steam environments typified by LWR accident scenarios, greater alloy

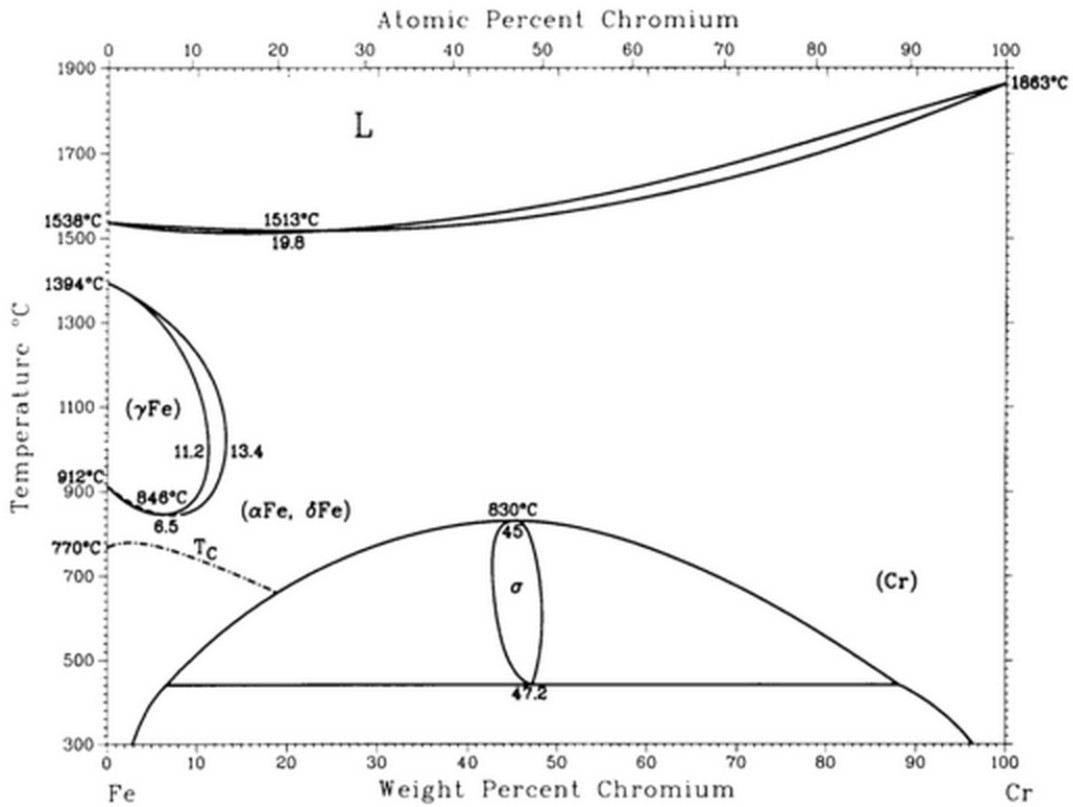

Figure 2.2: Fe-Cr binary phase diagram. Reproduced from [35].

Cr and Al content results in improved alloy passivation and survivability. Pint et al. have demonstrated this by testing several model and commercial Fe-Cr-Al alloys in either Ar-50%H_2O or 100%H_2O environments at 1200°C [37]. As shown in Figure 2.4, insufficient Cr and Al lead to rapid attack and corrosion of the material. As such, designing a Fe-Cr-Al alloy for nuclear applications requires that these major solute additions be balanced in such a way as to mitigate precipitation and embrittlement (Cr) and maintain workability (Al) while maintaining adequate mechanical and oxidation performance.

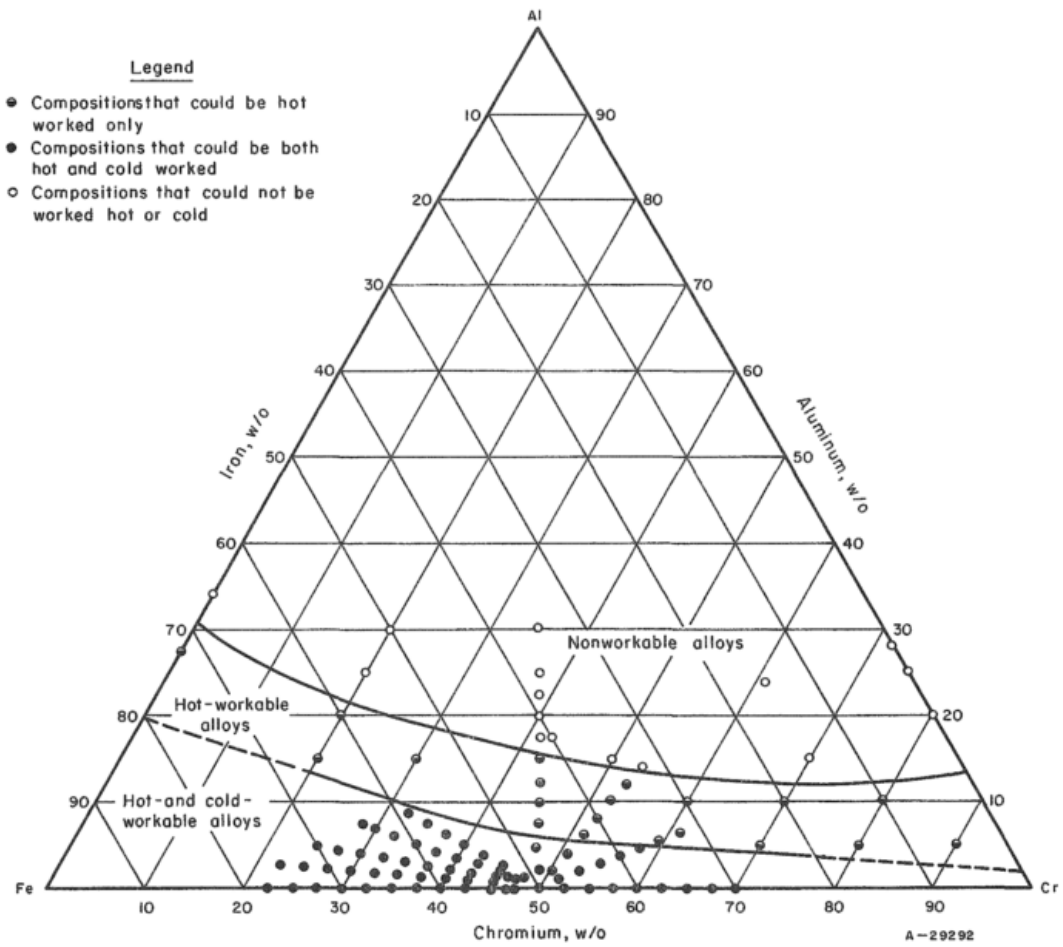

Figure 2.3: Effect of Cr and Al additions on the workability of Fe-based alloys. Reproduced from [33].

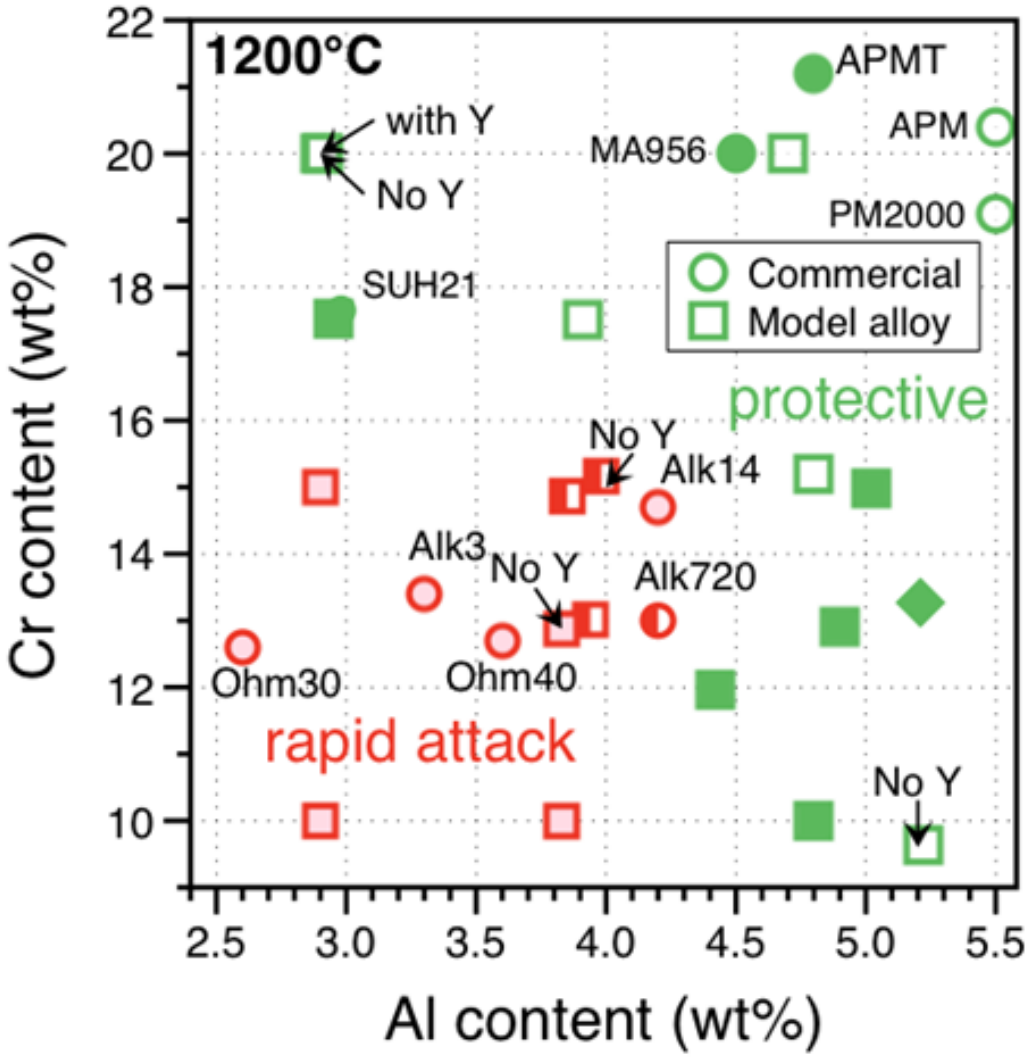

Figure 2.4: Effects of Cr and Al on the passivation and survivability of several model and commercial Fe-Cr-Al alloys following exposure at 1200°C in either Ar-50%H_2O or 100%H_2O. Open symbols represent Ar-50%H_2O tests, while closed symbols represent 100%H_2O, with half colored symbols indicated that it was tested in both environments, but only passivated in Ar-50%H_2O. Reproduced from [37].

2.2 Radiation Damage in Materials

2.2.1 Radiation Damage Mechanism and Kinetics

Understanding the mechanism of how radiation affects the local structure and induces damage is vital to performing an informed study of materials behavior in nuclear systems. In a radiation damage event an incident particle imparts energy to a lattice atom. If the incident particle has sufficient energy it will displace the atom from its lattice site, creating a primary knock-on atom (PKA). The PKA will then interact with other lattice atoms, displacing them as well if it has sufficient energy, resulting in a collision cascade. The PKA and following displaced atoms come to rest at interstitial sites, leaving behind vacancies at their original lattice positions. This process is illustrated in Figure 2.5. Though most of the resulting interstitials and vacancies recombine and annihilate during the cascade quench, a small portion remain in the material as freely migrating point defects. The net result of these events is a higher concentration of point defects in the material compared to the thermal equilibrium concentration at a given temperature.

The damage rate equation (R_D) allows us to model radiation damage in a known material and particle spectrum:

$$R_D = N \int_{\check{E}}^{\hat{E}} \phi(E_i)\sigma_D(E_i)dE_i \tag{2.1}$$

where N is the lattice atom density, $\phi(E_i)$ is the energy-dependent radiation flux and $\sigma_D(E_i)$ is the energy-dependent displacement cross section. The displacement cross

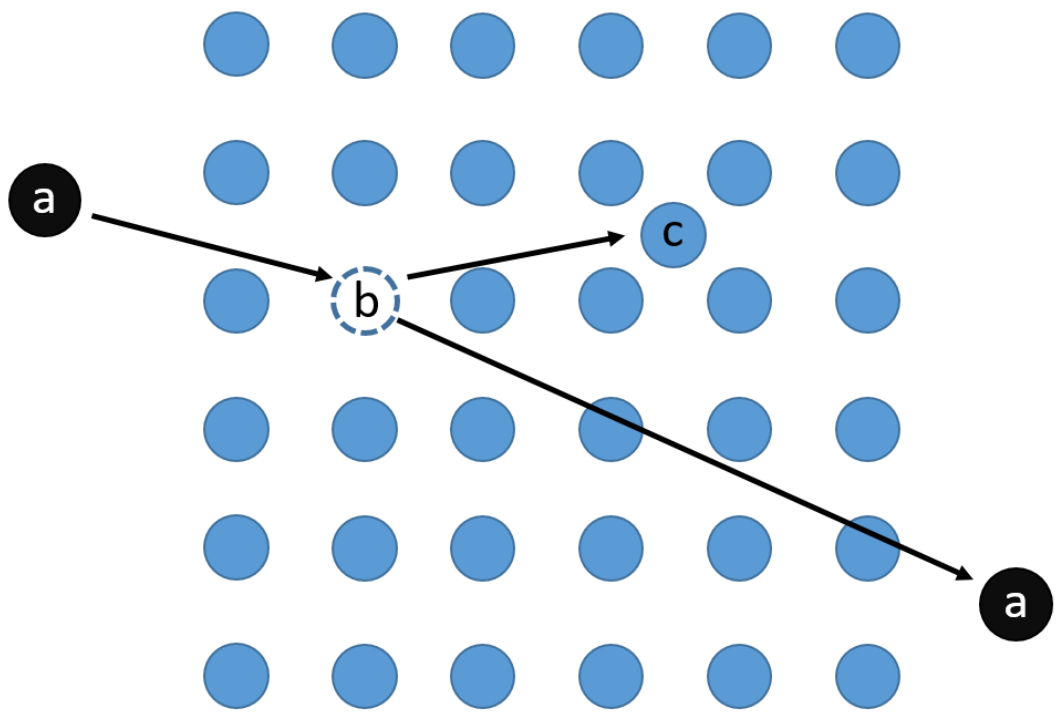

Figure 2.5: Schematic of a radiation damage event, in which incident energetic particle (a) displaces a lattice atom, resulting in a vacancy (b) and an interstitial (c), also known as Frenkel pair.

section represents the probability for a lattice atom to be displaced by incident particles and is given by:

$$\sigma_D(E_i) = \int_{\check{T}}^{\hat{T}} \sigma(E_i, T)\nu(T)dT \tag{2.2}$$

where $\sigma(E_i, T)$ is the energy transfer cross section, representing the probability that a particle of energy E_i will impart a recoil energy T to a lattice atom in a collision, and $\nu(T)$ is the number of atoms displaced in such a collision event [38]. The energy

transfer cross section, and thus displacement rate, is dependent on the incident particle type and energy. For neutron interactions, the damage event can be thought of as a purely ballistic collision and a hard-sphere approximation is used. However, for incident protons, atoms, or charged particles that are often used to simulate neutron damage in ion beam laboratories, this approximation becomes invalid as the energy transfer occurs primarily through electronic and nuclear interactions. A Coulomb, screened Coulomb or Born-Mayer potential is used to model these interactions depending on the minimum separation distance. Consequently, particles of different energies and types induce different damage cascade morphologies. Neutrons and heavy charged particles deposit most of their energy in a relatively small volume, resulting in large damage cascades where most of the defects produced either recombine or cluster and become immobile. Protons distribute their energy over a wider area and produce several smaller, more localized damage cascades with a larger percentage of freely migrating defects. This effect is illustrated in Figure 2.6.

Eq. 2.1 and Eq. 2.2 are typically used for quantifying neutron damage in reactor environments. However, the integrals are often non-trivial to solve; Eq. 2.1 can be simplified to give a rough approximation of radiation damage. By assuming isotropic and purely elastic scattering, Eq. 2.1 reduces to:

$$R_D = N\sigma_s \left(\frac{\gamma E_i}{4E_d}\right) \Phi \tag{2.3}$$

with

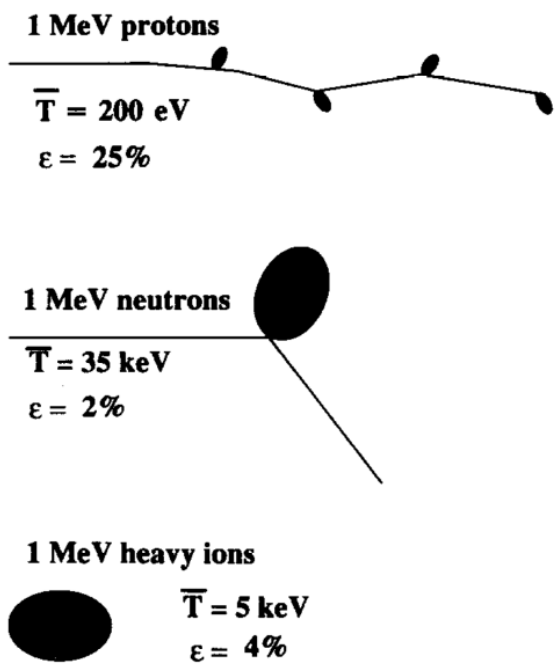

Figure 2.6: Comparison of damage cascade morphologies for different types of incident particles of the same energy. $\bar{T}$ is the average energy transferred to the PKA and ε is the percentage of defects produced that are freely migrating. Reproduced from [39].

$$\gamma = \frac{4M_1M_2}{(M_1 + M_2)^2} \tag{2.4}$$

where E_i is the average neutron energy, Φ is the total neutron flux above energy E_d/γ, E_d is the displacement energy for a lattice atom, and M is the particle mass. The quotient in Eq. 2.3 is the number of Frenkel pairs produced per neutron.

Due to the number of variables involved in how different particles impart damage into a given material, radiation damage is typically reported in units of displacements per atom (dpa) as opposed to in terms of particle fluence. Dpa is defined as the average

number of times an atom is displaced from a lattice site for a given fluence of particles. Thus, in a material that has been irradiated to 1 dpa, every lattice atom has, on average, been displaced once. Normalizing radiation damage in this fashion allows for cross-comparison of data collected from different irradiation experiments, especially those utilizing particles with different energy spectra.

2.2.2 Radiation-Induced Microstructural Features

The net result of radiation damage is an increased concentration of point defects and defect clusters as a result of the damage cascades. At the elevated temperatures typical to reactor systems, these point defects diffuse through the bulk lattice, forming 2D and 3D defects such as dislocations, dislocation loops, voids, bubbles and stacking faults. A high density of such defects within the crystal structure leads to changes in material properties due to phenomena such as irradiation hardening, irradiation creep, void swelling and helium embrittlement. An example of such damage and resulting defect structures can be found even in simple alloy systems such as Ni-Cr binary alloys, where dislocation loops, voids, and radiation-induced segregation (RIS) were observed. A more detailed discussion on the formation and quantitative nature of these defects, which were not the focus of later discussions, can be found in prior work by the author, summarized in Appendix F.

This increased point defect concentration is also known to influence precipitation. The kinetics of precipitation can be accelerated by the enhanced diffusion such that phase transformation occurs more rapidly than is typically expected. Additionally, clustering induced by the damage cascade or other radiation-induced defect structures can serve as nucleation sites for precipitation by the nucleation and growth mechanism.

Conversely, ballistic mixing effects can destabilize existing precipitates, resulting in precipitate dissolution that is sometimes observed in low-temperature irradiations of oxide dispersion-strengthened (ODS) alloys [40]. Finally, local changes in composition due to RIS can cause precipitation of phases that are not thermodynamically favorable in the original bulk composition.

2.3 Precipitation in Metals

2.3.1 Thermodynamics of Precipitation

The formation of precipitates, like all structural transformations at a constant temperature and pressure, is driven by a reduction in Gibbs free energy from the original to the final structure. As an example we consider the mixing of a simple binary system (which can be extended to the ternary system of interest in this study):

$$x_A A + x_B B \rightleftharpoons A(x_A)B(x_B) \tag{2.5}$$

where A and B are end-members of a solid solution series that mix to form an intermediate phase of mole fraction x_A, x_B, with $x_A + x_B = 1$ (for a binary system). The Gibbs free energy per mole $\Delta G(T)$, at constant pressure and temperature, T, is then expressed as:

$$\Delta G(T) = x_A G_A^0(T) + x_B G_B^0(T) + \Delta G_{mix} \tag{2.6}$$

where $G_A^0(T)$ and $G_B^0(T)$ are the standard Gibbs energies of the pure end-members A and B, and the Gibbs energy of mixing ΔG_{mix} consists of both an enthalpy ΔH_{mix} and entropy ΔS_{mix} term:

$$\Delta G_{mix} = \Delta H_{mix} - T\Delta S_{mix} \tag{2.7}$$

The enthalpy of mixing term is controlled by the energetics of the interactions, where a positive value of ΔH_{mix} suggests a preference for clustering of like species and precipitation, whereas a negative ΔH_{mix} indicates a bias for ordering of unlike species and the formation of intermediate compounds [41]. The entropy of mixing is given by:

$$\Delta S_{mix} = k_B(N_A \ln x_A + N_B \ln x_B) \tag{2.8}$$

where N_A and N_B are the number of atoms of each species and k_B is the Boltzmann constant [42].

There are two primary mechanisms for precipitation in solid solutions. The first is the nucleation and growth mechanism, in which random fluctuations in local composition allows a small region of a new phase to form within the matrix. This highly localized change in crystal structure and/or composition serves as a nucleus that can then grows into the initially untransformed matrix of the original phase. For diffusional phase transformations, this nucleus grows through thermally activated atom transfer across

the interface between the nucleus and the matrix. This transfer from the less stable to the more stable phase results in a decrease in the volume free energy, but the resulting increase in nucleus size causes an increase in the interfacial free energy, requiring that the nucleus achieve some critical radius before it is considered stable.

Conversely, the second mode of transformation is characterized by a highly delocalized demixing of the original matrix phase in which the magnitude of the initial composition change is generally small. This is generally referred to as spinodal decomposition. This process involves uphill diffusion, in which atoms diffuse from regions of low concentration to regions of high concentration, following the gradient in chemical potential instead of the composition gradient. Spinodal decomposition typically occurs in materials with compositions that fall in the spinodal region of the miscibility gap on a phase diagram. This region is bounded by the points where the curvature of the Gibbs free energy with respect to concentration is zero:

$$\frac{d^2G}{dc^2} = 0 \tag{2.9}$$

This relationship is shown graphically in Figure 2.7. Outside of this spinodal region, precipitation usually occurs by the nucleation and growth mechanism. Precipitation will continue by either the nucleation and growth or spinodal decomposition mechanism until the mixture reaches equilibrium and the compositions and volume fractions of the two phases become constant. However, the microstructure will continue to evolve as the new phase coarsens through Ostwald ripening, which is driven by the reduction of interfacial energy between the two phases.

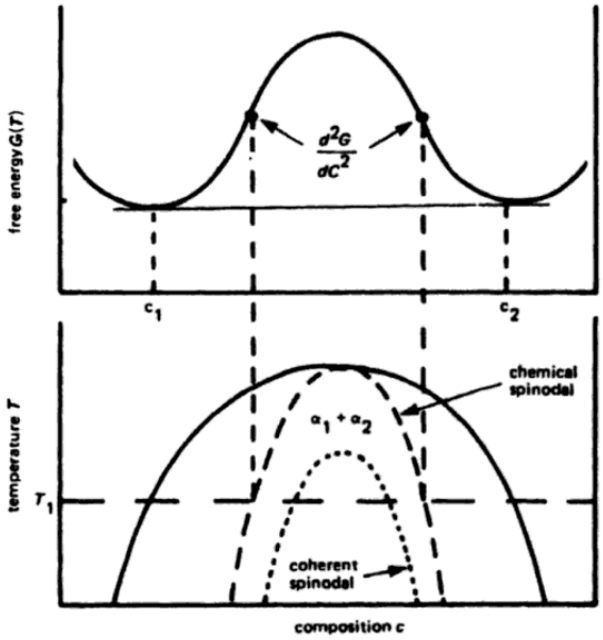

Figure 2.7: Free energy vs. Composition Curve at temperature T_1 (top) for the phase diagram demonstrating a miscibility gap (bottom). Reproduced from [43].

2.3.2 α' Precipitation in High-Cr Ferritics

α' phase precipitation, also historically known at 475°C or 885°F embrittlement, is observed in many aged and irradiated high-Cr (> 10 at.% Cr) ferritic alloys and steels and has been characterized in many model and commercial alloy systems [16, 18–26, 44–53]. These Cr-rich precipitates have a BCC structure that is semi-coherent with the α-Fe matrix and possess a slightly larger lattice parameter (2.88Å vs. 2.87Å) [48]. The strains induced by this misfit are the primary source of embrittlement in these alloys.

While the exact location of the phase boundary in binary Fe-Cr is a topic of debate, the solubility limit at 475°C is typically quoted to be between 9 and 10 at.% Cr [18, 23]. Kobayashi et al. demonstrated that Al additions serve to destabilize the α' phase based on hardness measurements of a diffusion multiple [26]. The resulting ternary phase

diagram proposed by Kobayashi et al. is shown in Figure 2.8. These findings were later verified through density functional theory (DFT) models, which suggested that Al likely affects the precipitate formation energy rather than the interfacial energy [54]. Furthermore, Capdevila et al. calculated the locations of the miscibility and spinodal gaps for the Fe-Cr and Fe-Cr-11at.%Al-0.5at.%Ti systems using the CALPHAD (Computer Coupling of Phase Diagrams and Thermochemistry) software [55, 56], the results of which are shown in Figure 2.9. These results suggest that all Fe-Cr-Al alloys studied in this work (10 to 18 at.% Cr) should be in the nucleation and growth precipitation regime.

Precipitation in the binary Fe-Cr system and other Al-free high-Cr ferritics has been extensively studied in both the thermally aged [19–21, 57] and irradiated [22, 23, 58, 59] conditions typically using either small-angle neutron scattering (SANS) or atom probe tomography (APT). In all cases, a higher volume fraction of precipitates was shown to occur with increasing alloy Cr content and time at temperature/radiation damage dose. Precipitation kinetics are not seen to vary greatly with Cr content [19], but have been shown to be accelerated during irradiation. The accelerated precipitation kinetics under irradiation allows for precipitation to be observed at lower temperatures than is typical [20]. These lower irradiation temperatures corresponded to increases in precipitate volume fraction [20, 59]. While dose rate effects in the neutron-irradiated materials have not been studied explicitly, α' precipitates have not been shown to form in heavy ion irradiation experiments which typically have much higher dose rates [53].

Until recently, studies of α' formation in the ternary Fe-Cr-Al system are limited to thermally aged studies on a pair of model alloys [25] or on the PM 2000™ commercial

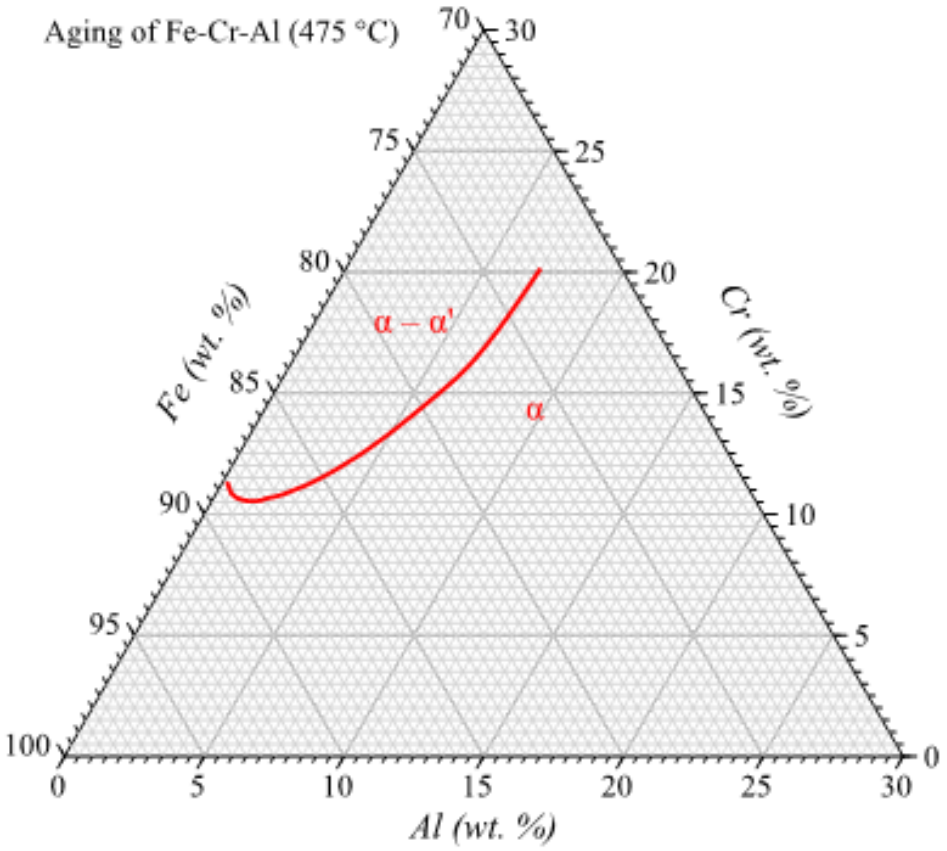

Figure 2.8: Proposed ternary phase diagram for Fe-Cr-Al alloys. Adapted from [26].

ODS Fe-Cr-Al alloy [27, 47, 55, 60, 61]. Messoloras et al. used SANS techniques to study the effect of minor Y additions on precipitation in a Fe-15.7at.%Cr-9.7at.%Al and found that Y appeared to encourage α′ formation, which was speculated to be due to the formation of Y-Al compounds that serve as nucleation sites [25]. The several APT studies by Capdevila et al. showed that the Cr content of precipitates increased with aging time and that Al depleted from precipitate volumes [47, 55, 60]. These studies have also shown that the initial microstructure serves to either promote or delay the precipitation response [27, 61]. The dependence of precipitate composition with time suggests that the phase separation cannot be described using traditional classical nucleation and

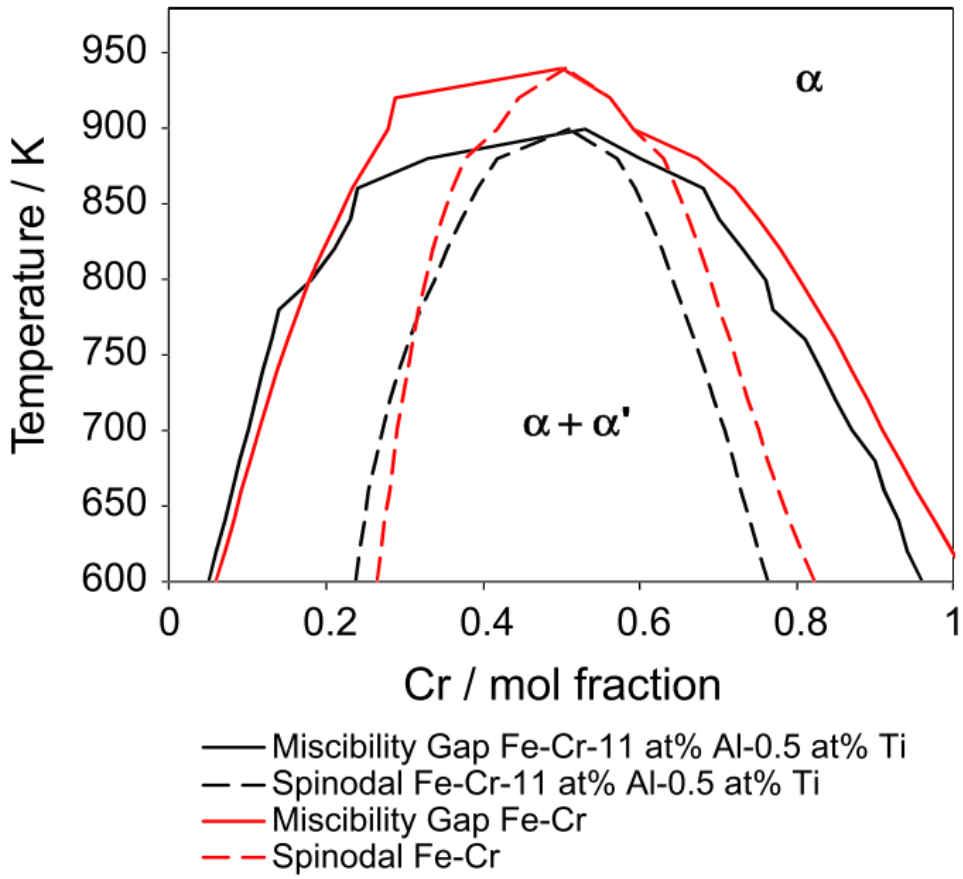

Figure 2.9: Comparison of miscibility and spinodal gaps for pure Fe-Cr and Fe-Cr-11at.%Al-0.5at.%Ti, as calculated by Capdevila et al. using the CALPHAD software [55].

growth or spinodal decomposition models [21]. Although these studies do indicate the presence of α' precipitates in these materials, they were not conducted using simulated normal conditions for LWR fuel claddings and core components. While some irradiation experiments were performed on Fe-Cr-Al alloys by General Electric in the 1960s [62–64], the modern characterization techniques for studying α' precipitation did not exist; hence no determination of the thermodynamics and kinetics of α' formation in irradiated Fe-Cr-Al alloys exists.

Clearly, several knowledge gaps need to be addressed regarding the numerous potential factors affecting precipitation in Fe-Cr-Al alloys. While the exact effect of Al additions can likely be inferred based on the phase diagram, a systematic study on the matter has not been performed. The irradiation effects and precipitate evolution with dose in the Fe-Cr-Al system has yet to be investigated. In addition, typically investigations of these systems have used APT, SANS, and STEM techniques individually, but they are rarely used in a correlative manner. A correlative microscopy approach allows for mitigation of the individual limitations of each technique, ultimately resulting in a more robust and holistic analysis of precipitate microstructure.

2.4 Introduction to Atom Probe Tomography

2.4.1 Principles of Atom Probe Tomography

APT allows for a near atomic scale investigations of material structure and chemistry and is an extremely useful tool for analysis of multi-phase materials. The modern local electrode atom probe (LEAP) instruments used today are advanced adaptations of the field ion microscope (FIM) that were originally used to image the arrangement of atoms on the surface of a sharp needle-shaped specimen. FIMs accomplish this by introducing a noble gas in the vicinity of the positively charged needle specimen, causing ionization of the gas. The gas atoms are then accelerated away from the needle and hit a phosphor screen, generating a two-dimensional image. An example field ion image is shown in Figure 2.10.

In contrast, APT is a destructive analysis technique that utilizes a local electrode to apply high-voltage pulses to a cryogenically-cooled needle specimen, resulting in field

Figure 2.10: Field ion image of ⟨110⟩ zone axis of tungsten. Reproduced from [65].

evaporation of the constituent atoms. The atoms are then accelerated toward a position-sensitive detector and the location of the detection event and the time-of-flight (TOF) allows for the original location and chemical identity of each atom to be determined. The end result is a digital, three-dimensional reconstruction of the original specimen that can be analyzed using computer algorithms and correlation functions. The size of the data set is sample-dependent and is ultimately limited by specimen failure resulting from the stress induced by the voltage pulsing.

There are a few notable variations on the basic LEAP instrument design. Most of the newest models come equipped with a focused high-speed laser that can be pulsed simultaneously with the electrode voltage. When aligned with the specimen tip it allows for increased evaporation efficiency at the cost of reduced TOF resolution due to the

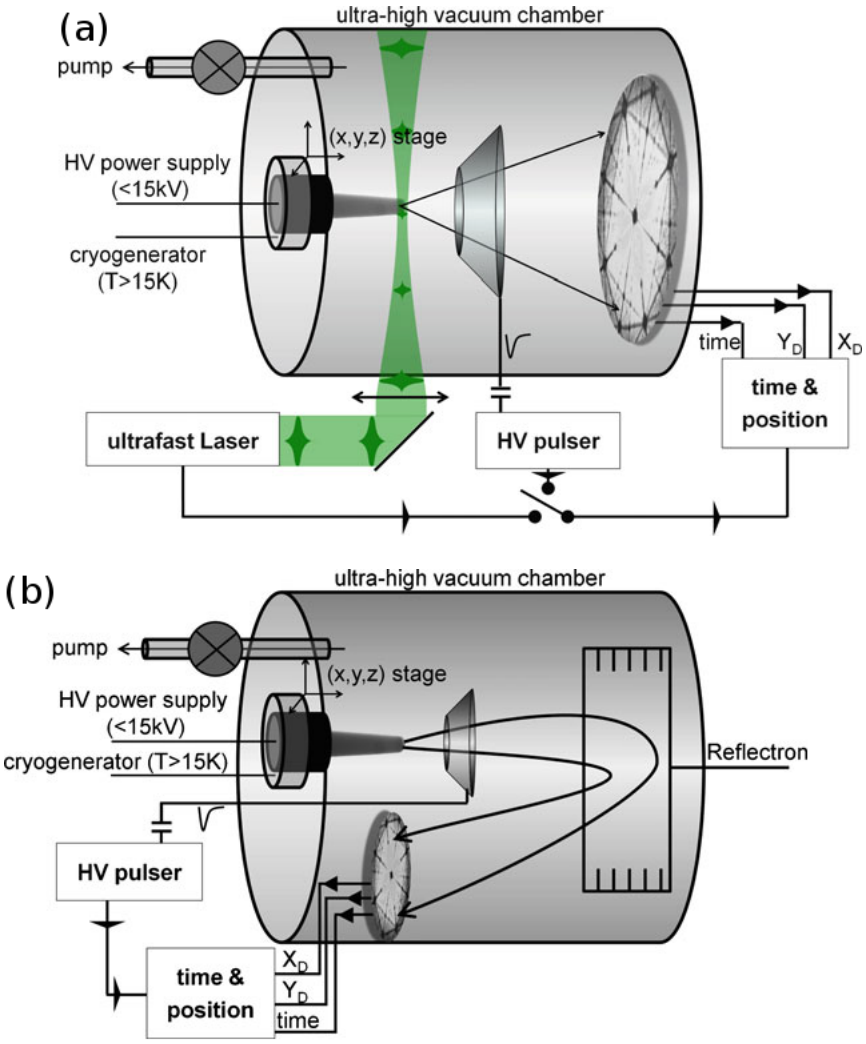

Figure 2.11: Diagram depicting internal configuration of (a) a straight flight path local electrode atom probe, and (b) a reflectron-equipped local electrode atom probe. Reproduced from [66].

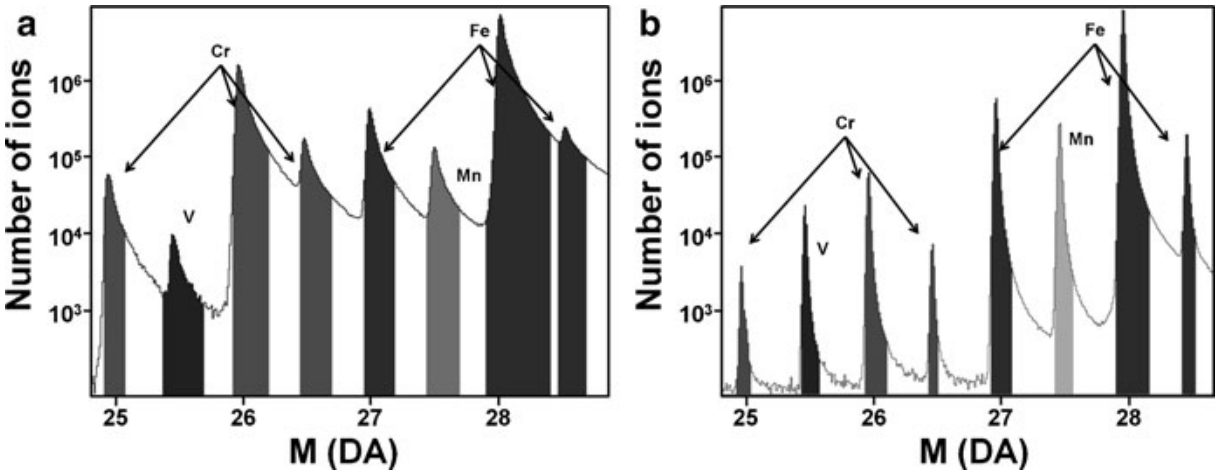

Figure 2.12: Comparison of TOF spectra obtained on a 304 stainless steel analyzed using (a) a straight flight path LEAP 3000X Si atom probe, and (b) a reflectron-equipped LEAP 3000 HR atom probe in the voltage-pulsed mode. Reproduced from [66].

thermal energy imparted to the evaporated ions. Ultimately, this can allow for the collection of larger data sets as the laser can reduce the voltage necessary to evaporate atoms, thus delaying specimen failure. Additionally, the LEAP can either have a straight flight path from the specimen to the detector or be equipped with a reflectron and have a curved flight path. The reflectron is configured in such a fashion that the paths of ions of the same species with different energies are adjusted such that they hit the detector in a more similar amount of time, thus improving TOF resolution. Straight flight path instruments without reflectrons sacrifice this improved TOF resolution for enhanced spatial resolution, as ion path is not perturbed by the reflectron's magnetic field. Simplified schematics of a straight flight path atom probe and a reflectron-equipped atom probe are shown in Figure 2.11a and 2.11b, respectively, and a comparison of the TOF spectra obtained from each for a 304 stainless steel specimen is shown in Figure 2.12.

2.4.2 Quantification of Precipitate Morphology & Chemistry

The three-dimensional, atomic-scale chemical information acquired from APT makes it particularly well-suited for studies of precipitation phenomena. Through the use of various statistical techniques and tools, solute clustering and ordering can be studied even in dilute solid solutions and in the early stages of precipitation when indications of clustering are not visibly identifiable [67]. Some of the methods used to identify these immature precipitates include the composition frequency distribution analysis [68–70], pair correlation function analysis [71], spatial distribution mapping [72], and the local chemistry method [73], while techniques for analysis of well-defined precipitates include Fourier and autocorrelation methods [74], the maximum separation method [75–77], the core-linkage clustering algorithm [78], and various tesselation-based techniques [79, 80].

The most prevalent technique for precipitate analysis is the maximum separation method, which is based on the fact that solute atoms in a precipitate will, on average, be closer to one another than the solute atoms in the matrix [67, 76, 78, 81]. The maximum separation cluster-finding algorithm requires two primary inputs: the maximum separation distance, d_{max}, defining the greatest distance at which solute atoms are considered to belong to the same precipitates, and minimum cluster size, N_{min}, defining the smallest number of atoms that can define a statistically significant precipitate. The values of d_{max} and N_{min} are chosen in such a way as to identify only precipitates of statistical significance by comparing the nearest-neighbor distribution and cluster size distributions to that of a randomly generated data set [22, 59, 76]. Careful selection of these parameters is essential for an accurate analysis, as improper values will result in either inclusion of artificially generated precipitates or omission of precipitate clusters that are statistically significant. Once precipitates have been isolated by the algorithm, their

sizes and compositions can be analyzed and the number density and volume fraction of precipitates in the materials can be determined.

2.4.3 Artifacts and Limitations of Atom Probe Tomography

The complex physics involved with field evaporation of materials, and especially multi-phase materals, can lead to a number of imperfections and artifacts that affect the spatial resolution in the resulting reconstruction of a specimen. Some of the most common of these artifacts include trajectory aberrations and local magnification, surface migration, and chromatic aberrations. Each of these phenomena ultimately result in the position of a portion of the atoms in the reconstructed data set to vary from its true position for a uniformly evaporated APT specimen.

Of primary interest in this study are trajectory aberrations and local magnification (often used interchangeably) artifacts, which arise from variation in the electric field near the surface of a specimen that cause lateral displacement of the atoms at the time they are evaporated. This results in regions of high or low atomic density in the resulting reconstruction depending on the relative local strength of the field. These artifacts are commonly seen at crystallographic poles and zone lines, where the electric field is discontinuous due to how the terraced local geometry of the crystal lattice varies from a smooth, spherical surface at the atomic level [82, 83]. These artifacts are also observed in materials containing precipitates in which the required field to evaporate the two phases is different. In these instances, the required field to evaporate the precipitate can either be lower or higher than the field required for the matrix, resulting in either an increased or decreased apparent density within the reconstructed precipitate, respectively [66, 84]. Figure 2.13 illustrates this effect for both low- and

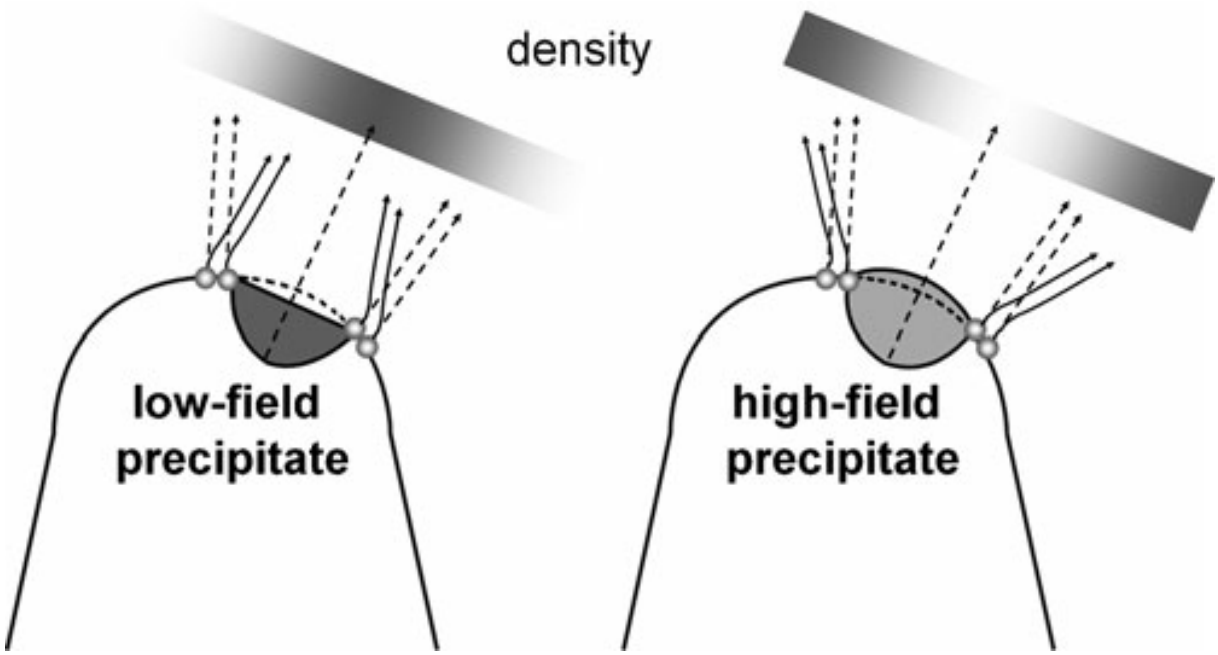

Figure 2.13: Illustration of how trajectory aberrations affect the atomic density of a reconstruction in the viscinity of precipitates. Reproduced from [66].

high-field precipitates. This perturbation of spatial resolution in the vicinity of low- and high-field precipitates can make it especially difficult to accurately quantify phase chemistry, as atoms originating in both the precipitate and matrix phases can end up being detected/reconstructed in the incorrect volume.

2.5 Introduction to Small-Angle Neutron Scattering

2.5.1 Principles of Small-Angle Neutron Scattering

SANS takes advantage of the wave-particle duality of neutrons to perform a diffraction-based analysis of material microstructure. While similar to both x-ray and electron diffraction techniques, neutrons have the advantage of being neutral, resulting in inter-

actions primarily with atomic nuclei rather than orbital electrons in addition to allowing for increased beam penetration through a specimen. The wavelength of a typical neutron beam (on the order of 0.1 nm, compared to 2.5 pm for 200 kV electrons and 0.154 nm for Cu K-alpha x-rays [85]) makes SANS a useful tool for studying objects with sizes ranging from ~ 1 nm to ~ 1 µm [86].

Neutrons scatter either through interaction with the nucleus (nuclear scattering) or through interactions between the magnetic moments of the incident neutron and unpaired electrons (magnetic scattering), the former being of primary interest for the purpose of characterizing radiation-induced microstructural features. If elastic nuclear scattering is assumed, the differential cross section is given by:

$$\frac{d\sigma}{d\Omega}(\mathbf{q}) = \frac{1}{N}\left|\sum_{i}^{N} b_i e^{i\mathbf{q}\cdot\mathbf{r}}\right|^2 \tag{2.10}$$

where b_i is the nuclear scattering length of nucleus i, and $\mathbf{q} = \mathbf{k_i} - \mathbf{k_s}$ is the scattering vector with $\mathbf{k_i}$ and $\mathbf{k_s}$ being the wave vectors of the incoming and scattered neutrons, respectively. This differential cross section is measured directly in neutron scattering experiments as intensity for a given $\mathbf{q}$ range. If we define the scattering length density as:

$$\rho = \frac{\sum_i^n b_i}{\overline{V}} \tag{2.11}$$

where $\overline{V}$ is the volume containing n atoms, the sum in Eq. 2.10 can be replaced by the integral of the scattering length density distribution across the whole sample which, after normalizing by volume, yields the Rayleigh-Gans Equation:

$$\frac{N}{V}\frac{d\sigma}{d\Omega}(\mathbf{q}) = \frac{1}{V}\left|\int_V \rho(\mathbf{r})\, e^{i\mathbf{q}\cdot\mathbf{r}} d\mathbf{r}\right|^2 \tag{2.12}$$

The Rayleigh-Gans Equation reveals that small angle scattering is a result of inhomogeneities in the scattering length density $\rho(\mathbf{r})$. The integral term represents the Fourier transform of the scattering length density distribution and the differential cross section is thus proportional to the square of its amplitude [85].

2.5.2 Small-Angle Neutron Scattering for Precipitation Investigation

When considering a two-phase material, the Rayleigh-Gans equation can be simplified to:

$$\frac{N}{V}\frac{d\sigma}{d\Omega}(\mathbf{q}) = \frac{1}{V}(\rho_1 - \rho_2)^2 \left|\int_{V_1} e^{i\mathbf{q}\cdot\mathbf{r}} d\mathbf{r_1}\right|^2 \tag{2.13}$$

in which the difference in scattering length densities depends on material and radiation properties while the integral term depends only on the spatial arrangement of the two phases in the material. The former is typically a known quantity, depending on composition, density and scattering lengths for a given specimen and experimental setup. Thus the integral term must be resolved in order to determine the geometry and

distribution of the two phases.

This integral term can be approximated using analytical models by making some assumptions regarding the geometry of the system. For most applications of precipitation in metals, some dispersion of spherical particles is assumed. For the simplest case of mono-disperse, spherically symmetric particles, the Rayleigh-Gans can be rewritten according to [87]:

$$\frac{d\sigma}{d\Omega}(\mathbf{q}) = n\Delta\rho^2 V^2 P(\mathbf{q}, r) S(\mathbf{q}) = I_0 P(\mathbf{q}, r) S(\mathbf{q}) \tag{2.14}$$

where n is the number density of particles, $\Delta\rho$ is the difference in the scattering length densities, V is the volume of the particles, $P(\mathbf{q}, r)$ is the particle form factor, and $S(\mathbf{q})$ is the structure factor. The form factor must satisfy $P(\mathbf{q} = 0, r) = 1$, while $S(\mathbf{q})$ approaches 1 for large $\mathbf{q}$. These boundary conditions give unique solutions for radius r, and leading coefficient, I_0, from which n and V can then be determined.

2.5.3 Artifacts and Limitations of Small-Angle Neutron Scattering

As SANS is a diffraction-based technique, it does not allow for direct observation and measurement of individual precipitates in the specimen microstructure. Instead, it provides a bulk-averaged diffraction pattern that can be interpreted through the use of various models and assumptions regarding the geometry and composition of the various phases. As such, SANS analyses are not able to capture local inhomogeneities in the material and some prior knowledge of the expected microstructure and microchemistry is required in order to reduce SANS diffractograms into a meaningful quantification of

the phase distribution in a given specimen.

In addition, a SANS diffractogram resulting from a magnetic specimen will contain contributions from both nuclear and magnetic scattering. The magnetic scattering component is generally less interesting from a precipitate characterization standpoint, but this signal is difficult to quantify and separate analytically. For this reason, most SANS experiments on magnetic materials are performed using an electromagnet to generate a saturated magnetic field in the specimen [20, 23, 25]. This effectively eliminates the ambiguous magnetic scattering signal, isolating the nuclear scattering component of interest for subsequent quantification efforts.

2.6 Introduction to Transmission Electron Microscopy

2.6.1 Principles of Transmission Electron Microscopy

Transmission electron microscopes (TEMs) have been in use since the late 1930s and are powerful and adaptable tools for studying nanoscale features in almost any material system, assuming an electron-transparent specimen can be generated [88]. For materials science studies, TEMs typically bombard specimens with a beam of 200 or 300 keV electrons, with images being formed by either the transmitted or diffracted particles (or both) interacting with a phosphor screen or specialized digital TEM cameras. By tilting a crystalline specimen and making an intelligent choice of which diffracted electron beam to use in forming an image, specific features of interest can be illuminated and studied. These diffraction contrast-based techniques are some of the most commonly used for investigation of crystal structures and defects.

Many modern TEMs will also come equipped with scanning transmission electron microscopy (STEM) capabilities. In STEM mode, a focused electron beam is rastered across an area of interest and the intensity of each pixel in the generated image is determined by the number of electrons detected for a given collection angle. The collection angle is chosen through selection of an annular detector. While the exact configuration varies by instrument, most instruments will have bright-field (BF), annular dark-field (ADF), and high-angle annular dark-field (HAADF) detectors which will collect mostly transmitted, weakly-diffracted, and strongly-diffracted electrons, respectively.

2.6.2 STEM/EDS for Microchemical Analysis

Scanning transmission electron microscopy is often coupled with energy dispersive x-ray spectroscopy (STEM/EDS) to study specimen chemistry. STEM/EDS measurements provide concentration line profiles or 2-dimensional composition maps of a given area of interest through analysis of the x-ray spectra produced by the excitation of atoms in a sample through interactions with the incident electron beam. As such, STEM/EDS is well-suited for analysis of nano- to micron-scale solute segregation in materials, and is particularly advantageous in that it is both non-destructive and that data acquisition times are relatively short, such that multiple scans can be taken in one microscope session. However, quantitative chemical analysis of precipitates can be difficult, as the x-ray signal will also include contributions from the surrounding matrix that the particle is embedded in, though this can sometimes be overcome using multivariate statistical analysis (MVSA) techniques [89, 90].

3 METHODS DEVELOPMENT FOR CORRELATIVE MICROSCOPY

3.1 Correlation of APT, SANS & STEM Data

As discussed in Chapter 2, APT, SANS and STEM are all useful individual tools for investigation of precipitates and multi-phase materials. However, utilization of these methods in a correlative manner allows for a more robust and holistic analysis of the precipitate microstructure. Such a methodology allow for a portion of the individual limitations of each technique to be overcome through comparison and correlation of results.

In this particular study, APT investigations provide a detailed, atomic-scale analysis of precipitate morphology and chemistry, but the data is subject to aberration artifacts which can affect the observed phase chemistry, and the analysis is performed on a very small sample volume (10^{-22} to 10^{-21} m^3 per sample), leading to uncertainty as to whether or not the observed microstructures are indicative of bulk alloy precipitation behavior. On the other hand, SANS provides the complementary bulk-average analysis of precipitate structure (10^{-9} m^3 per sample), but results are dependent on the assumed scattering length density and models used for analysis. Additionally, SANS has an inherent physical resolution limit for very small precipitates (< 1.5 nm diameter according to Hyde et al. [91], though the exact limit is dependent on the experimental configuration). Achieving agreement between the results and trends observed between these two techniques allows for the detailed chemical and morphological analysis provided by APT to be extrapolated to bulk alloy microstructure and behavior.

The STEM/EDS analysis performed in the present work is mostly qualitative in nature, with the goal of observing precipitate distributions in the vicinity of other microstructural features that are difficult to study using APT or SANS (e.g., dislocation loops and grain boundaries). APT and SANS are better suited for quantitative analysis when compared to STEM/EDS, which suffers from the "embedded particle issue" for quantification of precipitate chemistry, as the EDS spectra obtained for any given pixel corresponding to a precipitate will also contain contributions from the matrix phase above and below the particle. As such, while STEM/EDS investigations have contributed to the comprehensive understanding of precipitation in the Fe-Cr-Al system discussed herein, this chapter is focused on overcoming the challenges and obstacles associated with comparing the quantitative analyses resulting from APT and SANS techniques.

3.1.1 Sensitivity of SANS Results to Scattering Length Density

Analysis and reduction of the diffractograms generated by SANS in two-phase materials requires that the scattering length density of each phase be determined. From Eq. 2.11, this value is determined through knowledge of both the composition and density of a given phase. Subsequent quantification of precipitate number density and volume fraction can be acutely sensitive to the assumed compositions and densities of the two phases (though the average precipitate radius is independent of the scattering length density). Even a slight variance in the assumed composition between the two phases can drastically affect reported results, though, for the Fe-Cr-Al alloys system, this sensitivity is diminished as the phase compositions become more distinct. This is demonstrated by Figure 3.1 for a sample SANS data set from the current study.

In isolated SANS experiments, equilibrium phase compositions are typically assumed

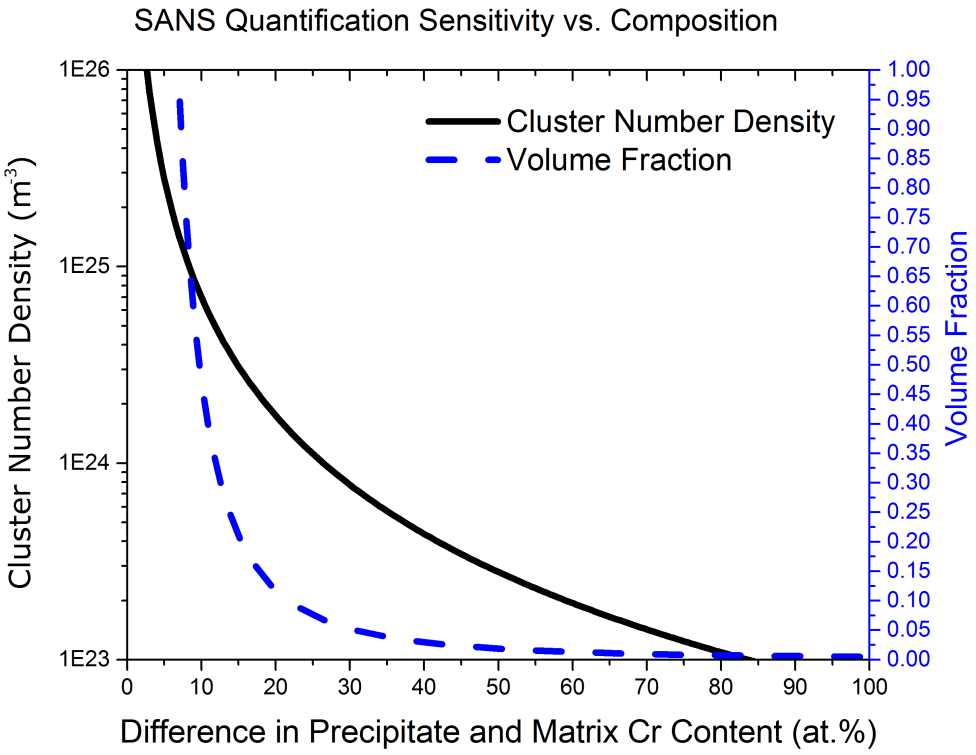

Figure 3.1: Demonstration of the acute sensitivity of the reported precipitate number density and volume fraction as determine by SANS on the assumed matrix and precipitate phase compositions. Other inputs acquired from SANS measurement of a Fe-18Cr-5.8Al specimen irradiated to 7 dpa at 320°C.

based on known phase diagrams or thermodynamics models. This allows for observation of trends and comparison between SANS results obtained from similar materials for data collected and analyzed in an individual study, but the reported results may not accurately reflect the physical material microstructure. In order to properly compare the results obtained using APT and SANS methods, detailed and accurate knowledge of the phase compositions, which can be measured directly via APT analyses, is required.

3.1.2 Interpretation of Phase Compositions in Fe-Cr-Al APT Data

In theory, analysis of phase compositions should be trivial to determine from APT data following the use of a cluster finding algorithm — once precipitate volumes are identified, the atoms contained therein simply need to be tallied based on their elemental identity. However, due to peak overlap in the time-of-flight (TOF) spectrum and trajectory aberration artifacts affecting spatial resolution in the APT reconstruction, compositions determined in this manner may not be representative of physical phase compositions. Thus, these artifacts must be accounted for in some fashion in order to accurately determine matrix and precipitate phase composition necessary to quantify SANS results.

This chapter proposes methodologies for accounting for the effects of both TOF peak overlap and trajectory aberration artifacts on reported phase composition. TOF spectrum peak deconvolution is a common practice in most APT experiments, but certain adjustments must be made to adapt these standard methods for analysis of neutron-irradiated material systems. The presented methods for trajectory aberration artifact correction are novel techniques based on quantifying the extent to which expected atomic density varies between the matrix and precipitate volumes. The desired result following application of these techniques are calculated phase compositions that are more representative of the physical chemistry of the material system of interest.

3.2 Correcting for Peak Overlap in the APT TOF Spectrum

3.2.1 TOF Peak Decomposition for Neutron-Irradiated Materials

Peak overlap in the TOF/mass-to-charge spectrum is commonly observed in APT data sets. It can occur when a subset of the detected ions are isotopes of different elements that share a mass number and charge state, or when two dissimilar elements are detected in different charge states such that they share a mass-to-charge ratio. As an example, there are two primary peak overlaps in the Fe-Cr-Al alloy system that must be accounted for: one at a mass-to-charge ratio of 27 daltons (Da), containing counts from $^{27}Al^{1+}$, $^{54}Cr^{2+}$, $^{54}Fe^{2+}$; and one at 54 Da, containing counts from $^{54}Cr^{1+}$ and $^{54}Fe^{1+}$.

Since there is no way to uniquely resolve the elemental identity of an ion causing a detector event in these ranges, all counts in a multi-peak must be assigned to a single isotope during the initial reconstruction. This results in an initially skewed compositional analysis that can be corrected using peak decomposition techniques. The Cameca Integrated Visualization & Analysis Software (IVAS) [92] has a built-in peak decomposition subroutine in which the background-corrected counts for peaks of a given element that are unambiguous (i.e., contain only contributions from a single isotope) are summed and the number of counts for that element in the multi-peak is calculated based on assumed natural isotopic abundances. However, in a neutron-irradiated material the isotopic distribution can change significantly, especially for heavier elements with multiple isotopes or for strong neutron absorbers.

In order to account for the effect of nuclear transmutation on this peak decomposition

step, new isotopic abundances that reflect the material in its post-irradiated state must be determined. As these adjusted isotopic abundances cannot currently be used in the IVAS analysis software, they must be manually applied to the peak decomposition procedure using the methodology outlined by Larson et al. [65]. This results in a system of equations:

$$\begin{cases} A_x = \sum_i M_i + \sum_j \alpha_x^j M_j \\ \sum_c \alpha_c^j = 1 \end{cases} \tag{3.1}$$

where A_x are the total number of counts for element x, M_i and M_j are the measured counts in unambiguous peak i or multi-peak j, and α_x^j is the fraction of counts in multi-peak j that can be attributed to element x. Solving for the values of α for all elements contributing to a given multi-peak allows for the peak counts to be distributed accordingly.

3.2.2 Application to Irradiated Fe-Cr-Al alloys

In the present analysis of irradiated Fe-Cr-Al alloys, post-irradiation isotopic abundances were determined using the ORIGEN-2.2 Isotope Generation and Depletion Code. This code simulates reactor-averaged nuclear reactions and decay based on material composition, the neutron energy spectrum and flux of a reactor, exposure time, and elapsed time between discharge from the reactor and APT data collection [93]. An example of how isotopics can change following irradiation and decay for a sample Fe-Cr-Al specimen is shown in Table 3.1.

Table 3.1: An example of the change in isotopic abundances for the primary constituent elements of a Fe-18Cr-5.8Al specimen following irradiation in HFIR to 7 dpa at 320 °C and decay for approximately 1 yr, corresponding to the time between specimen discharge and data collection. Predicted by the ORIGEN-2.2 Isotope Generation and Depletion Code.

Isotope	Natural Abundance	Irradiated Abundance
^{50}Cr	4.34%	3.69%
^{52}Cr	83.79%	83.68%
^{53}Cr	9.50%	8.52%
^{54}Cr	2.37%	4.11%
^{54}Fe	5.85%	5.71%
^{56}Fe	91.75%	89.32%
^{57}Fe	2.12%	4.52%
^{58}Fe	0.28%	0.36%
^{27}Al	100%	100%

Prior to peak deconvolution, the counts contained in the 27 Da peak were initially assigned to $^{27}Al^{1+}$ in the initial reconstruction, while the counts in the 54 Da peak are assigned to $^{54}Fe^{1+}$. Assignment of peak identity in this manner may lead to potentially conservative estimates for Cr clustering as the maximum separation cluster finding analysis treats atomic identity accordingly and Cr detection events that fall in the range of these multi-peaks are not. However, these events are expected to make up approximately 4% of total Cr detector events (based on adjusted isotopic abundance of ^{54}Cr) and, as such, this effect is expected to be minimal. Finally, some amount of Cr is lost following irradiation due to decay of ^{51}Cr to ^{51}V ($t_{1/2} = 27.7$d) resulting from neutron capture of ^{50}Cr. However, observed bulk V content was found to be less than 0.1 at.% in all specimens studied so it is assumed that this effect can be neglected.

3.3 Methods to Correct for Trajectory Aberrations in APT Data

As discussed in Section 2.4.3, trajectory aberration artifacts manifest as volumes of increased or decreased atomic density in an APT data set. They are commonly observed in the vicinity of an interface between phases due to differences in the strength of the local field necessary to evaporate constituent atoms. The ultimate result is a partial mixing of ions between the two phases, leading to perturbation of their apparent compositions.

The physics governing this phenomena are complex and not well understood, which makes their effect difficult to account for analytically. Experimenters in the atom probe research community generally attempt to "correct" for these artifacts through analysis of the proximity histogram for a select few precipitates [94]. The proximity histogram describes composition as a function of distance from the matrix/precipitate interface for a given precipitate. An example proxigram for precipitates studied in an irradiated Fe-18Cr-5.8Al specimen from the current work is shown in Figure 3.2. The compositions reported in these experiments are typically based on the elemental ratios identified in the precipitate core based on these histograms. However, composition error near the center of precipitates is typically high due to the smaller sampling volume in the precipitate core. In addition, this method also assumes that these aberration artifacts do not affect compositions in the center of precipitates, which may or may not be valid. Finally, for simplicity in analysis, these studies typically evaluate a handful of precipitates and hence do not fully utilize the analytical data set.

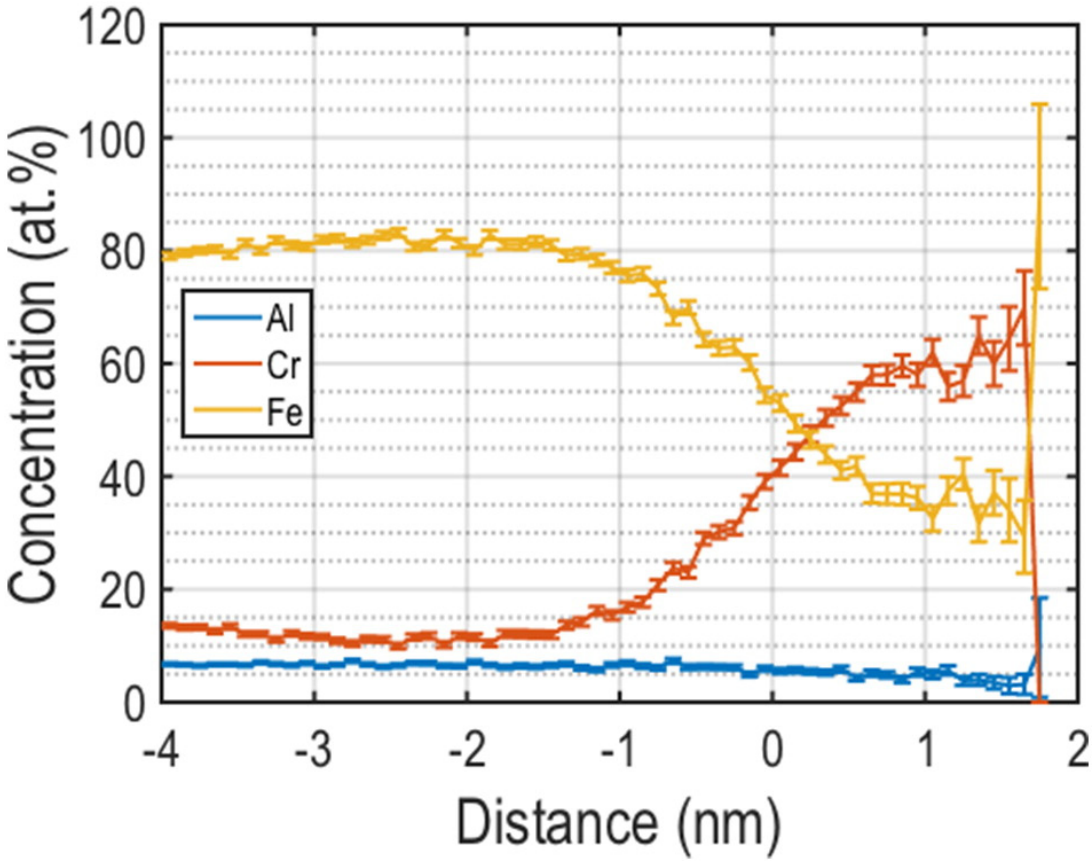

Figure 3.2: Example proximity histogram, averaged over 5 α' precipitates in an irradiated Fe-18Cr-5.8Al specimen from the current work. Reproduced from [95].

3.3.1 The APT POS File Format

APT reconstruction data is commonly output in the relatively compact POS file format. This format effectively contains four columns of data for each ion in the reconstruction: three columns for the x, y, and z Cartesian coordinates of a given ion (in nm), with the fourth containing the mass-to-charge state ratio (in amu) based on time-of-flight. Each element of this array is given in 32-bit floating-point format with no spaces, tabs, commas or other sort of delineating characters between entries. The methods outlined below were designed to read in position data from these POS files. Details regarding

other APT data file formats can be found in the text by Gault et al. [66].

3.3.2 Cubic Binning Methodology

Initial efforts to quantify differences in phase density in APT reconstructions used a simple cubic binning approach, in which precipitate volumes are identified by comparing concentration of clustering solute ions between bins. Following POS file import, the reconstruction is initially binned considering only the clustering solute ions using a user-defined bin size (Fig. 3.3a). A histogram comparing the number of solute ions in each bin is then generated (Fig. 3.3b). This histogram demonstrates a Gaussian- or Poisson-like distribution for lower solute bin counts, corresponding to the distribution of solute ions in the matrix, and a tail for higher solute bin counts, corresponding to the solute-rich precipitates. A threshold is then applied in which bins with solute counts below the specified value are considered empty. The cutoff value is currently selected by fitting a Gaussian to the matrix distribution (dashed red line in Fig. 3.3b) and selecting a value based on a a user-defined number of standard deviations from the mean (vertical dashed lines in Figure 3.3b). All bins with counts below the specified threshold are set to zero (Fig. 3.3c). The nonzero bins can then be applied as a mask to a binned data set containing all ranged ions (Fig. 3.3d) allowing for isolation of precipitate bin volumes containing all ions of interest (Fig. 3.3e). The bin density distribution for the precipitate bins can be compared to the distribution for the entirety of the data set, from which the matrix bin density distribution can be extracted by subtraction (Fig. 3.3f). The full MATLAB code implementing this method can be found in Appendix A.

For the final histogram generated in Figure 3.3f, the light blue bars represent the total bin density distribution, where the orange and dark blue bars represent the distribution

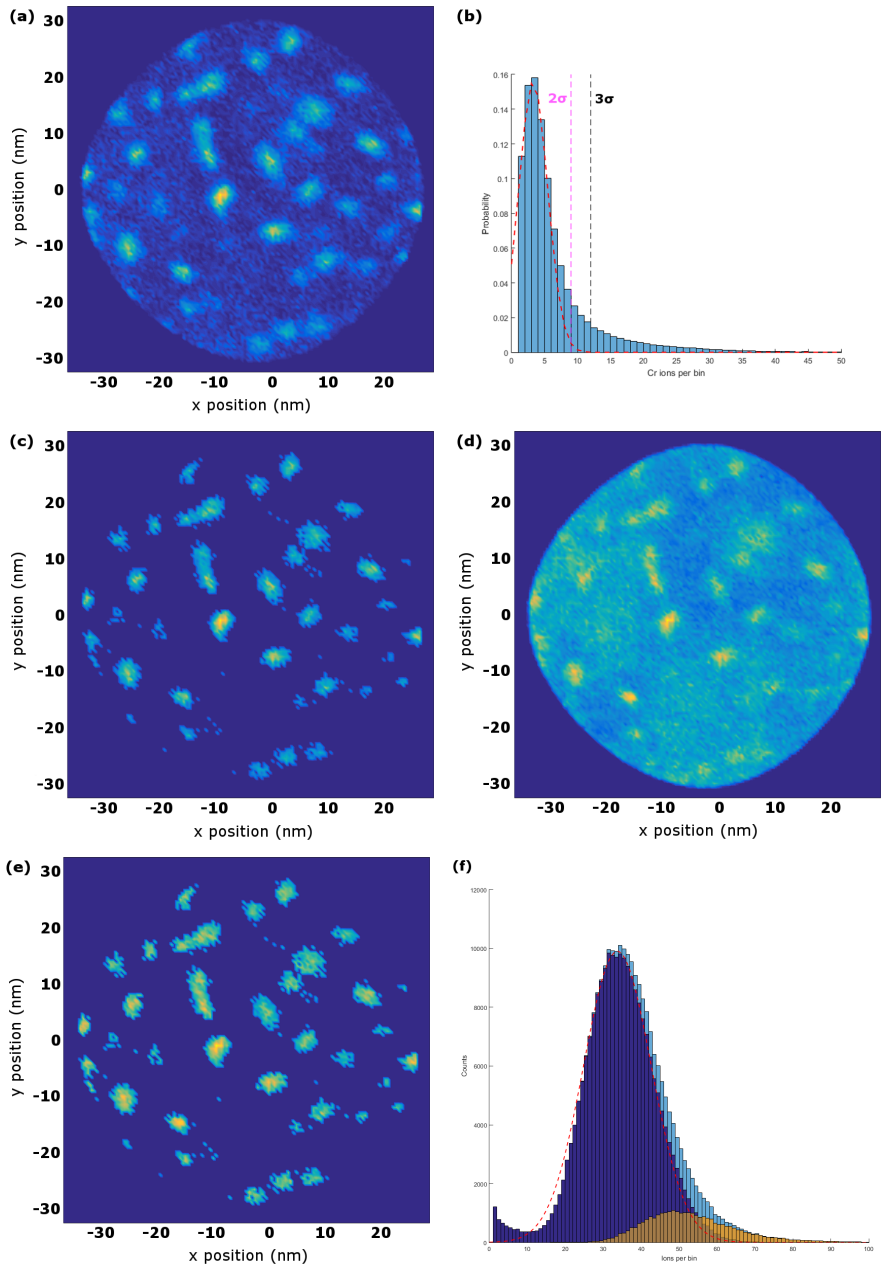

Figure 3.3: Example of computational methodology for evaluating matrix and cluster densities using the cubic binning methodology in a sample Fe-Cr-Al data set. A step-by-step description of the process is provided in the text.

for the precipitate and matrix volumes, respectively. The increased frequency for very low bin densities in the matrix distribution represent partially-filled bins on the edge of the reconstruction; these bins are not considered in comparing densities between the precipitate and matrix volumes. The density ratio is determined by dividing the mean bin densities for the matrix and precipitate bin density distributions.

3.3.2.1 Sensitivity to Bin Size & Thresholding Treatment

The two primary user inputs required to perform this cubic binning analysis are the bin size and the threshold density value that distinguishes matrix bins from precipitate bins. Improper selection of both of these values can have a significant effect on the calculated densification factor.

The ideal bin size is identified as the smallest possible size that still provides adequate statistics for counting and thresholding. Smaller bin sizes allow for cubic bins to more closely approximate the typically assumed spherical precipitate geometry with a smaller fraction of interfacial bins containing ions from both the matrix and precipitate volumes. However, assigning a threshold density value becomes difficult when bins are so small that they only contain a few ion counts. The described thresholding methodology, utilizing the standard deviation of a Gaussian fit to determine a threshold density, fails when bin size becomes too small and a Gaussian can not be properly fit to the resulting distribution.

The ideal threshold density is not as trivial to determine analytically. In essence, increasing this value requires that bins be more solute rich in order to be defined as precipitate volumes, which results in an increased densification factor. The current method for

selection of this threshold density is through analysis of the resulting precipitate mask (e.g., Fig. 3.3 e). A proper threshold density selection should be strict enough that matrix bins not associated with precipitates are excluded from this mask, but should be so strict as to exclude less dense bins at the precipitate/matrix interface.

In order to assess the sensitivity of both of these inputs on the calculated densification factor, a parametric study was performed on a sample Fe-Cr-Al alloy data set. The cubic binning algorithm was executed for square bin sizes ranging from 0.3 to 2.5 nm with a 0.05 nm step size, and for threshold densities corresponding to the mean density plus 2, 3, and 4 times the standard deviation of the Gaussian fit for the matrix bin density distribution of solute atoms. The results of this analysis are summarized in Figure 3.4. As was described previously, selection of small bin sizes result in the breakdown of the algorithm, while large bin sizes result in a decreased densification factor. Increasing the threshold density also increases the densification factor as the less Cr-rich bins are excluded from the analysis. Based on this analysis, the author suggests that a bin size of approximately 1 nm and a threshold density corresponding to 3σ yields the most physical interpretation of the density variation within this particular data set. A similar parametric analysis may be needed for analysis of different systems in this manner.

3.3.3 Delaunay Triangulation Methodology

3.3.3.1 Applications of Tessellation Algorithms for APT Analysis

Tessellation algorithms are generally used for generating cell volumes from a point cloud data set. The two most commonly used tessellation algorithms are Voronoi tessellation and Delaunay triangulation. Voronoi tessellation defines cells by constructing facets that bisect the distance between two neighboring points such that one cell is generated

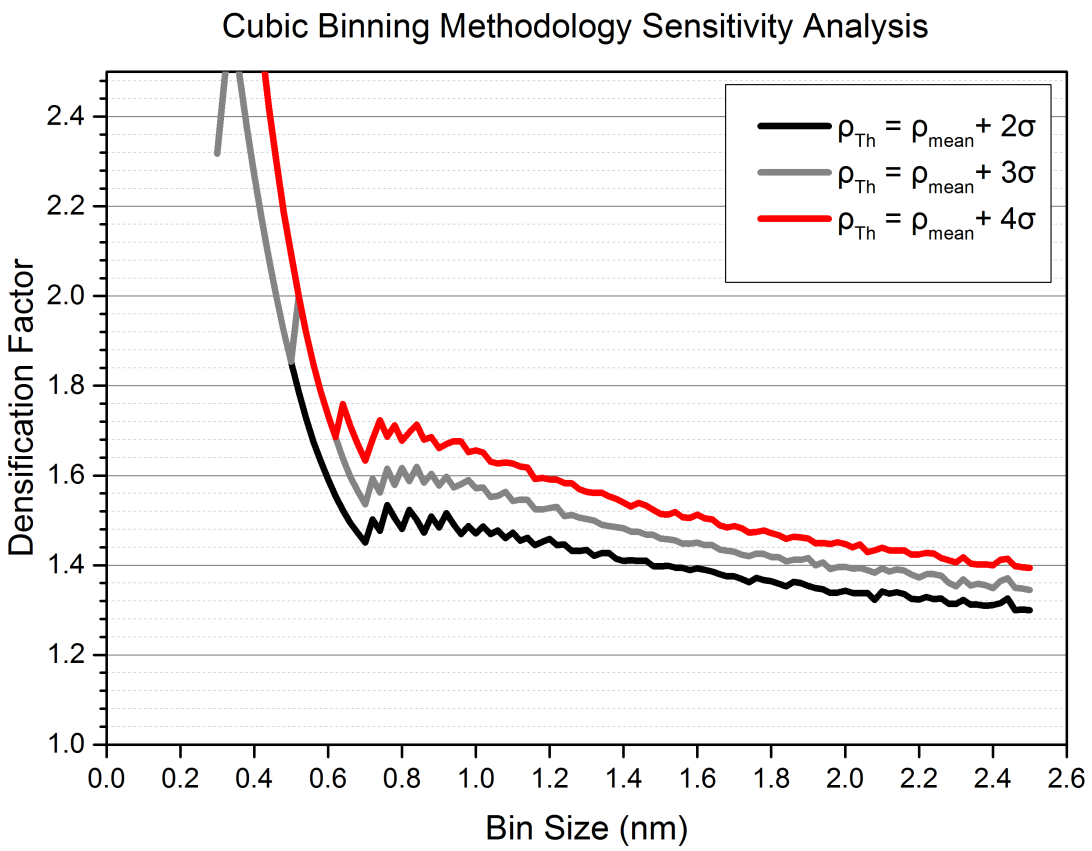

Figure 3.4: Summarized sensitivity analysis for the effects of user-defined inputs (bin size and threshold density) on the densification factor determined by the cubic-binning methodology.

for each point in a data set. In contrast, Delaunay triangulation instead treats each point as the vertex of a cell, generating a mesh of triangles in two-dimensional space, and tetrahedrons in three-dimensional space. In the three-dimensional case, Delaunay triangulation accomplishes this by constructing circumspheres with four neighboring points located on its circumference and constructs a tetrahedral cell if no other point is located within the sphere volume. A comparison of the cells resulting from application of each technique to the same two-dimensional data set is shown in Figure 3.5.

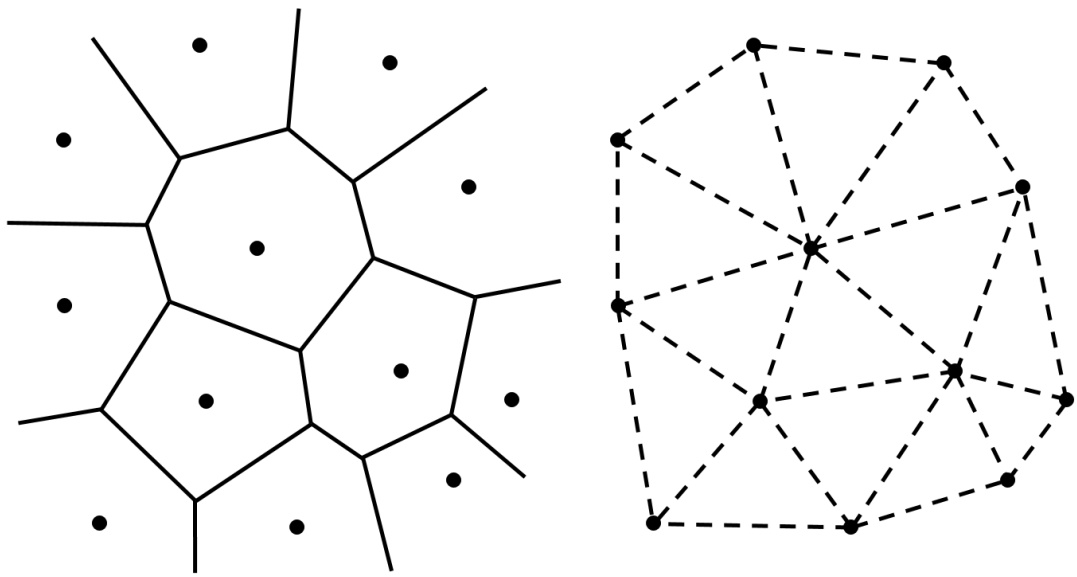

Figure 3.5: Comparison of cells resulting from Voronoi tessellation (left) and Delaunay triangulation (right) performed on the same two-dimensional data set.

As the final APT reconstruction is essentially a point cloud of atoms, tessellation algorithms are well-suited for analysis of APT data sets. In fact, both Voronoi and Delaunay tessellation techniques have previously been employed to identify precipitation and clustering in APT data sets as an alternative to the more commonly used maximum-separation method [79, 80]. These techniques take advantage of the fact that the cell volume or circumsphere radii scale with the density of points in the data set. Clusters are then identified based on regions of increased density for solute atoms of interest.

3.3.3.2 Delaunay Triangulation for Trajectory Aberration Correction

Using tessellation algorithms to quantify density enrichment due to trajectory aberrations proved to provide a few notable advantages over the cubic binning methods discussed previously. The primary benefit is that tessellation techniques are able to account for the spheroidal shapes of precipitates in the density calculation instead of

approximating these shapes with cubic voxels, ultimately leading to a more precise determination of relative precipitate density in an APT data set. In addition, the proposed methodology is able to identify precipitate volumes based on outputs from the standardized maximum separation method. Finally, these methods do not require user inputs that can potentially influence or bias the results.

Delaunay triangulation was selected as the preferred tessellation method for APT reconstruction analysis for the current application, primarily because it is more well-behaved at the boundary of a point cloud data set — Voronoi tessellation will often yield very large or infinite cell volumes for data points near the surface of a reconstruction. In addition, since the cells resulting from a three-dimensional Delaunay triangulation are all tetrahedral, their volumes are easily calculated from the coordinates of the cell vertices using the following formula:

$$V = \frac{1}{6} \left| \mathbf{d}_{21} \cdot (\mathbf{d}_{31} \times \mathbf{d}_{41}) \right| \tag{3.2}$$

where $\mathbf{d}_{ij}$ is the vector defining the edge/distance from vertex i to vertex j:

$$\mathbf{d}_{ij} = \mathbf{r}_i - \mathbf{r}_j \tag{3.3}$$

with the vector $\mathbf{r}_i$ containing the coordinates of vertex i. However, a drawback of the standard Delaunay triangulation algorithm is that it will not properly trace concave surfaces — instead, the algorithm will generate cells to fill these concave volumes.

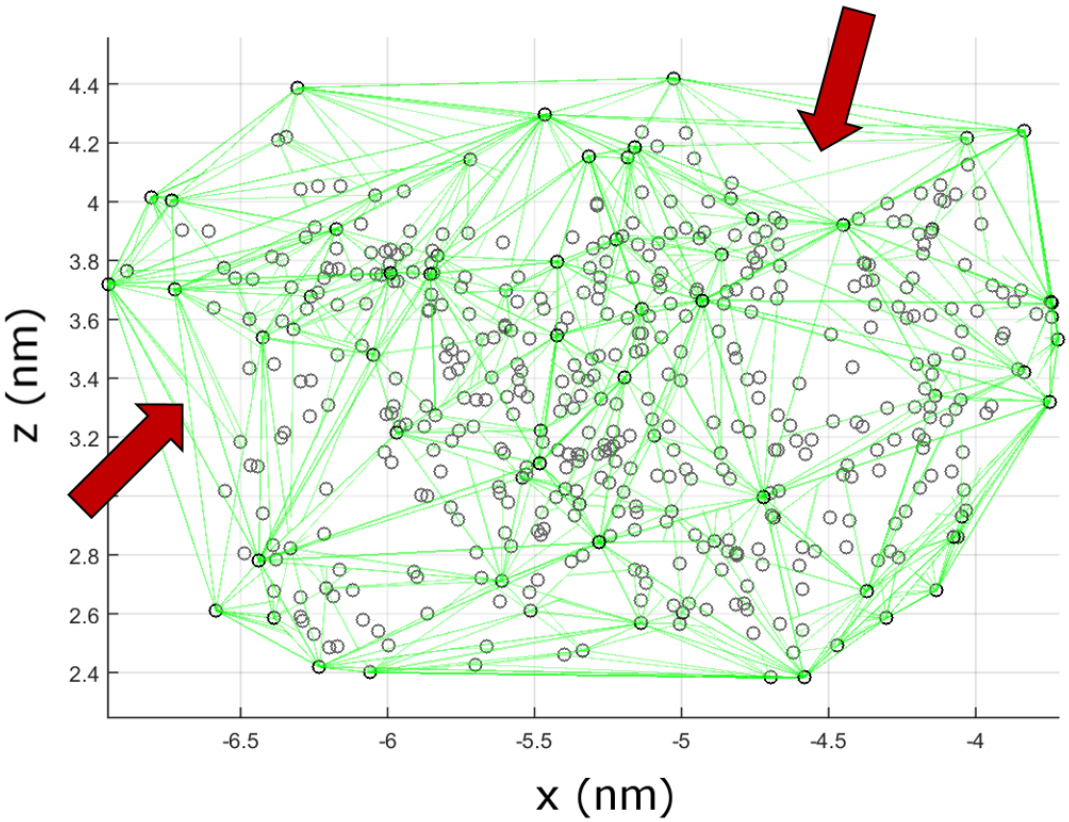

Figure 3.6: Three-dimensional cells resulting from a Delaunay triangulation of sample precipitate. Black circles represent precipitate atoms, red arrows highlight concave volumes filled by the tessellation algorithm.

This poses a challenge for volume calculations of irregularly-shaped precipitates, as demonstrated in Figure 3.6.

A couple of different approaches were employed in order to properly measure the volume, and thus, the density of precipitates with concave surfaces using the Delaunay tessellation method. The first approach takes advantage of the fact that the generated cells spanning these concave surfaces are larger on average when compared to cells that constitute the primary precipitate volume. As such, a majority of these cells can be

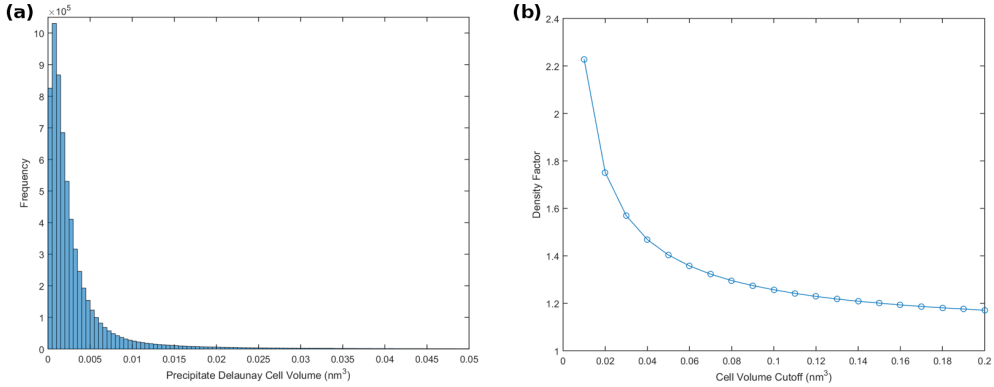

Figure 3.7: (a) Representative Delaunay cell volume distribution for precipitates in a sample Fe-Cr-Al data set. (b) Sensitivity of calculated densification factor to the assigned maximum cell volume threshold.

eliminated by applying a threshold designating the maximum cell volume considered. A representative Delaunay cell volume distribution for precipitates located in a sample APT data set is shown in Figure 3.7a. A high frequency of small cells is observed, corresponding to the core of precipitate volumes, with the distribution tailing off with respect to larger cell volumes — unfortunately there is not a significant feature in this distribution that might allow for discrimination between large precipitate cells and the cells occupying the concave volumes. While assigning an arbitrary threshold volume does eliminate a majority of these extraneous cells from consideration (Fig. 3.8), the resulting densification factor is acutely sensitive to the chosen cutoff value (Fig. 3.7b), leading to the final reported phase compositions being strongly dependent on user input.

An alternative approach to accounting for concave surfaces is to instead apply a threshold according to the Delaunay circumsphere radii of the cells instead of the volume. A similar methodology was employed by Lefebvre et al. in their work on discriminating precipitate volumes from matrix volumes using Delaunay triangulation techniques [79].

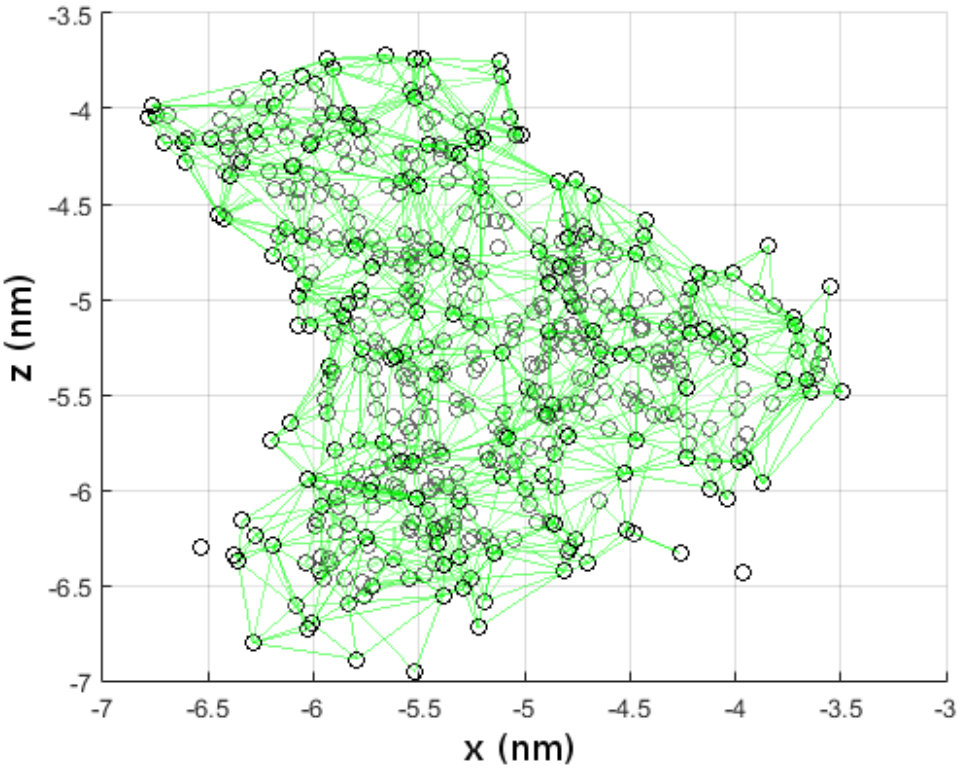

Figure 3.8: Three-dimensional cells resulting from a Delaunay triangulation of sample precipitate following maximum volume thresholding step.

Unfortunately, this technique faces the same issues as the previously described volume thresholding method in that the arbitrary threshold value assigned by the user greatly impacts the calculated densification factor. A representative Delaunay circumsphere radius distribution for a sample Fe-Cr-Al data set and the resulting densification factor sensitivity analysis are shown in Figures 3.9a and 3.9b, respectively.

The final and preferred method for measuring precipitate density from the tessellated data set is to fit the Delaunay radius distributions to those predicted by Muche et al. [96] and determine density analytically. The theoretical distribution for circumsphere radii

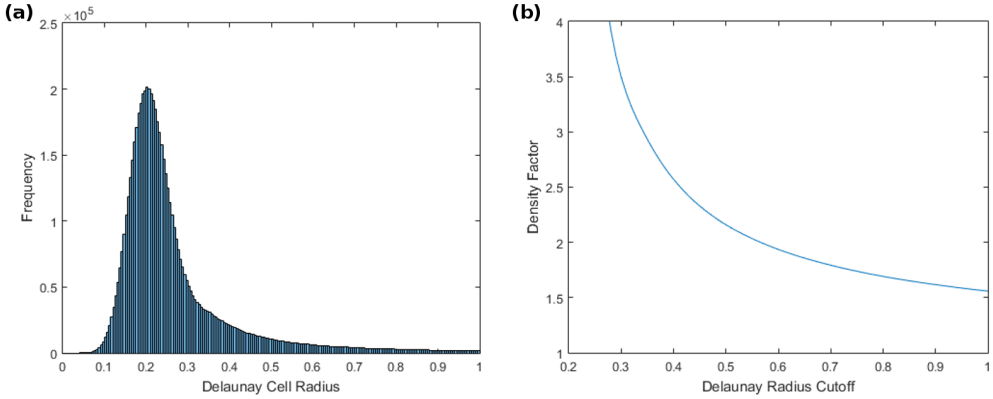

Figure 3.9: (a) Representative Delaunay circumsphere radius distribution for precipitates in a sample Fe-Cr-Al data set. (b) Sensitivity of calculated densification factor to the assigned maximum Delaunay circumsphere radius.

generated by Delaunay triangulation of a data set generated by a Poisson process is given by:

$$f(R_C) = \frac{32\pi^3\rho^3}{9} R_C^8 e^{-(4\pi\rho/3)R_C^3} \tag{3.4}$$

where R_C is the circumsphere radius and ρ is the density of points in the data set. While the distribution of atoms in an APT reconstruction is not a perfect Poisson distribution due to preservation of some of the lattice information from the original specimen, the imperfect spatial resolution of the instrument makes this a reasonable assumption [79]. The total distibution of circumsphere radii for a Delaunay triangulation of an entire APT reconstruction can then be though of as the sum of the distributions for the precipitate and matrix volumes. The precipitate circumsphere distribution is determined from a Delaunay triangulation performed on the indexed cluster POS file resulting from the maximum separation method analysis. Performing a second triangulation on the

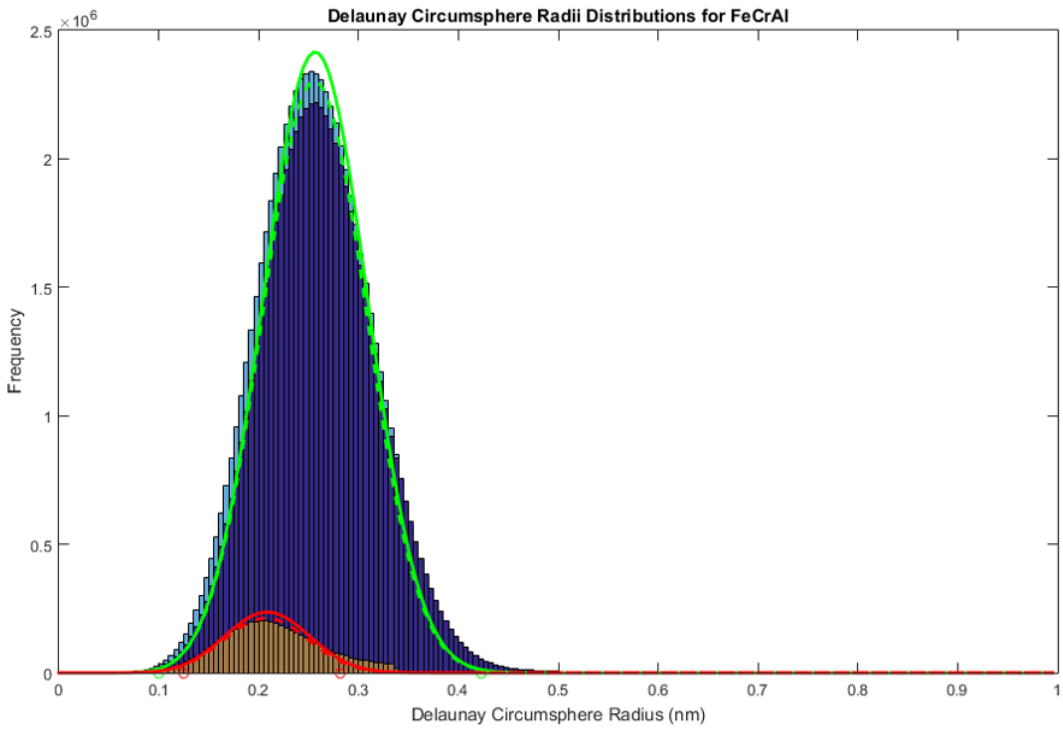

Figure 3.10: Comparison of Delaunay circumsphere radius distributions for the precipitate volumes (orange), the total reconstruction volume (light blue), and the matrix volume (dark blue, determined by difference). Fits of the theoretical distributions according to Eq. 3.4 are given by the red and green curves for the precipitate and matrix volumes, respectively.

originial POS file allows the matrix distribution to be determined by difference. Fitting curves with the form of Eq. 3.4 while using the density, ρ, as a fitting parameter, allows for the average densities of the precipitate and matrix volumes to be determined analytically with a minimal impact from the extraneous cells resulting from concave precipitate surfaces. An example of the resulting distributions for a sample Fe-Cr-Al data set is shown in Figure 3.10.

The final proposed methodology for density analysis using Delaunay triangulation is then as follows:

Step 1 Import position data from both the unfiltered reconstruction POS file and the indexed cluster POS file generated by the maximum separation method.

Step 2 Perform a Delaunay triangulation on each individual precipitate using the indexed cluster POS data. Determine precipitate Delaunay circumsphere radius distribution.

Step 3 Perform a Delaunay triangulation using the full reconstruction POS data. Using the Delaunay circumsphere distributions from the full reconstruction and the indexed cluster data, determine the matrix circumsphere distribution by difference.

Step 4 Fit the resulting precipitate and matrix circumsphere distributions using the theoretical functional form from Eq. 3.4, using density as a fitting parameter. Determine the densification factor from the ratio of the resulting densities.

The full MATLAB code implementing this method can be found in Appendix B.

3.3.4 Application of Trajectory Aberration Correction Methods to Experimental Data

Correction of phase composition using the densification factors resulting from these methods requires some fundamental assumptions regarding the mechanisms and physics of the trajectory aberration phenomenon. First, it is assumed that density variation at poles and zone lines has a minimal impact on the reported density factor, such that local contributions of these artifacts are canceled out after averaging over a complete data set. Second, it is assumed that there is no inherent difference in density between the two phases considered in a given data set. While these techniques can be

applied to systems in which phase densities are distinct, this is a fair assumption for the current material systems studied, as the theoretical atomic densities of the matrix and precipitate phases studied are nearly identical. Third, for the low-field precipitates considered, increase in density is due only to atoms from that matrix phase being detected in the precipitate phase. This allows for composition correction through removal of excess atoms in a proportion commensurate with the matrix composition. This final assumption can be loosened or expanded on with a more detailed knowledge of the evaporation physics of a particular system.

The cubic binning and Delaunay triangulation methods were applied to three different data sets in order to analyze whether or not the resulting composition correction using the calculated densification factor was effective and to ensure that the techniques could be applied to a variety of material systems. The first case study was performed on a sample Fe-Cr-Al alloy data set from the current study. The data was collected from the Fe-18Cr-5.8Al composition after it had been irradiated to 7 dpa at ~320°C in the High Flux Isotope Reactor (HFIR) at Oak Ridge National Laboratory (ORNL) and features a high number density of well-defined Cr-rich α' precipitates.

Table 3.2 summarizes the results of application of this density-based aberration correction to the sample Fe-Cr-Al data set. "Uncorrected" values are the naïve compositions resulting from the maximum separation method analysis. As is expected, the densification factor resulting from the Delaunay triangulation method is greater than what results from the cubic binning method. The compositions resulting from cubic binning correction are similar to those reported in studies of irradiated Fe-Cr alloys and aged Fe-Cr-Al alloys [22, 47]. However, the compositions resulting from the Delaunay tri-

Table 3.2: Comparison of reported α' precipitate compositions resulting from using the standard maximum separation method and the two aberration correction techniques detailed in this chapter for a Fe-18Cr-5.8Al specimen following neutron irradiation to 7 dpa at 320°C.

	Uncorrected	**Cubic Binning**	**Delaunay Triangulation**
Densification Factor	N/A	1.56	1.93
Fe (at.%)	34.8	9.1	-7.6
Cr (at.%)	61.3	88.5	106.6
Al (at.%)	3.7	2.3	1.4

angulation methodology are clearly non-physical, as a negative Fe content is reported, while calculated Cr content is greater than 100%. This could suggest that the Delaunay triangulation method is overestimating the relative density increase in the low-field precipitates or that there is a flaw in one of the fundamental assumptions involved in applying these corrections.

The second data set studied came from a reactor pressure vessel (RPV) steel that had been in service as a reactor surveillance material at the Ringhals Nuclear Power Plant. The surveillance materials are small coupons of material that are identical to the alloy used in fabricating the RPV that are removed periodically and examined to gauge changes in alloy microstructure and properties over the pressure vessel service lifetime. These particular materials are known to be susceptible to embrittlement due to the formation of Ni-Mn-Si-rich (NMS) precipitates [97–103]. Most APT investigations of these materials report that precipitate volumes are composed of more than 50 at.% Fe, though these values are suspected to be heavily influenced by trajectory aberration effects [66, 99, 104]. Recent studies coupling APT investigations with STEM/EDS studies utilizing multivariate statistical analysis techniques combined with simulated x-ray spectra suggest

Table 3.3: Comparison of reported Ni-Mn-Si precipitate compositions resulting from using the standard maximum separation method and the two aberration correction techniques detailed in this chapter for an irradiated Ringhals RPV surveillance material specimen.

	Uncorrected	**Cubic Binning**	**Delaunay Triangulation**
Densification Factor	N/A	1.40	1.99
Fe (at.%)	56.7	40.8	17.3
Ni (at.%)	21.2	29.2	41.0
Mn (at.%)	14.8	20.3	28.4
Si (at.%)	6.1	8.5	11.9

that these NMS precipitates likely contain much less Fe, with the precipitates in the materials investigated currently containing approximately 6 at.% Fe [105].

The results of aberration correction on the sample Ringhals RPV surveillance material data set are summarized in Table 3.3. Cubic binning techniques resulted in moderate reduction of calculated precipitate Fe content (56.7 to 40.8 at.% Fe), though do not approach the 6 at.% Fe predicted by literature [105]. Delaunay triangulation corrections resulted in a much more drastic reduction in reported precipitate Fe content (17.3 at.% Fe), though the compositions resulting from this method still failed to agree with literature values.

The third and final data set analyzed is a simulated data set generated using the Cameca TipSim analysis software. The TipSim software models the data collection process in a LEAP on a specimen of a user-defined geometry and composition. The resulting output is a .RHIT file that can be analyzed in the same fashion as an experimental APT data set. This allows for comparison of the final microstructure and chemistry in a reconstruction to an original, known state. This is clearly an incredibly useful tool for benchmarking

the described methodologies, assuming that the software is able to accurately represent the physics of the system. A simple model geometry was constructed for this purpose, consisting of a 100% Fe matrix oriented such that the $\langle 111 \rangle$ zone axis coincides with the tip axis. This matrix was populated with spherical precipitates with 1.79 nm radii and compositions of 85 at.% Cr and 15 at.% Fe.

A comparison of precipitate compositions and average radius reported by various techniques for evaporation of this simulated specimen geometry are shown in Table 3.4. It is clear that the naïve, uncorrected compositions resulting from the maximum separation method are non-physical and have a reduced Cr content and increased radius due to extra matrix atoms being detected in precipitate volumes. However, the Delaunay triangulation methodology greatly over-corrects for this phenomenon, resulting in precipitate compositions that are either negative or greater than 100%, similar to what was observed for the experimental Fe-Cr-Al data set. It is also demonstrated that there is a solution for the densification factor that results in precipitate composition and average radius that is similar to the initial known precipitate morphology and chemistry. Note that the cubic binning methodology was not applied to this data set, as the pure Fe matrix of this simulated geometry prevents precipitate volume discrimination using the standard deviation threshold density from the Gaussian fit to the matrix solute ion distribution.

3.4 Model Fittings & Interpretation of SANS Data

While proper determination of phase scattering length density is an important step for correlation of SANS results, it is just one facet of the data analysis required to reduce and quantify raw SANS data. As alluded to previously, the SANS results are also dependent

Table 3.4: Comparison of reported Cr-rich precipitate compositions and average radius resulting from using the standard maximum separation method and the Delaunay triangulation aberration correction technique to the known value for a simulated Fe-Cr data set resulting from the Cameca TipSim software. "Expected" column illustrates that reported composition and radius values do approach the known composition for a given densification factor.

	Known	**Uncorrected**	**Delaunay Triangulation**	**Expected**
Densification Factor	N/A	N/A	2.1	1.2
Fe (at.%)	15	28.05	-40.17	15.6
Cr (at.%)	85	71.95	140.17	84.4
Average Radius (nm)	1.79	1.92	1.50	1.80

on the models used to fit the data. The present work considers two analytical models — the first model assumes a monodisperse distribution of spherically-shaped precipitates with a size equal to the bulk average, while the second model allows for polydispersity in the precipitate size distribution.

3.4.1 SANS Diffractogram Reduction

An example of a raw, 2-dimensional SANS diffractogram resulting from SANS data collection of an irradiated Fe-Cr-Al alloy is shown in Figure 3.11. The precipitate signal manifests as the orange ring around the central, transmitted zero-beam in this system. This data is reduced to a 1-dimensional curve for model fitting by performing a radial average centered around the zero-beam. The final curve in Figure 3.12 is the result of performing this radial averaging on diffractograms resulting from three distinct detector configurations. The precipitate signal in this curve is mainly contained in the "hump" at $Q = 0.1$Å. Additional details of specific SANS acquisition parameters for the current study are found in Section 4.4.1.

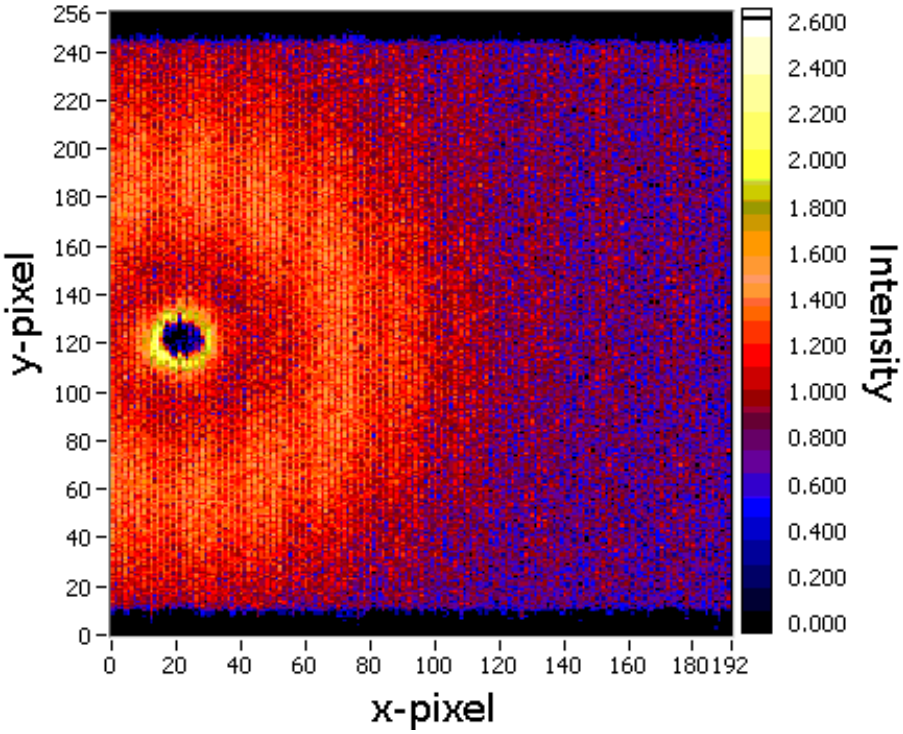

Figure 3.11: Raw, 2-dimensional SANS diffractogram from the Fe-18Cr-5.8Al specimen following irradiation to 1.8 dpa at 382°C, collected using the medium-length detector configuration.

3.4.2 Monodisperse SANS Model

Monodisperse model fits to experimental SANS data assume take the functional form from Pedersen [87]:

$$\frac{d\sigma(q)}{d\Omega} = n\Delta\rho^2 V^2 P(q,r) S(q,r) = I_0 P(q,r) S(q,r) \tag{3.5}$$

where n is the number density of particles, $\Delta\rho$ is the difference in the scattering contrast between the precipitate and matrix phases, V is the volume of the precipitates, $P(q,r)$

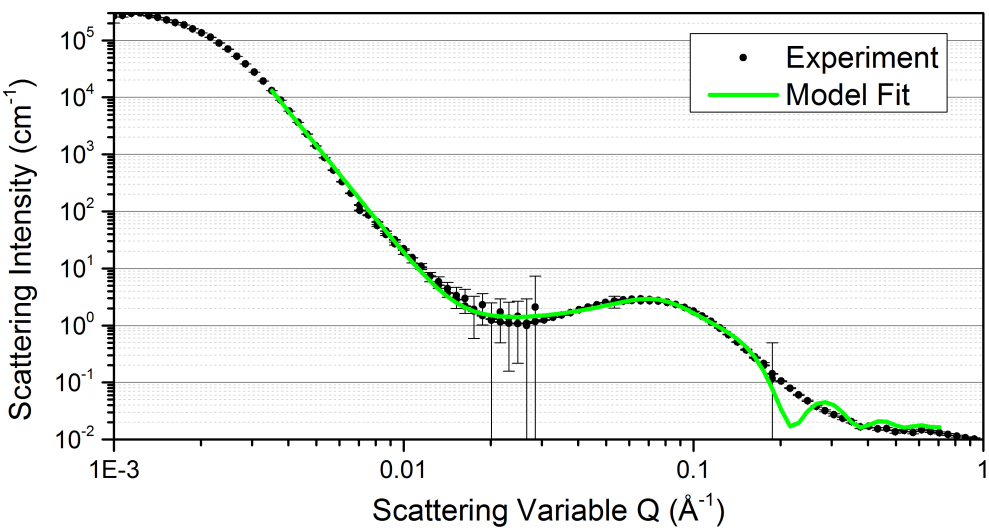

Figure 3.12: 1-dimensional SANS intensity curve following data reduction of the 2-dimensional diffractogram in Figure 3.11 and diffractograms from short- and long-length detector configurations. Model fit assuming a monodisperse distribution of spherical precipitates is shown for comparison.

is the particle form factor, and $S(q, r)$ is the structure factor describing scattering interference between particles. For spherical precipitates, the form factor takes the following functional form:

$$P(q, r) = \left[\frac{3\left(\sin(qr) - qr\cos(qr)\right)}{(qr)^3}\right]^2 \tag{3.6}$$

The structure factor assumes a hard-sphere potential, also given in [87]:

$$S(q, r) = \frac{1}{1 + 24\eta G(rq)/(rq)} \tag{3.7}$$

in which η is the hard-sphere volume fraction and:

$$\begin{aligned} G(A) &= \alpha\left(\sin A - A\cos A\right)/A^2 \\ &+ \beta\left(2A\sin A + (2-A^2)\cos A - 2/A^3\right) \\ &+ \gamma\left[-A^4\cos A + 4\left|(3A^2-6)\cos A + (A^3-6A)\sin A + 6\right|\right]/A^5 \end{aligned} \tag{3.8}$$

with:

$$\alpha = (1+2\eta)^2/(1-\eta)^4 \tag{3.9}$$

$$\beta = -6\eta(1+\eta/2)^2/(1-\eta)^2 \tag{3.10}$$

$$\gamma = \eta\alpha/2 \tag{3.11}$$

The form factor must satisfy $P(q=0,r) = 1$, while $S(q,r)$ approaches 1 for large q. These boundary conditions give unique solutions for radius r and the leading coefficient, I_0, from which n and V can then be determined.

3.4.3 Polydisperse SANS Model

The fundamental theory of the polydisperse SANS model is similar to that of the monodisperse model, except that the functional form of the fit from Eq. 3.5 becomes an integral term over precipitate radius. This term can be simplified by assuming a

modified Schulz-Zimm distribution for precipitate radius:

$$p(r)dr = \frac{a^{b+1}}{\Gamma(b+1)} r^b exp(-ar)dr \tag{3.12}$$

with:

$$a = 1/r_{avg} \tag{3.13}$$

$$b + 1 = (r_{avg}/rms)^2 \tag{3.14}$$

where r_{avg} is the average precipitate radius and rms is the root-mean square of the precipitate size distribution. This distribution is preferred to a Gaussian because it tends to zero for $r = 0$, and preferred to a log-normal distribution because it is closed-form integrable, allowing for an explicit solution of the integral form of Eq. 3.5.

3.4.4 Model Comparison

In comparing the two models, assuming a monodisperse size distribution is clearly a simplification of the physical precipitate geometry in the systems being studied. As such, the second model including polydispersity is expected to provide a better description of the physical form of the materials being studied. However, this more complex model was found to yield poor fits to the experimental data from irradiated Fe-Cr-Al specimens, especially for specimens with comparatively less precipitate-rich microstructures. The resulting quantification from application of the current polydisperse model yielded clearly nonsensical values for precipitate number density and volume fraction, that were, in some cases, several orders of magnitude different from observations made using APT techniques and in studies of similar systems from the literature.

In light of this, the monodisperse model was preferred for SANS data analysis. Though simple, it is still expected to provide an adequate description of material microstructure and reasonable agreement was able to be demonstrated between atom probe results. In addition, good fits to all experimental conditions studied allows for better comparisons between specimen microstructures and identification of trends in precipitation behavior.

3.5 Discussion

As demonstrated via analysis of sample APT data sets, application of the described, density-based aberration correction methods result in adjusted precipitate compositions that are, in general, shifted toward the expected physical values. However, it is apparent that some of the non-physical compositions resulting from application of these methods point to a flaw in some aspect of these correction processes, and suggest that they might be insufficient to robustly correct for trajectory aberration artifacts across multiple material systems. As such, further investigation and refinement of the described techniques is required.

The most likely reason for the shortcomings of these methods is the oversimplification of the physics of the trajectory aberration process in the translation of the measured density increase to the adjusted composition. Here, it has been assumed that the densification of the low-field precipitates is due to a flux of matrix ions across the matrix/precipitate interface, resulting in detection of these matrix ions in the precipitate volume (Fig. 3.13a). In reality, it is likely that there is additionally some flux of precipitate ions into the matrix volume, or that some precipitate ions are also directed inward, thus causing a density increase that is independent of the matrix ion flux (Fig. 3.13b). This complex behavior can be expected to vary as a function of the material system being analyzed, and may also

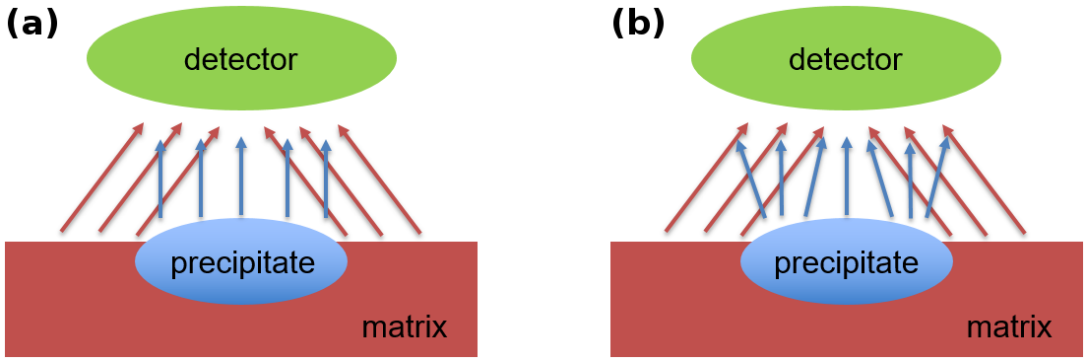

Figure 3.13: Comparison of (a) the assumed ion trajectory behavior responsible for the observed artifacts and (b) what is perhaps more representative behavior of the physics involved in field evaporation in the vicinity of different phases.

have dependencies on individual precipitate shape and/or size. The measured density difference is likely to play a key role in aberration correction, but does not accomplish this robustly on its own.

In comparing the cubic binning and Delaunay triangulation techniques, the tessellation-based method is expected to provide a more physical comparison of the density between matrix and precipitate volumes based on a number of factors. Most notably, the Delaunay triangulation method is able to more accurately capture precipitate volumes, as identified by the maximum separation method, whereas the cubic binning method depends on a simplified representation using cubic voxels, with matrix and precipitate volumes determined by relative solute enrichment. Additionally, the Delaunay triangulation method is able to determine density analytically, free of potential bias originating from user inputs. Despite this, the cubic binning methodology seems to produce a reasonable estimate for expected precipitate composition in the experimental Fe-18Cr-5.8 Al data set based on available literature, though this may just be coincidence resulting from the conservative estimate of densification combined with invalid assumptions.

The same cannot be said for the Ringhals RPV surveillance material, which reinforces that aberration behavior can vary greatly from material to material and that a robust understanding on the physics involved for a particular system of interest are required for these techniques to be fully quantitative.

Computational tools, such as the TipSim software utilized in this work, are expected to play a crucial role in determining how experimental variables, such as matrix and precipitate composition, precipitate size, crystallographic orientation, etc., affect the spatial resolution and solute ion redistribution in an evaporated data set compared to the original material. Having a detailed knowledge of the initial chemistry and geometry is obviously invaluable when trying to determine how that information has been perturbed in the process of data collection. In addition, being able to construct and run digital specimens also allows for parametric study of these factors without the associated experimental cost and effort.

For the purposes of correlative microstructural analysis, the experimental work presented in the next chapter will utilize composition data resulting from application of the cubic binning methodology to the APT data collected from the neutron-irradiated Fe-Cr-Al specimens for the purpose of calculating scattering length densities necessary to reduce and quantify SANS data. While the chosen method is not perfect, it allows for analytical aberration correction on a specimen-wide basis when compared to proximity histogram methods and produces reasonable phase compositions based on previous experimental results. Further refinement of these correction techniques should result in further improvements in the accuracy of phase compositions measurements using APT techniques, and the ability to achieve this more representative experimental data will

further enhance the capabilities of correlative microscopy and computational modeling efforts of precipitation in various material systems.

In addition to this scattering length data, the presented SANS results will utilize the model discussed here that assumes a monodisperse size distribution of spherical precipitates. The polydisperse model in its current state yields non-physical values for precipitate number density and volume fraction and requires additional refinement before it can be employed analytically. While the monodisperse model is a simplified representation of the complex physical microstructure, it has resulted in reasonable agreement in observed trends between APT and SANS experiments. In addition, comparatively good fits to all experimental conditions studied has allowed for cross-comparison of results between all materials and conditions within the SANS sample matrix.

4 EXPERIMENTAL

4.1 Materials Investigated

4.1.1 Sample Fabrication

Four ferritic ternary model Fe-Cr-Al alloys with nominal compositions ranging from 10-18 at.% Cr and 5.8-9.3 at.% Al were fabricated by arc melting pure element feedstocks of Fe and Cr with pre-alloyed Al-Y specimens. Yttrium is added as a reactive element to enhance high-temperature oxidation resistance by reducing the growth rate and increasing the adherence of the alumina scale that forms on the surfaces of exposed Fe-Cr-Al [106]. These specimens were then hot forged, rolled and heat treated using the conditions developed by Yamamoto et al. [11]. This resulted in a fully ferritic, BCC microstructure with grain sizes on the order of 20-50 µm. Following this heat treatment, the bulk specimens were cold-rolled with a 10% thickness reduction to emulate the cold-shaping process route required for fuel cladding tube production. Optical micrographs of the resulting grain structure for each alloy are shown in Figure 4.1. The compositions of these alloys, as determined by inductively coupled plasma optical emission spectroscopy (ICP-OES), are shown in Table 4.1 [16, 95]. The resulting Fe-Cr-Al material was cut to form SS-J2 sub-sized tensile specimens using electric discharge machining. The geometry of these tensile specimens is shown in Figure 4.2.

4.1.2 Irradiation Campaign

The sub-sized tensile specimens were loaded into capsules for irradiation in the High Flux Isotope Reactor (HFIR), located at ORNL. Images of the HFIR reactor core are

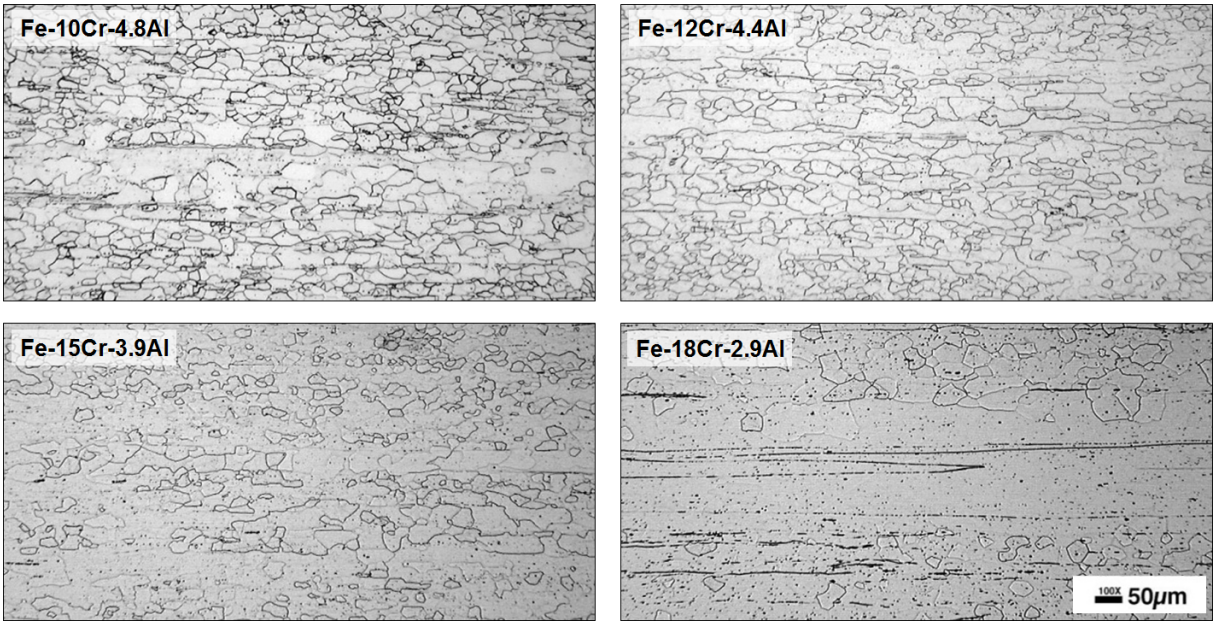

Figure 4.1: Optical micrographs for the four Fe-Cr-Al model alloys investigated demonstrating initial grain structure. Images courtesy of Y. Yamamoto (ORNL).

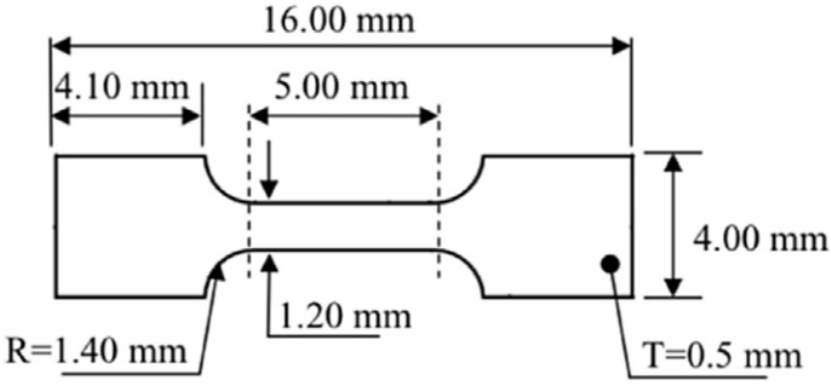

Figure 4.2: SS-J2 subsized tensile specimen geometry used in the HFIR irradiation. Reproduced from [16].

Table 4.1: Fe-Cr-Al alloy compositions in both at.% and wt.% [16, 95].

Alloy		Fe	Cr	Al	Y	C	S	O	N	P	Si
Fe-10Cr-9.3Al	at.%	bal.	**10.15**	9.34	0.023	0.022	0.0016	0.0043	0.0011	0.010	<0.02
	wt.%	bal.	**10.01**	4.78	0.038	0.005	0.0010	0.0013	0.0003	0.006	<0.01
Fe-12Cr-8.7Al	at.%	bal.	**12.16**	8.66	0.016	0.022	0.0021	0.0056	0.0034	0.0	0.02
	wt.%	bal.	**11.96**	4.42	0.027	0.005	0.0013	0.0017	0.0009	0.0	0.01
Fe-15Cr-7.7Al	at.%	bal.	**15.33**	7.70	0.021	0.022	0.0007	0.0083	0.0026	<0.003	0.02
	wt.%	bal.	**15.03**	3.92	0.035	0.005	0.0004	0.0025	0.0007	<0.002	0.01
Fe-18Cr-5.8Al	at.%	bal.	**18.00**	5.81	0.010	0.022	0.0010	0.0050	0.0042	<0.003	<0.02
	wt.%	bal.	**17.51**	2.93	0.017	0.005	0.0006	0.0015	0.0011	<0.002	<0.01

shown in Figure 4.3, and a schematic of the target capsule design for housing Fe-Cr-Al tensile specimens is shown in Figure 4.4. Engineering drawings of the target capsules can be found in Appendix C. Each irradiation target capsule housed six tensile specimens of each Fe-Cr-Al composition and were backfilled with an inert He atmosphere. Capsules were irradiated at a target temperature of 320°C to achieve multiple distinct fluences across all compositions, corresponding to nominal damage doses of 0.3, 0.8, 1.8, 7, and 13.8 displacements per atom (dpa), though only specimens up to 7 dpa have been studied thus far due to radiation safety concerns. The 0.3 and 0.8 dpa capsules were irradiated using the hydraulic tube facility; all other capsules were irradiated in the central flux trap in static positions. It should be noted that the low dose capsules did not contain all four model alloys — the 12%Cr and 15%Cr alloys were irradiated in the 0.3 dpa capsule, while the 10%Cr and 18%Cr alloys were irradiated in the 0.8 dpa capsule. All other capsules contained samples from all model alloy compositions.

Some thermal gradient is expected in the irradiation target capsules. In order to assess the magnitude of this gradient and ensure similar irradiation temperatures between tensile specimens in a single capsule, a finite element model was constructed using the ANSYS Workbench software. The heat generation rate and convection parameters

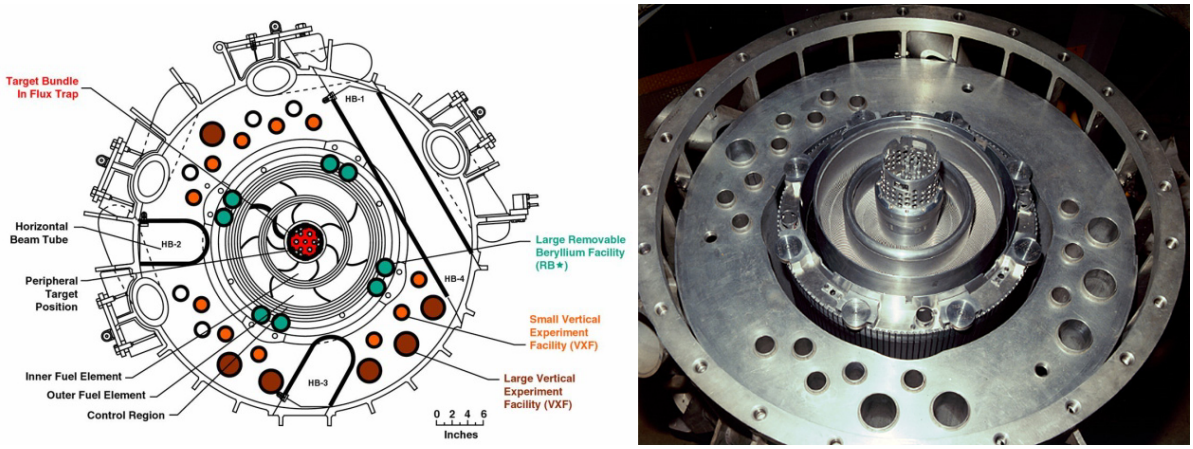

Figure 4.3: (a) Diagram of experimental positions in the HFIR core. (b) Image of a full-scale model of the HFIR core assembly.

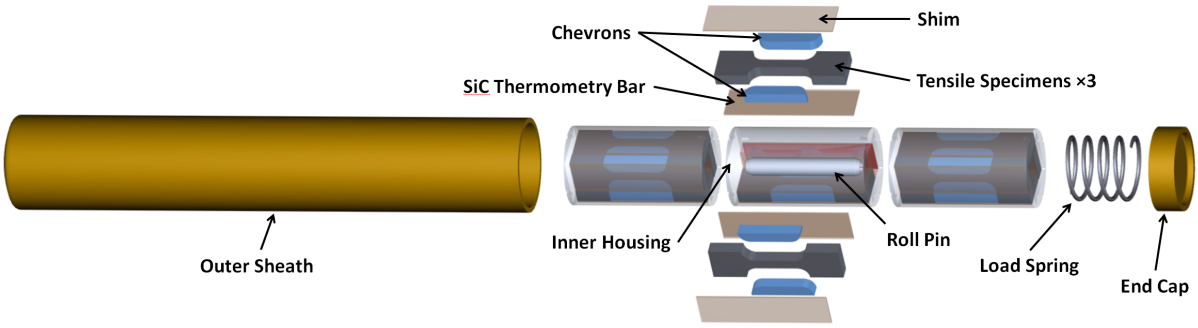

Figure 4.4: Diagram of irradiated target capsule design, capable of housing 36 SS-J2 subsized tensile specimens. Reproduced from [107].

for the known capsule position in the HFIR core was used to perform this analysis for the target temperature of 320°C. Temperature contour plots illustrating expected temperature gradients for the different specimens contained in an irradiation target capsule are shown in Figure 4.5. A summary of the average temperature and the 95% temperature span (i.e., 95% of the area of the part on the cutting plane will have a temperature between the endpoints of the span) resulting from this analysis is given in Table 4.2.

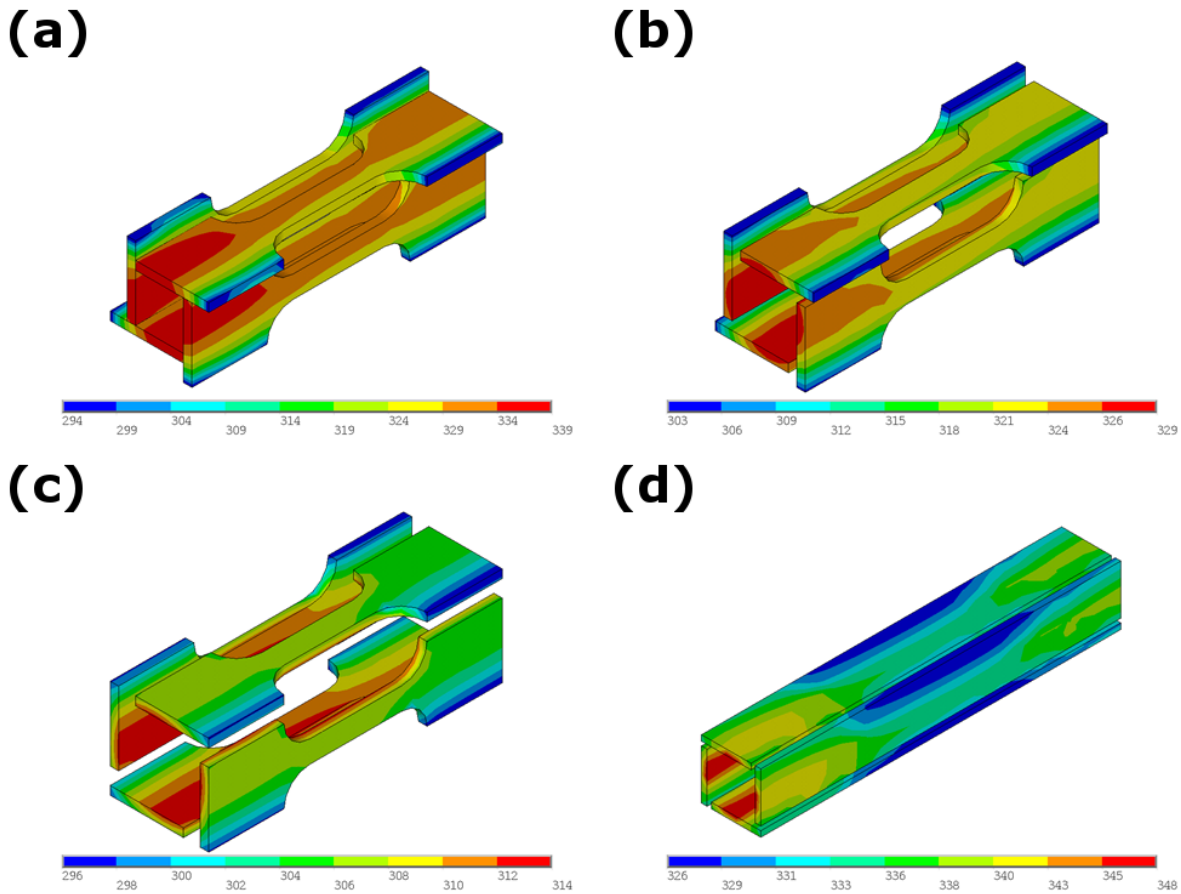

Figure 4.5: Temperature contour plots in °C for (a) inner most tensile specimens (TENSILE 1), (b) middle layer tensile specimens (TENSILE 2), (c) outer most tensile specimens (TENSILE 3), and (d) SiC thermometry specimens. Full design analysis and calculation (DAC) document is found in Appendix D.

Table 4.2: Summary of calculated specimen temperatures according to results of the finite element model developed using the ANSYS Workbench software. The minimum and maximum temperatures listed indicate a 95% temperature span by area.

Design ID	Holder Material Fill Gas	Design Temperature (°C)	Tensile Specimen	Specimen Temperature (°C) Average (Min-Max)
TRRH-2	Aluminum holder Helium fill gas	320	TENSILE 1	328 (294-339)
			TENSILE 2	321 (303-329)
			TENSILE 3	307 (296-314)
			THERMOMETRY	336 (328-344)

Table 4.3: Summary of irradiation conditions for each target capsule exposed in HFIR.

Capsule ID	Exposure Time (hrs)	Neutron Flux (n/cm^2s) E >0.1 MeV	Neutron Fluence (n/cm^2) E >0.1 MeV	Dose Rate (dpa/s)	Dose (dpa)	Irradiation Temperature (°C)
FCAY-01	120	8.54×10^{14}	3.69×10^{20}	7.7×10^{-7}	0.3	334.5 ± 0.6
FCAY-02	301	8.54×10^{14}	9.25×10^{20}	7.7×10^{-7}	0.8	355.1 ± 3.4
FCAY-03	614	8.84×10^{14}	1.95×10^{21}	8.1×10^{-7}	1.8	381.9 ± 5.4
FCAY-04	2456	8.74×10^{14}	7.73×10^{21}	7.9×10^{-7}	7.0	319.9 ± 12.7

Actual capsule irradiation temperature was measured by performing a dilatometric analysis of passive SiC thermometry bars also contained in the irradiation target capsules using the methodology proposed by Campbell et al. [108]. In applying this technique, length change of the SiC bar is recorded as temperature is increased to a temperature of at least 600°C before being returned to room temperature. Above the irradiation temperature, irradiation-induced defects begin to anneal out of the microstructure, resulting in a decrease in the volume of the SiC specimen. By comparing the heating and cooling curves resulting from this analysis, the irradiation temperature can be identified by the point at which the two curves diverge. An example of the result of this analysis is shown in Figure 4.6 for a representative SiC thermometry bar from the FCAY-04 (7 dpa) irradiation capsule. The reported error in irradiation temperature is given by the standard deviation of at least 3 separate analyses of SiC thermometry specimens contained within the same capsule. A summary of these irradiation conditions can be found in Table 4.3. It should be noted that, based on the results of the finite element analysis presented in Table 4.2, actual specimen irradiation temperatures are expected to exist about 20°C below these reported values.

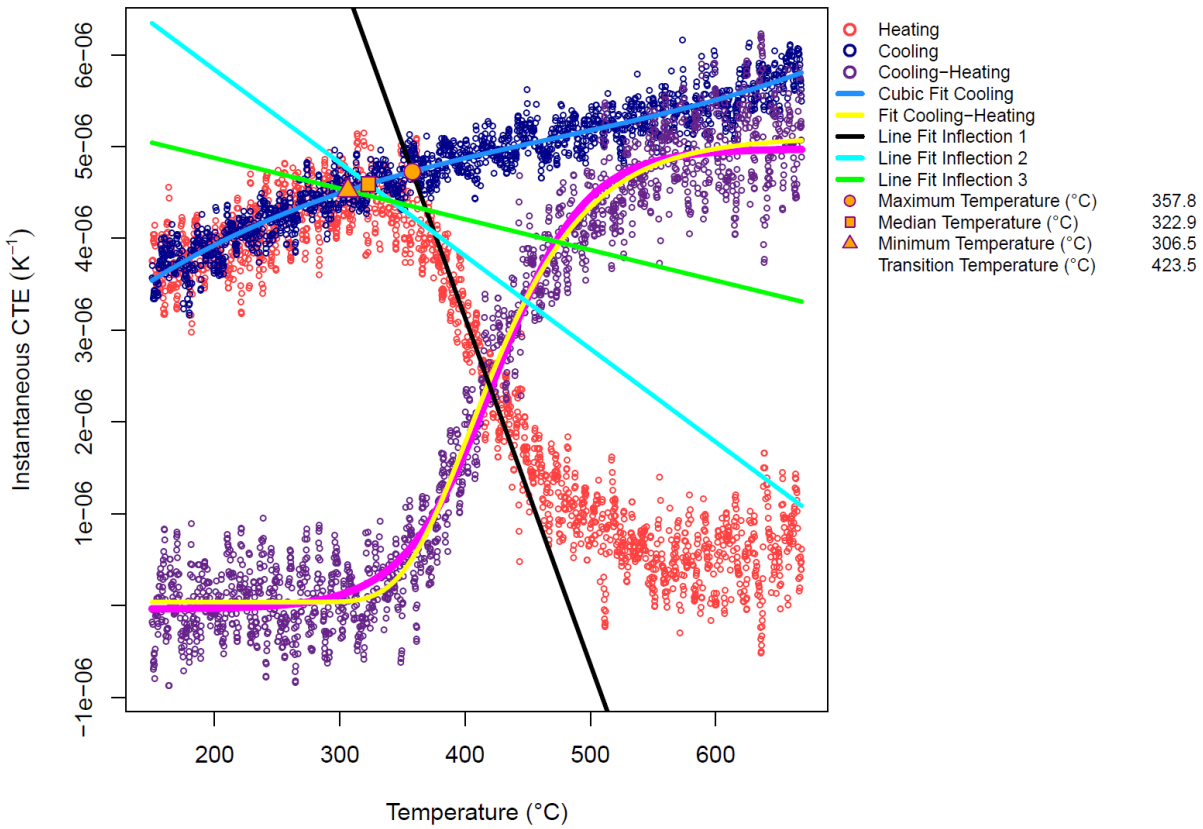

Figure 4.6: Result of dilatometric analysis of a SiC thermometry bar from the FCAY-04 irradiation capsule.

4.2 Mechanical Testing

Room temperature uniaxial tensile tests were performed on both the unirradiated and irradiated tensile specimens in order to assess change in mechanical properties. Tests were performed using shoulder loading at a strain rate of 10^{-3} s^{-1} on a screw-driven machine. The engineering strain was determined from the recorded crosshead separation using the initial gauge length of 5.0 mm, while the engineering stress was determined by dividing the applied load by the initial cross-sectional area (0.6 mm^2). Room temperature tests were performed at approximately 24 °C in air. Results of these tensiles tests

are reported elsewhere [109].

4.3 APT Data Collection & Analysis Methods

4.3.1 APT Sample Preparation

Specimens for APT analysis were prepared from the fractured half tensile specimens following room temperature tensile testing. Standard metallography techniques were used to mechanically polish broken half tensile specimens for focused ion beam (FIB) sample preparation. Atom probe needles were prepared using the FIB liftout method [110] from the non-deformed head area of the half tensile specimens opposite of the strained neck. Liftouts were prepared from each of the four Fe-Cr-Al compositions in the 7 dpa condition in addition to the unirradiated, 0.8 dpa and 1.8 dpa conditions of the Fe-18Cr-5.8Al composition, allowing for investigation of both composition and dose dependencies of α' precipitation in this system. FIB sample preparation was performed at both the Low Activation Materials Development and Analysis (LAMDA) facility at Oak Ridge National Laboratory (ORNL) using either a FEI Quanta 3D DualBeam FIB or a FEI Versa 3D DualBeam FIB [111]; and the Microscopy and Characterization Suite (MaCS) at the Center for Advanced Energy Studies (CAES) using a FEI Quanta 3D Field Emission Gun (FEG) FIB. All specimens were mounted on silicon microtip coupons. Final sample sharpening was performed just prior to data collection to mitigate potential sample oxidation and degradation. This final sharpening step included a 15 second, 5 kV milling step in order to minimize implanted Ga in the analyzed volume. A scanning electron microscope (SEM) micrograph illustrating the final specimen geometry is shown in Figure 4.7.

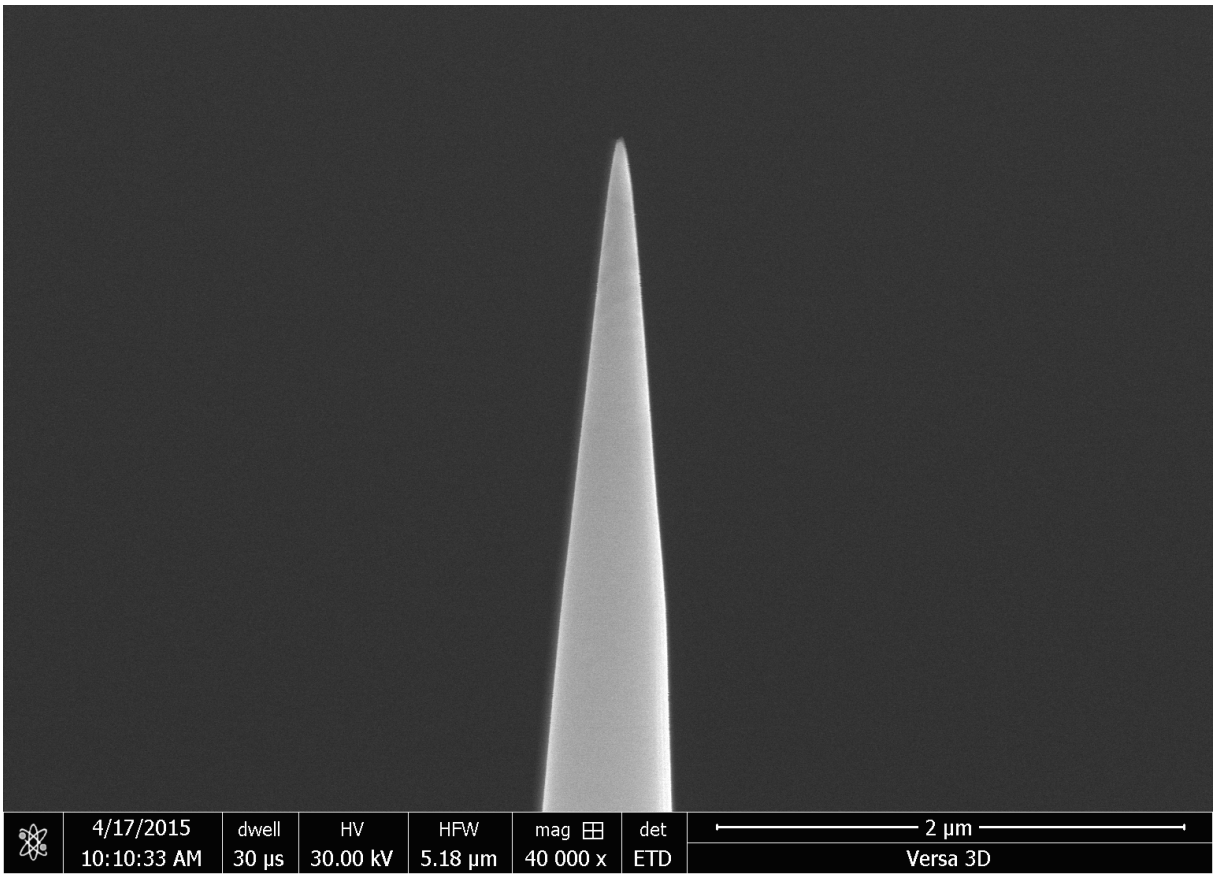

Figure 4.7: SEM micrograph of a representative sharpened microtip prepared for APT analysis.

4.3.2 APT Data Acquisition

Atom probe data was collected on a Cameca Local Electrode Atom Probe (LEAP) 4000X HR located at either the Center for Nanophase Materials Science (CNMS) at ORNL, or at the MaCS facility at CAES. The LEAP was operated in the laser-pulsed mode at a base specimen temperature of 50 K, pulse repetition rate of 200 kHz, and a laser energy of 50 pJ, with the detection rate typically set at 0.5%. Data sets of at least 10 million ions were collected from a minimum of two microtips for each condition.

4.3.3 APT Data Analysis

Atom probe data was reconstructed and analyzed using the IVAS 3.6.8 software [92]. α' precipitates were characterized using the maximum separation cluster-finding algorithm (discussed in Section 2.4.2) that is packaged with the IVAS software. Phase composition analysis employed both the TOF peak decomposition and trajectory aberration correction methodologies discussed in Chapter 3. Expected isotopic abundances for peak decomposition was calculated using the ORIGEN-2.2 Isotope Generation & Depletion software code for each individual Fe-Cr-Al composition and irradiation condition studied and decay-corrected to the date of analysis. Trajectory aberration correction utilized the cubic binning methodology with a bin size of 1 nm and and a threshold density value of the matrix mean bin density plus 3 times the standard deviation of the Gaussian fit.

4.4 SANS Data Collection & Analysis Methods

4.4.1 SANS Data Acquisition

SANS data was acquired from the fractured half tensile specimens on the CG-2 general-purpose SANS beamline (GP-SANS) at the HFIR facility at ORNL [112]. Three distinct detector configurations were used for data collection—two utilized 0.472 nm neutrons at detector distances of 1.079 and 7.779 m, with the third utilizing 1.2 nm neutrons at a detector distance of 19.279 m. In addition, the detector was laterally offset by 0.4 m in each measurement to maximize the accessible range of momentum transfer (Q). These configurations allow SANS measurements to span a Q range of $0.01<Q<10$ nm^{-1}. This data was converted to the cm^{-1} scale by correcting the medium length data for sample thickness and transmission before normalizing to the attenuated direct beam. Data

from the other two detector configurations was then scaled to match the medium-length data to generate the full, combined scattering curves. All data was collected at room temperature and multiple scattering corrections were deemed negligible.

4.4.2 SANS Data Analysis

Models assuming a monodisperse distribution of spherical precipitates was applied to the SANS data following radial averaging of the 2-dimensional diffractograms into 1-dimensional scattering intensity curves. The details of this method can be found in Section 3.4.

4.5 STEM/EDS Data Collection & Analysis Methods

4.5.1 STEM/EDS Sample Preparation

Specimens for STEM/EDS analysis were also prepared using FIB liftout techniques from fractured half tensile specimens following room temperature tensile testing. Specimens were prepared from the non-deformed areas of the half tensile specimens after mechanical polishing. Liftouts were prepared from various Fe-Cr-Al compositions in the 7 dpa condition. FIB sample preparation was performed at the ORNL LAMDA facility using either a FEI Quanta 3D DualBeam FIB or a FEI Versa 3D DualBeam FIB [111]. Final sample thinning procedure included a 5 kV milling step followed by a 2 kV final cleaning step to remove FIB-induced damage artifacts from the sample surface. A SEM micrograph showing a representative final specimen geometry is shown in Figure 4.8.

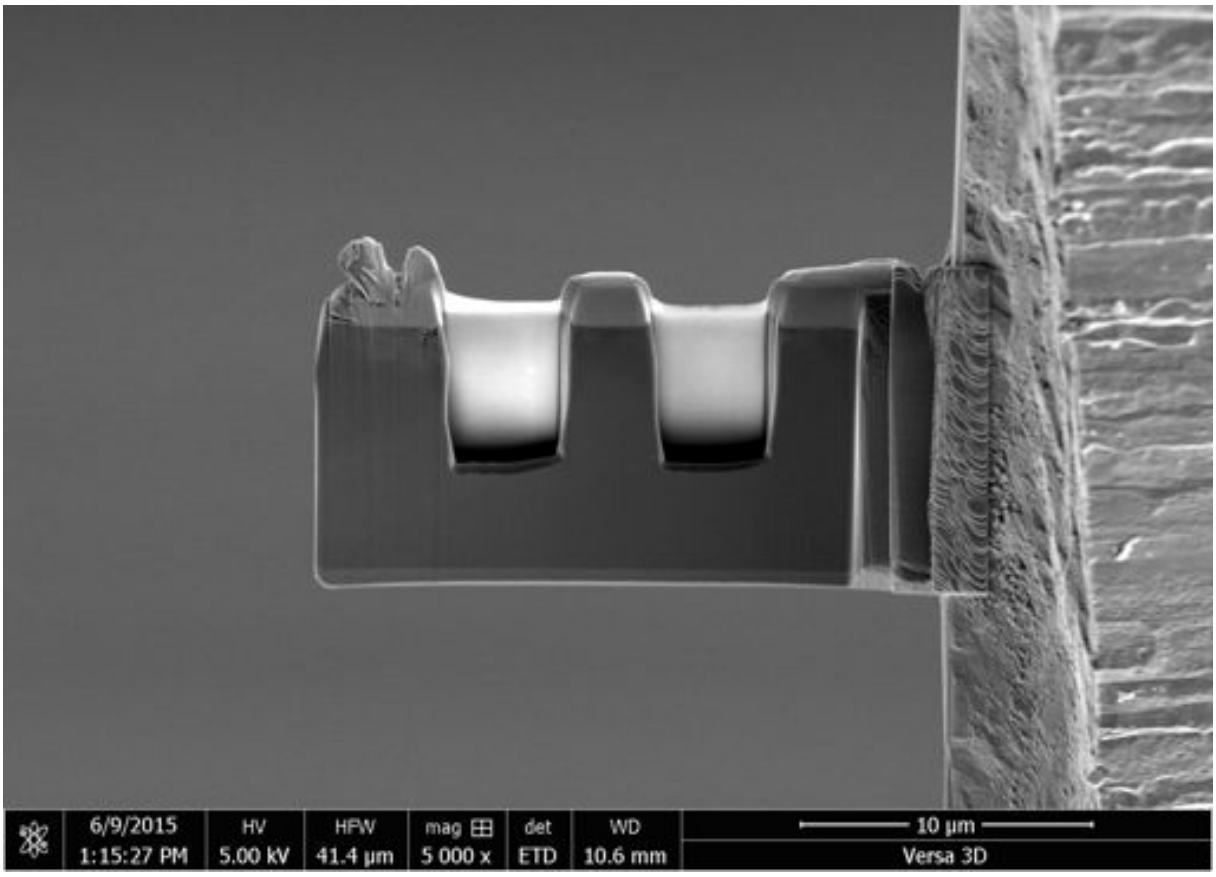

Figure 4.8: SEM micrograph of a representative specimen lamella prepared for STEM/EDS analysis.

4.5.2 STEM/EDS Data Acquisition

STEM/EDS analysis was performed on the FEI Talos F200X S/TEM located at the ORNL LAMDA facility. The chemically-sensitive EDS analysis is required to observe α' precipitates due to the semi-coherency of the precipitate phase with the matrix [48]. STEM images were acquired simultaneously with EDS spectral image maps to correlate precipitation nucleation sites with both dislocation loops and grain boundaries. When imaging dislocation loops, the specimen is oriented such that electrons are incident on the [100] zone axis, allowing for simultaneous imaging of both the $a\langle 100\rangle$ and $a/2\langle 111\rangle$

dislocation loop variants that are known to form in irradiated BCC ferritic materials [90]. When grain boundaries were imaged, the specimen was oriented such that the boundary was "edge-on," with the incident electron beam parallel to the boundary interface. Images and spectra were collected using a 200 kV accelerating voltage and a spot size of 3, with images collected using either the ADF or HAADF detectors at a camera length of 98 mm.

4.6 Results

4.6.1 APT Results

The unirradiated Fe-18Cr-5.8Al specimen was analyzed to serve as a representative sample of the alloys in their as-received state to assess whether or not α' phase clustering was present in these materials prior to irradiation. Evidence of statistically significant clustering was not observed in atom maps, concentration isosurfaces, nearest neighbor distribution analyses, or χ^2 statistical analyses [61, 66] generated from this data set.

All irradiated specimens analyzed exhibited indications of Cr atom clustering regardless of irradiation dose or material composition. Full reconstructions from a representative specimen from each condition studied can be found in Appendix E. A summary of the results of the completed atom probe analysis, including the final matrix and precipitate compositions and precipitate morphology data for all compositions and irradiation conditions studied, is given in Table 4.4. Representative atom probe reconstructions illustrating cluster morphology for each composition irradiated to 7 dpa are shown in Figures 4.9 (indexed clusters) and 4.10 (atom maps). The resulting precipitate volume fraction in the 7 dpa specimens is shown to follow a nearly linear trend with alloy Cr

content and is generally accompanied by increasing number density and average radii. Furthermore, alloys with a higher Al content exhibit a diminished Cr concentration (58-65 at.% Cr) in the precipitate volumes when compared to the ~85% Cr precipitates reported in studies for the binary Fe-Cr system [22], suggesting that Al additions do indeed partially destabilize the α' phase. Furthermore, Al is shown to be preferentially rejected from the precipitates.

Representative atom probe reconstructions demonstrating α' precipitate morphology evolution with dose for the Fe-18Cr-5.8Al alloy are shown in Figures 4.11 (indexed clusters) and 4.12 (atom maps). Significant precipitation is observed for all three dose conditions studied. In the lowest dose condition (0.8 dpa at 355 °C), a high number density of smaller, less mature (as indicated by composition) precipitates were observed. Precipitate volume fraction was shown to increase in the specimen irradiated to 1.8 dpa at 382 °C, accompanied by a decrease in precipitate number density and an increase in average radius. Volume fraction is not appreciably changed by continued irradiation to 7 dpa, while number density is seen to decrease as cluster radius increases, suggesting a transition to a coarsening regime past 1.8 dpa. It should be noted that variation in the irradiation temperature of these specimens due to the inherent nature of neutron irradiation experiments may affect the observed trends.

Table 4.4: Summary of results of APT analysis of α' precipitates for all compositions and dose conditions studied. Compositions are given in at.%

Alloy	Irradiation Dose (dpa)	Irradiation Temp (°C)	**Matrix Composition** Fe	Cr	Al	**Mean Cluster Composition** Fe	Cr	Al	$N_{\alpha'}$ ($\times 10^{24}$ m^{-3})	$f_{\alpha'}$ (%)	$\overline{R}_{\alpha'}$ (nm)
Fe-10Cr-9.3Al	7.0 dpa	319.9 ± 12.7	80.99	9.26	9.54	31.19 ± 8.39	64.88 ± 9.56	3.80 ± 2.47	0.51 ± 0.11	1.78 ± 0.45	1.49 ± 0.90
Fe-12Cr-8.7Al	7.0 dpa	319.9 ± 12.7	80.69	10.61	8.57	37.10 ± 6.24	58.22 ± 6.65	4.52 ± 1.46	0.69 ± 0.01	3.24 ± 0.20	1.82 ± 0.84
Fe-15Cr-7.7Al	7.0 dpa	319.9 ± 12.7	80.30	11.91	7.60	22.71 ± 7.62	73.71 ± 8.07	3.45 ± 1.61	2.2 ± 0.11	5.79 ± 0.41	1.57 ± 0.62
Fe-18Cr-5.8Al	0.8 dpa	355.1 ± 3.4	79.11	14.90	5.90	27.84 ± 6.05	69.62 ± 6.30	2.48 ± 1.00	3.1 ± 0.03	5.70 ± 0.21	1.50 ± 0.41
	1.8 dpa	381.9 ± 5.4	80.61	13.21	6.07	18.25 ± 6.81	79.52 ± 7.17	2.16 ± 1.05	2.9 ± 0.31	7.44 ± 0.73	1.58 ± 0.51
	7.0 dpa	319.9 ± 12.7	80.61	13.13	6.02	8.49 ± 7.02	89.22 ± 7.41	2.18 ± 1.29	1.9 ± 0.06	6.72 ± 1.73	1.78 ± 0.66

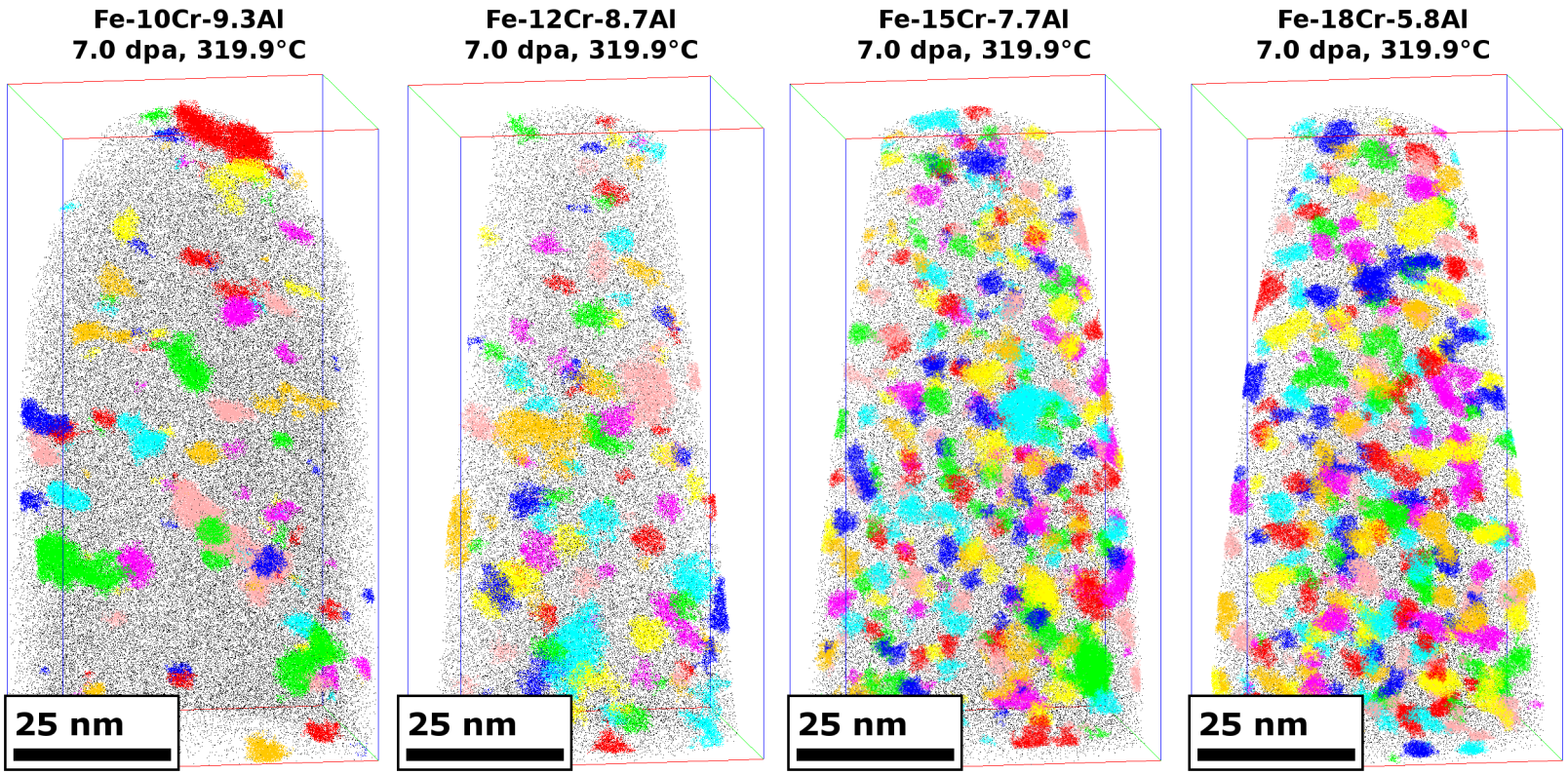

Figure 4.9: Representative APT reconstructions for the various compositions of Fe-Cr-Al irradiated to 7 dpa at 320 °C, in which a unique color is assigned to each α' precipitate detected using the maximum-separation method cluster finding algorithm native to IVAS. Figures are cropped to $50 \times 50 \times 100$ nm volumes to allow for direct comparison.

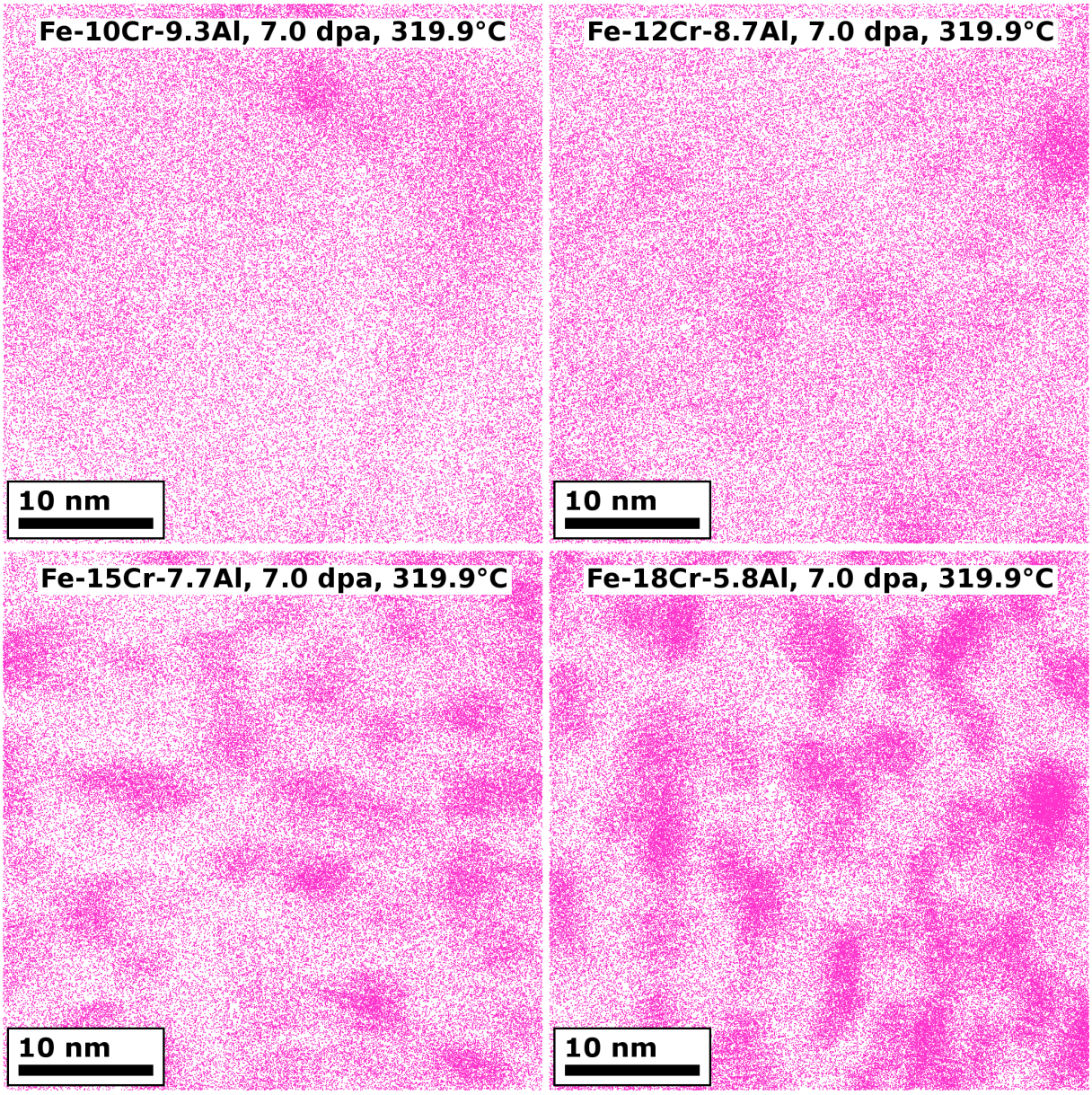

Figure 4.10: Representative Cr atom maps show evidence of clustering in all Fe-Cr-Al compositions studied when irradiated to 7 dpa at 320 °C. Maps represent a thickness of 20 nm.

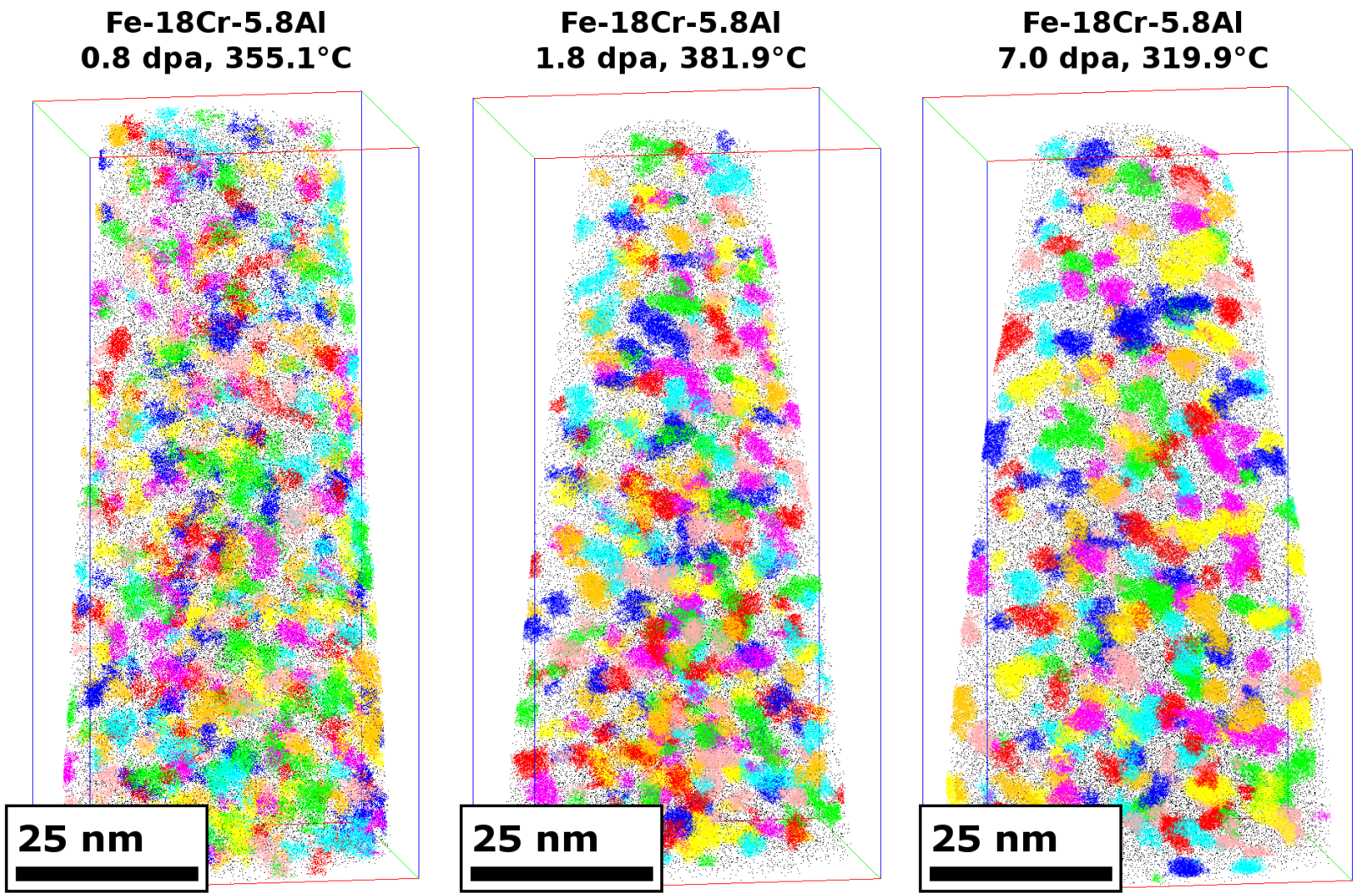

Figure 4.11: Representative APT reconstructions for the various irradiation conditions studied for Fe(18)CrAl, in which a unique color is assigned to each α' precipitate detected using the maximum-separation method cluster finding algorithm native to IVAS. Figures are cropped to $50 \times 50 \times 100$ nm volumes.

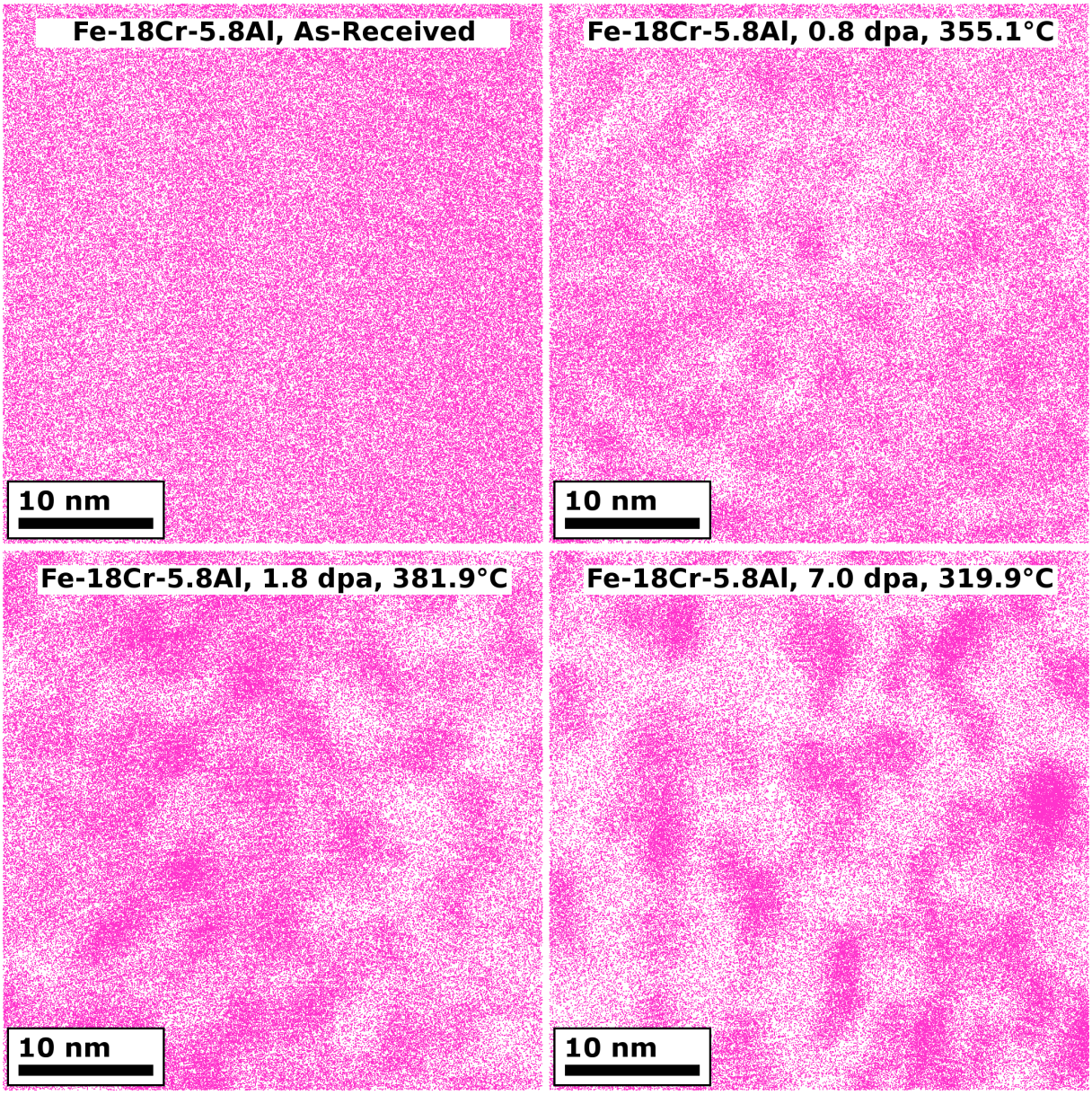

Figure 4.12: Representative Cr atom maps illustrate the progression of α' clustering in Fe(18)CrAl as radiation dose is increased up to 7 dpa.

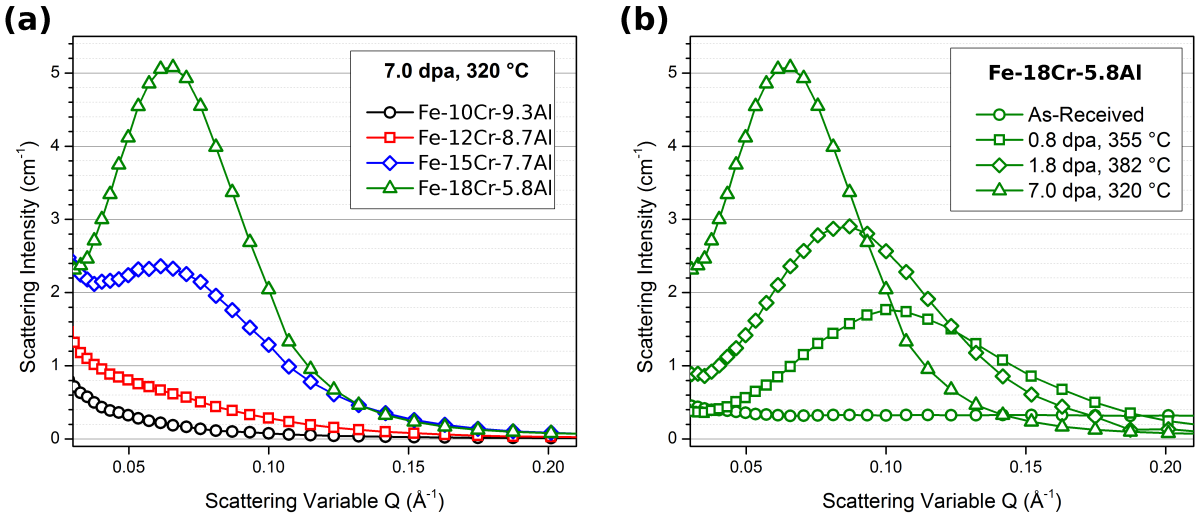

Figure 4.13: Scattering intensities of model Fe-Cr-Al specimens obtained by SANS analysis after irradiation, (a) for varying alloy contents irradiated to 7 dpa at 320 °C, and (b) for varied irradiation conditions for the Fe-18Cr-5.8Al alloy composition.

4.6.2 SANS Results

Plots comparing scattering intensities for $Q \geqslant 0.5$ nm^{-1} for the four Fe-Cr-Al alloys in the 7 dpa condition are shown in Figure 4.13a. A similar plot comparing the scattering intensities for the various irradiation conditions of the model Fe-18Cr-5.8Al alloy is shown in Figure 4.13b. Changes in the scattering intensity are clearly observed both for increasing alloy Cr content with constant dose and for increasing irradiation dose with constant alloy composition. These intensity trends are similar to those seen in other SANS investigations of α' precipitation in aged Fe-Cr-Al alloys and irradiated Fe-Cr alloys by several authors [16, 20, 25, 113, 114]. This qualitative agreement, in addition to reasonable fits to the experimental data in the range of $0.5 < Q < 2.0$ nm^{-1}, validated the use of the spherical exclusion model to assess α' precipitation in the SANS data.

Table 4.5: Summary of results of SANS analysis of α' clustering for all composition and dose conditions studied. Scattering contrast was determined using matrix and precipitate compositions determined through APT analyses.

Alloy	Irradiation Dose (dpa)	Irradiation Temp (°C)	$N_{\alpha'}$ ($\times 10^{24}$ m^{-3})	$f_{\alpha'}$ (%)	$\overline{R}_{\alpha'}$ (nm)
Fe-10Cr-9.3Al	0.8 dpa	355.1 ± 3.4	0.73	2.55	2.03
	1.8 dpa	381.9 ± 5.4	0.46	2.01	2.18
	7.0 dpa	319.9 ± 12.7	0.06	0.57	2.40
Fe-12Cr-8.7Al	0.3 dpa	334.5 ± 0.6	10.44	11.25	1.37
	1.8 dpa	381.9 ± 5.4	5.81	14.91	1.83
	7.0 dpa	319.9 ± 12.7	0.94	3.81	2.13
Fe-15Cr-7.7Al	0.3 dpa	334.5 ± 0.6	46.81	30.61	1.16
	1.8 dpa	381.9 ± 5.4	7.57	18.81	1.81
	7.0 dpa	319.9 ± 12.7	2.27	9.39	2.15
Fe-18Cr-5.8Al	0.8 dpa	355.1 ± 3.4	18.89	27.79	1.52
	1.8 dpa	381.9 ± 5.4	6.64	17.61	1.85
	7.0 dpa	319.9 ± 12.7	1.34	9.08	2.53

As discussed in Section 3.4, the models used to fit and quantify SANS data assumed a monodisperse distribution of spherical precipitates, with scattering length densities based on APT phase composition data following trajectory aberration correction. Table 4.5 summarizes the calculated α' precipitate morphologies resulting from applications of these models.

4.6.3 STEM/EDS Results

A STEM-ADF image and a STEM/EDS map acquired simultaneously from the same region of a Fe-18Cr-5.8Al specimen following neutron irradiation to 7.0 dpa at 320°C are shown in Figures 4.14a and 4.14b, respectively. As demonstrated by the overlay image in Figure 4.14c, there appears to be no correlation between dislocation loop structures and the α' precipitates. These images suggest that α' precipitates nucleate homogeneously

in the bulk material. These findings provide additional confidence in the assumption that precipitate microstuctures observed in the APT are representative of bulk alloy behavior.

The one exception to this homogeneous nucleation was observed at grain boundaries. As demonstrated by Figure 4.15, a precipitate denuded zone on the order of 10-20 nm in width is observed at the grain boundary. The denuded zone is accompanied with a "w-shaped" Cr radiation-induced segregation profile. This competing solute redistribution effect implies that precipitation response could be assuaged by developing nanostructured Fe-Cr-Al variants with a high density of defect sinks. As the APT analysis was performed on specimens prepared from within grains, these interfacial effects were not captured. This further highlights the necessity of a correlative microscopy approach to fully characterize the resulting precipitate microstructure.

4.7 Discussion

4.7.1 Comparing SANS & APT Data

In comparing the quantitative analysis of precipitate morphologies between the APT and the SANS results, it became clear that, despite the efforts to correlate results from the two techniques, there is some disparity between the reported values — specifically with regard to the SANS precipitate number density and volume fraction, both of which are dependent on the assumed scattering contrast. These differences can be attributed to a number of factors associated with assumptions and uncertainties inherent in each of these analysis techniques.

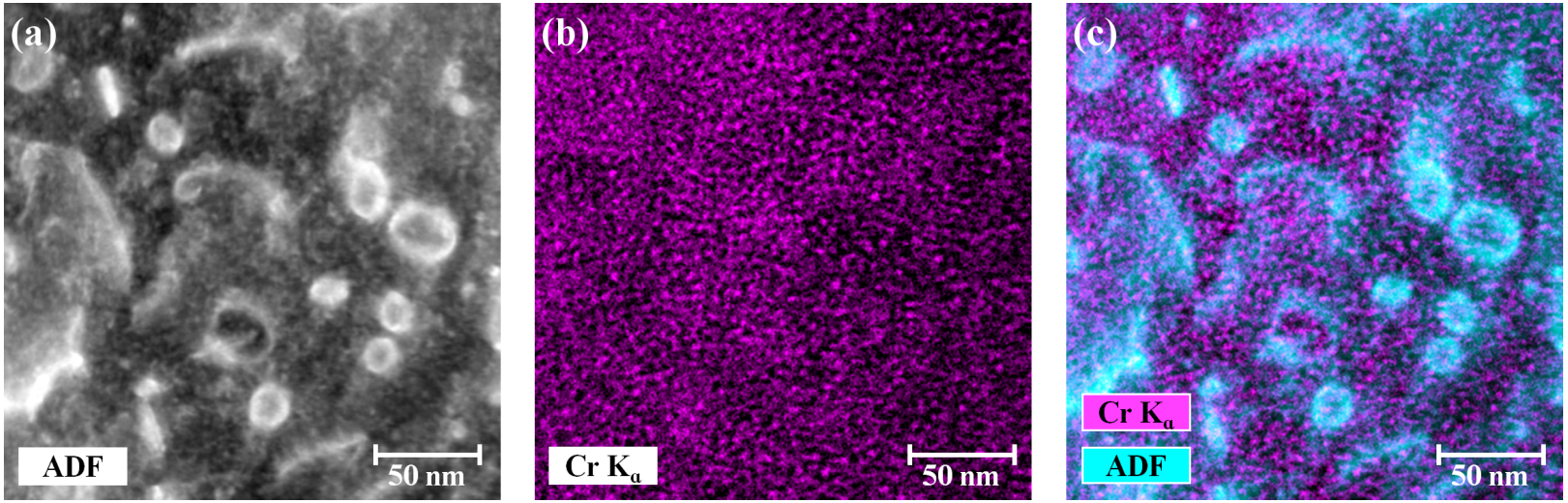

Figure 4.14: (a) STEM-ADF image, acquired on the [100] zone axis. (b) STEM/EDS map for Cr-K_α x-rays. (c) Color overlay of ADF image and EDS map. All images from the Fe-18Cr-5.8Al alloy irradiated to 7.0 dpa at 320°C.

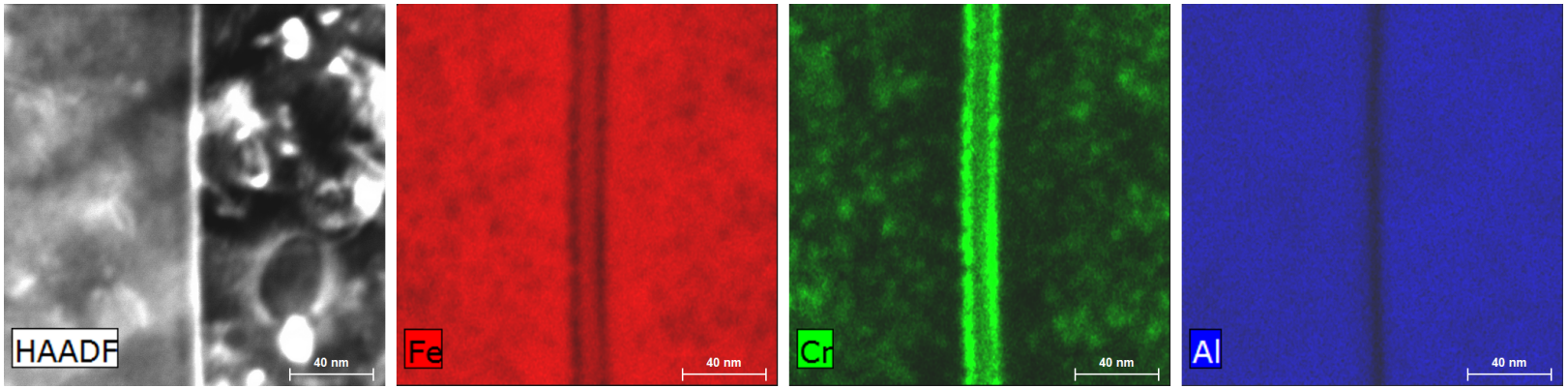

Figure 4.15: High-angle annular dark-field STEM image and x-ray maps derived from EDS spectrum images showing both α' precipitates (green clusters) and RIS at a grain boundary for the Fe-12Cr-8.7Al model alloy following irradiation to 7 dpa at 320°C. Denuded zones on the order of 10-20 nm in width are seen on either side of the boundary.

First, both techniques are unable to resolve small clusters. SANS has an instrument-dependent physical resolution limit for observed cluster diameters in the range of 0.5–1.5 nm [91, 115]. APT is able to resolve precipitates smaller than this, but clusters that are on the same length scale as those found as a result of composition fluctuations in a random solid solution are not identified. It is expected that this would result in the average radius reported by SANS being slightly larger than the precipitate size reported by APT, which is consistent with the present findings.

Analysis of the SANS data using models that assume a monodisperse precipitate size distribution is also clearly not physical. Attempts were made to fit the more complex polydisperse models to the data, but good fits were not able to be achieved for all conditions and the resulting quantification for those cases were nonsensical. Furthermore, in addition to the previously mentioned trajectory aberrations, TOF peak overlap, and neutron transmutation effects that were accounted for in the present APT analysis, other artifacts, such as surface migration and chromatic aberration artifacts, can still affect the presented results. Quantification of precipitate morphologies using the maximum separation algorithms can also be very sensitive to the input parameters used [67, 76].

Finally, the assumptions involved in determining SANS scattering contrast can greatly influence the resulting SANS quantification. Extrapolation of scattering contrasts for specimens not characterized using APT adds additional uncertainty to the SANS quantification for those samples. Furthermore, the present analysis assumes pure nuclear scattering and ignores magnetic scattering contributions. As the ferritic α-Fe matrix was plainly ferromagnetic (although the α' phase precipitates are not, according to [44]), this assumption is clearly inadequate. However, it is very difficult to rigorously compensate

for this magnetism analytically; therefore, SANS data collection for these types of alloys is usually conducted in a saturated magnetic field, allowing for the separation of the nuclear and magnetic scattering contributions to the SANS intensity. Assuming pure nuclear scattering in the presence of magnetic scattering, as was done in this study, is expected to result in inflated values for number density and volume fraction. A more detailed discussion of some of the challenges of comparing SANS and APT results is presented in the context of reactor pressure vessel steel precipitate characterization by Hyde et al. [91].

4.7.2 Trends and Significance of Observed Precipitate Microstructures

Despite the quantitative disagreements in the APT and SANS data sets, the observed trends between them remained fairly consistent. A high density of smaller α' precipitates formed initially at low doses, and these precipitates coarsened over time with increasing dose. Increasing Cr content generally resulted in higher number densities and volume fractions of precipitates. As demonstrated by Figure 4.16, these general trends agree with the results of past studies on aged and irradiated binary Fe-Cr alloys and high-Cr ferritics [19–22, 45, 59, 116–118] and studies of aged Fe-Cr-Al alloys by Messoloras et al. [25]. However, the spread in the reported data reinforces the importance of systematic studies of α' precipitation in high-Cr ferritic alloys. Variations in alloy composition, aging or irradiation temperature, time at temperature, and even measurement technique (as discussed prior) have resulted in reported precipitate number densities that span three orders of magnitude, and the number of variables involved can make direct comparison between studies challenging. For example, the composition of the materials investigated by Messoloras et al. are arguably similar to the model alloys studied here, yet the number

densities they report are far lower in comparision, which can be attributed to differences in material treatment (aged vs. irradiated, both at different temperatures) and in the models used to reduce and fit the SANS data [25].

Based on the α-α' ternary phase boundary proposed by Kobayashi et al. (Fig. 2.8) [26], precipitation is not necessarily expected to occur in the Fe-10Cr-9.3Al and Fe-12Cr-8.7Al alloys studied herein, but indications of Cr clustering in these materials are observed in both the APT and SANS investigations. However, the phase boundary proposed by Kobayashi et al. is based solely on change in Vickers hardness (ΔH_V) and not on direct observation of precipitate microstructure — thus, it is possible that the precipitates in these alloys are not contributing significantly to the increase in hardness. The less Cr-rich precipitate compositions observed may serve to reduce the defect barrier strength, as speculated by Edmondson et al. [95], and the decreased precipitate densities observed are expected to result in a diminished hardening response in accordance with the dispersed barrier hardening model [121]. The change in yield strength ($\Delta\sigma_y$) associated with α' precipitates in the Fe-10Cr-9.3Al and Fe-12Cr-8.7Al alloys in the 1.8 dpa condition was determined to be 75 and 200 MPa, respectively, by Field et al. [16]. Assuming $\Delta\sigma_y$ can be related to the change in hardness by $\Delta\sigma_y = 3.06\Delta H_V$ for ferritics according to Busby et al. [122], the expected ΔH_V is expected to fall between 25 and 65 kg/mm^2, both of which are very close to the arbitrary boundary drawn by Kobayashi at 50 kg/mm^2. Furthermore, the materials investigated by Kobayashi et al. did not contain Y additions, which have been shown to enhance the rate of embrittlement in similar systems [25]. Finally, the proposed boundary is defined for an aging temperature of 475°C, while the investigated materials were irradiated at temperatures between 320 and 382°C. The diminished Cr solubility at these lower temperatures may be sufficient to induce

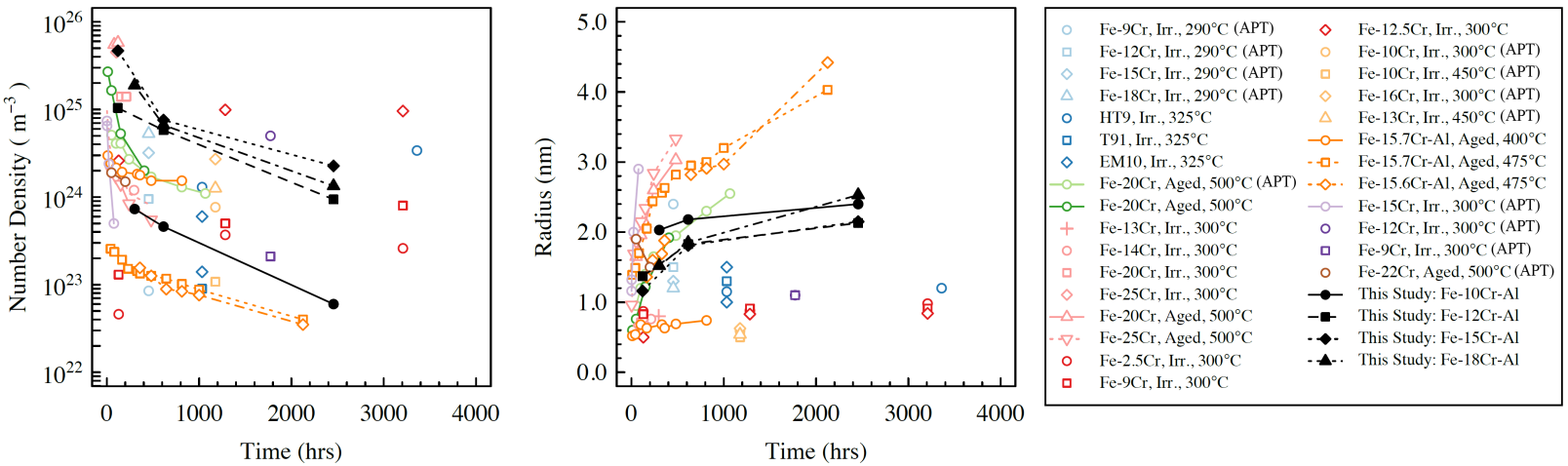

Figure 4.16: Comparison of SANS data from the current study with results published in literature for various aged and irradiated Fe-Cr and Fe-Cr-Al alloys [19–22, 25, 49, 50, 53, 118–120]. Data points are color-coded by source and were determined through SANS investigations unless otherwise indicated.

α' precipitation in these less Cr-rich alloys in current work.

Substantial work has been performed on characterizing precipitates in the PM 2000™ (nominal composition Fe-18.5 at.% Cr-10.10 at.% Al + Ti,Y) commercial oxide dispersion-strengthened (ODS) Fe-Cr-Al alloy by Capdevila et al. [27, 47, 55, 60, 61]. The partitioning of Al to the matrix phase observed in the current work was also observed in PM 2000™. However, the commercial alloys did not exhibit the reduced precipitate Cr contents at saturation seen in the model alloys investigated here. While a number of differences exist between the two studies, Capdevila et al. did report significant changes in phase composition as a function of aging time and temperature [55] which may suggest that the precipitates in the alloys with lower Cr contents and higher Al contents required more time at temperature/irradiation dose to mature. However, precipitate compositions for binary Fe-Cr alloys reported by Bachhav et al. appeared to approach theoretical saturation values after irradiation to just 1.82 dpa at 290°C [22]. As this study achieved doses beyond this, one might conclude that Al may not suppress the equilibrium phase composition, but may instead retard the precipitate maturation kinetics. Unfortunately, as neither Cr nor Al content are held constant in the materials used in this study, further systematic investigation is required in order to reach a decisive conclusion on this matter.

4.7.3 Comparison of Precipitation Kinetics to LSW/UOKV Model Behavior

Additional insight into the kinetics of the coarsening behavior of the α' precipitates in the Fe-Cr-Al alloys system can be gained by looking at the SANS results in the context of the Umantsev-Olson-Kuehmann-Voorhees (UOKV) model [123, 124]. The UOKV model is an adaptation of the seminal model for diffusion-limited coarsening in binary alloys

developed by Lifshitz and Slyozov [125] and Wagner [126] (LSW model) that extends its predictive capabilities to ternary alloy systems. Both of these models make use of a set of fundamental assumptions [127, 128]: (1) both terminal phase states are dilute solutions, so that a linearized version of the Gibbs-Thomson equation is valid; (2) the precipitated volume fraction is close to zero, so that interparticle interactions can be neglected; (3) the precipitated volume fraction is constant, i.e., the model applies to the late stages of precipitation in which the matrix is no longer supersaturated; (4) coarsening occurs in a stress-free matrix; and (5) precipitates have a spherical morphology. The ultimate conclusion of the LSW and UOKV models is that precipitate coarsening with time can be described by the following temporal power laws:

$$\overline{R}_{\alpha'}(t) = K_R t^{1/3} \tag{4.1}$$

$$N_{\alpha'}(t) = K_N t^{-1} \tag{4.2}$$

$$\Delta c(t) = K_C t^{-1/3} \tag{4.3}$$

where $\Delta c(t)$ is the solute saturation in the matrix (difference between matrix solute content at time t and the equilibrium matrix solute content) and K_R, K_N, and K_C are rate constants for the radius, number density, and solute composition evolution, respectively.

Figures 4.17a and 4.17b plot average precipitate radius and number density, respectively, based on the current SANS investigation versus time at temperature (i.e., irradiation time). SANS results were preferred to APT data in this case because these results spanned the full dose range for each model alloy composition, whereas dose evolution

data from APT is limited to the 18%Cr alloy composition. Figure 4.17a demonstrates that cluster radius temporal evolution in the Fe-Cr-Al materials studied gives a reasonable fit to the power law functional form predicted by the UOKV model. Furthermore, the slope of these curves is shown to increase with increasing Cr content, corresponding to an increasing rate constant for radius evolution, which is to be expected as the driving force for precipitation increases. Note that the 1.8 dpa specimen, which was irradiated at a higher temperature, consistently shows increased coarsening kinetics in this plot. Additionally, Figure 4.17b shows that number density trends are also in line with predictions based on the UOKV model.

Two statements can be made based on the demonstrated experimental agreement with predicted behavior: (1) α' precipitation in irradiated Fe-Cr-Al is a diffusion-limited phenomenon, and (2) the mechanism for precipitation is similar in thermally aged and irradiated Fe-Cr and Fe-Cr-Al alloys. In comparing experimental fits from the present work with data reported for Fe-20Cr aged at 500°C reported by Novy [21] and for Fe-15.7Cr-9.7Al-0.19Y (at.%) aged at 475°C reported by Messoloras [25] — both of which also demonstrate a reasonable fit to LSW/UOKV models — it is shown that both aging experiments yield higher rate constants for radius evolution than the irradiated alloys presented herein. This suggests that thermal aging experiments can be used to provide insight into precipitation phenomena in the irradiated system, especially if some rigor is applied to determine the temperature shift required to emulate a given irradiation condition.

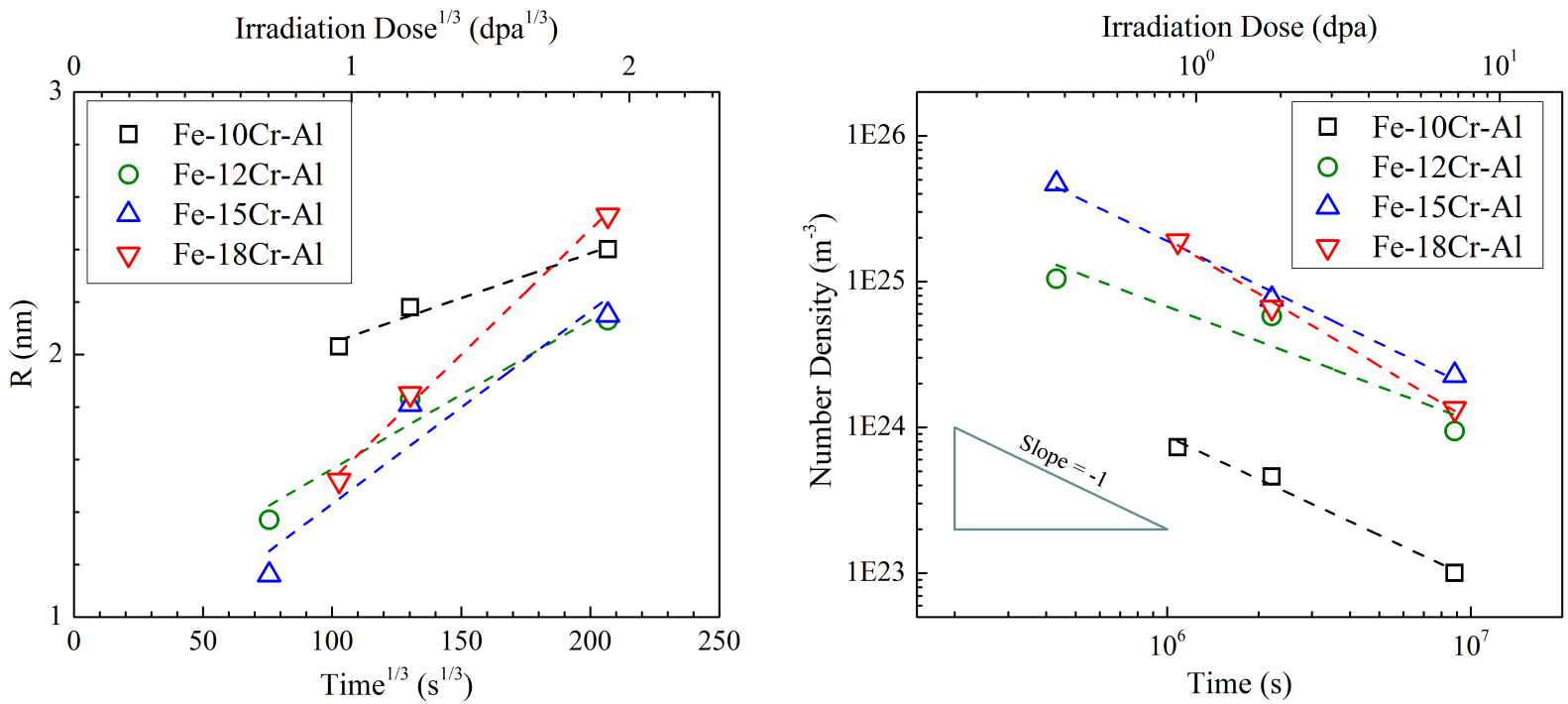

Figure 4.17: Comparison of precipitate coarsening trends with behavior predicted by the LSW/UOKV models. Reasonable fits to the SANS results are achieved, with the plot shown in (a) demonstrating $\overline{R}_{\alpha'} \propto t^{1/3}$ and (b) demonstrating $N_{\alpha'} \propto t^{-1}$ for the irradiated Fe-Cr-Al alloys. Dashed lines indicate least squares fit of present data to predicted model trends for each Fe-Cr-Al composition studied.

4.7.4 Impact of Findings on Fe-Cr-Al In-Reactor Performance

It has been shown that the irradiation-induced embrittlement resulting from the precipitation of the α' phase that has historically limited the viability of high-Cr ferritics for radiation environments is expected to continue to be an issue for Fe-Cr-Al alloys. As such, it is likely that steps must be taken to mitigate the precipitation response when designing such an alloy for nuclear applications. Based on the present findings, there are a number of potential ways in which this can be accomplished.

The most obvious method for mitigating α' precipitation in Fe-Cr-Al alloys would be to minimize alloy Cr content while maximizing alloy Al content. However, based on discussions from Section 2.1, there is a limit to which this can be done without sacrificing the oxidation performance and workability that make Fe-Cr-Al an attractive material system in the first place. It should be noted that, assuming that α' precipitates are weak barriers to dislocation motion, some amount of α' phase in the microstructure is likely acceptable as long as the extent of the resulting material hardening and embrittlement is not application-limiting. This is supported by the findings of Kobayashi et al. and other studies that have successfully correlated α' precipitate microstructure with the change in material hardness using the dispersed-barrier hardening (DBH) model or similar structure/property relationship models [16, 26, 103]. If Al does indeed suppress precipitation by retarding the kinetics of formation, it is possible that there is some amount of Al that can delay application-limiting embrittlement for relatively short-lived in-core components — for example, LWR fuel claddings are typically exposed for only three fuel cycles (~15 dpa, based on [6]) before being removed. Other forms of composition adjustment through minor alloying element additions may also suppress α' precipitation, though early studies of hardness change in thermally aged Fe-Cr alloys

with minor Ti, Mo, Nb, and C additions suggest that alloying in most instances only serves to exacerbate the embrittlement response [129, 130].

Furthermore, as evidenced by STEM/EDS investigations, precipitates are not observed in the vicinity of grain boundaries, which suggests that precipitate nucleation may be inhibited in the presence of strong defect sinks. This implies that α' embrittlement could be mitigated by engineering the microstructure to include a fine, nanoscale grain structure or a high density of nanoscale oxide particles (i.e., ODS variants). Such microstructural modifications would have the added benefit of supplementing the relatively poor high-temperature strength of these ferritic alloys when compared to austenitic stainless steels.

5 CONCLUSIONS

5.1 Summary

The precipitation of the α' phase in Fe-Cr-Al alloys is a complex process that can potentially limit the applications of these alloys in radiation environments. A correlative microscopy approach has been employed in order to study both the composition and dose dependencies of this precipitation process in a series of model Fe-Cr-Al alloys. The experimental results and developed techniques contribute to an enhanced understanding of precipitation phenomena in Fe-Cr-Al alloys and other high-Cr ferritic materials.

As expected, alloys with higher Cr contents exhibited an increased precipitation response, resulting in comparatively higher precipitate number densities and volume fractions for similar irradiation treatments. Al additions appear to partially destabilize the α' phase, resulting in precipitates with reduced Cr contents when compared to binary Fe-Cr systems by either retarding precipitate maturation kinetics or changing the equilibrium phase composition. In addition, Al was shown to be preferentially rejected from the precipitate volume, instead partitioning to the α-Fe matrix. These findings would suggest that an optimal Fe-Cr-Al alloy composition that mitigates precipitation in radiation environments would minimize Cr content and maximize Al content while maintaining adequate properties based on other performance metrics.

Observed microstructural evolution with dose suggests that α' precipitate nucleation appears to proceed rapidly, entering a coarsening regime before 1.8 dpa in the current study. Reasonable agreement was achieved between the coarsening behavior observed

in the SANS data and the behavior predicted by the UOKV model for diffusion-limited coarsening. This strongly suggests that α' precipitation in irradiated Fe-Cr-Al alloys is a diffusion-limited process with a similar mechanism to the thermally aged system. This ultimately implies that the precipitation response in neutron-irradiated alloys can be pre-screened using thermal aging experiments.

Correlating APT and SANS results has been shown to be non-trivial due to the differences and inherent limitations of each measurement technique. One of the primary obstacles in doing so is determination of phase compositions from APT data in lieu of trajectory aberration effects. To overcome this, two methods have been proposed for comparing atomic densities between phase volumes in an APT reconstruction, allowing for composition correction through use of simplifying assumptions regarding the physics of the trajectory aberration process. Unfortunately, these physics are complex and dependent on the material composition and geometry, and a more detailed understanding of the factors that govern the aberration behavior is required to accurately and robustly apply these corrections to a specific material. As they stand, these techniques provide a method for specimen-wide composition correction with notable statistical advantages over the widely-used proximity histogram technique. Though quantitative agreement between APT and SANS results was not achieved, the observed trends were generally preserved between the two techniques.

Ultimately, performing APT, SANS, and STEM/EDS analyses in tandem have led to a more holistic understanding of the precipitation process in neutron-irradiated Fe-Cr-Al alloys. Knowledge of precipitate and matrix chemistry from APT improves SANS quantification, while STEM/EDS analyses allow for identification of potential relationships

between precipitate nucleation sites and dislocation loops and grain boundaries not easily observed using the other techniques. Correlation of these results allows the detailed microstructural and microchemical information gained from the APT analysis of small volumes to be extrapolated to bulk alloy behavior.

5.2 Contribution to the State of the Art

The described work details the most systematic compilation of experimental data on α' precipitation in Fe-Cr-Al alloys to date. Furthermore, through application and development of correlative techniques, the author has established novel methods for reconciling APT and SANS data and bringing results closer to a 1:1 correlation. The multimethod approach employed, in which the same specimens are used for all experimental analyses, is an effort that is not routinely accomplished and highlights some of the inherent limitations of each technique that must be considered when interpreting results. Understanding these sources of error is especially critical in the development of robust predictive models for α' precipitation that will undoubtedly use experimental data from the current study and others like it for benchmarking purposes.

The experimental results presented here provide valuable insight into how Al additions affect the formation of α' precipitates in high-Cr ferritic alloys by either shifting the phase boundary or retarding precipitate maturation kinetics. Regardless of the mechanism, these results suggest that Al additions may serve to mitigate some of the irradiation-induced hardening and embrittlement issues while simultaneously improving high-temperature oxidation and corrosion behavior in a wide range of high-Cr ferritic alloy compositions. Furthermore, the results have demonstrated that the proposed phase boundary by Kobayashi et al. (Fig. 2.8, [26]) needs significant refinement to be used at

the lower temperatures of interest for LWR applications, as irrefutable evidence has been shown here that α' precipitates form even in low Cr Fe-Cr-Al alloys at these conditions.

The methods for correlative microscopy established in this work are anticipated to provide a foundation for the development of robust, density-based trajectory aberration correction techniques for APT data collected from a wide range of multiphase materials. The described techniques, specifically those utilizing tessellation algorithms, are believed to yield an accurate comparison of the relative densities between the matrix and precipitate volumes in an APT data set. These relative densities, along with a comprehensive understanding of the physics that govern these aberration processes, are necessary in order to correct phase compositions for these artifacts in a given APT reconstruction. Further refinement and standardization of these techniques is expected to have a wide-reaching impact on improving the accuracy of reported phase compositions in APT investigations.

5.3 Future Work

This work has explored some of the factors that influence α' precipitation in a set of neutron-irradiated model Fe-Cr-Al alloys and has developed methods to correlate precipitate microstructure data between APT and SANS experiments. While significant advancements have been made on both fronts, further work is required to address knowledge gaps that still remain. Based on the presented findings, the following paths forward are suggested.

This study has identified that Al additions seem to suppress the α' precipitation response in Fe-Cr-Al alloys. However, further systematic studies are required to make defini-

tive conclusions as to the mechanism of this interaction. This could be accomplished through a similar study to the presented work in which the model alloys studied contain varying amounts of Al while holding Cr content constant. Additionally, thermodynamic simulations using a software such as Thermo-Calc could provide additional insight into how the α-α' phase boundary shifts with Al content.

Exploring more complex alloy compositions and microstructures could also result in a more robust, nuclear grade Fe-Cr-Al alloy. Minor alloying element additions could either promote or impede precipitation and embrittlement responses. Further more, oxide dispersion-strengthened Fe-Cr-Al variants could potentially enhance radiation tolerance by increasing the density of point defect sinks.

The dose evolution of α' precipitates in Fe-Cr-Al has been studied for a single irradiation temperature (with some capsule-to-capsule variation) and damage dose rate. Different irradiation conditions may result in vastly different precipitate microstructures. Higher or lower irradiation temperatures are likely to affect precipitation formation kinetics and may also influence equilibrium phase compositions. High damage dose rates, such as those commonly employed in ion irradiation experiments, have been shown to prevent α' precipitation in similar systems due to cascade mixing and injected interstitial effects [53]; however, as the HFIR reactor has a greater damage dose rate than most commercial LWRs, studying the impact of lower damage dose rates might be of more practical interest.

Finally, gaining a deeper understanding of the underlying mechanisms of the trajectory aberration process is required to refine the presented aberration correction methods in

order for them to robustly account for phase mixing in APT reconstructions. Modeling and simulation efforts are expected to play a key role in exploring the factors affecting this process such that the behavior can be predicted for a given material composition and precipitate geometry. Detailed knowledge of the ion flux between precipitate and matrix volumes during APT data collection should allow the density-based correction techniques presented here to more accurately determine the physical phase compositions in multi-phase materials.

APPENDIX A

MATLAB Code for APT Aberration Correction: Cubic Binning

The MATLAB code utilized for matrix/precipitate density comparison utilizing the cubic binning methodology outlined in Section 3.3.2 is displayed below. The MATLAB .m files can be downloaded at: `https://github.com/grizzle13/APT_Aberration_Correction`.

```
function pos_density_cubic_bin

%% This function reads in position data from a standard IVAS .pos file and
%  looks at density variation in precipitate volumes across the
%  reconstruction by sorting the ranged ions into user-defined bins,
%  discriminating by TOF, and fitting Gaussian curves to the resulting
%  distributions.
clear all
close all
clc

% Read in pos data
[posdata,pos_filename] = posread();

filename = pos_filename(1:end-4);

% Define run input parameters
[BinStartSize,BinEndSize,BinStepSize,zSkip,zTrunc,if_save] = binselect();

% Define peaks for TOF discrimination
```

```
% TOFselect utilizes a manual selection based on TOF spectrum
% staticTOF allows for specification of peak mass-to-charge limits
TOFposdata = TOFselect(posdata);
%TOFposdata = staticTOF(posdata,24.92,25.11,25.91,26.18,26.42,26.64);

csvoutput = zeros(length(BinStartSize:BinStepSize:BinEndSize)*3,13);

%Loop over defined bin sizes
n=1;
for BinSize = BinStartSize:BinStepSize:BinEndSize
    %Generate bins based on bin size
    [BinLimits,BinRanges,BinVectors,BinIndices] = makebins(posdata,...
        BinSize,zTrunc,zSkip);

    edges = cell(1,2);
    edges{1} = BinVectors{1};
    edges{2} = BinVectors{2};

    %Populate bins based on TOF of interest
    TOFcounts = posmap(TOFposdata,BinSize,BinLimits(5),BinIndices,edges);
    %Fit Gaussian and define minimum bin size to threshold
    nsigma = 2;
    for nsigma = 2:4
        figure(3*n-2)
        [cutoff,threshgof] = thresholdcounts(TOFcounts,nsigma);
        str = sprintf(['Thresholding for Bin Size = %1.2f, Threshold '...
            '= %u\\sigma'],BinSize,nsigma);
        title(str)
        if if_save == 'Y'
            ThresholdOut = sprintf('_Thresholding_bin%1.2f_%usigma',...
                BinSize,nsigma);
            ThresholdOut = strrep(ThresholdOut,'.','p');
            ThresholdOutName    = strcat(filename,ThresholdOut);
            print(ThresholdOutName,'-dpng');
```

```
end
%Repopulate bins based on threshold
Threshcounts = posmap(TOFposdata,BinSize,BinLimits(5),...
    BinIndices,edges,cutoff);
counts = posmap(posdata,BinSize,BinLimits(5),BinIndices,edges);
figure(3*n-1)
subplot(1,2,1)
pcolor(edges{1},edges{2},counts(:,:,round(11/BinSize))'),...
    shading interp,axis square
filtercounts = counts;
filtercounts(Threshcounts==0)=0;
subplot(1,2,2)
pcolor(edges{1},edges{2},filtercounts(:,:,round(11/BinSize))'),...
    shading interp,axis square
str = sprintf(['Density Hitmaps for Bin Size = %0.2f, Threshold'...
    '= %u\\sigma'],BinSize,nsigma);
set(gcf,'NextPlot','add');
axes;
h = title(str);
set(gca,'Visible','off');
set(h,'Visible','on');
if if_save == 'Y'
    HitmapOut = sprintf('_Hitmap_bin%1.2f_%usigma',BinSize,nsigma);
    HitmapOut = strrep(HitmapOut,'.','p');
    HitmapOutName    = strcat(filename,HitmapOut);
    print(HitmapOutName,'-dpng');
end
figure(3*n)
str = sprintf(['Density Histograms for Bin Size = %0.2f, '...
    'Threshold = %u\\sigma'],BinSize,nsigma);
[densification_factor,histogof] = histogen(counts,filtercounts);
title(str)
if if_save == 'Y'
    HistogramOut = sprintf('_Histogram_bin%1.2f_%usigma',...
```

```
            BinSize,nsigma);
        HistogramOut = strrep(HistogramOut,'.','p');
        HistogramOutName    = strcat(filename,HistogramOut);
        print(HistogramOutName,'-dpng');
    end
    csvoutput(n,1) = BinSize;
    csvoutput(n,2) = nsigma;
    csvoutput(n,3) = densification_factor;
    csvoutput(n,4) = threshgof.sse;
    csvoutput(n,5) = threshgof.rsquare;
    csvoutput(n,6) = threshgof.dfe;
    csvoutput(n,7) = threshgof.adjrsquare;
    csvoutput(n,8) = threshgof.rmse;
    csvoutput(n,9) = histogof.sse;
    csvoutput(n,10) = histogof.rsquare;
    csvoutput(n,11) = histogof.dfe;
    csvoutput(n,12) = histogof.adjrsquare;
    csvoutput(n,13) = histogof.rmse;
    n = n+1;
  end
  close all
end

if if_save == 'Y'
  csvwrite(strcat(filename,'_SensitivityAnalysis.csv'),csvoutput)
end

end

%%%%%%%%%%%%%%%%%%%%%%%%%%%%%%%%%%%%%%%%%%%%%%%%%%%%%%%%%%%%%%%%%%
%% Begin custom functions

function [cutoff,gof] = thresholdcounts(TOFcounts,threshcoeff)
%% Discriminates between matrix and precipitate volumes based on the bin
```

```
%   density distribution of solute ions based on the filtered position
%   data (TOFcounts) and a threshold density number of standard deviations
%   based on a number (threshcoeff) of standard deviations from the mean of
%   a Gaussian fit to the matrix bin density distribution.
    TOFpdfcount = TOFcounts(:);
    TOFpdfcount = TOFpdfcount(TOFpdfcount~=0);
    TOFpdfcount = sort(TOFpdfcount);
    TOFdist = histogram(TOFpdfcount,0:1:max(TOFpdfcount),...
        'normalization','pdf');
    TOFxdist = 0:1:length(TOFdist.Values)-1;
    TOFhisto = TOFdist.Values;

    % Currently uses Matlab curve-fitting add-on software package
    [xData, yData] = prepareCurveData( TOFxdist, TOFhisto );

    % Set up fittype and options.
    ft = fittype( 'gauss1' );
    opts = fitoptions( 'Method', 'NonlinearLeastSquares' );
    opts.Display = 'Off';
    opts.Lower = [-Inf -Inf 0];

    % Fit model to data.
    [fitresult, gof] = fit( xData, yData, ft, opts );

    hold on
    gaussfit1 = fitresult.a1*exp(-((TOFxdist-fitresult.b1)...
        /fitresult.c1).^2);
    plot(TOFxdist,gaussfit1,'--r','LineWidth',1.5)

    cutoff=floor(fitresult.b1+threshcoeff*fitresult.c1);
    plot(cutoff,0,'og')
end

function [TOFcounts] = posmap(TOFposdata,BinSize,zmin,Nz,edges,varargin)
```

```
%% Populate bins for with ions based input position data (TOFposdata) and
%  bin size parameters. varargin{1} assigns a density threshold, such that
%  bins with populations below this value are set to 0.
   for k = 1:Nz
      zslicedata = TOFposdata;
      zslicedata = zslicedata(:,zslicedata(3,:)>=(zmin+(k-1)*BinSize));
      zslicedata = zslicedata(:,zslicedata(3,:)<(zmin+k*BinSize));

      TOFcountmap = hist3([transpose(zslicedata(1,:)),...
         transpose(zslicedata(2,:))],'Edges',edges);
      if nargin > 5
         TOFcountmap(TOFcountmap<varargin{1})=0;
      end

      TOFcounts(:,:,k) = TOFcountmap;
   end
end

function [posdata,pos_filename] = posread()
%% Reads in data from a standard .POS file generated by the IVAS software.
   disp('choose pos file');
   % prompt to read pos file
   [pos_filename,pos_path] = uigetfile({'*.pos'},'open');
   file_name=[pos_path pos_filename];

   pos_filename

   % reads position and mass-to-charge data from pos file
   fid = fopen(file_name, 'r');
   fseek(fid,0,-1);
   disp('loading position data');
   posdata=fread(fid, inf, 'float32', 0, 'b');
   posdata = reshape(posdata, [4 length(posdata)/4]); %Separates x, y, z,
                                                      %m/n columns in .pos data
```

```
    disp('position data loaded');
end

%%%%%%

function [BinStartSize,BinEndSize,BinStepSize,zSkip,zTrunc,if_save]...
    = binselect()
%% Generates dialogue for inputting bin size parameters. Also allows for
%  truncation of the top and bottom parts of an APT data set to eliminate
%  some edge effects, and asks whether generated figures should be saved.
    disp('Input image resolution parameters (bin size)');
    prompt = {'start bin size (nm)','end bin size (nm)',...
        'bin step size (nm)','z depth to skip (nm)',...
        'z depth to truncate (nm)','save PNG + fig (Y/N)'};
    dlg_title = 'resolution parameters';
    num_lines = 1;
    def = {'.1','4','.05','8','16','N'};
    answer = (inputdlg(prompt,dlg_title,num_lines,def));

    BinStartSize = str2num(cell2mat(answer(1)));
    BinEndSize  = str2num(cell2mat(answer(2)));
    BinStepSize = str2num(cell2mat(answer(3)));
    zSkip = str2num(cell2mat(answer(4)));
    zTrunc = str2num(cell2mat(answer(5)));
    if_save = cell2mat(answer(6));

    if if_save(1)=='n'
        if_save='N'
    end
    if if_save(1)=='y'
        if_save='Y'
    end
end
```

```
%%%%%%%

function [TOFposdata] = TOFselect(posdata)
%% Procedure for manually selecting solute ion peaks in the TOF spectrum
%  using a graphical user interface.
    figure
    histogram(posdata(4,:),0:0.01:ceil(max(posdata(4,:))))
    hold on
    xlabel('mass-to-charge (amu)')
    ylabel('counts')
    temp = input(['Adjust plot area to highlight desired ROI.'...
        ' Press enter when ready to continue']);
    disp('Click on the left boundary for the desired TOF range');
    title(['Click on the left boundary for the desired TOF range']);
    start_range=ginput(1)
    plot(start_range(1),0,'og')
    disp('Click on the right boundary for the desired TOF range');
    title(['Click on the right boundary for the desired TOF range']);
    end_range=ginput(1)
    plot(end_range(1),0,'og')
    if end_range<=start_range
        temp=start_range;
        start_range=end_range;
        end_range=temp;
        clear temp
    end
    TOFposdata = posdata;
    TOFposdata = TOFposdata(:,TOFposdata(4,:)>=start_range(1));
    TOFposdata = TOFposdata(:,TOFposdata(4,:)<=end_range(1));

    choice = questdlg('Define additional ranges to include?', ...
        'Add ranges?','yes','no','no');

    switch choice
```

```
    case 'yes'
        flag_stop_ranges = 0;
    case 'no'
        flag_stop_ranges = 1;
end

while flag_stop_ranges<1
    figure(gcf)
    temp = input(['Adjust plot area to highlight desired ROI.'...
        ' Press enter when ready to continue']);

    disp('Click on the left boundary for the desired TOF range');
    title(['Click on the left boundary for the desired TOF range']);
    start_range=ginput(1)
    plot(start_range(1),0,'og')

    disp('Click on the right boundary for the desired TOF range');
    title(['Click on the right boundary for the desired TOF range']);
    end_range=ginput(1)
    plot(end_range(1),0,'og')

    if end_range<=start_range
        temp=start_range;
        start_range=end_range;
        end_range=temp;
        clear temp
    end

    TOFposdata1 = posdata;
    TOFposdata1 = TOFposdata1(:,TOFposdata1(4,:)>=start_range(1));
    TOFposdata1 = TOFposdata1(:,TOFposdata1(4,:)<=end_range(1));
    TOFposdata = [TOFposdata,TOFposdata1];
    clear TOFposdata1
```

```
        choice = questdlg('Define additional ranges to include?', ...
        'Add ranges?','yes','no','no');

        switch choice
            case 'yes'
                flag_stop_ranges = 0;
            case 'no'
                flag_stop_ranges = 1;
        end
    end

    close(figure(gcf))

end

%%%%%%

function [TOFposdata] = staticTOF(posdata,varargin)
%% Allows for selection of solute ion peaks based on known peak positions
%  on the TOF spectrum (i.e., from a IVAS .rng file).
    k = (nargin-1)/2;
    for i = 1:k
        posrefdata = posdata;
        posrefdata = posrefdata(:,posrefdata(4,:)>=varargin{2*i-1});
        posrefdata = posrefdata(:,posrefdata(4,:)<=varargin{2*i});
        if i==1
           TOFposdata = posrefdata;
        else
           TOFposdata = horzcat(TOFposdata,posrefdata);
        end
    end
end

%%%%%%
```

```
function [BinLimits,BinRanges,BinVectors,BinIndices] ...
    = makebins(posdata,BinSize,zTrunc,zSkip)
%% Generates bin edges, limits and indices based on input parameters.
    xmin = min(posdata(1,:));
    xmax = max(posdata(1,:));
    ymin = min(posdata(2,:));
    ymax = max(posdata(2,:));
    %zmin = min(posdata(3,:));
    zmin = min(posdata(3,:))+zTrunc;
    %zmax = max(posdata(3,:));
    zmax = max(posdata(3,:))-zSkip;

    xrange = xmax - xmin;
    yrange = ymax - ymin;
    zrange = zmax - zmin;

    BinRanges = [xrange,yrange,zrange];

    xmin = xmin + rem(xrange,BinSize)/2;
    xmax = xmax - rem(xrange,BinSize)/2;
    ymin = ymin + rem(yrange,BinSize)/2;
    ymax = ymax - rem(yrange,BinSize)/2;
    zmin = zmin + rem(zrange,BinSize)/2;
    zmax = zmax - rem(zrange,BinSize)/2;

    BinLimits = [xmin,xmax,ymin,ymax,zmin,zmax];

    x = transpose(xmin:BinSize:xmax);
    y = transpose(ymin:BinSize:ymax);
    z = transpose(zmin:BinSize:zmax);

    BinVectors = cell(1,3);
    BinVectors{1} = x;
```

```
    BinVectors{2} = y;
    BinVectors{3} = z;

    Nx = length(x)-1;
    Ny = length(y)-1;
    Nz = length(z)-1;
    Ndat = length(posdata);

    BinIndices = [Nx,Ny,Nz,Ndat];
end

%%%%%%

function [densification_factor,gof] = histogen(counts,filtercounts)
%% Generates final histogram comparing bin densities in the matrix and in
%  the precipitate volumes and outputs the final densification factor.
    pdfcount = counts(:);
    pdfcount = pdfcount(pdfcount~=0);
    pdfcount = sort(pdfcount);

    filterpdfcount = filtercounts(:);
    filterpdfcount = filterpdfcount(filterpdfcount~=0);
    filterpdfcount = sort(filterpdfcount);

    hold on
    h_tot = histogram(pdfcount,0:1:max([filterpdfcount;pdfcount])+1);
    h_filt = histogram(filterpdfcount,...
        0:1:max([filterpdfcount;pdfcount])+1);
    h_net = h_tot.Values - h_filt.Values;
    xpdf = 0:1:length(h_net)-1;
    bar(xpdf+.5,h_net,1)
    h_filt = histogram(filterpdfcount,...
        0:1:max([filterpdfcount;pdfcount])+1);
```

```
    % Currently uses Matlab curve-fitting add-on software package
    [xData, yData] = prepareCurveData( xpdf, h_net );

    % Set up fittype and options.
    ft = fittype( 'gauss1' );
    opts = fitoptions( 'Method', 'NonlinearLeastSquares' );
    opts.Display = 'Off';
    opts.Lower = [-Inf -Inf 0];
    %opts.StartPoint = [9515 31 6.713674128637 15];

    % Fit model to data.
    [fitresult, gof] = fit( xData, yData, ft, opts );

    gaussfit2 = fitresult.a1*exp(-((xpdf-fitresult.b1)/fitresult.c1).^2);
    plot(xpdf,gaussfit2,'--g','LineWidth',1.5)

    bulk_dens = fitresult.b1;
    cluster_dens = mean(h_filt.Data);
    densification_factor = cluster_dens/bulk_dens
end
```

APPENDIX B

MATLAB Code for APT Aberration Correction: Delaunay Triangulation

The MATLAB code utilized for matrix/precipitate density comparison utilizing the Delaunay triangulation methodology outlined in Section 3.3.3 is displayed below. The MATLAB .m files can be downloaded at: `https://github.com/grizzle13/APT_Aberration_Correction`.

```
function [density_factor_cells] = pos_density_delaunay()

%% This function reads in position data from both a standard IVAS
% reconstruction .pos file and an indexed cluster .pos file generated by
% the maximum separation cluster search algorithm. This code measures
% density by determining precipitate volume by using Delaunay tessellation
% on the indexed precipitates and comparing that to the density calculated
% from the standard .pos file for the entire data set.

clear all
close all
clc

% Read in indexed cluster pos data
disp('Choose indexed cluster .pos file');
[clusterposdata,clusterpos_filename] = posread();

clusterfilename = clusterpos_filename(1:end-4);
```

```
% Read in unfiltered pos data
disp('Choose standard .pos file');
[posdata,pos_filename] = posread();

filename = pos_filename(1:end-4);

% Ion count is equal to length of pos files
N_c = length(clusterposdata); %Cluster ions
N_mat = length(posdata)-N_c; %Total - clusters = matrix ions

%Initialize outputs
k = max(clusterposdata(4,:));
V_clust = zeros(k,1);
V_cells = [];
coords_c = [];
index_c = [];
tic

index_edge = zeros(length(k-1));
for i = 1:k
    posdata_c = clusterposdata(:,clusterposdata(4,:)==i);

    [V,clustcoords,clustindex,DT] = DelaunayTess(posdata_c);
    if i > 1
        clustindex = clustindex+max(max(index_c));
        index_edge(i-1) = max(max(index_c));
    end
    coords_c = [coords_c;clustcoords];
    index_c = [index_c;clustindex];
end
toc

DT = triangulation(index_c,coords_c);
[cc,r] = circumcenter(DT);
```

```
rdist = histogram(r,0:0.005:1);
rxdist = rdist.BinEdges;
rxdist(length(rxdist)) = [];
rhisto = rdist.Values;
disp(['Click on the cutoff edge for the maximum Delaunay'...
    ' circumsphere radius']);
title(['Click on the cutoff edge for the maximum Delaunay'...
    ' circumsphere radius']);
start_range=ginput(1)
cutoff = start_range(1);
hold on
plot(cutoff,0,'og')

rthresh = r;
rthresh(rthresh>cutoff) = [];
rdist = histogram(rthresh,0:0.005:1);
rxdist = rdist.BinEdges;
rxdist(length(rxdist)) = [];
rhisto = rdist.Values;

CellFilt = DT.ConnectivityList(r<cutoff,:);

P21 = DT.Points(CellFilt(:,2),:) - DT.Points(CellFilt(:,1),:);
P31 = DT.Points(CellFilt(:,3),:) - DT.Points(CellFilt(:,1),:);
P41 = DT.Points(CellFilt(:,4),:) - DT.Points(CellFilt(:,1),:);

V_clust = 1/6*abs(dot(P21,cross(P31,P41,2),2));

clusterdenscells = N_c/sum(V_clust);

tic

[V,matrixcoords,matrixindex,DTm] = DelaunayTess(posdata);
```

```
V_tot = sum(V);
V_mat = sum(V)-sum(V_clust);

toc

matdenscells = N_mat/V_mat;

density_factor_cells = clusterdenscells/matdenscells

[ccm,rm] = circumcenter(DTm);

figure
rmdist = histogram(rm,0:0.005:1);
rmxdist = rmdist.BinEdges;
rmxdist(length(rmxdist)) = [];
rmhisto = rmdist.Values;
disp(['Click on the cutoff edge for the maximum Delaunay'...
    ' circumsphere radius']);
title(['Click on the cutoff edge for the maximum Delaunay'...
    ' circumsphere radius']);
start_range=ginput(1)
cutoffm = start_range(1);

hold on
plot(cutoffm,0,'og')

rmthresh = rm;
rmthresh(rmthresh>cutoffm) = [];

figure(2)
x = 0:0.005:1;
rmdist = histogram(rmthresh,x);
hold on
rdist = histogram(rthresh,x)
```

```
rmxdist = rmdist.BinEdges;
rmxdist(length(rmxdist)) = [];
rmhisto = rmdist.Values;
rxdist = rdist.BinEdges;
rxdist(length(rxdist)) = [];
rhisto = rdist.Values;
nethisto = rmhisto-rhisto;
bar(rxdist+.005/2,nethisto,1)
histogram(rthresh,x)

netscale = trapz(0:0.005:0.995,nethisto);
netnorm = nethisto/netscale;
clusterscale = trapz(0:0.005:0.995,rhisto);
rnorm = rhisto/clusterscale;

disp('Click on the left cutoff edge for matrix curve fitting');
title(['Click on the left cutoff edge for matrix curve fitting']);
start_range=ginput(1)
leftedgeM = start_range(1);

plot(leftedgeM,0,'og')

disp('Click on the right cutoff edge for matrix curve fitting');
title(['Click on the right cutoff edge for matrix curve fitting']);
start_range=ginput(1)
rightedgeM = start_range(1);

plot(rightedgeM,0,'og')

disp('Click on the left cutoff edge for precipitate curve fitting');
title(['Click on the left cutoff edge for precipitate curve fitting']);
start_range=ginput(1)
leftedgeC = start_range(1);
```

```
plot(leftedgeC,0,'or')

disp('Click on the right cutoff edge for precipitate curve fitting');
title(['Click on the right cutoff edge for precipitate curve fitting']);
start_range=ginput(1)
rightedgeC = start_range(1);

plot(rightedgeC,0,'or')

leftindexM = find(rxdist == floor(leftedgeM*200)/200);
rightindexM = find(rxdist == ceil(rightedgeM*200)/200);
excludeM = [1:leftindexM,rightindexM:length(rxdist)];

leftindexC = find(rxdist == floor(leftedgeC*200)/200);
rightindexC = find(rxdist == ceil(rightedgeC*200)/200);
excludeC = [1:leftindexC,rightindexC:length(rxdist)];

%% Fit normalized curves (matrix data) (single constant)
[xData, yData] = prepareCurveData( rxdist, netnorm );

% Set up fittype and options.
ft = fittype( '1.5*a1^3*x^8*exp(-a1*x^3)', 'independent', 'x',...
    'dependent', 'y' );
excludedPoints = excludedata( xData, yData, 'Indices', excludeM );
opts = fitoptions( 'Method', 'NonlinearLeastSquares' );
opts.Display = 'Off';
opts.Lower = 0;
opts.StartPoint = 200;
opts.Exclude = excludedPoints;

% Fit model to data.
[fitresult1, gof1] = fit( xData, yData, ft, opts );

%% Fit normalized curves (precipitate data) (single constant)
```

```
[xData, yData] = prepareCurveData( rxdist, rnorm );

% Set up fittype and options.
ft = fittype( '1.5*a1^3*x^8*exp(-a1*x^3)', 'independent', 'x',...
    'dependent', 'y' );
excludedPoints = excludedata( xData, yData, 'Indices', excludeC );
opts = fitoptions( 'Method', 'NonlinearLeastSquares' );
opts.Display = 'Off';
opts.Lower = 0;
opts.StartPoint = 200;
opts.Exclude = excludedPoints;

% Fit model to data.
[fitresult2, gof2] = fit( xData, yData, ft, opts );

%% Fit normalized curves (matrix data) (double constant)

[xData, yData] = prepareCurveData( rxdist, netnorm );

% Set up fittype and options.
ft = fittype( '1.5*a1^3*x^8*exp(-b1*x^3)', 'independent', 'x',...
    'dependent', 'y' );
excludedPoints = excludedata( xData, yData, 'Indices', excludeM );
opts = fitoptions( 'Method', 'NonlinearLeastSquares' );
opts.Display = 'Off';
opts.StartPoint = [0.959492426392903 0.655740699156587];
opts.Exclude = excludedPoints;

% Fit model to data.
[fitresult3, gof3] = fit( xData, yData, ft, opts );

%% Fit normalized curves (precipitate data) (double constant)
[xData, yData] = prepareCurveData( rxdist, rnorm );
```

```
% Set up fittype and options.
ft = fittype( '1.5*a1^3*x^8*exp(-b1*x^3)', 'independent', 'x',...
    'dependent', 'y' );
excludedPoints = excludedata( xData, yData, 'Indices', excludeC );
opts = fitoptions( 'Method', 'NonlinearLeastSquares' );
opts.Display = 'Off';
opts.Lower = [0 -Inf];
opts.StartPoint = [200 0.421761282626275];
opts.Exclude = excludedPoints;

% Fit model to data.
[fitresult4, gof4] = fit( xData, yData, ft, opts );

%%

figure(2)

x=rxdist;
a1 = fitresult1.a1;
p1 = plot(x,netscale*1.5*a1^3*x.^8.*exp(-a1*x.^3),'g')
p1.LineWidth = 2;

a1 = fitresult2.a1;
p2 = plot(x,clusterscale*1.5*a1^3*x.^8.*exp(-a1*x.^3),'r')
p2.LineWidth = 2;

a1 = fitresult3.a1;
b1 = fitresult3.b1;
p3 = plot(x,netscale*1.5*a1^3*x.^8.*exp(-b1*x.^3),'--g')
p3.LineWidth = 2;

a1 = fitresult4.a1;
b1 = fitresult4.b1;
p4 = plot(x,clusterscale*1.5*a1^3*x.^8.*exp(-b1*x.^3),'--r')
```

```
p4.LineWidth = 2;

xlabel('Delaunay Circumsphere Radius (nm)')
ylabel('Frequency')
title('Delaunay Circumsphere Radii Distributions for FeCrAl')

matrixdens_fit = fitresult1.a1*3/4*pi();
clustdens_fit = fitresult2.a1*3/4*pi();

dens_factor_fit = clustdens_fit/matrixdens_fit

end

function [posdata,pos_filename] = posread()
    % prompt to read pos file
    [pos_filename,pos_path] = uigetfile({'*.pos'},'open');
    file_name=[pos_path pos_filename];

    pos_filename

    % reads position and mass-to-charge data from pos file
    fid = fopen(file_name, 'r');
    fseek(fid,0,-1);
    disp('loading position data');
    posdata=fread(fid, inf, 'float32', 0, 'b');
    posdata = reshape(posdata, [4 length(posdata)/4]); %Separates x, y, z,
                                                       %m/n columns in .pos data
    disp('position data loaded');
end

function [volume,coords,index] = DelaunayTess(posdata)
    DT = delaunayTriangulation(posdata(1,:)',posdata(2,:)',posdata(3,:)');
    coords = DT.Points;
    index = DT.ConnectivityList;
```

```
    P21 = DT.Points(DT.ConnectivityList(:,2),:) ...
        - DT.Points(DT.ConnectivityList(:,1),:);
    P31 = DT.Points(DT.ConnectivityList(:,3),:) ...
        - DT.Points(DT.ConnectivityList(:,1),:);
    P41 = DT.Points(DT.ConnectivityList(:,4),:) ...
        - DT.Points(DT.ConnectivityList(:,1),:);

    volume = 1/6*abs(dot(P21,cross(P31,P41,2),2));
end
```

APPENDIX C

FeCrAl Target Capsule Drawings

This appendix includes engineering drawings for the capsules used to contain the SS-J2 type Fe-Cr-Al tensile specimens that were irradiated in HFIR. Details of the HFIR irradiation campaign from the present work are found in Section 4.1.2. Drawings courtesy of R. Howard (ORNL).

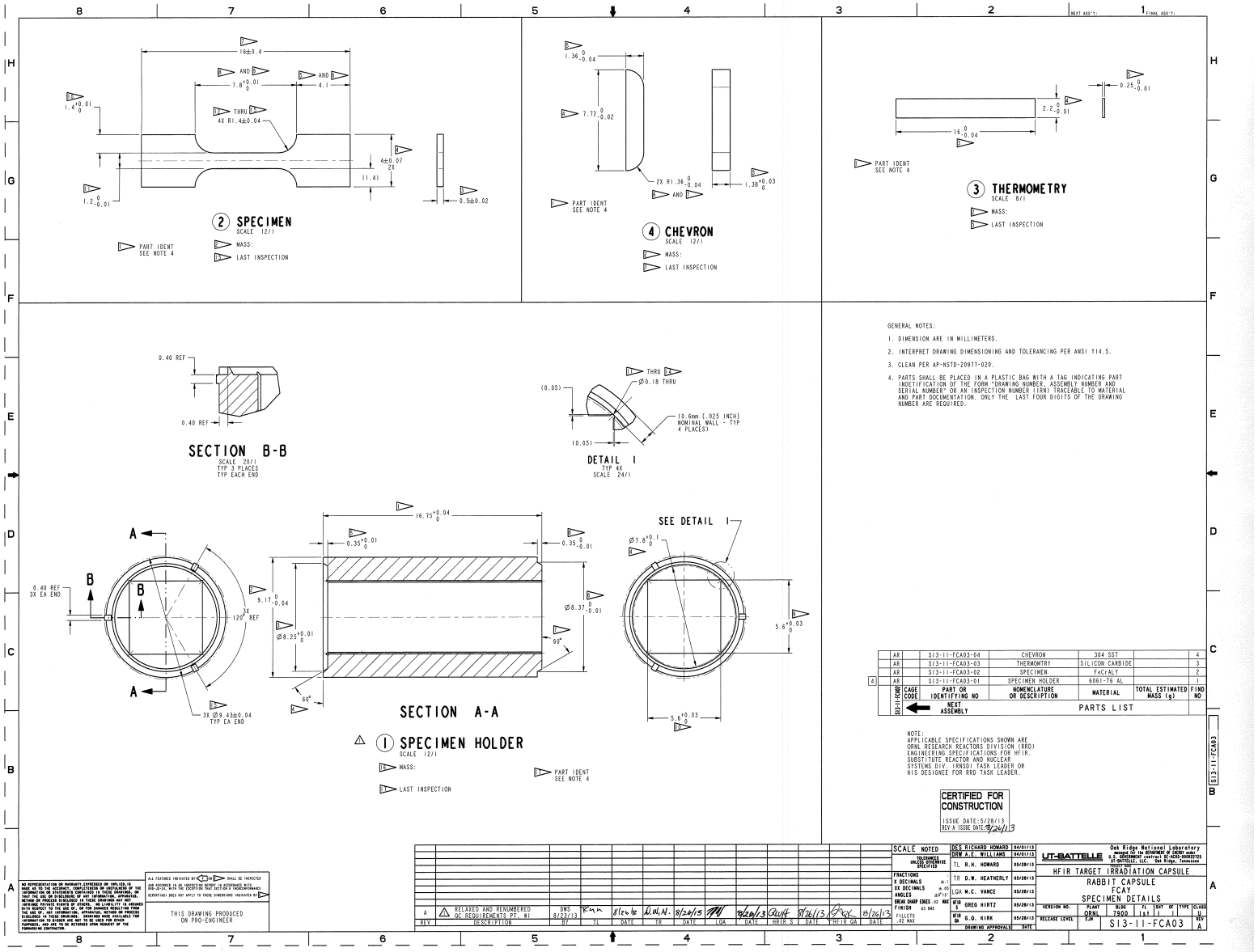
2 SPECIMEN
SCALE 12/1
PART IDENT SEE NOTE 4
MASS:
LAST INSPECTION
4 CHEVRON
SCALE 12/1
3 THERMOMETRY
SCALE 8/1
SECTION B-B
SCALE 20/1
TYP 3 PLACES
TYP EACH END
DETAIL I
TYP 4X
SCALE 24/1
SEE DETAIL I
SECTION A-A
1 SPECIMEN HOLDER
SCALE 12/1
GENERAL NOTES:
1. DIMENSION ARE IN MILLIMETERS.
2. INTERPRET DRAWING DIMENSIONING AND TOLERANCING PER ANSI Y14.5.
3. CLEAN PER AP-NSTD-20977-020.
4. PARTS SHALL BE PLACED IN A PLASTIC BAG WITH A TAG INDICATING PART INDETIFICATION OF THE FORM "DRAWING NUMBER, ASSEMBLY NUMBER AND SERIAL NUMBER" OR AN INSPECTION NUMBER (IRN) TRACEABLE TO MATERIAL AND PART DOCUMENTATION. ONLY THE LAST FOUR DIGITS OF THE DRAWING NUMBER ARE REQUIRED.
PARTS LIST
NOTE:
APPLICABLE SPECIFICATIONS SHOWN ARE ORNL RESEARCH REACTORS DIVISION (RRD) ENGINEERING SPECIFICATIONS FOR HFIR. SUBSTITUTE REACTOR AND NUCLEAR SYSTEMS DIV. (RNSD) TASK LEADER OR HIS DESIGNEE FOR RRD TASK LEADER.
CERTIFIED FOR CONSTRUCTION
ISSUE DATE: 5/28/13
REV A ISSUE DATE: 8/26/13
THIS DRAWING PRODUCED ON PRO-ENGINEER
UT-BATTELLE
HFIR TARGET IRRADIATION CAPSULE
RABBIT CAPSULE
FCAY
SPECIMEN DETAILS
S13-11-FCA03

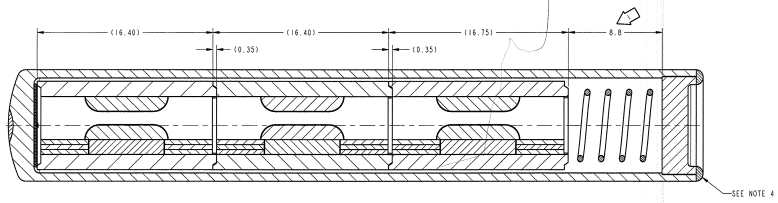

SECTION D-D

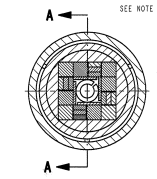

SECTION B-B

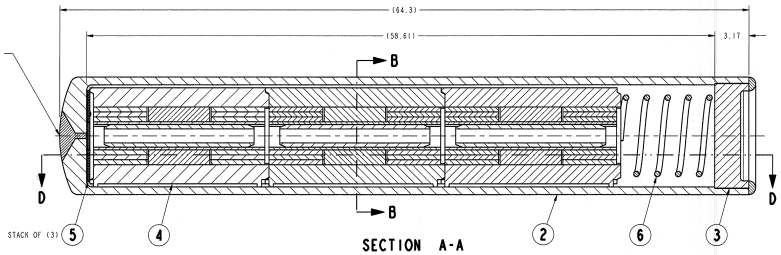

SECTION A-A

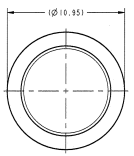

GENERAL NOTES:

1. DIMENSION ARE IN MILLIMETERS.
2. INTERPRET DRAWING DIMENSIONING AND TOLERANCING PER ANSI Y14.5.
3. PART SHALL BE PLACED IN A PLASTIC BAG WITH A TAG INDICATING ASSEMBLY INDETIFICATION OF THE FORM "DRAWING NUMBER, ASSEMBLY NUMBER AND SERIAL NUMBER" OR AN INSPECTION NUMBER (IRN) TRACEABLE TO MATERIAL AND PART DOCUMENTATION. ONLY THE LAST FOUR DIGITS OF THE DRAWING NUMBER ARE REQUIRED.
4. SEE DRAWING X3E02097TA536 FOR FINAL ASSEMBLY, WELDING AND TESTING INSTRUCTIONS

1 FCAY RABBIT CAPSULE ASM

SCALE 8/1

MASS:

LAST INSPECTION

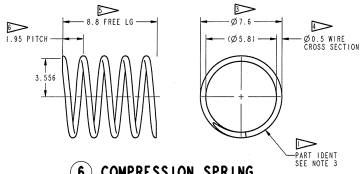

6 COMPRESSION SPRING

OPEN ENDS GROUND

SCALE 8/1

MASS:

LAST INSPECTION

THIS DRAWING	CAGE CODE	PART OR IDENTIFYING NO	NOMENCLATURE OR DESCRIPTION	MATERIAL		FIND NO
	1	-6	COMPRESSION SPRING	300 SERIES SST	PURCHASED	6
	3	-5	DISK - 8.5 OD X2.5 ID X 0.4 THK	GRAFOIL		5
	3	S13-11-FAC02-01	SPECIMEN HOLDER ASM	---	---	4
	1	X3E02097TA538-2	HOUSING END CAP	---	---	3
	1	X3E02097TA538-1	HOUSING			2
X	1	FCAY RABBIT ASM	FCAY RABBIT ASM			1

NEXT ASSEMBLY

PARTS LIST

NOTE:
APPLICABLE SPECIFICATIONS SHOWN ARE ORNL RESEARCH REACTORS DIVISION (RRD) ENGINEERING SPECIFICATIONS FOR HFIR. SUBSTITUTE REACTOR AND NUCLEAR SYSTEMS DIV. (RNSD) TASK LEADER OR HIS DESIGNEE FOR RRD TASK LEADER.

CERTIFIED FOR CONSTRUCTION
ISSUE DATE: 5/6/13

S13-11-FCA01

NO REPRESENTATION OR WARRANTY,EXPRESSED OR IMPLIED,IS MADE AS TO THE ACCURACY, COMPLETENESS OR SUFFICIENCY OF THE INFORMATION OR STATEMENTS CONTAINED IN THESE DRAWINGS. OR THAT THE USE OF DISCLOSURE OF ANY INFORMATION, APPARATUS, METHOD OR PROCESS DISCLOSED IN THESE DRAWINGS WILL NOT INFRINGE PRIVATELY OWNED RIGHTS OF OTHERS. NO LIABILITY IS ASSUMED WITH RESPECT TO THE USE OF, OR FOR DAMAGES RESULTING FROM THE USE OF, ANY INFORMATION, APPARATUS, METHOD OR PROCESS DISCLOSED IN THESE DRAWINGS. THESE DRAWINGS ARE PROVIDED FOR INFORMATION TO BIDDERS AND ARE NOT TO BE USED FOR OTHER PURPOSES, AND ARE TO BE RETURNED UPON REQUEST OF THE FABRICATING CONTRACTOR.

ALL FEATURES INDICATED BY ▷ SHALL BE INSPECTED AND RECORDED IN AN INSPECTION REPORT.
ALL FEATURES INDICATED BY ▷ SHALL BE INSPECTED AND RECORDED IN AN INSPECTION REPORT.
REPORT(S) DOES NOT APPLY TO THOSE DIMENSIONS INDICATED BY ▷

THIS DRAWING PRODUCED ON PRO-ENGINEER

REV	DESCRIPTION	BY	IL	DATE	TR	DATE	LGA	DATE	HHIR S	DATE	HFIR QA	DATE

SCALE NOTED

TOLERANCES UNLESS OTHERWISE SPECIFIED
FRACTIONS
X DECIMALS ±.1
XX DECIMALS ±.05
ANGLES ±0°15'
BREAK SHARP EDGES .01 MAX
FINISH 63 RMS
FILLETS .02 MAX

DES	RICHARD HOWARD	04/01/13
DRW	A.E. WILLIAMS	04/01/13
TL		5/6/13
TP		5/6/13
		5/6/13
HFIR		5/6/13
HFIR		5/6/13

DRAWING APPROVALS

UT-BATTELLE

Oak Ridge National Laboratory
Managed for the DEPARTMENT OF ENERGY under U.S. GOVERNMENT Contract DE-AC05-00OR22725
UT-BATTELLE, LLC. Oak Ridge, Tennessee

TITLE
HFIR TARGET IRRADIATION CAPSULE
RABBIT CAPSULE
FCAY
HOLDER ASSEMBLY

VERSION NO.	PLANT	BLDG	FL	SHT	OF	TYPE	CLASS
0	ORNL	7900	1st	1	1	U	U
RELEASE LEVEL	EJM	S13-11-FCA01				REV 0	

GENERAL NOTES:

1. DIMENSION ARE IN MILLIMETERS.
2. INTERPRET DRAWING DIMENSIONING AND TOLERANCING PER ANSI Y14.5.
3. CLEAN PER AP-NSTD-20977-020.
4. SPRING PIN IDENTIFYING NUMBER REFERENCES McMASTER-CARR CATALOG NUMBER. (A SPRING PIN OF EQUIVILANT VALUE MAY BE SUBSTITUTED WITH ORNL APPROVAL.)

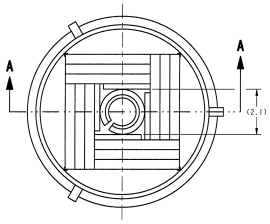

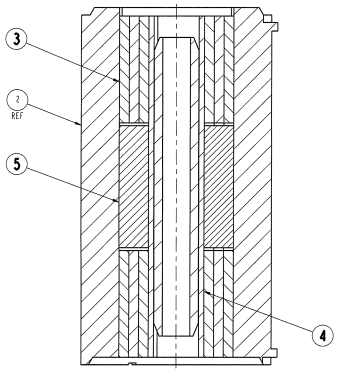

SECTION A-A

1 SPECIMEN HOLDER ASM
SCALE 16/1

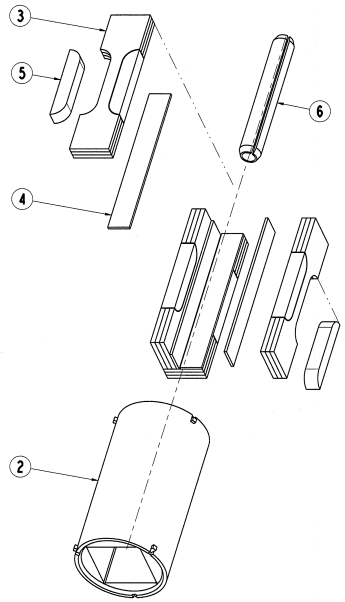

EXPLODED VIEW
SCALE 8/1

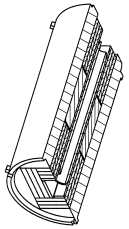

REFERENCE SECTION VIEW

	1	2.MM.ROLLPIN	SPG PIN, 2.0 MM DIA X 14 MM LG	18-8 SST	ASME B18.82	6
	8	S13-11-FCA03-04	CHEVRON	---	---	5
	4	S13-11-FCA03-03	THERMOMETRY	---	---	4
	12	S13-11-FCA03-02	SPECIMEN	---	---	3
	1	S13-11-FCA03-01	SPECIMEN HOLDER	---	---	2
	X	S13-11-FCA02-01	SPECIMEN HOLDER ASM	---	---	1
S13-11-FCA01	CAGE CODE	PART OR IDENTIFYING NO	NOMENCLATURE OR DESCRIPTION	MATERIAL	TOTAL ESTIMATED MASS (g)	FIND NO
	←	NEXT ASSEMBLY	PARTS LIST			

NOTE:
APPLICABLE SPECIFICATIONS SHOWN ARE ORNL RESEARCH REACTORS DIVISION (RRD) ENGINEERING SPECIFICATIONS FOR HFIR. SUBSTITUTE REACTOR AND NUCLEAR SYSTEMS DIV. (RNSD) TASK LEADER OR HIS DESIGNEE FOR RRD TASK LEADER.

CERTIFIED FOR CONSTRUCTION
ISSUE DATE 5/20/13

NO REPRESENTATION OR WARRANTY,EXPRESSED OR IMPLIED,IS MADE AS TO THE ACCURACY, COMPLETENESS OR SUFFICIENCY OF THE INFORMATION CONTAINED HEREIN, OR THAT THE USE OF ANY INFORMATION, APPARATUS, METHOD OR PROCESS DISCLOSED IN THESE DRAWINGS MAY NOT INFRINGE PRIVATELY OWNED RIGHTS. NEITHER THE UT-BATTELLE NOR ORNL ASSUMES WITH RESPECT TO THE USE OF, OR FOR DAMAGES RESULTING FROM THE USE OF, ANY INFORMATION, APPARATUS, METHOD OR PROCESS DISCLOSED IN THESE DRAWINGS. THESE DRAWINGS ARE PROVIDED FOR INFORMATION TO BIDDER AND NOT TO BE USED FOR OTHER PURPOSES, AND ARE TO BE RETURNED UPON REQUEST OF THE FABRICATION CONTRACTOR.

ALL FEATURES INDICATED BY ⟨1⟩ TO ⟨2⟩ SHALL BE INSPECTED AND RECORDED ON AN INSPECTION REPORT, IN ACCORDANCE WITH: RRD-QC-24, W-TH TYPE, EXCEPTION THAT SECTION 6 TOLERANCE/PERFORMANCE REPORT:NAD DOES NOT APPLY TO THOSE DIMENSIONS INDICATED BY ⟨2⟩

THIS DRAWING PRODUCED ON PRO-ENGINEER

REV	DESCRIPTION	BY	TL	DATE	TR	DATE	LQA	DATE	HFIR S	DATE	HFIR QA	DATE

SCALE NOTED
TOLERANCES UNLESS OTHERWISE SPECIFIED
FRACTIONS ±1/16
X DECIMALS ±.1
XX DECIMALS ±.05
ANGLES ±0°15'
BREAK SHARP EDGES .X2 MAX
FINISH 63 RMS
FILLETS .02 MAX

DRAWING APPROVALS		DATE
DES RICHARD HOWARD		04/01/13
DRW A.E. WILLIAMS		04/01/13
TL	R.M.Howard	5/20/13
TR		5/20/13
LQA		5/20/13
HFIR S		5/20/13
HFIR QA		5/20/13

UT-BATTELLE
Oak Ridge National Laboratory
managed for the DEPARTMENT OF ENERGY under
U.S. DEPARTMENT OF ENERGY CONTRACT DE-AC05-00OR22725
UT-BATTELLE, LLC Oak Ridge, Tennessee

TITLE
HFIR TARGET IRRADIATION CAPSULE
RABBIT CAPSULE
FCAY
SPECIMEN ASM

VERSION NO.	PLANT	BLDG	FC	SHT	OF	TYPE	CLASS
	ORNL	7900	1a1	1		U	U
RELEASE LEVEL	EJM	S13-11-FCA02					REV 0

S13-11-FCA02

APPENDIX D

FeCrAl Target Capsule DAC

This appendix includes the design analysis and calculation (DAC) documentation evaluating the expected thermal gradients in the capsules design for irradiation of Fe-Cr-Al tensile specimens in HFIR. Details of the HFIR irradiation campaign from the present work are found in Section 4.1.2. Courtesy of R. Howard (ORNL).

DESIGN ANALYSIS AND CALCULATION

CALCULATION NO.:	DAC-13-11-FCAY01, Rev.0
CALCULATION TITLE:	Design Analysis for FeCrAlY Tensile Rabbits
ORGANIZATION:	Reactor & Nuclear Systems Division, Thermal Hydraulics & Irradiation Engineering Group
PROJECT/TASK:	FeCrAlY Tensile Rabbits
REVISION:	0
PREPARED:	
CHECKED/VERIFIED:	
GROUP LEADER:	

ABSTRACT:

The FeCrAlY experiment is designed to irradiate iron alloy tensile specimens in the flux trap of HFIR at 320°C. Each rabbit contains three sets of 12 tensile specimens. SiC passive thermometry accompanies the specimens, and the capsule holders are made from Al-6061. The primary outer containment is an Al-6061 tube with an outer diameter of 10.96 mm (0.432"). The specimen temperature is controlled by the axial location, fill gas, and the size of the gap between the holder and housing. Helium is used as the fill gas inside the experiments. This calculation documents the analyses performed to determine the size of the gas gap for the specimen holder.

CALCULATION REVISION LOG

TITLE: Design Analysis for FeCrAlY Tensile Rabbits		
CALCULATION IDENTIFIER: DAC-13-11-FCAY01, Rev.0		
REVISION NUMBER	**DESCRIPTION OF REVISION**	**DATE APPROVED**
0	Initial issue	

Calc Title:	Design Analysis for FeCrAlY Tensile Rabbits		Page i of ii
Calc ID:	DAC-13-11-FCAY01, Rev.0	Prep by:	Ck'd by:

Table of Contents

Page

1. PURPOSE 1

2. ASSUMPTIONS 1

3. CALCULATION INPUT AND SOURCES OF INPUT 1

3.1. HFIR RABBIT IRRADIATION FACILITIES 1
3.2. DESIGN DESCRIPTION 3
3.3. MATERIALS OF CONSTRUCTION 3
3.4. THERMAL BOUNDARY CONDITIONS 4
3.5. FINITE ELEMENT MODEL 4

4. COMPUTATIONS AND ANALYSES 5

4.1. THERMAL DESIGN 6

5. SUMMARY OF RESULTS 8

6. CONCLUSIONS 8

7. REFERENCES 9

Table of Appendices and Attachments

Page

APPENDIX A ANSYS SCRIPT USED TO EVALUATE CAPSULE DESIGNS A-1

APPENDIX B FECRALY ANSYS REPORT B-1

Calc Title:	Design Analysis for FeCrAlY Tensile Rabbits		Page ii of ii
Calc ID:	DAC-13-11-FCAY01, Rev.0	Prep by:	Ck'd by:

Index of Tables

Table Name **Page**
Table 3-1. Neutron Flux Characteristics of the HFIR 2
Table 3-2. Neutron Flux Characteristics for the Rabbit Irradiation Locations 3
Table 3-3. Tensile Creep Experiment Design Drawings 3
Table 3-4. Material Property References 3
Table 3-5. Thermal Boundary Conditions 4
Table 4-1: Design Diameters for TRRH 2 position 6
Table 4-2: Temperature Details for the TRRH 2 design (320°C Tensile Assembly) 6
Table 5-1. Design Summary for FeCrAlY Rabbits 8

Index of Figures

Figure Name **Page**
Figure 3-1. Cross-section Through HFIR Illustrating the Primary Experimental Sites (left) and a Picture of the Reactor Core (right) 1
Figure 3-3. View of the Irradiation Capsule Design 3
Figure 4-1. Temperature Contour Plot (°C) inner most tensile specimens (noted as TENSILE 1) 7
Figure 4-2. Temperature Contour Plot (°C) middle layer of tensile specimens (noted as TENSILE 2) 7
Figure 4-3. Temperature Contour Plot (°C) outer most tensile specimens (noted as TENSILE 3) 7
Figure 4-4. Temperature Contour Plot (°C) for Tensile Thermometry 7

Calc Title:	Design Analysis for FeCrAlY Tensile Rabbits		Page 1 of 8
Calc ID:	DAC-13-11-FCAY01, Rev.0	Prep by:	Ck'd by:

1. Purpose

For these steel alloy material experiments, the specimen temperature is controlled by the axial location, fill gas, and the size of the gap between the holder and housing. This calculation documents the analyses performed to determine the size of the gas gap for each design.

2. Assumptions

The position 2 target rod rabbit holder location is assumed to be analogous to the position 7 peripheral target position location and the position 5 hydraulic tube position. These locations have similar maximum neutron fluxes (E > 0.1 MeV) and heat generation rates.

3. Calculation Input and Sources of Input

3.1. HFIR Rabbit Irradiation Facilities

HFIR is a beryllium-reflected, pressurized, light-water-cooled and moderated flux-trap-type reactor. The core consists of aluminum-clad involute-fuel plates, which currently utilizes highly enriched ^{235}U fuel at a power level of 85 MWt.

The reactor core, illustrated in Figure 3-1, consists of two concentric annular regions, each approximately 61 cm in height. The flux trap is ~12.7 cm in diameter, and the outer fueled region is ~43.5 cm in diameter. The fuel region is surrounded by a beryllium annular reflector approximately 30.5 cm in thickness. The beryllium reflector is in turn backed up by a water reflector of effectively infinite thickness. In the axial direction, the reactor is reflected by water. The reactor core assembly is contained in a 2.44 m diameter pressure vessel, which is located in a 5.5 m cylindrical pool of water.

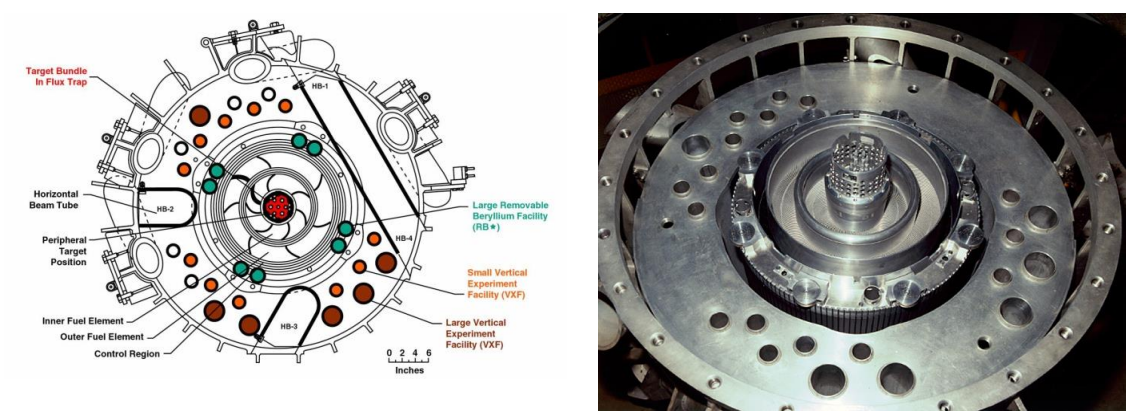

Figure 3-1. Cross-section Through HFIR Illustrating the Primary Experimental Sites (left) and a Picture of the Reactor Core (right)

Figure 3-2 shows the flux trap configuration of HFIR for Cycle 446, which finished in January 2013. The FeCrAlY rabbits in this design will be placed in the flux trap of HFIR in the various rabbit holder positions and the hydraulic tube, shown as orange and red respectively in Figure 3-2. Table 3-1 summarizes the neutron flux characteristics for these types of positions.

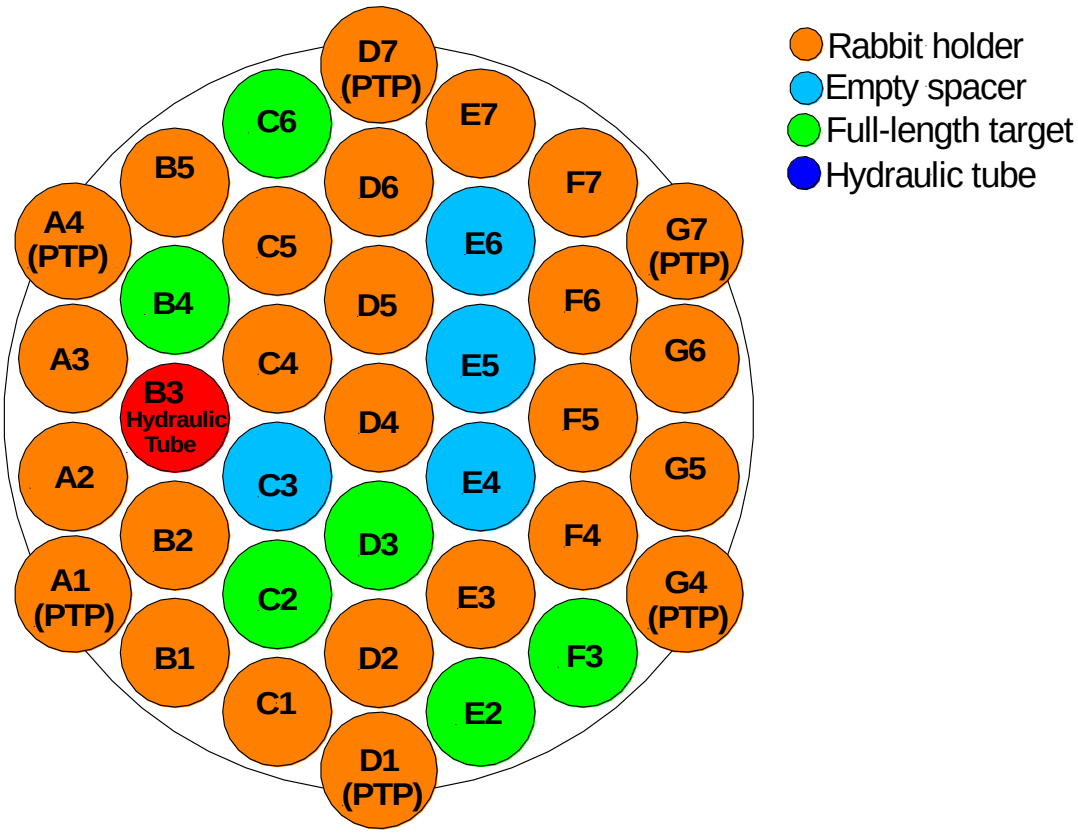

Figure 3-2. Flux Trap Irradiation Locations

Table 3-1. Neutron Flux Characteristics of the HFIR

Parameter		
Midplane fast flux (10^{15} n/cm²·sec) [E > 0.1 MeV]	1.09	Rabbit Holder (TRRH)
Axial peaking factor profile[1]	$1 + 1.95\cdot10^{-4}\cdot z - 9.75\cdot10^{-4}\cdot z^2$	
Midplane fast flux (10^{15} n/cm²·sec) [E > 0.1 MeV]	1.11	PTP Rabbit Holder
Axial peaking factor profile[1]	$1 - 9.85\cdot10^{-4}\cdot z^2$	
Midplane fast flux (10^{15} n/cm²·sec) [E > 0.1 MeV]	0.89	Hydraulic Tube
Axial peaking factor profile[1]	$1 + 1.23\cdot10^{-4}\cdot z - 8.62\cdot10^{-4}\cdot z^2$	

[1] *peaking factor is the ratio of the local flux at a distance z from the reactor midplane (in cm) to the flux at the reactor midplane*

The current design assumes that the rabbits will be placed in the Target Rod Rabbit Holder (TRRH) position in axial location 2, within the peripheral target position (PTP) in location 7, or in the Hydraulic Tube (HT) position 4. Given the symmetric shape of the flux in the HFIR flux trap, position 6 in the HT is assumed to be analogous with HT position 6. The bottom stop location in the TRRH is -23.37 cm (measured from the reactor midplane), and the typical rabbit length is 6.534 cm [1]. Table 3-2 summarizes the fluence characteristics for all three positions.

Table 3-2. Neutron Flux Characteristics for the Rabbit Irradiation Locations

Parameter	TRRH-2	PTP-7	HT-4
Bottom location	-16.2	11.7	-3.8
Top location	-10.2	17.8	-1.2
Peaking factor (integral average)	0.825	0.786	0.994
Midplane fast flux (10^{14} n/cm²·sec) [E > 0.1 MeV]	8.28	8.78	8.57

3.2. Design Description

Table 3-3 lists design drawings and titles for the FeCrAlY experiment.

Table 3-3. Tensile Creep Experiment Design Drawings

Drawing No.	Title
X3E020977A538, Rev. 0	Target Capsule Housing/ End Cap Detail [2]
X3E020977A536, Rev. B	Target Capsule Housing Assembly [3]
S13-11-FCA01, Rev.0	Rabbit Capsule FCAY Holder Assembly [4]
S13-11-FCA02, Rev.0	Rabbit Capsule FCAY Specimen Assembly [5]
S13-11-FCA03, Rev.0	Rabbit Capsule FCAY Specimen Details [6]

The overall design is shown in the view of

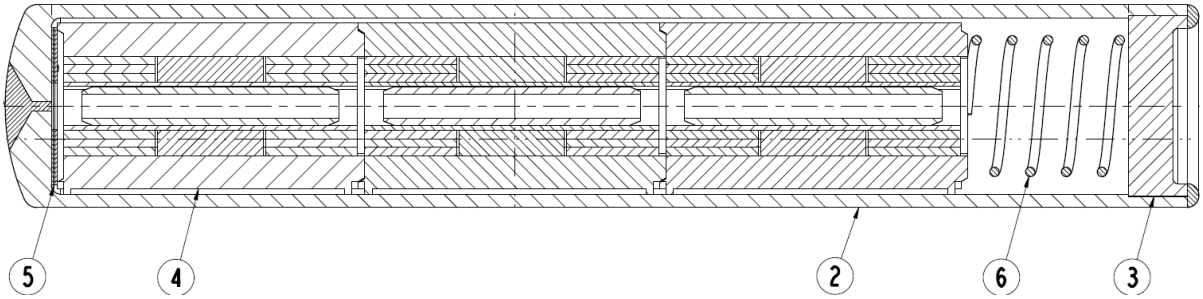

Figure 3-3. The capsule contains three identical specimen assemblies. Each assembly contains 12 FeCrAlY alloy tensile specimens and 4 passive Silicon Carbide (SiC) thermometry pieces. The tensile specimens are fitted with stainless steel chevrons to equalize heat generation and heat transfer in the gauge length of the specimens. Stainless steel was also selected for the FeCrAlY specimen material. The three assemblies are set within aluminum housings that are fabricated from alloy 6061. The entire assembly in

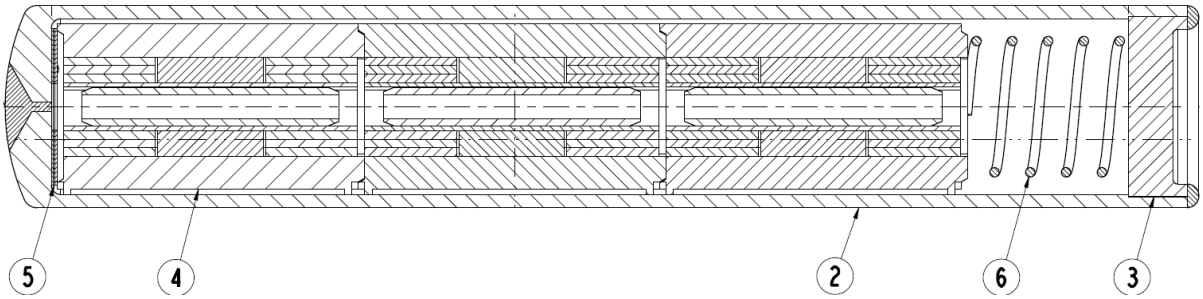

Figure 3-3 is shown within the standard Al6061 housing.

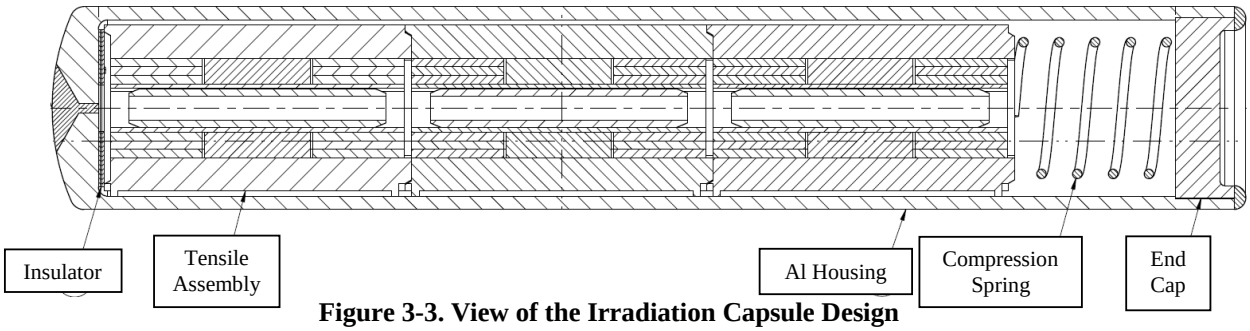

Figure 3-3. View of the Irradiation Capsule Design

3.3. Materials of Construction

Material properties for this calculation are taken from the design and analysis calculations (DACs) shown in Table 3-4:

Table 3-4. Material Property References

Helium	DAC-10-02-PROP_HELIUM [7]
Aluminum 6061-T6	DAC-10-03-PROP_AL6061 [8]
Irradiated SiC	DAC-10-06-PROP_SIC(IRR) [9]
Stainless steel	DAC-10-16-PROP_SS304 [10]

The SiC requires a dose for determining the property set. The dose used for this project is 10 dpa, given the long term irradiation schedule for these capsules.

3.4. Thermal Boundary Conditions

The heat generation rates for all materials and the axial profile are taken from DAC-10-18-RAB02 [11] and summarized in Table 3-5. The convection parameters (heat transfer coefficient and bulk temperature) are taken from DAC-11-01-RAB03 [1] for the hydraulic tube.

Table 3-5. Thermal Boundary Conditions

Item	Value	Source
Heat transfer coefficient (TRRH)	47.1 kW/m²·°C	DAC-11-01-RAB03 [1]
Bulk fluid temperature (TRRH)	52°C	
Correlating parameter (σ)	30.05 cm	DAC-10-18-RAB02 [11]
Peak heat generation rate for Al-6061	32.5 W/g	
Peak heat generation rate for stainless steel	40.0 W/g (PTP)	
Peak heat generation rate for SiC	30.6 W/g	

The local heat generation rate is estimated with the following profile:

$$q(material, z) = q_{peak}(material) \cdot exp\left[-\left(\frac{z}{\sigma}\right)^2\right]$$

where:

q — local heat generation rate as a function of the material and axial location
q_{peak} — heat generation rate at the HFIR midplane as a function of material
z — axial location in HFIR, where the midplane is at zero
σ — correlating parameter

3.5. Finite Element Model

The design drawings for this project were created in Pro-E, and Initial Graphics Exchange Specification (IGES) files were exported from Pro-E or simplified geometries using dimension from the Pro-E models were used to provide geometry data for ANSYS Workbench. These geometric models are stored electronically this report on a THEIG managed server. Also, the ANSYS input script used to evaluate these models is included in Appendix A. Other ANSYS input scripts used to evaluate the models and summarize the results are documented elsewhere [12]. Aside from the assumptions described in section 2, modeling simplifications include (1) modeling tensile spring pins as octagons to improve model meshing, and (2) certain filets and rounds were removed to improve the mesh. Also, only one tensile assembly located at the center of the target position was analyzed to reduce computation time. Given the parts are designed to reach the same temperature axial heat transfer should be minimal, validating this assumption. Figure 3-4 and meshed models for the tensile assembly.

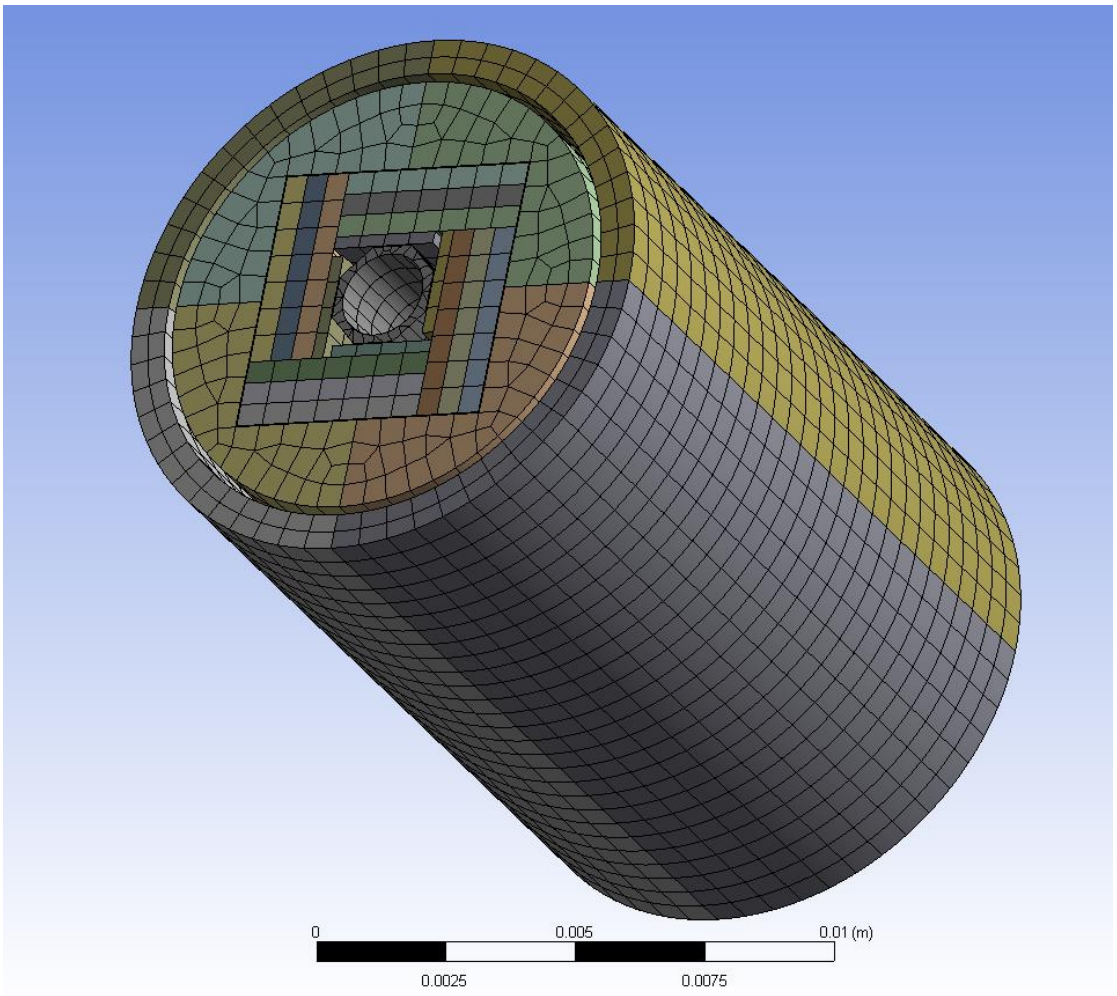

Figure 3-4. Mesh for the tensile assembly

4. Computations and Analyses

The sections below describe the results for each design. The T.025 and T.975 temperatures for each part are the 95% boundaries by volume. In other words, 95% of the volume of the part will have a temperature between these endpoints. The two target temperatures for this design cases are 330°C (max) and 200°C (min).

4.1. Thermal Design

The tensile design has been optimized for 320°C. The fill gas is helium. The resultant design diameter can be found in Table 4-1.

Table 4-1: Design Diameters for TRRH 2 position

FeCrAlY Tensile Assembly	320°C (Design Temperature)
	9.17 mm (0.361 in)

Temperature data for the 320°C tensile assembly case can be seen in Table 4-2Table 4-2. Temperature contour plots for the 320°C tensile specimens and thermometry can be found in Figure 4-1 through Figure 4-3Figure 3-1 and Figure 4-4, respectively.

Table 4-2: Temperature Details for the TRRH 2 design (320°C Tensile Assembly)

Name	Material	Temperature (°C)				
		Tavg	Tmin	Tmax	T.025	T.975
NORTH TENSILE 1	SS304	328	294	339	305	337
SOUTH TENSILE 1	SS304	328	294	339	305	337
EAST TENSILE 1	SS304	328	294	339	306	337
WEST TENSILE 1	SS304	327	294	339	306	337
NORTH TENSILE 2	SS304	321	303	329	307	327
SOUTH TENSILE 2	SS304	321	303	329	307	327
EAST TENSILE 2	SS304	321	303	329	307	327
WEST TENSILE 2	SS304	321	303	329	307	327
NORTH TENSILE 3	SS304	307	296	314	299	311
SOUTH TENSILE 3	SS304	307	296	314	299	311
EAST TENSILE 3	SS304	307	296	314	299	311
WEST TENSILE 3	SS304	307	296	314	299	311
THERMOMETRY	SiC	336	326	348	328	344
WALL CHEVRONS	SS304	309	294	322	302	318
INTERIOR CHEVRONS	SS304	320	298	330	313	327
PIN	SS304	346	342	353	342	352
HOUSING	AL-6061	59	58	60	59	59
HOUSING	AL-6061	59	58	60	59	59
HOUSING	AL-6061	59	58	60	59	59
HOLDER	AL-6061	288	286	291	286	290

Calc Title:	Design Analysis for FeCrAlY Tensile Rabbits		Page 8 of 8
Calc ID:	DAC-13-11-FCAY01, Rev.0	Prep by:	Ck'd by:

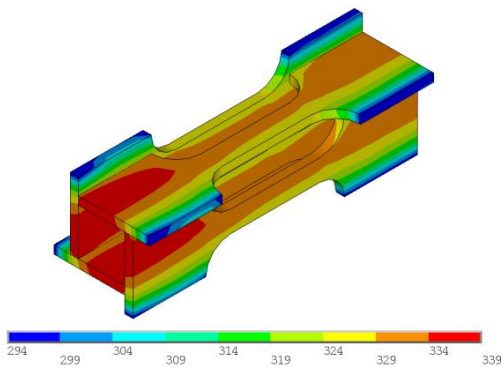

Figure 4-1. Temperature Contour Plot (°C) inner most tensile specimens (noted as TENSILE 1)

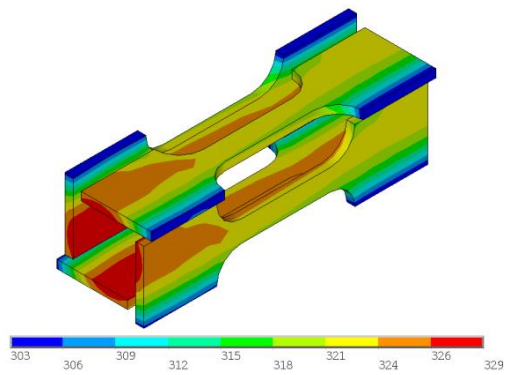

Figure 4-2. Temperature Contour Plot (°C) middle layer of tensile specimens (noted as TENSILE 2)

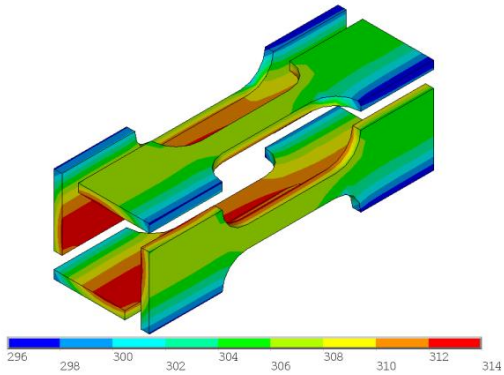

Figure 4-3. Temperature Contour Plot (°C) outer most tensile specimens (noted as TENSILE 3)

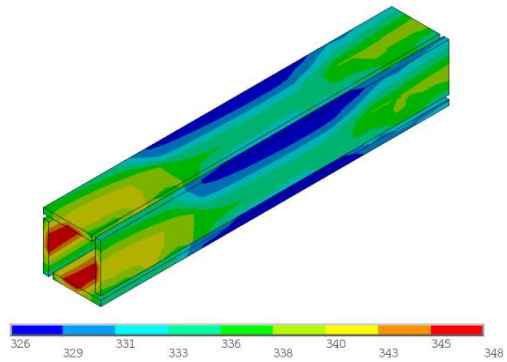

Figure 4-4. Temperature Contour Plot (°C) for Tensile Thermometry

5. Summary of Results

Table 5-1 summarizes the specimen temperatures for the FeCrAlY design considered in this report. The stated temperature range indicates a 95% span by area (i.e., 95% of the area of the part on the cutting plane will have a temperature between the endpoints of the span).

Table 5-1. Design Summary for FeCrAlY Rabbits

Design ID	Holder Material Fill Gas Location	Design Temperature (°C)	Design Diameter	Specimen Temp (°C) Average (Min-Max)
TRRH-2	Aluminum holder Helium fill gas	320	TENSILE 1	328(294-339)
			TENSILE 2	321(303-329)
			TENSILE 3	307(296-314)

6. Conclusions

This calculation establishes design diameters and expected temperatures for the FeCrAlY rabbits. These capsules are designed to irradiate various iron alloy tensile specimens in the flux trap of HFIR at 320°C. The specimens are contained within aluminum holders. The primary outer containment is an Al-6061 tube with an outer diameter of 10.96 mm. Helium is used as the fill gas inside the experiment. The specimen temperature is controlled by the axial location, fill gas, and the size of the gap between the holder and housing.

7. References

[1] J. L. McDuffee, "Heat Transfer Coefficients and Bulk Temperatures for HFIR Rabbit Facilities," 2011.

[2] Oak Ridge National Laboratory, Thermal Hydraulics & Irradiation Engineering Group, "Target Capsule Housing / End Cap Detail," 2007.

[3] Oak Ridge National Laboratory, Thermal Hydraulics & Irradiation Engineering Group, "Target Capsule Housing Assembly," 2008.

[4] Oak Ridge National Laboratory, "Rabbit Capsule FCAY Holder Assembly," 2013.

[5] Oak Ridge National Laboratory, "Rabbit Capsule FCAY Specimen Assembly," 2013.

[6] Oak Ridge National Laboratory, "Rabbit Capsule FCAY Specimen Details," 2013.

[7] J. L. McDuffee, "Thermophysical Properties for Helium," 2010.

[8] J. L. McDuffee, "Thermophysical Properties for AL6061," 2013.

[9] J. L. McDuffee, "Thermophysical Properties for Irradiated SiC," 2013.

[10] J. L. McDuffee, "Thermophysical Properties for 304 Stainless Steel," 2013.

[11] J. L. McDuffee, "Heat Generation Rates for Various Rabbit Materials in the Flux Trap of HFIR," Oak Ridge, TN, 2010.

[12] J. L. McDuffee, "Solve Macros for ANSYS Finite Element Models With Contact Elements," 2013.

APPENDIX A

Calc Title:	Design Analysis for FeCrAlY Tensile Rabbits		Page A-1 of 5
Calc ID:	DAC-13-11-FCAY01, Rev.0	Prep by:	Ck'd by:

APPENDIX A

ANSYS Script Used to Evaluate Capsule Designs

APPENDIX A

Calc Title:	Design Analysis for FeCrAlY Tensile Rabbits		Page A-2 of 4
Calc ID:	DAC-13-11-FCAY01, Rev.0		

```
!*************************************************************************
!*    MACRO RUN_FeCrAlY                                                  *
!*                                                                       *
!*************************************************************************

 FINISH
/CLEAR
/BATCH
/INPUT,'GEOMT','INP'
/PREP7

NUMCMP,NODE
NUMCMP,ELEM
!-------------------------------------------------------------------------
! INPUT SPECIFICATIONS
!-------------------------------------------------------------------------

 PI=3.1415926536
 in=0.0254
 SymAngle=360

! HEAT TRANSFER COEFFICIENT (DAC-11-01-RAB03, PTP with average bulk temperature)
 Hfilm=47100          ! heat transfer coefficient (W/m²·°C)
 Tcoolant=52          ! bulk coolant temperature (°C)


! Target temperature
 Ttarget=320 ! °C
!-------------------------------------------------------------------------
!     SETUP PROBLEM
!-------------------------------------------------------------------------

*GET,giMaxType,ETYP,0,NUM,MAX
*DO,iType,1,giMaxType
     *GET,ElemType,ETYP,iType,ATTR,ENAM
     *IF,ElemType,EQ,174,OR,ElemType,EQ,172,THEN
           KEYOPT,iType,1,1
           xprpSurfaceRoughness(iType)=64E-06*in
     *ELSEIF,ElemType,EQ,170,THEN
           xprpSurfaceRoughness(iType)=64E-06*in
     *ELSEIF,ElemType,EQ,186,THEN
          ET,iType,SOLID226,11,0
     *ELSEIF,ElemType,EQ,187,THEN
          ET,iType,SOLID227,11,0
     *ENDIF
*ENDDO

! DEFINE INITIAL LOAD STEP ARRAY
 RampSteps=3
 LoadSteps=
*DIM,LoadSteps,ARRAY,3,4
! Define time for each load step
 LoadSteps(1,1)=1,2,3
! Define power factors for each load step
 LoadSteps(1,2)=0.0,0.5,1.0
! Define substeps for each load step
 LoadSteps(1,3)=1,3,3
! Define when to use transient effects (0=steady state, 1=transient)
 LoadSteps(1,4)=1,0,0

*ULIB,CONTACT_LIBRARY_R2,ULIB

*USE,SETUP,'3D','HE',1,SymAngle,,Tcoolant

!* ARG1 - Problem type:  '2D'  - 2D in the r-theta plane                 *
!*                       '2DA' - 2D axisymmetric                         *
!*                       '3D'  - 3D                                      *
!* ARG2 - Gas material (i.e., 'AR', 'HE', or 'NE')                       *
```

APPENDIX A

Calc Title:	Design Analysis for FeCrAlY Tensile Rabbits		Page A-3 of 4
Calc ID:	DAC-13-11-FCAY01, Rev.0		

```
!* ARG3 - Radiation [0 = include; 1 = exclude]                              *
!* ARG4 - Symmetry angle [default=360]                                      *
!* ARG5 - Internal gas pressure [default=101325 Pa]                         *
!* ARG6 - Sink temperature (°C) [default=60°C]                              *
!* ARG7 - Contact pressure exponent (typically, 0.6-0.94)                   *
!*           0.95       = optically flat surfaces, Gaussian distribution     *
!*           0.6 - 0.75 = surfaces with waviness, flatness deviation, etc.   *
!*           0.68       =  default value                                     *
!-----------------------------------------------------------------------------
!     GET DIMENSIONS FROM WORKBENCH-SUPPLIED MODEL
!-----------------------------------------------------------------------------

CSYS,1

ESEL,S,MAT,,30,33  ! HOLDER
NSLE,S,ALL
Rsink_o=NX(NODE(1,0,0))



ESEL,S,MAT,,26,29! HOUSING
NSLE,S,ALL
Rhous_o=NX(NODE(1,0,0))
Rhous_i=NX(NODE(0,0,0))

ALLSEL
!Lmodel=NZ(NODE(0,0,1))

!-----------------------------------------------------------------------
!     CREATE BOUNDARY CONDITION FILES
!-----------------------------------------------------------------------
/COM, SETTING BOUNDARY CONDITION INPUT FOR CONVECTION
/OUTPUT,'BC','INP'
/COM, CMSEL,S,'CONVECTIVE'
/COM, SF,ALL,CONV,Hfilm,Tcoolant
/COM,
/COM, ! SETTING BOUNDARY CONDITION INPUT FOR DISPLACEMENT CONSTRAINTS

! Set Y-restraint
/COM, CSYS,0
!/COM  ESEL,S,MAT,,1,last_body
/COM, CMSEL,S,'SYMY'
/COM, D,ALL,UY,0.0
/COM,

! Set Z-restraint
/COM, CSYS,0
!/COM  ESEL,S,MAT,,1,last_body
/COM, CMSEL,S,'SYMZ'
/COM, D,ALL,UZ,0.0
/COM,

! Set x-restraint
/COM, CSYS,0
!/COM  ESEL,S,MAT,,1,last_body
/COM, CMSEL,S,'SYMX'
/COM, D,ALL,UX,0.0
/COM,
/OUTPUT

 ALLSEL

/COM, CALCULATING INTERNAL HEAT GENERATION FOR EACH ELEMENT
*USE,HEAT_GENERATION,-0.132 !TRRH 2


!-----------------------------------------------------------------------------
!     SOLVE
```

APPENDIX A

Calc Title:	Design Analysis for FeCrAlY Tensile Rabbits		Page A-4 of 4
Calc ID:	DAC-13-11-FCAY01, Rev.0		

```
!-----------------------------------------------------------------------------
 SAVE

!*USE,TRANSIENT_SOLVER,'BC','LoadSteps'
*USE,STATIC_SOLVER,'BC',5
!-----------------------------------------------------------------------------
!     POST PROCESSING
!-----------------------------------------------------------------------------
 SAVE
/DELETE,'BC','INP'
 SAVE

/POST1
 SET,LAST
*CFOPEN,'FeCrAlY_OUTPUT','txt'
*VWRITE,
 ******************************************************************************
*VWRITE,
   FeCrAlY Steel Tensile ANALYSIS%/&
   WITH CONTACT ELEMENTS%/&
*****************************************************************************
*VWRITE,
 -------------------------------------------------------------------------------%/&
 DESCRIPTION%/%/&
 * 3-dimensional analysis with contact elements%/&
 * Al-6061 housing%/&
 * Steel Core%/&
 * Helium fill gas%/

*VWRITE,
 ------------------------------------------------------------------------------%/&
 COLD MODEL DIMENSIONS%/

*VWRITE,2*1000*Rhous_o,2*Rhous_o/0.0254
  ('  Outer housing diameter  = ',F6.3,' mm (',F6.4,' in)')
*VWRITE,2*1000*Rhous_i,2*Rhous_i/0.0254
  ('  Inner housing diameter  = ',F6.3,' mm (',F6.4,' in)')
*VWRITE,2*1000*Rsink_o,2*Rsink_o/0.0254
  ('  Outer sink diameter     = ',F6.3,' mm (',F6.4,' in)')

*VWRITE,
%/ ------------------------------------------------------------------------------%/&
 BOUNDARY CONDITIONS %C %/

*VWRITE,Hfilm,Tcoolant
  Heat transfer coefficient = %7.0F W/m²·°C %/&
 Bulk coolant temperature  = %7.1F °C %/

*USE,REPORT_TABLE,'HGEN'
*USE,REPORT_TABLE,'TEMP'
*USE,REPORT_TABLE,'PROP'
*USE,REPORT_TABLE,'ENER'


*VWRITE,
%/  ------------------------------------------------------------------------------%/&
 RADIAL DIMENSIONS AND GAP SUMMARY FOR THE CORE-HOUSING GAP

*USE,REPORT_TABLE,'GAP',,170

*CFCLOS
 ALLSEL
*ULIB
```

APPENDIX B

FeCrAlY ANSYS Report

APPENDIX B

Calc Title:	Design Analysis for FeCrAlY Tensile Rabbits			Page B-2 of 5
Calc ID:	DAC-13-11-FCAY01, Rev.0			

```
*****************************************************************************
  FeCrAlY Steel Tensile ANALYSIS
   WITH CONTACT ELEMENTS
*****************************************************************************
-----------------------------------------------------------------------------
 DESCRIPTION

 * 3-dimensional analysis with contact elements
 * Al-6061 housing
 * Steel Core
 * Helium fill gas

-----------------------------------------------------------------------------
 COLD MODEL DIMENSIONS

 Outer housing diameter  = 10.960 mm (0.4315 in)
 Inner housing diameter  =  9.520 mm (0.3748 in)
 Outer sink diameter     =  9.170 mm (0.3610 in)

-----------------------------------------------------------------------------
 BOUNDARY CONDITIONS

 Heat transfer coefficient =  47100. W/m²·°C
 Bulk coolant temperature  =    52.0 °C

-----------------------------------------------------------------------------
 HEAT GENERATION
```

Part	Material	Heat Gen. @Midplane (W/kg)	------ Heat Load ----- @Midplane (W)	@Location (W)
1) TENSILE_S_3	SS304	38100.	6.2	5.0
2) TENSILE_E_3	SS304	38100.	6.2	5.0
3) TENSILE_N_1	SS304	38100.	6.2	5.0
4) TENSILE_W_1	SS304	38100.	6.2	5.0
5) TENSILE_N_3	SS304	38100.	6.2	5.0
6) TENSILE_W_3	SS304	38100.	6.2	5.0
7) TENSILE_S_2	SS304	38100.	6.2	5.0
8) TENSILE_E_2	SS304	38100.	6.2	5.0
9) TENSILE_N_2	SS304	38100.	6.2	5.0
10) TENSILE_W_2	SS304	38100.	6.2	5.0
11) TENSILE_S_1	SS304	38100.	6.2	5.0
12) TENSILE_E_1	SS304	38100.	6.2	5.0
13) THERMO_S	SiC(Irr)	32900.	0.9	0.7
14) THERMO_E	SiC(Irr)	32900.	0.9	0.7
15) THERMO_N	SiC(Irr)	32900.	0.9	0.7
16) THERMO_W	SiC(Irr)	32900.	0.9	0.7
17) CHEV_S_2	SS304	38100.	4.1	3.3
18) CHEV_E_2	SS304	38100.	4.1	3.3
19) CHEV_N_2	SS304	38100.	4.1	3.3
20) CHEV_W_2	SS304	38100.	4.1	3.3
21) CHEV_S_1	SS304	38100.	4.1	3.3
22) CHEV_E_1	SS304	38100.	4.1	3.3
23) CHEV_N_1	SS304	38100.	4.1	3.3
24) CHEV_W_1	SS304	38100.	4.1	3.3
25) PIN	SS304	38100.	5.8	4.7
26) HOUSING	AL-6061	32500.	8.2	6.6
27) HOUSING	AL-6061	32500.	8.2	6.6
28) HOUSING	AL-6061	32500.	8.2	6.6
29) HOUSING	AL-6061	32500.	8.2	6.6
30) HOLDER	AL-6061	32500.	12.9	10.4
31) HOLDER	AL-6061	32500.	12.9	10.4
32) HOLDER	AL-6061	32500.	12.9	10.4
33) HOLDER	AL-6061	32500.	12.9	10.4
			200.6	161.3

APPENDIX B

Calc Title:	Design Analysis for FeCrAlY Tensile Rabbits		Page B-3 of 5
Calc ID:	DAC-13-11-FCAY01, Rev.0		

CAPSULE TEMPERATURE SUMMARY

Name	Material	Tavg	Tmin	Tmax	T.025	T.975
1) TENSILE_S_3	SS304	307.	296.	314.	299.	311.
2) TENSILE_E_3	SS304	307.	296.	314.	299.	311.
3) TENSILE_N_1	SS304	328.	294.	339.	305.	337.
4) TENSILE_W_1	SS304	327.	294.	339.	306.	337.
5) TENSILE_N_3	SS304	307.	296.	314.	299.	311.
6) TENSILE_W_3	SS304	307.	296.	314.	299.	311.
7) TENSILE_S_2	SS304	321.	303.	329.	307.	327.
8) TENSILE_E_2	SS304	321.	303.	329.	307.	327.
9) TENSILE_N_2	SS304	321.	303.	329.	307.	327.
10) TENSILE_W_2	SS304	321.	303.	329.	307.	327.
11) TENSILE_S_1	SS304	328.	294.	339.	305.	337.
12) TENSILE_E_1	SS304	328.	294.	339.	306.	337.
13) THERMO_S	SiC(Irr)	336.	326.	348.	328.	344.
14) THERMO_E	SiC(Irr)	336.	326.	348.	328.	343.
15) THERMO_N	SiC(Irr)	336.	326.	348.	328.	343.
16) THERMO_W	SiC(Irr)	336.	326.	348.	328.	343.
17) CHEV_S_2	SS304	309.	294.	322.	302.	318.
18) CHEV_E_2	SS304	309.	294.	322.	302.	318.
19) CHEV_N_2	SS304	309.	294.	322.	302.	318.
20) CHEV_W_2	SS304	309.	294.	322.	302.	318.
21) CHEV_S_1	SS304	320.	298.	330.	313.	327.
22) CHEV_E_1	SS304	320.	298.	330.	313.	327.
23) CHEV_N_1	SS304	320.	298.	330.	313.	327.
24) CHEV_W_1	SS304	320.	298.	330.	313.	327.
25) PIN	SS304	346.	342.	353.	342.	352.
26) HOUSING	AL-6061	59.	58.	60.	59.	59.
27) HOUSING	AL-6061	59.	58.	60.	59.	59.
28) HOUSING	AL-6061	59.	58.	60.	59.	59.
29) HOUSING	AL-6061	59.	58.	60.	59.	59.
30) HOLDER	AL-6061	288.	286.	291.	286.	290.
31) HOLDER	AL-6061	288.	286.	291.	286.	290.
32) HOLDER	AL-6061	288.	286.	291.	286.	290.
33) HOLDER	AL-6061	288.	286.	291.	286.	290.

PROPERTY SUMMARY AT THE AVERAGE PART TEMPERATURE

Name	Material	Thermal Cond. (W/m·°C)	Thermal Exp. Coeff. (µm/m·°C)	Emis (---)
1) TENSILE_S_3	SS304	19.525	19.40	0.143
2) TENSILE_E_3	SS304	19.525	19.40	0.143
3) TENSILE_N_1	SS304	19.808	19.73	0.143
4) TENSILE_W_1	SS304	19.807	19.73	0.143
5) TENSILE_N_3	SS304	19.526	19.40	0.143
6) TENSILE_W_3	SS304	19.525	19.39	0.143
7) TENSILE_S_2	SS304	19.715	19.63	0.143
8) TENSILE_E_2	SS304	19.716	19.63	0.143
9) TENSILE_N_2	SS304	19.716	19.63	0.143
10) TENSILE_W_2	SS304	19.715	19.63	0.143
11) TENSILE_S_1	SS304	19.808	19.73	0.143
12) TENSILE_E_1	SS304	19.807	19.73	0.143
13) THERMO_S	SiC(Irr)	6.050	3.37	0.900
14) THERMO_E	SiC(Irr)	6.050	3.37	0.900
15) THERMO_N	SiC(Irr)	6.050	3.37	0.900
16) THERMO_W	SiC(Irr)	6.050	3.37	0.900
17) CHEV_S_2	SS304	19.553	19.43	0.143
18) CHEV_E_2	SS304	19.553	19.43	0.143
19) CHEV_N_2	SS304	19.553	19.43	0.143
20) CHEV_W_2	SS304	19.553	19.43	0.143
21) CHEV_S_1	SS304	19.705	19.62	0.143

22) CHEV_E_1	SS304	19.705	19.62	0.143
23) CHEV_N_1	SS304	19.705	19.62	0.143
24) CHEV_W_1	SS304	19.705	19.62	0.143
25) PIN	SS304	20.071	20.01	0.143
26) HOUSING	AL-6061	166.529	24.21	0.050
27) HOUSING	AL-6061	166.529	24.21	0.050
28) HOUSING	AL-6061	166.529	24.21	0.050
29) HOUSING	AL-6061	166.529	24.21	0.050
30) HOLDER	AL-6061	176.000	25.39	0.056
31) HOLDER	AL-6061	176.000	25.39	0.056
32) HOLDER	AL-6061	176.000	25.39	0.056
33) HOLDER	AL-6061	176.000	25.39	0.056

STORED ENERGY SUMMARY AT THE AVERAGE PART TEMPERATURE

Name	Material	Mass (g)	Tavg (°C)	Specific Heat (J/kg°C)	Stored Energy (J)
1) TENSILE_S_3	SS304	0.165	307.	388.	18.
2) TENSILE_E_3	SS304	0.165	307.	388.	18.
3) TENSILE_N_1	SS304	0.165	328.	390.	20.
4) TENSILE_W_1	SS304	0.165	327.	390.	20.
5) TENSILE_N_3	SS304	0.165	307.	388.	18.
6) TENSILE_W_3	SS304	0.165	307.	388.	18.
7) TENSILE_S_2	SS304	0.165	321.	389.	19.
8) TENSILE_E_2	SS304	0.165	321.	389.	19.
9) TENSILE_N_2	SS304	0.165	321.	389.	19.
10) TENSILE_W_2	SS304	0.165	321.	389.	19.
11) TENSILE_S_1	SS304	0.165	328.	390.	20.
12) TENSILE_E_1	SS304	0.165	328.	390.	20.
13) THERMO_S	SiC(Irr)	0.028	336.	1038.	9.
14) THERMO_E	SiC(Irr)	0.028	336.	1038.	9.
15) THERMO_N	SiC(Irr)	0.028	336.	1038.	9.
16) THERMO_W	SiC(Irr)	0.028	336.	1038.	9.
17) CHEV_S_2	SS304	0.109	309.	389.	12.
18) CHEV_E_2	SS304	0.109	309.	389.	12.
19) CHEV_N_2	SS304	0.109	309.	389.	12.
20) CHEV_W_2	SS304	0.109	309.	389.	12.
21) CHEV_S_1	SS304	0.109	320.	389.	13.
22) CHEV_E_1	SS304	0.109	320.	389.	13.
23) CHEV_N_1	SS304	0.109	320.	389.	13.
24) CHEV_W_1	SS304	0.109	320.	389.	13.
25) PIN	SS304	0.155	346.	391.	20.
26) HOUSING	AL-6061	0.252	59.	884.	9.
27) HOUSING	AL-6061	0.252	59.	884.	9.
28) HOUSING	AL-6061	0.252	59.	884.	9.
29) HOUSING	AL-6061	0.252	59.	884.	9.
30) HOLDER	AL-6061	0.405	288.	1023.	111.
31) HOLDER	AL-6061	0.405	288.	1023.	111.
32) HOLDER	AL-6061	0.405	288.	1023.	111.
33) HOLDER	AL-6061	0.405	288.	1023.	111.
		5.750			867.

RADIAL DIMENSIONS AND GAP SUMMARY FOR THE CORE-HOUSING GAP

	Minimum	Maximum	Average
Contact status	1.0	1.0	1.0
Contact temperature (°C)	214.	216.	215.
Target temperature (°C)	59.	60.	60.
Gap (µm)	149.927	150.690	150.404
Contact pressure (MPa)	0.000	0.000	0.000
Conductance coefficient (W/m²·°C)	1290.	1297.	1292.
Total heat flux (kW/m²)	292.33	295.29	293.55

APPENDIX B

Calc Title:	Design Analysis for FeCrAlY Tensile Rabbits		Page B-5 of 5
Calc ID:	DAC-13-11-FCAY01, Rev.0		

Gap conductance heat flux (kW/m²)	292.33	295.29	293.55
Radiation heat flux (kW/m²)	0.00	0.00	0.00
Contact conduction heat flux (kW/m²)	0.00	0.00	0.00

APPENDIX E

Representative APT Reconstructions

This appendix includes representative APT reconstructions of the various FeCrAl compositions and conditions studied in this work. Figures display each of the three major alloying elements in each reconstructed data set separately.

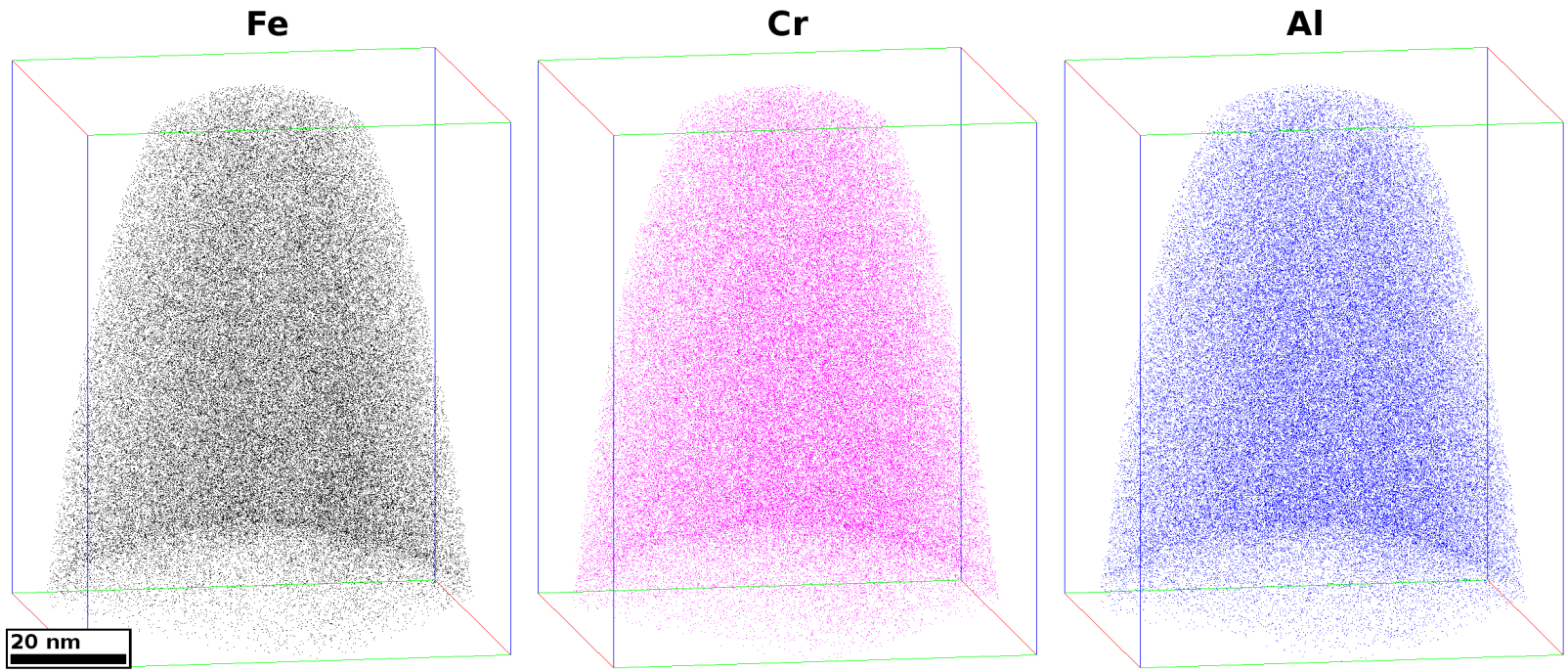

Figure E.1: Representative reconstructions of individual major alloying elements for the as-received Fe-18Cr-5.8Al specimen. Reconstruction dimensions are approximately 74.0 nm $\times$ 72.8 nm $\times$ 91.5 nm.

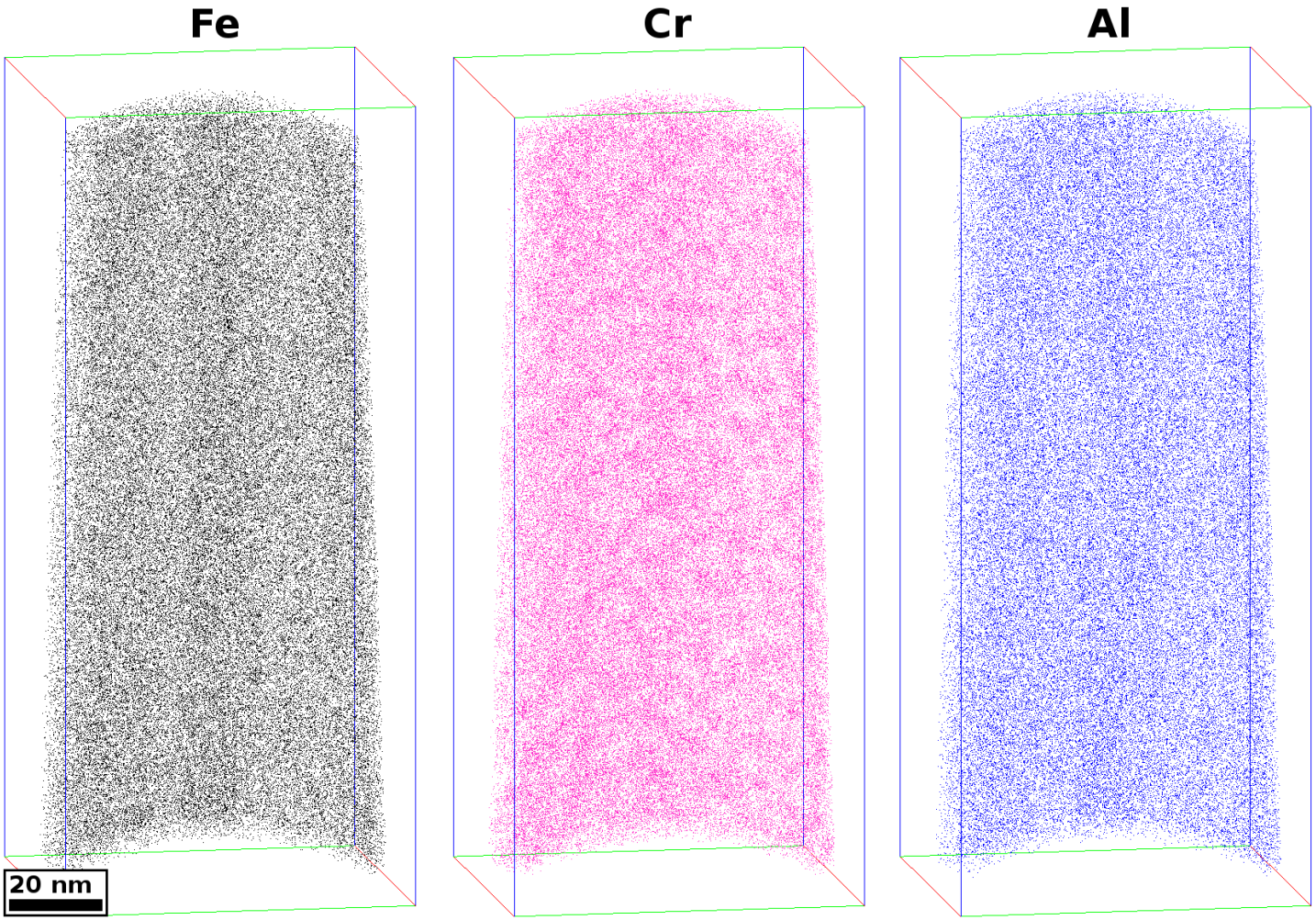

Figure E.2: 15 nm-thick slices of representative reconstructions of individual major alloying elements for a Fe-18Cr-5.8Al specimen following irradiation to 0.8 dpa at 355 °C. Reconstruction dimensions are approximately 74.0 nm × 75.1 nm × 171.3 nm.

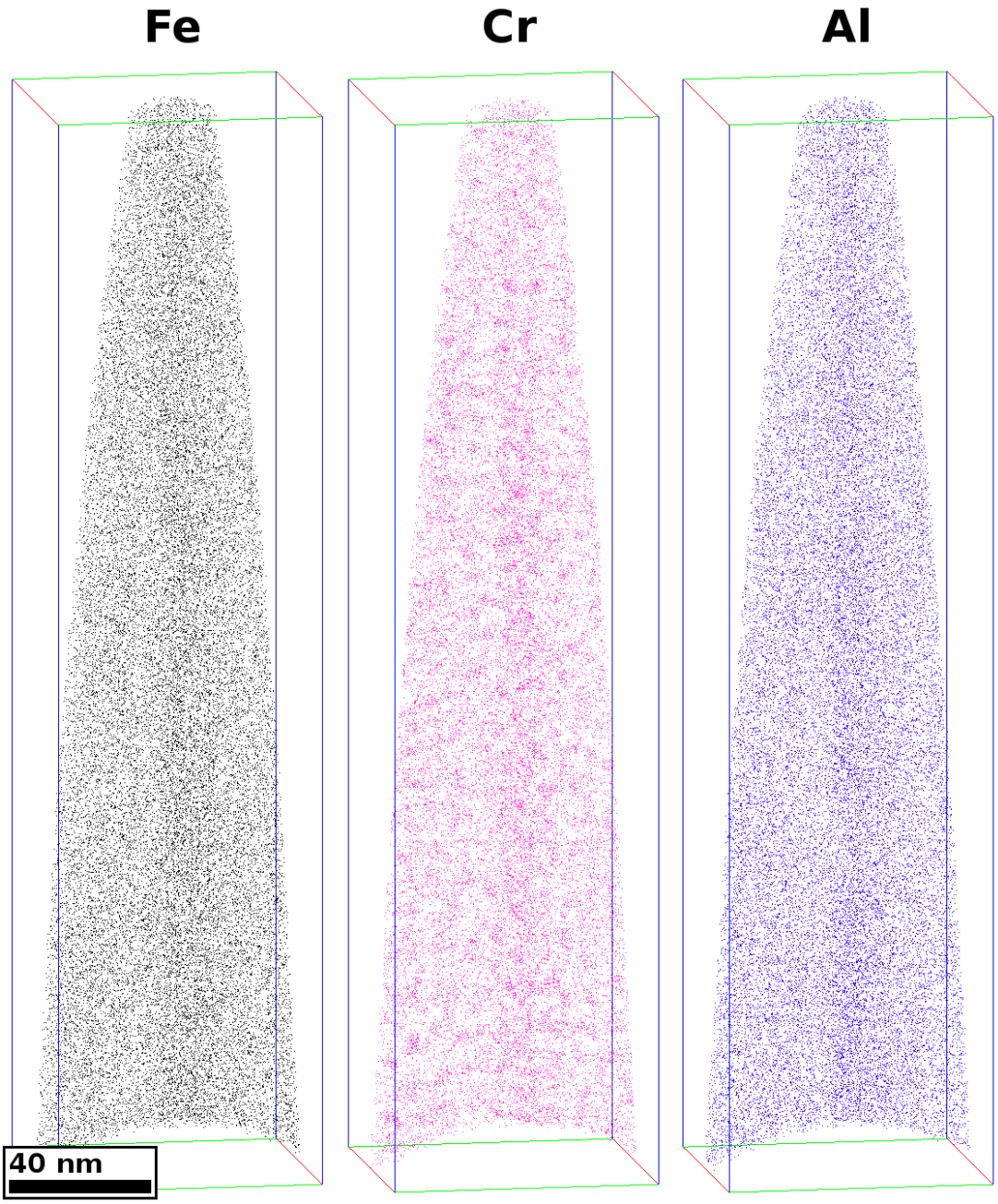

Figure E.3: 15 nm-thick slices of representative reconstructions of individual major alloying elements for a Fe-18Cr-5.8Al specimen following irradiation to 1.8 dpa at 382 °C. Reconstruction dimensions are approximately 74.1 nm × 73.6 nm × 299.6 nm.

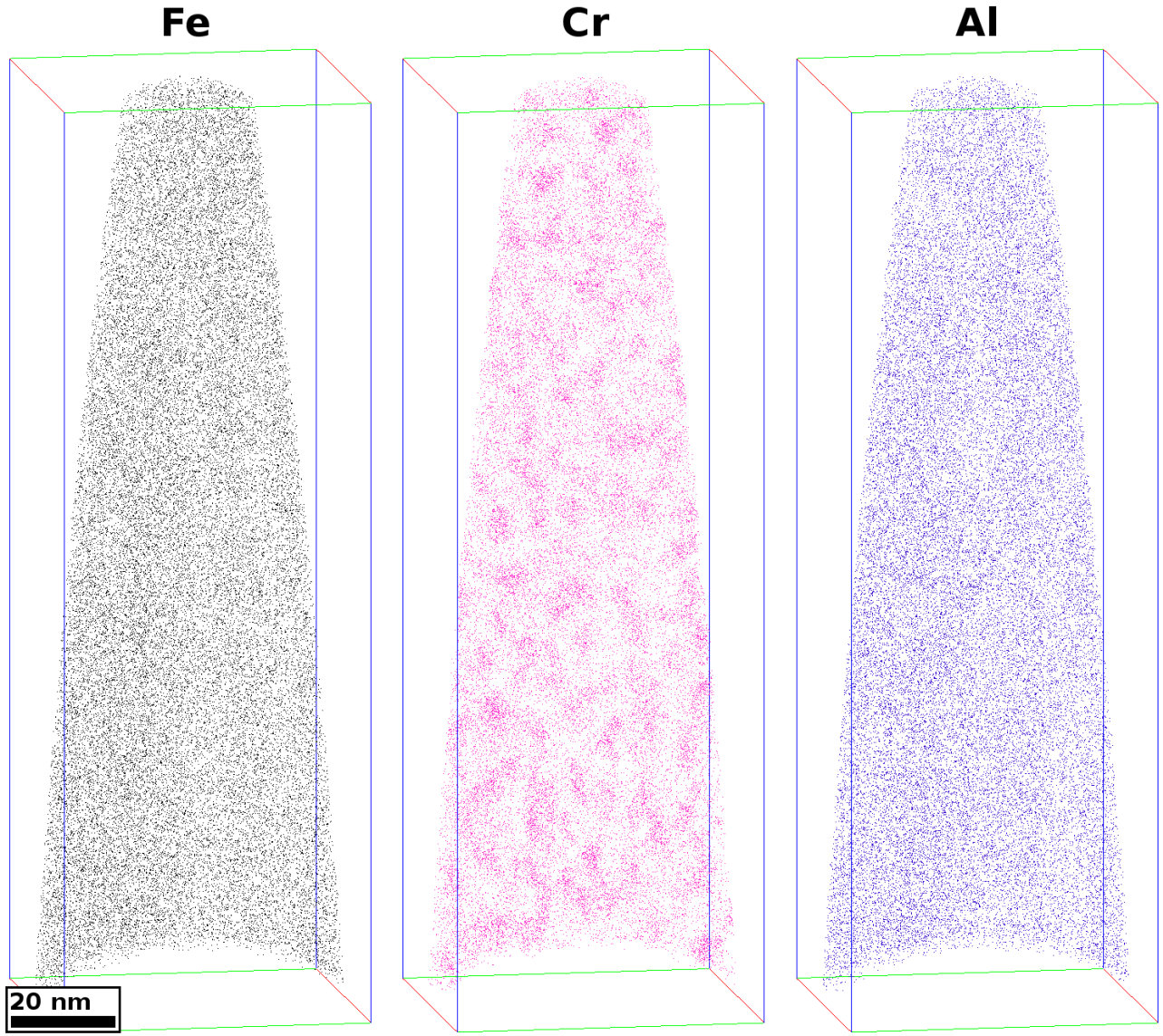

Figure E.4: 15 nm-thick slices of representative reconstructions of individual major alloying elements for a Fe-18Cr-5.8Al specimen following irradiation to 7.0 dpa at 320 °C. Reconstruction dimensions are approximately 58.5 nm × 59.4 nm × 175.3 nm.

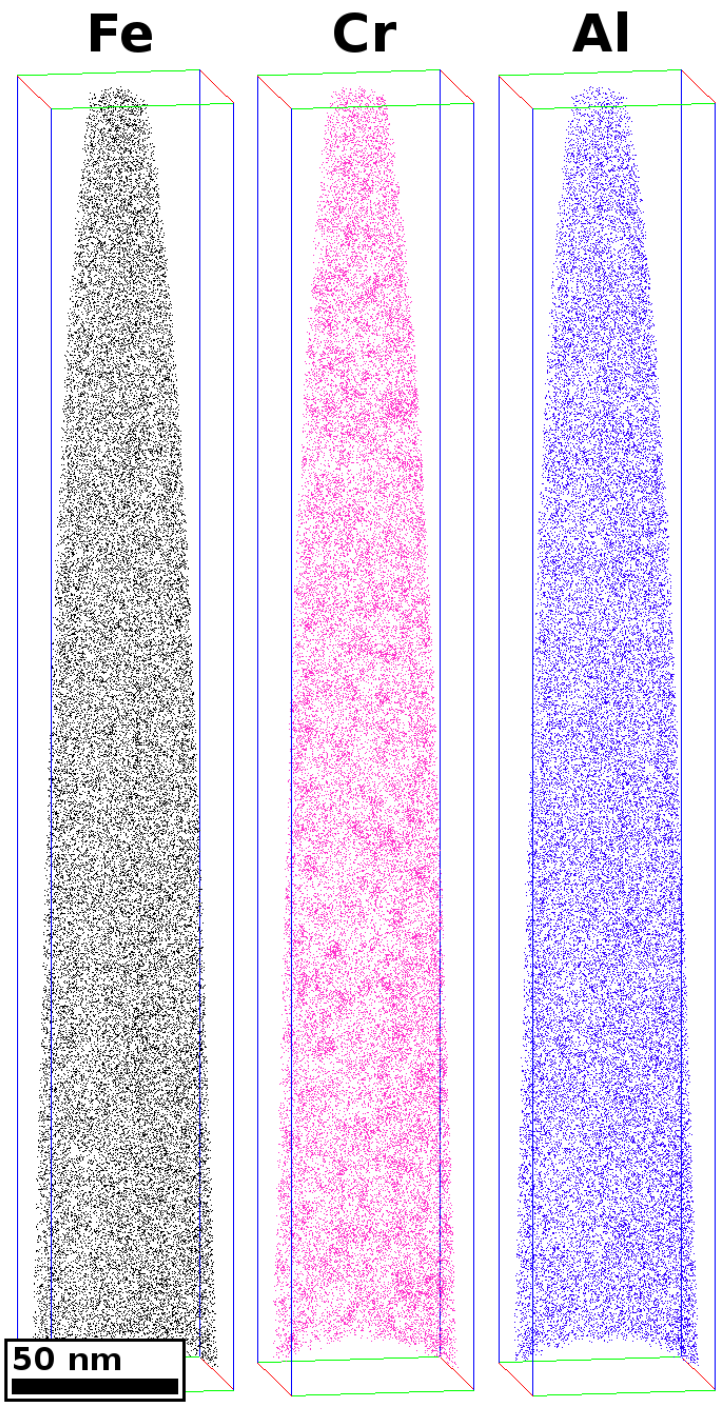

Figure E.5: 15 nm-thick slices of representative reconstructions of individual major alloying elements for a Fe-15Cr-7.7Al specimen following irradiation to 7.0 dpa at 320 °C. Reconstruction dimensions are approximately 54.9 nm × 57.8 nm × 386.1 nm.

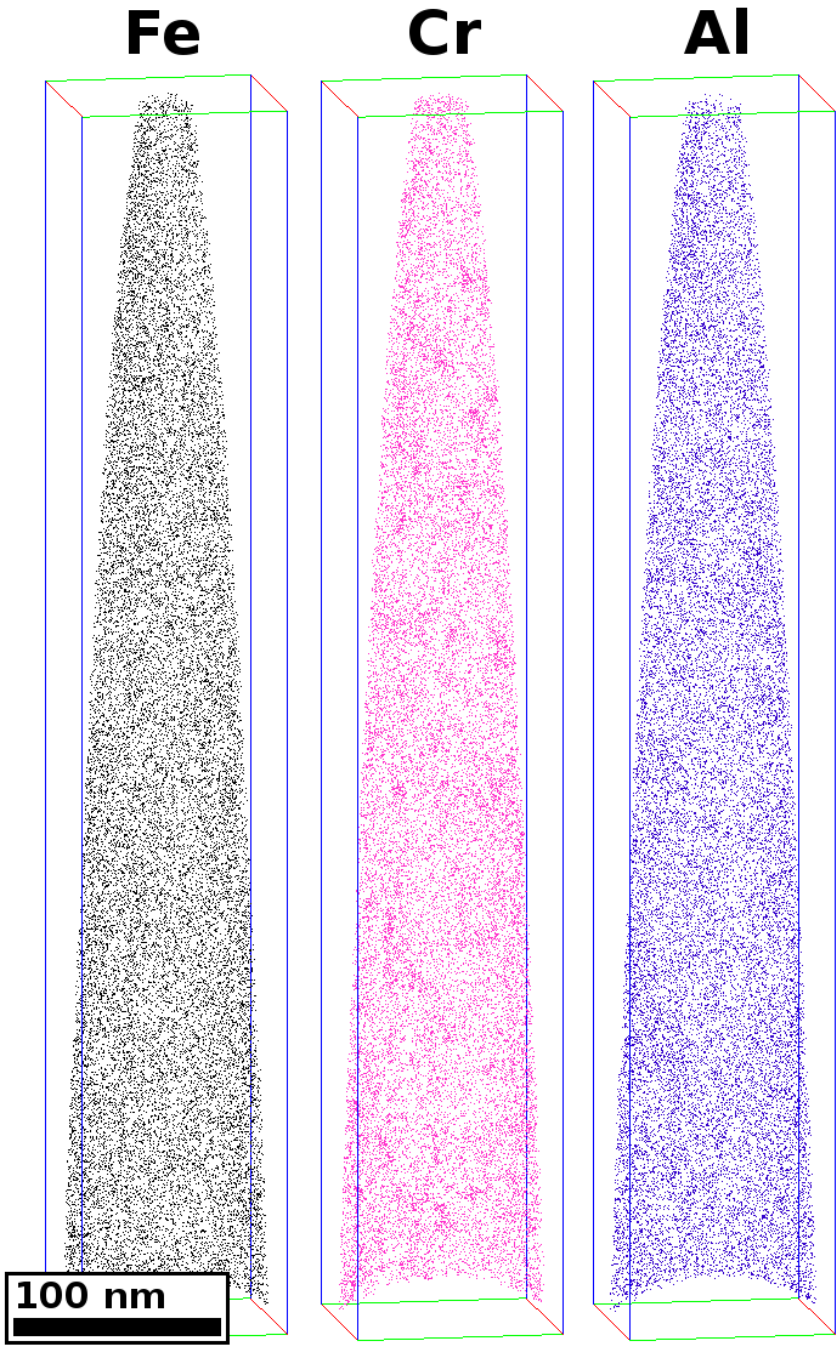

Figure E.6: 15 nm-thick slices of representative reconstructions of individual major alloying elements for a Fe-12Cr-8.7Al specimen following irradiation to 7.0 dpa at 320 °C. Reconstruction dimensions are approximately 98.3 nm × 99.8 nm × 588.4 nm.

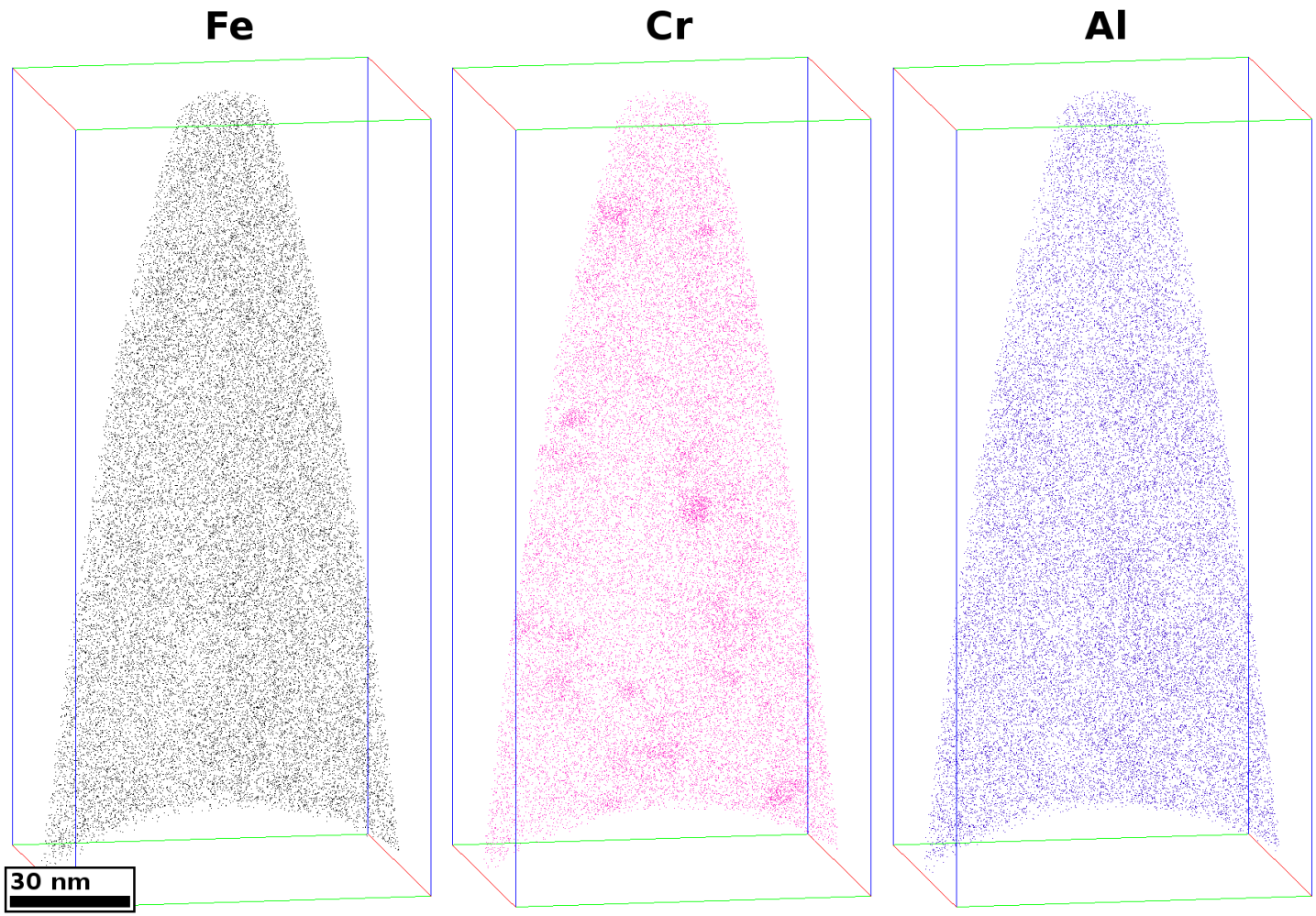

Figure E.7: 15 nm-thick slices of representative reconstructions of individual major alloying elements for a Fe-10Cr-9.3Al specimen following irradiation to 7.0 dpa at 320 °C. Reconstruction dimensions are approximately 83.6 nm × 83.9 nm × 182.6 nm.

APPENDIX F

Studies of Radiation Damage in Ni-Cr Binary Alloys

This appendix details additional research works completed by S.A. Briggs prior to the presented research during his tenure at the Department of Engineering Physics graduate program at the University of Wisconsin - Madison. This research concerns itself primarily with the characterization of radiation damage effects in binary Ni-Cr model alloys following ion irradiation exposures, including the formation of dislocation loops, voids, and radiation-induced segregation in these materials. This work was not included in the main body of this dissertation in order to maintain this document's focus on α' precipitation in neutron-irradiated Fe-Cr-Al alloys, but still fits within the overarching theme of studies of radiation damage effects in reactor-relevant alloys systems. As such, a brief summary of the conducted research is presented here.

This work is divided into two parts. The first details a study of dislocation loop and void formation binary Ni-Cr alloys as a function of composition, irradiation temperature, and irradiating species (proton vs. heavy ion). This work is titled, "Observations of defect structure evolution in proton and Ni ion irradiated Ni-Cr binary alloys," and has been published in the *Journal of Nuclear Materials* [131]. The second reports on observations of the effects of grain boundary migration during the course of the irradiation treatment on radiation-induced segregation in the proton-irradiated Ni-Cr alloys. This article is titled, "Observations of anomalous radiation-enhanced grain boundary migration and solute segregation in Ni-Cr binary alloys," and is in preparation for submission to *Scripta Materialia*.

Executive Summary

The excellent high temperature creep strength of Ni-based alloys has led to their ubiquity in high temperature applications and suggests that they may be an effective structural material for nuclear reactor components. While, historically, these materials have not been employed in radiation environments due to issues with radiation-induced embrit-

tlement, there has been a renewed interest in the radiation tolerance of these materials due to their chemical compatibility with the molten salt coolant environments proposed by some next-generation reactor designs. In these applications, chromium, typically alloyed to increase aqueous oxidation resistance, is detrimental to alloy performance as it is preferentially leached by the salt. As such, a greater understanding of how radiation damage affects low-Cr Ni-based alloys is required.

These studies employ proton and heavy ion irradiation to simulate neutron damage exposure in reactor environments and induce the dislocation loop, void, and radiation-induced segregation (RIS) features of interest in two binary Ni-Cr alloys containing either 5 or 18 wt.% Cr. Dislocation loops are primary contributors to irradiation-induced hardening and embrittlement, while voids cause swelling of in-core components. RIS causes solute enrichment or depletion at grain boundaries and other point defect sinks in these materials, often affecting local mechanical and oxidation properties and potentially leading to failures through irradiation-assisted stress corrosion cracking (IASCC) or similar mechanisms. Finally, ion irradiation experiments have long been used to simulate neutron damage, as comparable damage levels are achieved much more rapidly, but the best method for reconciling the differences in the resulting microstructures arising from the dissimilarities in damage mechanisms between different irradiating species is a topic of some debate. This study also compares the microstructures resulting from proton and Ni ion irradiation in these materials at two different temperatures in order to provide insight into how these different damage mechanisms affect the final microstructure in Ni-based alloys.

With these experimental goals in mind, the two binary Ni-Cr alloys of interest (referred to henceforth as Ni-5Cr and Ni-18Cr) were irradiated with either 2 MeV protons at the University of Wisconsin Ion Beam Lab at target temperatures of 400 and 500°C, or with 20 MeV Ni ions at the Sandia National Laboratories Ion Beam Lab at a target temperature of 500°C. FIB-prepared specimen volumes with nominal damage doses of 1.6 dpa and 3.4 dpa were studied in the proton and Ni ion irradiated materials, respectively. Frank loop, void, and RIS features were imaged using either TEM relrod dark field imaging, STEM-HAADF imaging, or STEM/EDS spectral imaging techniques.

Comparison of resulting microstructures revealed that higher irradiation temperatures resulted in lower densities of larger dislocation loops and voids, likely due to the increased mobility of point defects at higher temperatures making it more likely for defects to find and combine with existing defect clusters as opposed to nucleating new clusters. Increased Cr results in a higher number density of dislocation loops, most likely by affecting loop nucleation behavior. This hypothesis was supported by good agreement of experimental observations with cluster dynamics simulations showing that a small change in interstitial binding energy could account for the difference in the microstructures. Ni-irradiated specimens showed much higher densities of smaller voids compared to proton-irradiated materials. This is most likely caused by the higher dose rate coupled with a much shorter time at temperature, giving voids less time to grow together and coarsen.

RIS observations in proton-irradiated materials were anomalous when compared to expected behavior reported in literature. Instead of sharp segregation profiles, large micron-scale regions of Cr depletion were observed on one side of the grain boundary. It is speculated that these findings are the result of combined radiation-enhanced grain boundary migration and solute segregation effects. This unusual behavior was observed at every grain boundary studied with the exception of less mobile $\Sigma 3$ coincidence site lattice (CSL) boundaries. Formation of these features likely requires little to no pinning obstacles to boundary migration, and the lack of back diffusion and recovery at positions far from the interface seems to suggest a rapid, oscillatory, random-walk grain boundary migration mechanism as opposed to grain growth in a single direction. Similar phenomena have been observed in previous electron irradiation studies, which have approximately 100 times greater dose rates, though the resulting asymmetric segregation profiles are distinct.

Observations of defect structure evolution in proton and Ni ion irradiated Ni-Cr binary alloys

Samuel A. Briggs[a,*], Christopher M. Barr[b], Janne Pakarinen[a,c], Mahmood Mamivand[a], Khalid Hattar[d], Dane D. Morgan[a], Mitra Taheri[b], Kumar Sridharan[a]

[a] *University of Wisconsin-Madison, 1415 Engineering Drive, Madison, WI 53706*
[b] *Drexel University, 3141 Chestnut Street, Philadelphia, PA 19104*
[c] *SKC•CEN Belgian Nuclear Research Centre, Boeretang 200, B-2400 Mol, Belgium*
[d] *Sandia National Laboratories, PO Box 5800, Albuquerque, NM 87185*

Abstract

Two binary Ni-Cr model alloys with 5 wt.% Cr and 18 wt.% Cr were irradiated using 2 MeV protons at 400 and 500 °C and 20 MeV Ni^{4+} ions at 500 °C to investigate microstructural evolution as a function of composition, irradiation temperature, and irradiating ion species. Transmission electron microscopy (TEM) was applied to study irradiation-induced void and faulted Frank loops microstructures. Irradiations at 500 °C were shown to generate decreased densities of larger defects, likely due to increased barriers to defect nucleation as compared to 400 °C irradiations. Heavy ion irradiation resulted in a larger density of smaller voids when compared to proton irradiations, indicating in-cascade clustering of point defects. Cluster dynamics simulations were in good agreement with the experimental findings, suggesting that increases in Cr content lead to an increase in interstitial binding energy, leading to higher densities of smaller dislocation loops in the Ni-18Cr alloy as compared to the Ni-5Cr alloy.

Keywords: radiation damage, Frank loops, voids, nickel alloys, scanning/transmission electron microscopy

1. Introduction

Ni-based alloys are commonly used in high-temperature applications due to their superior high temperature creep strength and were considered for nuclear reactor systems during fast reactor development programs in the '70s and '80s [1–6]. High-Cr Ni-based alloys are currently used primarily in systems in which there is no neutron flux, such as steam generators, as they have been found to be susceptible to irradiation-induced embrittlement [6]. However, there is a renewed interest in radiation damage effects in Ni-based alloys due to their excellent corrosion resistance, especially in molten salt reactor environments [7, 8]. In these environments Cr-content, usually added to increase oxidation resistance, is considered detrimental as it is preferentially leeched by the fluoride salts [9]. As such, an understanding of radiation damage effects in low-Cr Ni-based alloys is desired.

Many prior radiation effects studies on Ni-based alloys focused on the Nimonic PE16 Ni-Fe-Cr alloy [1–5] and there is considerable literature on composition effects in austenitic stainless steels and ternary model alloy systems [3, 10–13]. However, only a few fundamental studies have been performed to study Cr content effects on the radiation response of Ni-based alloys. Hudson and Ashby showed that increases in Cr content tended to reduce swelling in Ni-irradiated Ni-Cr binary systems and swelling rates for Ni-Cr continued to increase for higher damage doses, rather than saturate as for pure Ni [14]. Garner has postulated that atomic ordering effects may influence void swelling [15], and Robinson and Jenkins have demonstrated weak dependence of dislocation loop formation on Cr content [16]. Finally, Barr *et al.* investigated the effects of grain boundary character on the radiation-induced segregation response in a Ni-5Cr alloy [17]. Extrapolation of data from these analogous systems can help to develop Ni-based alloys for the next generation reactor applications. However, more work is required to understand the fundamentals of the radiation response of these alloys.

Ion irradiation experiments have long been used to simulate neutron radiation damage in reactor environments; comparable damage levels are achieved much more rapidly and the resulting samples are typically non-radioactive, making the logistics of sample handling post-irradiation much easier. In this study both protons and Ni ions have been used to induce damage with the purpose of comparing the effect of dose rate on the induced microstructure, though other factors such as the efficiency of producing mobile point defects and gradients in induced damage must be considered in the context of the presented results. While no neutron irradiation experiments have been performed in the current work, the insights gained can be extrapolated to predict in-core radiation response, though the best way to reconcile the differences in the resulting microstructures induced by neutrons and different types of ions is a topic of debate and has been the focus of several studies [18–23].

The present study investigates the effects of Cr content, irradiation temperature, and irradiating species on the resulting microstructure of ion irradiated Ni-based alloys with a focus

*Corresponding author: Samuel A. Briggs (✉: sabriggs2@wisc.edu)

on the formation of dislocation loops and voids. The dislocation loop structures seen in this system are faulted Frank loops commonly seen in other irradiated austenitic steels [24, 25] and are the primary contributors to radiation-induced hardening and embrittlement effects. Voids are responsible for radiation-induced void swelling, and both are typically considered to be detrimental to materials performance.

2. Experimental details

Two binary model Ni-Cr alloys of nominal composition 5 wt.% Cr and 18 wt.% Cr (referred to henceforth as Ni-5Cr and Ni-18Cr, respectively) were vacuum arc melted and cast in a water-cooled copper hearth and recrystallized by cold-rolling to 50% of their original thickness followed by annealing for one hour at 1050 °C. These two compositions were selected because they represent binary analogs to a broader family of Ni-based alloys that contain Cr primarily for high-temperature oxidation resistance and creep strength. Their relatively pure compositions allow us to eliminate the effects of minor alloying elements from this study. The composition of these materials was verified using inductively coupled plasma optical emission spectroscopy (ICP-OES). The results of this analysis are shown in Table 1. Observed impurities are dilute enough such that differences in their concentration between the two materials are not expected to significantly affect radiation response behavior.

Table 1: Summary of bulk alloy compositions for Ni-5Cr and Ni-18Cr in weight percent

Alloy	Cr	Ni	C	Si	Co	P	S	Other Minors
Ni-5Cr	5.00	94.94	0.007	0.01	0.01	<0.005	0.005	<0.01
Ni-18Cr	17.90	82.02	0.016	0.01	0.01	<0.005	0.006	<0.01

After recrystallization, the samples were examined using electron backscatter diffraction (EBSD). Defect-free sample surfaces were prepared by mechanical polishing with SiC paper to 800 grit before electropolishing with an electrolyte solution of 30% nitric acid, 10% sulfuric acid, 10% orthophosphoric acid and 50% glacial acetic acid [26].

Proton irradiations were conducted at the University of Wisconsin Ion Beam Lab (UW-IBL) on a 3.4 MV Pelletron tandem accelerator with 2 MeV ions for approximately 100 hours until a final fluence of 2.58×10^{19} ions/cm^2 was achieved at a nominal flux of 6.77×10^{13} ions/cm^{2}s. Target temperatures of 400 and 500 ± 15 °C were monitored using two thermocouples mounted on either end of the sample stage and was controlled primarily by optimizing beam current through minimal adjustments. Ni ion irradiations were performed at the Sandia National Laboratories Ion Beam Laboratory on the 6 MV tandem Van de Graaff accelerator using 20 MeV ions for approximately 4 hours until a final fluence of 1.9×10^{16} ions/cm^2 was achieved at a nominal flux of 1.32×10^{12} ions/cm^{2}s. Temperature was controlled using a button heater coupled with LabVIEW software and was monitored using spot-welded thermocouples and maintained at 500 ± 10 °C.

Damage profiles for both the proton and Ni ion irradiations were computed using the SRIM-2008 code [27]. The parameters were selected to comply with the methodology established by Stoller *et al.* [28]. The resulting damage profiles for the proton and Ni-ion irradiations are shown in Figure 1. A nominal dose of approximately 1.6 displacements per atom (dpa) was achieved in the region examined for the proton-irradiated materials, which extended to a maximum depth of 10 µm, at an average damage rate of 4.2×10^{-6} dpa/s. The dose achieved in the Ni-irradiated specimens varied more significantly with depth prior to the end of range damage—as such, analysis was performed at a depth of 1 µm corresponding to a nominal dose of 3.4 dpa. The higher dose in the Ni-ion irradiation experiment was required to saturate radiation-induced segregation in this material, the results of which has been reported previously [17].

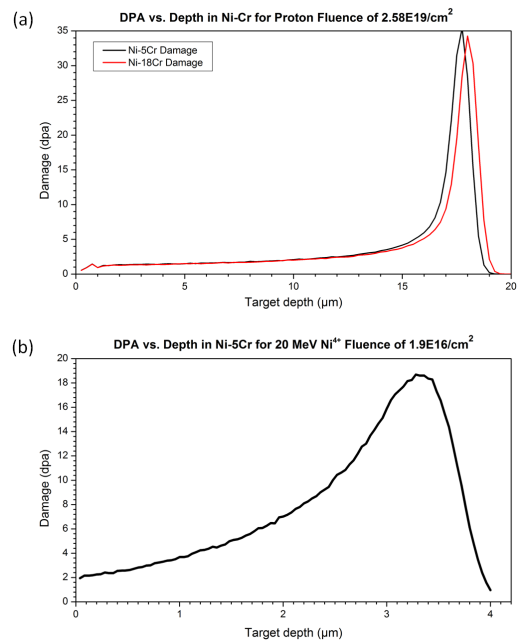

Figure 1: (a) Damage profile for 2 MeV proton irradiations in both Ni-Cr alloys. Damage profiles are extremely similar and are assumed to be equivalent for the purpose of this experiment (studied region from 0 to 10 μm). (b) Damage profile for 20 MeV Ni^{4+} irradiations in Ni-5Cr. Microstructural investigation took place at a target depth of 1μm, corresponding to a nominal damage dose of 3.4 dpa. Damage profiles generated using the SRIM-2008 software [27].

Transmission electron microscopy (TEM) techniques were employed to investigate the irradiated microstructures. Samples for TEM analysis were prepared from the unirradiated specimens using electrolytic jet thinning utilizing the same electrolyte solution used for EBSD sample preparation. TEM specimens from irradiated materials were prepared using the focused ion beam (FIB) lift-out method on the FEI Quanta 3D FEG at the Microscopy and Characterization Suite located at the Center for Advanced Energy Studies (CAES) in Idaho. The specimens were prepared from random locations on the irradiated surface and sampled multiple grains. Lift-outs were mounted on cop-

per Omniprobe FIB grids and cleaned with a 5 kV (Ga) FIB beam to minimize FIB-induced radiation damage. Frank loops residing on the four {111} planes of the face centered cubic (fcc) lattice with Burgers vector $a/3\{111\}$ were imaged using a relrod dark field imaging technique with a 200 kV accelerating voltage on the FEI Tecnai TF-30 TEM/STEM and the JEOL JEM2100 TEM/STEM at the University of Wisconsin-Madison and Drexel University, respectively. The imaging conditions were set in selected area diffraction mode by tilting from the [011] zone axis until a two beam condition was met with the $\mathbf{g} = 31\bar{1}$ reflection and then centering the smallest objective aperture between the [200] and $[11\bar{1}]$ diffraction spots [24]. Voids were imaged using scanning transmission electron microscopy high-angle annular dark field (STEM-HAADF) imaging with 200 kV electrons on the FEI Titan Aberration-corrected (S)TEM at the University of Wisconsin-Madison. Areal defect densities were obtained through manual counting in the ImageJ software [29]. At least three separate micrographs from different sample regions were used for statistical analysis. Sample thicknesses for number density determination were calculated using the electron energy loss spectroscopy (EELS) log-ratio method with an assumed electron mean free path for pure Ni of 98 nm for 200 keV electrons [30]. EELS thickness measurements were taken at five different regions for each sample and averaged to determine the mean specimen thickness.

A cluster dynamics (CD) model was used for simulating loop evolution under proton irradiation to understand mechanisms for loop evolution behavior in Ni-5Cr and Ni-18Cr. The CD simulation technique predicts microstructure evolution in a system described as a gas of non-interacting clusters. The clusters are defined by a single parameter, their size or the number of atoms they contain. The evolution of clusters is deduced from reaction rate theory equations. A previously established CD model for defect evolution based on Duparc *et al.* and Pokor *et al.* [31, 32] was used in this study. In this model only single interstitials and single vacancies are considered mobile. In-cascade clustering of defects [33, 34] under proton irradiation based on Gan *et al.* is also included in the model [35]. The material parameters, cascade production properties, and environmental parameters (dose rate and temperature) for the CD model are listed in Table 2. In most cases the properties of pure Ni were considered due to lack of data for specific Ni-5Cr and Ni-18Cr alloys. The binding energy of dimer interstitials is used as fitting parameter, as discussed below.

3. Results and discussion

3.1. Unirradiated microstructure

Inverse pole figure maps for each material obtained via EBSD are shown in Figure 2. It can be seen that the grains are equiaxed, with an area averaged grain size (including twin boundaries) of 163.9 and 106.6 microns for the Ni-5Cr and Ni-18Cr specimens, respectively. Due to these large grain sizes compared to implantation and analysis depths in these materials the presented results are expected to be representative of bulk material behavior.

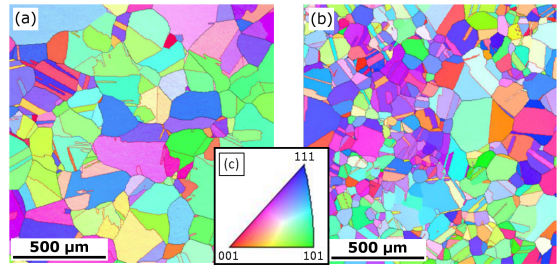

Figure 2: Representative inverse pole figure (IPF) of (a)Ni-5Cr and (b) Ni-18Cr sample materials prior to irradiation. IPF key is shown in (c).

TEM investigation on the unirradiated jet-polished specimens showed a clean microstructure with very few dislocation structures and a complete absence of voids. In addition, TEM examination of the Ni-irradiated foils in regions beyond the damage range showed minimal FIB damage artifacts. Based on these observations it is concluded that all obvious microstructural defects are a result of the ion irradiation treatment.

3.2. Frank loops in irradiated Ni-Cr

Frank loops in irradiated Ni-Cr specimens showed distinct differences in density and size for different compositions and irradiation conditions. Representative TEM relrod micrographs showing these loop structures for the five investigated conditions are shown in Figure 3 and plots illustrating the loop sizes and densities are shown in Figure 4. As is evident from Figure 5, irradiations at 400 °C tended to result in a higher density of Frank loops as compared to irradiations at 500 °C and the higher irradiation temperature induced a slight increase in the loop size. Simulation of annealing effects in 304L stainless steels by Busby *et al.* have illustrated that loop stability can be greatly affected by the temperature increase from 400 to 500 °C, especially over the course of a 100 hr irradiation [40]. These observations imply that an increase in point defect recombination and annihilation due to enhanced mobility at 500 °C combined with increased thermal emission ultimately results in a reduced number of dislocation loops. Furthermore, the loops that do nucleate tend to absorb more point defects and increase in size. In addition, the lower density of Frank loops at 500 °C could be attributed to the unfaulting of Frank loops to network, perfect $1/2\langle 111\rangle$ dislocations. Zhang *et al.* recently indicated unfaulting of interstitial Frank loops at 500 °C during 1 MeV Kr^{2+} irradiations of Inconel X-750 while also indicating a lower density of total loops observed at 500 °C than at 400 °C [41]. The growth and subsequent unfaulting of Frank loops at higher temperatures is consistent with the slightly larger loop size and small Frank loop density observed between 400 and 500 °C examined in the proton irradiations. These temperature trends are consistent with observed loop morphologies in Ni ion and neutron irradiated 316L stainless steel systems [42–44].

Additionally, it was observed that the self-ion irradiated Ni-5Cr showed a higher density of larger loops than the proton-irradiated Ni-5Cr at 500 °C. Due to the differences in dose it is

Table 2: Parameters used for Ni-5Cr and Ni-18Cr cluster dynamics model.

Parameter	Value	Reference
Lattice parameter	3.524Å	
Temperature	400 °C	
Interstitial migration energy	0.12 eV	[36]
Vacancy migration energy	1.02 eV	[37]
Interstitial pre-exponential	8×10^{-10} m^2/s	Calculated assuming D_i is equal to austenitic steels
Vacancy pre-exponential	6.7×10^{-7} m^2/s	[37]
Interstitial formation energy	4.16 eV	[36]
Vacancy formation energy	1.79 eV	[38]
Binding energy of interstitial dimer	Fitting parameter	
Binding energy of vacancy dimer	0.05 eV	[39]
Recombination radius	0.7 nm	[32]
Dislocation density	1×10^{12} m^{-2}	
Average grain size	100 μm	
Burgers vector of the loop assumed to be prismatic	$a/\sqrt{3}$	
Capture efficiency for interstitial by dislocation net	1.2	[32]
Capture efficiency for vacancy by dislocation net	1.0	[32]
Dose rate	3.9×10^{-6} dpa/s	
Damage efficiency	0.90	[35]
In-cascade interstitial clustering fraction for 2i	1%	[35]
In-cascade interstitial clustering fraction for 3i	1%	[35]
In-cascade interstitial clustering fraction for 4i	0.1%	[35]
In-cascade interstitial clustering fraction for vacancy	10%	[35]
Radius of vacancy clusters	0.5 nm	[35]

difficult to make one-to-one quantitative comparisons and extricate the effects of using a different irradiating ion species. However, Frank loop morphologies are known to eventually saturate with dose in similar irradiated systems [24, 45], specifically in the 1-1.5 dpa range for ion-irradiated materials [41, 46]. If it is assumed that saturation behavior is similar for the presently considered Ni-irradiated Ni-5Cr alloy, the higher density of observed loops would suggest that the immobile defect clusters generated during the more chaotic damage cascades can aid in loop nucleation. Additionally, the larger loop size distribution may indicate that a larger portion of the produced defects are being absorbed by this high density of nucleated loops instead of annihilating, or that nucleated loops may interact with/absorb these defect clusters to grow at an increased rate.

While an increase in the irradiation temperature increased the loop size for the two compositions studied, changing the Cr content also had an effect on the loop density. For 400 °C irradiation, Ni-18Cr showed a higher loop density by approximately a factor of two when compared to Ni-5Cr. This higher density was accompanied with a slight decrease in average loop size. A similar trend is observed as a result of 500 °C irradiation but with a larger difference in the loop densities between the two compositions. This contradicts observations in a study of room temperature tungsten-irradiated Ni-8Cr and Ni-17Cr by Robinson *et al.* in which a lower Cr content resulted in a higher defect yield (defined as the fraction of displacement cascades which collapse to form point-defect clusters), though the differences in the densities was much less dramatic than observed here and within the reported error bars [16]. It is postulated here that the primary cause for the changes in defect morphologies with different compositions are due to the differences in the energetics of loop nucleation. This was investigated further by using cluster dynamics simulations discussed in the next section. It is noted that the Ni-5Cr specimen irradiated with protons at 500 °C appears to be an outlier in this study, due to the order of magnitude difference in the density of dislocation loops observed as compared to the other specimens. As such, the cluster dynamics simulations focus on the 400 °C proton-irradiated materials to study the composition effects, as variation of model parameters commensurate with what is expected for such a temperature shift did not yield good fits to this experimental data.

3.3. Cluster dynamics modeling results

It is hypothesized that the different loop behavior between Ni-5Cr and Ni-18Cr is due to changes in the initial energetics of the loop, which alters its nucleation. *Ab initio* calculations have reported strong binding energies between Cr and interstitials in Ni-Cr alloys, with differences between Ni-Ni and Cr-

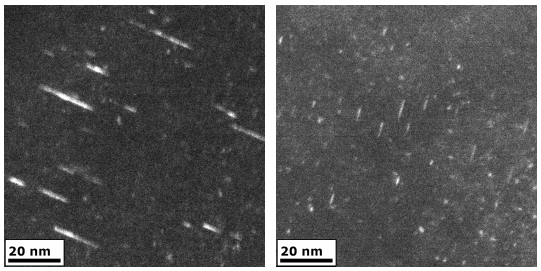

(a) Ni-5Cr, 400 °C, H^+ (b) Ni-18Cr, 400 °C, H^+

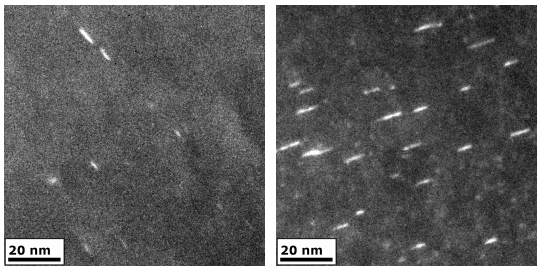

(c) Ni-5Cr, 500 °C, H^+ (d) Ni-18Cr, 500 °C, H^+

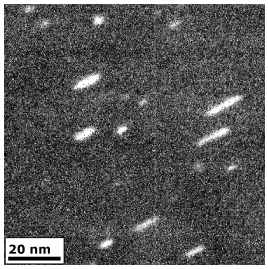

(e) Ni-5Cr, 500 °C, Ni^{4+}

Figure 3: Representative TEM relrod micrographs of Frank loop structures in the irradiated Ni-Cr materials.

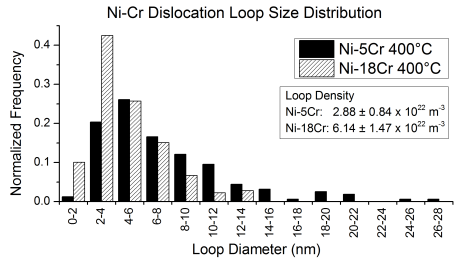

(a) H^+-irradiated Ni-Cr at 400 °C

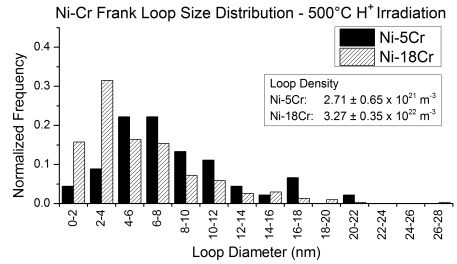

(b) H^+-irradiated Ni-Cr at 500 °C

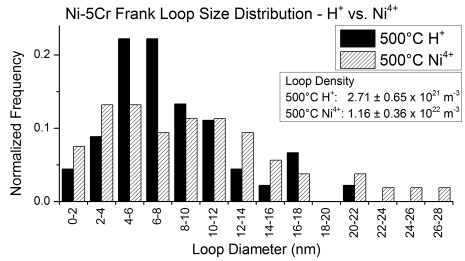

(c) H^+- vs. Ni^{4+}-irradiated Ni-5Cr at 500 °C

Figure 4: Comparison of Frank loop densities and size distributions for the different material conditions investigated. Reported error represents one standard deviation for calculated number densities for individual TEM micrographs.

Cr dumbbell stability approaching 1 eV/dumbbell [47]. Therefore, it is expected that increases in Cr concentration would increase binding energy between dimer interstitials in Ni-Cr alloys, likely on the scale of approximately 0.1 eV for a 10 wt.% change in Cr content. An increase in interstitial binding will increase loop nucleation, which in turn will increase number density and decrease size. This is exactly what is observed when increasing Cr content from 5 to 18 wt.% Cr at 400 °C.

To further assess if this intuitive understanding is plausible, the aforementioned cluster dynamics (CD) model is used to explore if changes in the dimer interstitial binding energy (E_{b2i}, which is the decrease in energy of an interstitial pair relative to isolated interstitials) on the scale of 0.1 eV can yield the type of changes observed in the experiments. It should be noted that this is a highly approximate model and it is being used only to qualitatively assess if the arguments about E_{b2i} are plausible, not provide predictive accuracy. Therefore, E_{b2i} is used as a fitting parameter to explore what changes in this quantity are needed to explain the data. The fitted values are selected to best represent the loop size and number density. For Ni-5Cr the best fit value of E_{b2i} is 0.73 eV and for Ni-18Cr the best fit value of E_{b2i} is 0.9 eV at 400 °C. Figure 5 shows the results of CD model compared with experimental data for both Ni-5Cr and Ni-18Cr at 400 °C. The good agreement for both size and number density suggests that the present simple model can provide useful qualitative guidance. The 0.17 eV change in E_{b2i} is fully consistent with our hypothesis that changes in the nucleation energetics, or equivalently, in E_{b2i}, on the scale of approximately 0.1 eV is responsible for the changes in loop properties with Cr concentration.

3.4. Voids in irradiated Ni-Cr

Voids were imaged using STEM HAADF imaging and differences in the void structures were apparent. Representative images of void structures in the various irradiated Ni-Cr conditions are shown in Figure 6 and histograms comparing the void

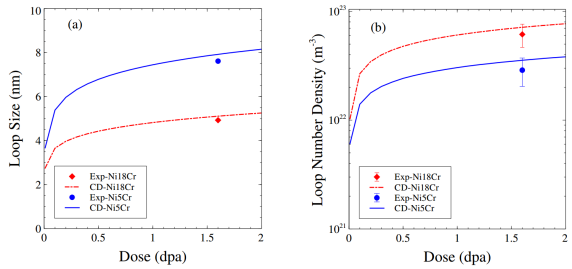

Figure 5: Loop size (a) and number density (b) evolution for Ni-5Cr and Ni-18Cr at 400 °C under proton irradiation. Fitted dimer interstitial binding energy (E_{b2i}) for Ni-5Cr (0.73 eV) and Ni-18Cr (0.9 eV) shows a reasonable coupling between Cr concentration and E_{b2i} (see text for more discussion).

sizes and densities are shown in Figure 7. Void swelling was calculated from the ratio of the volume of the observed voids (assuming spherical geometries) to the total volume analyzed.

Increase in temperature resulted in similar effects for void morphologies as for dislocation loops. Higher temperature irradiations induced a lower density of larger voids. However, this change in morphology with temperature was much more pronounced for voids, with approximately 50× and 3× decrease in the observed densities going from 400 °C to 500 °C irradiations for Ni-5Cr and Ni-18Cr, respectively. Upon high temperature irradiation some voids showed double the diameter of those seen in the lower-temperature irradiated specimens. These results are consistent with observations made in similar systems, and likely originate from increased void nucleation at lower temperatures and from more favorable driving forces for void growth at high temperatures [15, 48].

For the 400 °C irradiation, the void size distributions are similar and the error associated with the calculated densities overlap for the Ni-5Cr and Ni-18Cr, whereas the 500 °C irradiated materials show dramatically different size distributions and an order of magnitude difference in the void densities. The 400 °C proton-irradiated materials are likely more indicative of composition dependence, in which case Cr additions suppresses swelling, likely by changing void nucleation behavior. This conclusion is consistent with results from earlier studies on void swelling binary and ternary Ni-based alloys in which initial swelling is suppressed by Cr additions but steady-state swelling rates are more or less unaffected [12, 14, 15].

The differences in void microstructure resulting from Ni-ion irradiation is also dramatic with a higher density of much smaller voids observed when compared to proton-irradiated materials. This result is consistent with the hypothesis that lower dose rates incur more swelling and larger voids for the same dose, which has been well supported in austenitic steel systems [49]. In this case there is likely a large effect just due to time held at temperature - the Ni-ion irradiations took approximately 4 hours whereas the proton irradiation took a little over 100 hours, giving much more time for point defect diffusion and void agglomeration. The higher density of voids generated in the shorter Ni-irradiation may be indicative that higher disorder caused by in-cascade clustering effects aid in the void nucleation process.

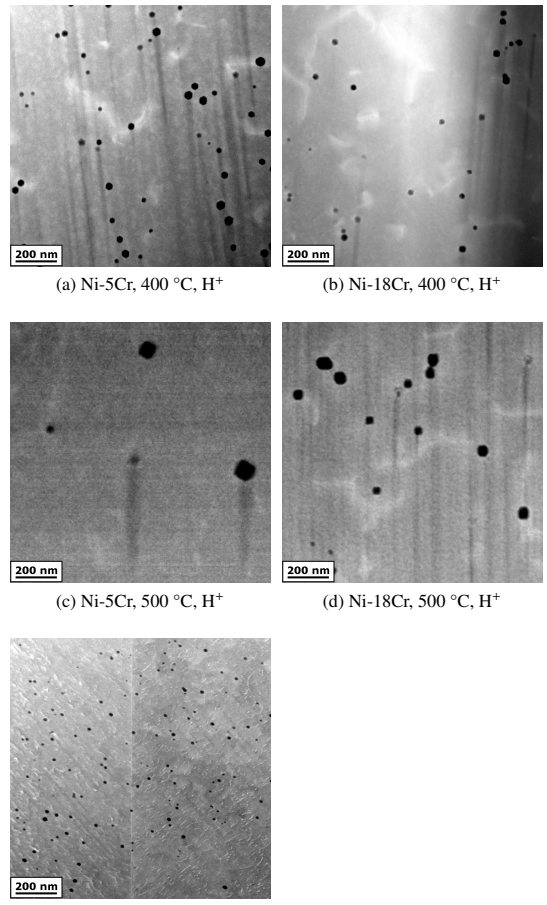

(a) Ni-5Cr, 400 °C, H^+ (b) Ni-18Cr, 400 °C, H^+

(c) Ni-5Cr, 500 °C, H^+ (d) Ni-18Cr, 500 °C, H^+

(e) Ni-5Cr, 500 °C, Ni^{4+}

Figure 6: Representative STEM HAADF images showing void structures in the irradiated Ni-Cr alloys.

4. Conclusions

In this study, the irradiation microstructures of Ni-5Cr and Ni-18Cr model alloys were investigated using analytical transmission electron microscopy techniques. A summary of this analysis is provided in Table 3. Most notably, our results indicate that the irradiation temperature has a distinct effect on the damage morphology. By increasing the proton irradiation temperature from 400 °C to 500 °C, an increase in size and a decrease in density was observed for dislocation loop and voids. This effect is proposed to originate from increased thermal motion of point defects, which results in more defects finding and combining with existing clusters than nucleating new clusters. Cluster dynamic simulations were in good agreement with the most robust experimental observations, and suggested that Cr

Table 3: Summary of the observed Frank loop and void morphologies for all conditions studied.

Condition	Number of Loops Identified	Volume Analyzed (nm^3)	Loop Number Density (m^{-3})	Average Loop Diameter (nm)	Number of Voids Identified	Volume Analyzed (nm^3)	Void Number Density (m^{-3})	Average Void Diameter (nm)	Estimated Swelling
Ni-5Cr, 400 °C, H^+, 1.6 dpa	157	2.15×10^7	$2.88 \pm 0.84 \times 10^{22}$	7.6	176	7.68×10^8	$2.28 \pm 0.71 \times 10^{20}$	26.4	0.30%
Ni-5Cr, 500 °C, H^+, 1.6 dpa	46	8.28×10^7	$2.71 \pm 0.65 \times 10^{21}$	8.7	41	1.32×10^{10}	$4.31 \pm 2.23 \times 10^{18}$	58.7	0.10%
Ni-18Cr, 400 °C, H^+, 1.6 dpa	188	1.23×10^7	$6.14 \pm 1.47 \times 10^{22}$	4.7	204	1.50×10^9	$1.37 \pm 0.57 \times 10^{20}$	24.2	0.05%
Ni-18Cr, 500 °C, H^+, 1.6 dpa	305	3.72×10^7	$3.27 \pm 0.35 \times 10^{22}$	5.6	421	1.28×10^{10}	$3.34 \pm 1.00 \times 10^{19}$	37.7	0.14%
Ni-5Cr, 500 °C, Ni^{4+}, 3.4 dpa	53	1.84×10^7	$1.16 \pm 0.36 \times 10^{22}$	10.1	222	2.15×10^8	$9.93 \pm 1.17 \times 10^{20}$	11.2	0.07%

content might be enhancing dislocation loop nucleation behavior through increasing the stability of the smallest clusters. Assigning interstitial binding energies of 0.73 eV to 0.9 eV for 5 wt.% Cr and 18 wt.% Cr alloys, respectively, resulted in a good fit to the experimental data.

Ni-irradiated Ni-Cr specimens showed higher densities of much smaller voids than the proton-irradiated samples, which is likely a consequence of the much higher dose rate coupled with less time at temperature for defect structures to organize over the shorter course of the Ni irradiation (4h) as compared to proton irradiation (100h). However, the higher density of voids upon Ni-irradiation may be indicative of in-cascade clustering effects aiding in void nucleation. While comparing the effects of proton and heavy ion irradiations is valuable, further study on neutron irradiated Ni-Cr alloys is required, as the ultimate goal of ion irradiations is to emulate neutron damage in the best possible way. Additionally, the alloys that will be employed in nuclear components such as, for example, in molten salt reactor systems will likely not be binary systems. However, this fundamental study of radiation tolerance in binary Ni-Cr alloys gives insight into the mechanisms of defect formation and serves as a basis for comparison for these future studies.

Acknowledgements

Research was sponsored by the US National Science Foundation, Grant No. 1105640. Proton irradiation of Ni-Cr alloys was performed at the UW Ion Beam Laboratory. Ni ion irradiation of Ni-Cr alloys was fully supported by the Division of Materials Science and Engineering, Office of Basic Energy Sciences, U.S. Department of Energy. Sandia National Laboratories is a multi-program laboratory managed and operated by Sandia Corporation, a wholly owned subsidiary of Lockheed Martin Corporation, for the U.S. Department of Energy's National Nuclear Security Administration under contract DE-AC04-94AL85000. Focused ion beam sample preparation was performed at the MaCS Laboratory at the Center for Advanced Energy Studies at Idaho National Laboratory. Scanning and transmission electron microscopy was performed at the University of Wisconsin-Madison Materials Science Center. Funding for SAB was provided by the DOE Office of Nuclear Energy's Nuclear Energy University Programs.

References

[1] J.F. Bates and R.W. Powell. Irradiation-induced swelling in commercial alloys. *Journal of Nuclear Materials*, 2:200–213, 1980.

[2] K. Farrell and N.H. Packan. Damage structure in Nimonic PE16 alloy ion bombarded to high doses and gas levels. *Journal of Nuclear Materials*, 103-104:1059–1062, 1981.

[3] L.E. Thomas and D.S. Gelles. Swelling in commercial Fe-Cr-Ni based alloys under electron irradiation. *Journal of Nuclear Materials*, 109:490–503, 1982.

[4] W.J.S. Yang. Grain boundary segregation in solution-treated Nimonic PE16 during neutron irradiation. *Journal of Nuclear Materials*, 108-109:339–346, 1982.

[5] R.M. Boothby. The microstructure of fast neutron irradiated nimonic PE16. *Journal of Nuclear Materials*, 230(2):148–157, 1996.

[6] R.M. Boothby. 4.04 - Radiation Effects in Nickel-Based Alloys. In Rudy J.M. Konings, editor, *Comprehensive Nuclear Materials*, pages 123–150. Elsevier Inc., 2012.

[7] Y. Guérin, G.S. Was, and S.J. Zinkle. Materials Challenges for Advanced Nuclear Energy Systems. *MRS Bulletin*, 34(January):13, 2009.

[8] T. Yonezawa. 2.08 - Nickel Alloys: Properties and Characteristics. In Rudy J.M. Konings, editor, *Comprehensive Nuclear Materials*, pages 233–266. Elsevier Inc., 2012.

[9] W.D. Manly, J.W. Allen, W.H. Cook, J.H. DeVan, D.A. Douglas, H. Inouye, D.H. Jansen, P. Patriarca, T.K. Roche, G.M. Slaughter, A. Taboada, and G.M. Tolson. Construction Materials for Molten-Salt Reactors. In J.A. Lane, editor, *Fluid-Fueled Reactors*, chapter 13. Addison-Wesley, NY, 1958.

[10] F.A. Garner and W.G. Wolfer. Factors which determine the swelling behavior of austenitic stainless steels. *Journal of Nuclear Materials*, 123:201–206, 1984.

[11] H.R. Brager, F.A. Garner, and M.L. Hamilton. The influence of composition on microstructural evolution and mechanical properties of irradiated Fe-Ni-Cr ternaries. *Journal of Nuclear Materials*, 133-134:594–598, 1985.

[12] T. Muroga, F.A. Garner, and S. Ohnuki. Microstructural investigation of swelling dependence on nickel content in fast neutron-irradiated Fe-Cr-Ni austenitic ternaries. *Journal of Nuclear Materials*, 179-181:546–549, 1991.

[13] F.A. Garner, C.A. Black, and D.J. Edwards. Factors which control the swelling of Fe-Cr-Ni ternary austenitic alloys. *Journal of Nuclear Materials*, 245:124–130, 1997.

[14] J.A. Hudson and S.J. Ashby. Void formation in a binary nickel alloy. Technical report, Atomic Energy Research Establishment, 1974.

[15] F.A. Garner. The possible influence of order-disorder transformations on the swelling of 85Ni-15Cr nichrome alloy. *Journal of Nuclear Materials*, 148(3):288–293, 1987.

[16] T. M. Robinson and M. L. Jenkins. Heavy-ion irradiation of nickel and nickel alloys. *Philosophical Magazine A*, 43(4):999–1015, 1981.

[17] C.M. Barr, L. Barnard, J.E. Nathaniel, K. Hattar, K.A. Unocic, I. Szlufarska, D.D. Morgan, and M.L. Taheri. Grain boundary character dependence of radiation-induced segregation in a model Ni-Cr alloy. *Journal of Materials Research*, 30(09):1290–1299, 2015.

[18] G.S. Was and T.R. Allen. Intercomparison of microchemical evolution under various types of particle irradiation. *Journal of Nuclear Materials*, 205(Oct 1993):332–338, 1993.

[19] G.S. Was, J.T. Busby, T.R. Allen, E.A. Kenik, A. Jenssen, S.M. Bruemmer, J. Gan, A.D. Edwards, P.M. Scott, and P.L. Andresen. Emulation of neutron irradiation effects with protons: validation of principle. *Journal of Nuclear Materials*, 300:198–216, 2002.

[20] T.R. Allen, J.I. Cole, J. Gan, G.S. Was, R. Dropek, and E.A. Kenik. Swelling and radiation-induced segregation in austenitic alloys. *Journal of Nuclear Materials*, 342(1-3):90–100, jun 2005.

[21] G.S. Was and R.S. Averback. 1.07 - Radiation Damage Using Ion Beams.

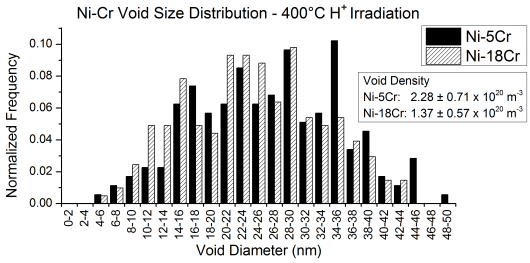

(a) H^+-irradiated Ni-Cr at 400 °C

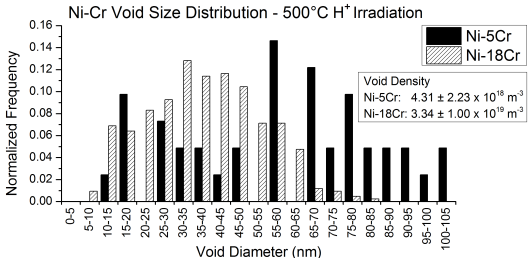

(b) H^+-irradiated Ni-Cr at 500 °C

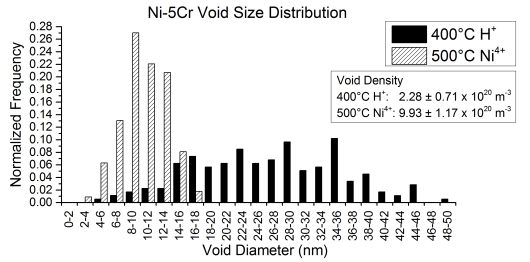

(c) H^+- vs. Ni^{4+}-irradiated Ni-5Cr at 400 and 500 °C, respectively.

Figure 7: Comparison of void densities and size distributions for the different material conditions investigated. Reported error represents one standard deviation for calculated number densities for individual STEM micrographs.

In Rudy J.M. Konings, editor, *Comprehensive Nuclear Materials*, pages 195–221. Elsevier Inc., 2012.

[22] M.J. Swenson and J.P. Wharry. The comparison of microstructure and nanocluster evolution in proton and neutron irradiated Fe-9%Cr ODS steel to 3 dpa at 500 °C. *Journal of Nuclear Materials*, 467:97–112, 2015.

[23] S. Ishino, N. Sekimura, K. Murakami, and H. Abe. Some remarks on in-situ studies using TEM-heavy-ion accelerator link from the stand point of extracting radiation damage caused by fast neutrons. *Journal of Nuclear Materials*, pages 1–8, 2015.

[24] D.J. Edwards, E.P. Simonen, and S.M. Bruemmer. Evolution of fine-scale defects in stainless steels neutron-irradiated at 275 °C. *Journal of Nuclear Materials*, 317(1):13–31, apr 2003.

[25] J. Gan, E.P. Simonen, S.M. Bruemmer, L. Fournier, B.H. Sencer, and G.S. Was. The effect of oversized solute additions on the microstructure of 316SS irradiated with 5 MeV Ni++ ions or 3.2 MeV protons. *Journal of Nuclear Materials*, 325(2-3):94–106, feb 2004.

[26] T.R. Allen. *Modeling of radiation-induced segregation in austenitic Fe-Cr-Ni alloys*. PhD thesis, University of Michigan, 1997.

[27] J.F. Ziegler, J.P. Biersack, and M.D. Ziegler. *SRIM - The Stopping and Range of Ions in Matter*. Ion Implantation Press, 2008.

[28] R.E. Stoller, M.B. Toloczko, G.S. Was, A.G. Certain, S. Dwaraknath, and F.A. Garner. On the use of SRIM for computing radiation damage exposure. *Nuclear Instruments and Methods in Physics Research Section B: Beam Interactions with Materials and Atoms*, 310:75–80, 2013.

[29] C.A. Schneider, W.S. Rasband, and K.W. Eliceiri. NIH Image to ImageJ: 25 years of image analysis. *Nature Methods*, 9(7):671–675, 2012.

[30] R.F. Egerton. *Electron Energy-Loss Spectroscopy in the Electron Microscope*. Springer, third edition, 2011.

[31] A.H. Duparc, C. Moingeon, N. Smetniansky-De-Grande, and A. Barbu. Microstructure modelling of ferritic alloys under high flux 1 MeV electron irradiations. *Journal of Nuclear Materials*, 302(2-3):143–155, 2002.

[32] C. Pokor, Y. Brechet, P. Dubuisson, J. P. Massoud, and a. Barbu. Irradiation damage in 304 and 316 stainless steels: Experimental investigation and modeling. Part I: Evolution of the microstructure. *Journal of Nuclear Materials*, 326(1):19–29, 2004.

[33] John A. Brinkman. On the nature of radiation damage in metals. *Journal of Applied Physics*, 25(8):961–970, 1954.

[34] G.S. Was. *Fundamentals of Radiation Materials Science*. Springer, 2007.

[35] J. Gan, G.S. Was, and R.E. Stoller. Modeling of microstructure evolution in austenitic stainless steels irradiated under light water reactor condition. *Journal of Nuclear Materials*, 299:53–67, 2001.

[36] N.Q. Lam and L. Dagens. Calculations of the properties of single and multiple defects in nickel. *Journal of Physics F: Metal Physics*, 16(10):1373, 1986.

[37] L. Zhao, R. Najafabadi, and D. J. Srolovitz. Determination of vacancy and atomic diffusivities in solid solution alloys. *Acta Materialia*, 44(7):2737–2749, 1996.

[38] P. Ehrhart, P. Jung, H. Schultz, and H. Ullmaier. *Atomic Defects in Metals*. Springer, 1991.

[39] E.H. Megchiche, C. Mijoule, and M. Amarouche. First principles calculations of vacancy-vacancy interactions in nickel: thermal expansion effects. *Journal of Physics: Condensed Matter*, 22(48):485–502, 2010.

[40] J.T. Busby, G.S. Was, and E.A. Kenik. Isolating the effect of radiation-induced segregation in irradiation-assisted stress corrosion cracking of austenitic stainless steels. *Journal of Nuclear Materials*, 302(1):20–40, apr 2002.

[41] H.K. Zhang, Z. Yao, M.R. Daymond, and M.A. Kirk. Elevated temperature irradiation damage in CANDU spacer material Inconel X-750. *Journal of Nuclear Materials*, 445(1-3):227–234, 2014.

[42] N. Azam, L. LeNaour, and J. Delaplace. Évolution de la densité de dislocations dans des aciers austénitiques du type 316 L irradiés par des ions Ni+ de moyenne energie. *Journal of Nuclear Materials*, 49:197–208, 1973.

[43] H.R. Brager and J.L. Straalsund. Defect Development in Neutron Irradiated Type 316 Stainless Steel. *Journal of Nuclear Materials*, 46:134–158, 1973.

[44] F.A. Garner. Evolution of microstructure in face-centered cubic metals during irradiation. *Journal of Nuclear Materials*, 205:98–117, 1993.

[45] B.H. Sencer, G.S. Was, M. Sagisaka, Y. Isobe, G.M. Bond, and F.A. Garner. Proton irradiation emulation of PWR neutron damage microstructures in solution annealed 304 and cold-worked 316 stainless steels. *Journal of Nuclear Materials*, 323(1):18–28, 2003.

[46] A. Etienne, M. Hernández-Mayoral, C. Genevois, B. Radiguet, and P. Pareige. Dislocation loop evolution under ion irradiation in austenitic stainless steels. *Journal of Nuclear Materials*, 400(1):56–63, 2010.

[47] J.D. Tucker, R. Najafabadi, T.R. Allen, and D. Morgan. Ab initio-based diffusion theory and tracer diffusion in Ni-Cr and Ni-Fe alloys. *Journal of Nuclear Materials*, 405(3):216–234, oct 2010.

[48] J.F. Stubbins and F.A. Garner. Swelling and microstructure of high purity nickel irradiated with fast neutrons in EBR-II. *Journal of Nuclear Materials*, 191-194:1295–1299, 1992.

[49] T. R. Allen, J. I. Cole, C. L. Trybus, D. L. Porter, H. Tsai, F.A. Garner, E.A. Kenik, T. Yoshitake, and J. Ohta. The effect of dose rate on the response of austenitic stainless steels to neutron radiation. *Journal of Nuclear Materials*, 348(1-2):148–164, 2006.

Observations of anomalous radiation-enhanced grain boundary migration and solute segregation in Ni-Cr binary alloys

Samuel A. Briggs[a,*], Janne Pakarinen[a,b], Dane D. Morgan[a], Kumar Sridharan[a]

[a] *University of Wisconsin-Madison, 1415 Engineering Drive, Madison, WI 53706*
[b] *SKC•CEN Belgian Nuclear Research Centre, Boeretang 200, B-2400 Mol, Belgium*

Abstract

Two binary Ni-Cr alloys with 5 wt.% Cr and 18 wt.% Cr were irradiated using 2 MeV protons at 500°C to 1.6 dpa to investigate radiation-induced grain boundary segregation (GB-RIS). Scanning transmission electron microscopy coupled with energy dispersive x-ray spectroscopy was applied to study GB-RIS at specific grain boundaries. Asymmetric GB-RIS profiles with micron-scale Cr depleted regions were observed at all studied grain boundaries with the exception of Σ3 coincidence site lattice (CSL) boundaries. The Cr depleted regions were denuded in voids. *Ex situ* electron backscatter diffraction analysis of unirradiated specimens, thermally aged for the same time and temperature as the irradiation, showed that grain growth occurred in these alloy systems. It is proposed that the asymmetric GB-RIS profiles were due to rapid radiation-enhanced random walk grain boundary migration effects in a pure binary model alloy system over the course of the 100 hour irradiation at 500°C.

Keywords: radiation damage, grain boundary segregation, grain boundary migration, nickel alloys, scanning/transmission electron microscopy

Ni-based alloys are prevalent in high-temperature applications due to their excellent high temperature creep strength and have shown promise for nuclear applications since fast reactor development programs in the '70s and '80s [1–6]. Ultimately their in-core applications were limited by a perceived susceptibility to irradiation-induced embrittlement [6]. However, there has been a resurgence of interest regarding radiation damage effects in Ni-based alloys due to, for example, their excellent chemical compatibility with molten salt reactor environments [7, 8]. Chromium, typically alloyed to increase oxidation resistance, is detrimental to the performance of these systems as it is preferentially leached by the salt [9]. As such, it is necessary to understand how radiation damage affects Ni-based alloys with low Cr content.

Radiation-induced solute segregation at grain boundaries (GB-RIS), in which alloying elements either enrich or deplete locally at grain boundaries, is caused by differences in the diffusivities of alloying elements by vacancy and interstitial transport. In Ni-based alloys and austenitic steels, Cr typically depletes at the grain boundaries [10–14]. The Cr depletion is considered as a deleterious effect as it can compromise a material's corrosion resistance and result in increased susceptibility to irradiation-assisted stress corrosion cracking (IASCC) [15, 16]. Additional known microstructural transformations associated with grain boundaries are grain boundary migration and grain growth. Both of these transformations are typically considered as thermally-activated, diffusion-driven processes and, as such, can be affected by the increased diffusion resulting from irradiation [17–20]. Usually there is a driving force associated with grain growth which tends to reduce the overall grain boundary area, but grain boundary mobility via different mechanisms is also possible [21, 22]. Grain boundary migration is difficult to study by *ex situ* experiments, which only capture snapshots of grain boundary position. Furthermore, *in situ* transmission electron microscopy experiments are prone to the influence of surface effects due to thin specimen geometries.

In this study we have investigated GB-RIS in Ni-Cr model alloys upon proton irradiation at 500°C to clarify the solute segregation mechanism relevant for high-temperature nuclear applications. Our observations showed evidence of pronounced grain boundary migration in combination with GB-RIS which may have an impact on the current understanding of radiation enhanced diffusion in these materials.

The two binary Ni-Cr alloys used in this study were prepared with nominal composition of 5 wt.% chromium and 18 wt.% chromium (referred to henceforth as Ni-5Cr and Ni-18Cr, respectively) by vacuum arc melting and casting in a water-cooled copper hearth. These compositions represent binary analogs to a broad family of Ni-based alloys which contain Cr primarily for high-temperature oxidation resistance and creep strength. The specimens were recrystallized by cold-rolling to 50% of their original thickness followed by annealing for one hour at 1050°C. Recrystallization was confirmed using electron backscatter diffraction (EBSD) mapping and the grain size was determined to be on the order of 100-150 μm for both Ni-5Cr and Ni-18Cr. Material compositions were verified by inductively coupled plasma optical omission spectroscopy (ICP-

*Corresponding author
Email addresses: sabriggs2@wisc.edu (Samuel A. Briggs), jpakarin@sckcen.com (Janne Pakarinen), ddmorgan@wisc.edu (Dane D. Morgan), kumar@engr.wisc.edu (Kumar Sridharan)

OES), the results of which are shown in Table 1. The relatively pure composition of the alloys eliminates the effects of other alloying elements and allows for a better understanding of GB-RIS of the binary system. Both samples were irradiated to a dose of 1.6 displacements per atom (dpa) at 500°C at the University of Wisconsin Ion Beam Lab (UW-IBL) (See details from [23]). The irradiation time required to achieve this level of damage was approximately 100 hours.

Table 1: Summary of bulk alloy compositions for Ni-5Cr and Ni-18Cr in wt.% as determined by the ICP-OES technique.

	Cr	Ni	C	Si	Co	P	S	Other Minors
Ni-5Cr	5.00	94.94	0.007	0.01	0.01	<0.005	0.005	<0.01
Ni-18Cr	17.90	82.02	0.016	0.01	0.01	<0.005	0.006	<0.01

Scanning transmission electron microscopy coupled with energy dispersive x-ray spectroscopy (STEM/EDS) was applied for collecting RIS profiles for the selected grain boundaries. The STEM samples were prepared using the focused ion beam (FIB) lift-out method at the Microscopy and Characterization Suite located at the Center for Advanced Energy Studies at Idaho National Laboratory. Coarse-trenched sample lamellas were mounted on copper Omniprobe FIB grids and cleaned with a 5 kV Ga FIB beam. As a final step, low-kV Ar nanomilling was applied to minimize FIB-induced damage. The misorientation of the boundaries was determined using the transmission Kikuchi diffraction technique using the Zeiss LEO 1550 scanning electron microscope (SEM) at the University of Wisconsin-Madison Materials Science Center (UW-MSC) [24, 25]. Drift-corrected EDS line scans were acquired on the FEI Titan aberration-corrected (S)TEM at UW-MSC using a 200kV electron beam. EDS spectral images were collected on the FEI Talos F200X FEG-S/TEM at Oak Ridge National Laboratory's Low Activation Materials Development and Analysis (LAMDA) facility. Specimens were tilted prior to the spectrum data collection in such a way that the grain boundaries were in an "edge-on" (boundary plane parallel to incident electron beam) condition and that similar diffraction conditions were met for both grains comprising the boundary, while minimizing shadowing of the EDS detector.

The materials were first investigated in their as-received condition. EDS line scans showed no GB-RIS prior to irradiation - all measured segregation is thus a result of the high-temperature proton irradiation.

Both proton-irradiated Ni-5Cr and Ni-18Cr materials showed asymmetric GB-RIS behavior on the scale of several microns. An example of such an EDS line scan across grain boundary is shown in Figure 1 for Ni-18Cr. At the grain boundary, Cr depleted rapidly from its bulk composition (~ 18 wt.%) to 13 wt.% and appeared to remain depleted for several microns on the other side of the grain boundary. To further examine the extent of this asymmetric broad GB-RIS profile, STEM-EDS spectral images were collected for the grain boundaries, examples of which are shown in Figures 2 and 3a for high angle grain boundaries (HAGB) of Ni-18Cr and Ni-5Cr, respectively. The spectral images show extended Cr depletion in the vicinity of the boundary for both compositions. Interestingly, as is

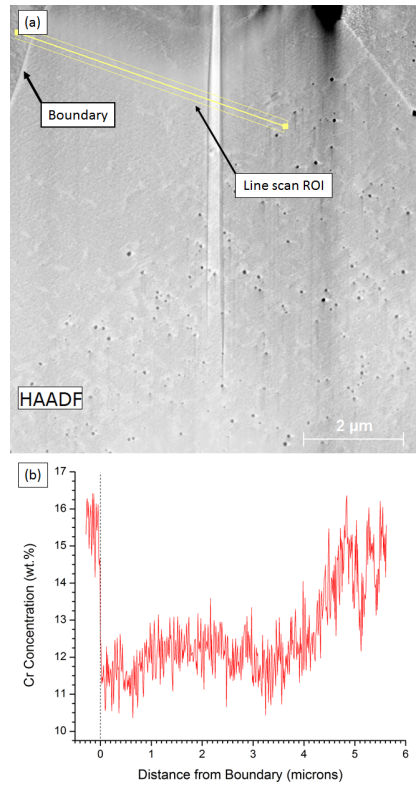

Figure 1: (a) STEM image of a typical grain boundary for Ni-18Cr alloy shows a region denuded of radiation induced defects. The region of interest (ROI) for the line scan is shown in yellow. (b) STEM/EDS line scan profile across FIB-prepared lamella showing micron-scale regions of Cr depletion on one side of the grain boundary. Grain boundary considered above is a Σ7 CSL boundary.

evident from Figure 2, the Cr depleted region was almost completely denuded of any physical irradiation damage. Several grain boundaries with different misorientation angles were examined (summarized in Table 2) and all high angle grain boundaries showed similar wide and asymmetric GB-RIS profiles. The only exceptions to this behavior were Σ3 CSL boundaries where no depletion or denuded zones were observed, shown in Figure 3b.

Asymmetric GB-RIS profiles have been previously reported for ternary Fe-Cr-Ni alloys and austenitic steels [26, 27]. These GB-RIS profiles were usually observed during *in situ* TEM under high-temperature electron irradiation with a much higher dose rate than was applied in the present study (~ 10^{-4} dpa/s with electrons [27] vs. ~ 10^{-6} dpa/s with protons). Rate theory models have also been applied to study the asymmetric GB-RIS profiles [28, 29]. Nonetheless, the reported profiles show sharper Cr depletion as compared to the micron-scale denuded zones in proton-irradiated Ni-5Cr and Ni-18Cr observed in this study.

Due to this discrepancy, one must question whether or not this behavior can actually be attributed to a grain boundary migration effect. In pure Ni the grain boundary mobility has

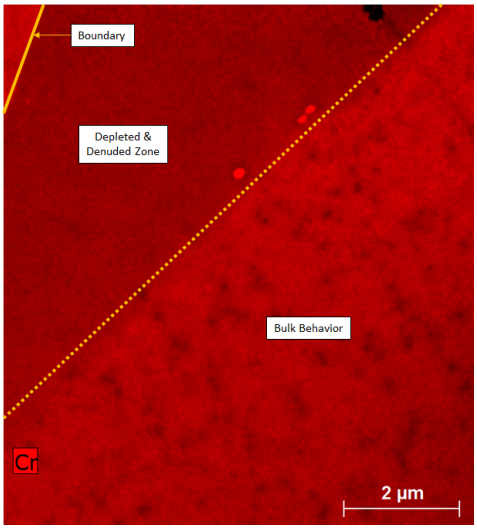

Figure 2: STEM/EDS spectral imaging shows that Cr-depleted region correlates with void denuded zone. Scanned area is the same ROI as in Figure 1. Areas with more Cr x-ray counts, corresponding to a high Cr content, appear brighter.

been calculated using molecular dynamics simulations and is predicted to be between 4E-8 and 4E-7 $m^4/J \cdot s$ at 1400K for high-angle grain boundaries [30–34]. Assuming Arrhenius behavior, this corresponds to a mobility of between 5.3E-9 and 5.3E-8 $m^4/J \cdot s$ at 773K (the irradiation temperature of this study). Assuming a diffusion coefficient D according to Eq. 1:

$$D = \frac{2Mk_BT}{A_{GB}} \tag{1}$$

where M is the grain boundary mobility, k_B is the Boltzmann constant T is temperature and A_{GB} is the grain boundary area (assumed unity), and the migration length scale L is given by Eq. 2:

$$L \approx \sqrt{Dt} \tag{2}$$

with time $t = 100$ hrs corresponding to time at temperature during irradiation, the expected migration length scale is on the order of 6.5 to 20 μm, which is on the same scale as the observed Cr-depleted regions in this work. Furthermore, irradiation may enhance diffusion effects. Considering the results of recent density-functional theory (DFT) calculations demonstrating that Cr has little effect on the properties of grain boundaries in Ni alloys, these mobilities are likely valid for our binary Ni-Cr alloys as well [35].

Table 2: Summary of grain boundaries studied in the present work. It is shown that large depleted zones were seen for every grain boundary except for Σ3 boundaries.

Composition	Misorientation	GB Type	Depleted Zone Observed?	Approx. Cr Depletion (wt.%)
Ni-5Cr	55.5°	HAGB	Yes	-2.5%
	48°	HAGB	Yes	-2.5%
	60°	Σ3	No	-3%
	56°	HAGB	Yes	-3%
	46.5°	HAGB	Yes	-2.5%
Ni-18Cr	38°	HAGB	Yes	-4.5%
	36.5°	HAGB	Yes	-5%
	26°	HAGB	Yes	-4%
	36°	Σ7	Yes	-4.5%
	60°	Σ3	No	-4%

Grain boundary mobilities less than those theoretically predicted are generally seen in practice due to the pinning effects of defects and impurities, which inhibit grain boundary motion. In an attempt to confirm or refute whether grain boundary migration is occurring in the model Ni-Cr system studied, a thermal annealing study without irradiation was conducted. Samples of each composition were first analyzed via EBSD mapping to characterize the initial grain positions. These samples were then encapsulated in quartz tubes in an Ar atmosphere (in order to maintain the surface quality) and annealed for 100 hours at 500°C to simulate the thermal history of the irradiated samples. EBSD mapping was then repeated at the same location as before annealing to observe if the grain boundaries had migrated.

Figure 3c overlays the pre- and post-anneal EBSD maps from the Ni-5Cr specimen. Grains of a given orientation are highlighted in a certain color and grain boundaries are shown as the interfaces between these grains. It can be seen that the grains did indeed grow as a result of the annealing. As such it seems reasonable to conclude continuous solute segregation and denudation in the vicinity of the interface during grain boundary migration over the course of the 100 hour irradiation treatment can account for the observed behavior.

Another interesting aspect of the observed profiles is that there does not seem to be significant recovery to bulk behavior far away from the grain boundary. One can estimate the time it takes for the grain boundary to traverse the observed depleted region by studying the gradient of Cr back-diffusion into this depleted region. To do this STEM/EDS line scans were acquired perpendicularly across the edge of the depleted region opposite the grain boundary. The length scale L of Cr back diffusion, given by the width of the region where Cr concentration transitions from its bulk value to the observed depleted value, was found to range from 0.2 - 0.6 μm. From this an approximate timescale for grain boundary migration across this region can be calculated from Equation 2. An effective diffusion coefficient for Cr at 500°C in this system is calculated to be 3.29E-16m^2/s by assuming Arrhenius behavior, with $D_0 = 2.26$E-4m^2/s and activation energy $Q = 2.89eV$ [36], and by assuming an irradiation enhancement factor of 10^7 [37]. This yields a timescale for grain boundary transit across the depleted region of 2 to 20 minutes. This approximation seems to support a radiation-enhanced random-walk mechanism for grain boundary motion and may be the most rapid grain migration ever reported. If the grain boundary had been moving in a single direction during the course of the irradiation it would be expected that Cr would segregate to the interface and that the region immediately around the boundary would become denuded, but that radiation-enhanced diffusion effects would support the formation of voids and cause Cr content to recover to bulk values in that area once the boundary has changed positions. In order to maintain such

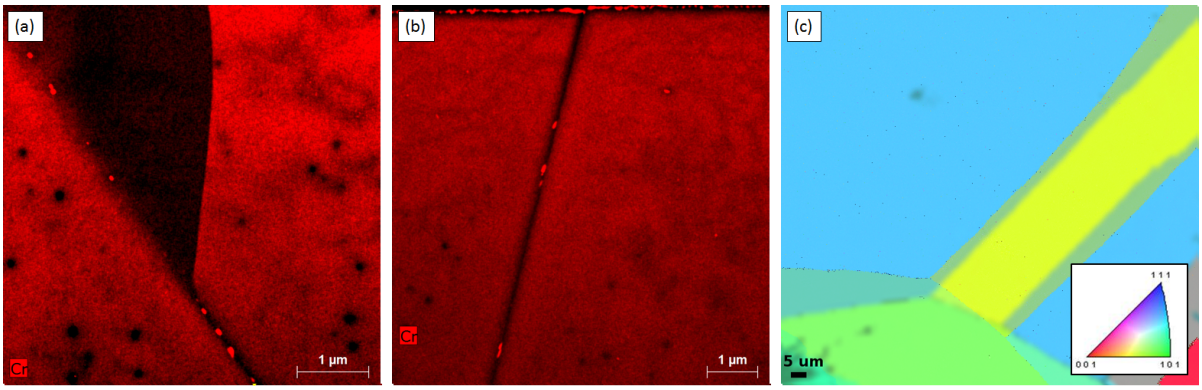

Figure 3: (a) Spectral image showing Cr depletion behavior at a high-angle grain boundary (HAGB) in Ni-5Cr. (b) Spectral image showing expected RIS behavior (no grain boundary migration effects) at a Σ3 CSL boundary in Ni-5Cr. (c) Pre- and post-anneal EBSD maps of Ni-5Cr overlaid on one another indicating micron-scale differences in grain boundary positions after furnace treatment.

a large depleted and denuded region the boundary must travel back and forth across this volume and prevent this sort of recovery behavior. It is possible that the grain boundary's area of influence is very localized at first but that defects that would normally pin grain boundary motion are absorbed by the interface; as such the grain boundary is allowed to move through an increasing volume as these pinning features are removed.

The observed phenomena is obviously very rate dependent - the boundary must move at a rate at which local segregation and denudation is allowed to occur. This can also explain why this behavior is not seen at the Σ3 twin boundaries. While grain boundary mobility is fairly independent of misorientation angle for high angle grain boundaries, coherent twins have been shown to be essentially immobile, while incoherent twins can have mobilities up to an order of magnitude higher than other grain boundary types [34].

To summarize and conclude:

- Cr depleted regions that were also denuded in radiation-induced defect structures on the order a few microns in width were observed on one side of several grain boundaries in Ni-5Cr and Ni-18Cr specimens irradiated with protons to 1.6 dpa at 500°C.
- These regions are suspected to be caused by grain boundary migration during irradiation, but differ from profiles observed in electron irradiations in similar systems. This is speculated to be due to the presence of fewer obstacles to grain boundary motion and prolonged irradiations at a lower dose rate.
- Lack of significant recovery to bulk behavior at locations far from the final grain boundary position seems to suggest an extremely rapid, oscillatory, random-walk grain boundary migration mechanism as opposed to grain growth in a single direction.
- The observed behavior is not seen at Σ3 grain boundaries due to large differences in mobility compared to other CSL and high angle grain boundaries.

Acknowledgements

Research was sponsored by the US National Science Foundation, Grant No. 1105640. Proton irradiation of NiCr alloys was performed at the UW Ion Beam Laboratory. Focused ion beam sample preparation was performed at the MaCS Laboratory at the Center for Advanced Energy Studies at Idaho National Laboratory. Scanning and transmission electron microscopy was performed at the University of Wisconsin-Madison Materials Science Center and at the LAMDA facility at Oak Ridge National Laboratory. Funding for SAB was provided by the DOE Office of Nuclear Energy's Nuclear Energy University Programs.

References

[1] J.F. Bates and R.W. Powell. Irradiation-induced swelling in commercial alloys. *Journal of Nuclear Materials*, 2:200–213, 1980.

[2] K. Farrell and N.H. Packan. Damage structure in Nimonic PE16 alloy ion bombarded to high doses and gas levels. *Journal of Nuclear Materials*, 103-104:1059–1062, 1981.

[3] L.E. Thomas and D.S. Gelles. Swelling in commercial Fe-Cr-Ni based alloys under electron irradiation. *Journal of Nuclear Materials*, 109:490–503, 1982.

[4] W.J.S. Yang. Grain boundary segregation in solution-treated Nimonic PE16 during neutron irradiation. *Journal of Nuclear Materials*, 108-109:339–346, 1982.

[5] R. M. Boothby. The microstructure of fast neutron irradiated nimonic PE16. *Journal of Nuclear Materials*, 230(2):148–157, 1996.

[6] R.M. Boothby. 4.04 - Radiation Effects in Nickel-Based Alloys. In Rudy J.M. Konings, editor, *Comprehensive Nuclear Materials*, pages 123–150. Elsevier Inc., 2012.

[7] Y. Guérin, G.S. Was, and S.J. Zinkle. Materials Challenges for Advanced Nuclear Energy Systems. *MRS Bulletin*, (January):13, 2009.

[8] T. Yonezawa. 2.08 - Nickel Alloys: Properties and Characteristics. In Rudy J.M. Konings, editor, *Comprehensive Nuclear Materials*, pages 233–266. Elsevier Inc., 2012.

[9] W.D. Manly, J.W. Allen, W.H. Cook, J.H. DeVan, D.A. Douglas, H. Inouye, D.H. Jansen, P. Patriarca, T.K. Roche, G.M. Slaughter, A. Taboada, and G.M. Tolson. Construction Materials for Molten-Salt Reactors. In J.A. Lane, editor, *Fluid-Fueled Reactors*, chapter 13. Addison-Wesley, NY, 1958.

[10] T.R. Allen. *Modeling of radiation-induced segregation in austenitic Fe-Cr-Ni alloys*. PhD thesis, University of Michigan, 1997.

[11] T.R. Allen, J.I. Cole, J. Gan, G.S. Was, R. Dropek, and E.A. Kenik. Swelling and radiation-induced segregation in austentic alloys. *Journal of Nuclear Materials*, 342(1-3):90–100, jun 2005.

[12] T.R. Allen, L. Tan, G.S. Was, and E.A. Kenik. Thermal and radiation-induced segregation in model Ni-base alloys. *Journal of Nuclear Materials*, 361(2-3):174–183, apr 2007.

[13] M. Nastar and F. Soisson. 1.18 - Radiation-Induced Segregation. In Rudy J.M. Konings, editor, *Comprehensive Nuclear Materials*, pages 471–496. Elsevier Inc., 2012.

[14] C.M. Barr, G.A. Vetterick, K.A. Unocic, K. Hattar, X. Bai, and M.L. Taheri. Anisotropic radiation-induced segregation in 316L austenitic stainless steel with grain boundary character. *Acta Materialia*, 67:145–155, apr 2014.

[15] G.S. Was and S.M. Bruemmer. Effects of irradiation on intergranular stress corrosion cracking. *Journal of Nuclear Materials*, 216:326–347, oct 1994.

[16] P. Scott. A review of irradiation assisted stress corrosion cracking. *Journal of Nuclear Materials*, 211:101–122, 1994.

[17] B.N. Singh and T. Leffers. Grain boundary migration during 1 MeV electron irradiation. *Scripta Metallurgica*, 8:549–552, 1974.

[18] Dale Alexander and Gary Was. Thermal-spike treatment of ion-induced grain growth: Theory and experimental comparison. *Physical Review B*, 47(6):2983–2994, 1993.

[19] D. Kaoumi, a. T. Motta, and R. C. Birtcher. A thermal spike model of grain growth under irradiation. *Journal of Applied Physics*, 104(7):1–13, 2008.

[20] Eric R. Homer, Elizabeth a. Holm, Stephen M. Foiles, and David L. Olmsted. Trends in grain boundary mobility: Survey of motion mechanisms. *Jom*, 66(1):114–120, 2014.

[21] G. Gottstein and L.S. Shvindlerman. *Grain Boundary Migration in Metals*. CRC Press, 1999.

[22] Zachary T Trautt, Moneesh Upmanyu, and Alain Karma. Interface mobility from interface random walk. *Science (New York, N.Y.)*, 314(5799):632–5, oct 2006.

[23] S.A. Briggs, C.M. Barr, J. Pakarinen, M. Mahmivand, D.D. Morgan, M.L. Taheri, and K. Sridharan. Observations of defect structure evolution in proton and Ni ion irradiated Ni-Cr binary alloys. *Journal of Nuclear Materials*, 2016.

[24] R.R. Keller and R.H. Geiss. Transmission EBSD from 10 nm domains in a scanning electron microscope. *Journal of Microscopy*, 245(3):245–251, mar 2012.

[25] P.W. Trimby. Orientation mapping of nanostructured materials using transmission Kikuchi diffraction in the scanning electron microscope. *Ultramicroscopy*, 120:16–24, sep 2012.

[26] K. Nakata and I. Masaoka. Solute segregation along non-migrated and migrated grain boundaries during electron irradiation in austenitic stainless steels. *Journal of Nuclear Materials*, 150:186–193, 1987.

[27] S. Watanabe, N. Sakaguchi, N. Hashimoto, and H. Takahashi. Quantitative studies of irradiation-induced segregation and grain boundary migration in Fe-Cr-Ni alloy. *Journal of Nuclear Materials*, 224:158–168, 1995.

[28] S. Watanabe, N. Sakaguchi, N. Hashimoto, M. Nakamura, H. Takahashi, C. Namba, and N.Q. Lam. Radiation-induced segregation accompanied by grain boundary migration in austenitic stainless steel. *Journal of Nuclear Materials*, 232:113–118, 1996.

[29] N. Sakaguchi, S. Watanabe, and H. Takahashi. A new model for radiation-induced grain boundary segregation with grain boundary movement in concentrated alloy system. *Journal of Materials Science*, 40(4):889–893, 2005.

[30] Koenraad G F Janssens, D.L. Olmsted, Elizabeth a Holm, Stephen M Foiles, Steven J Plimpton, and Peter M Derlet. Computing the mobility of grain boundaries. *Nature materials*, 5(February):124–127, 2006.

[31] S Foiles and J Hoyt. Computation of grain boundary stiffness and mobility from boundary fluctuations. *Acta Materialia*, 54(12):3351–3357, jul 2006.

[32] Hao Zhang, David J. Srolovitz, Jack F. Douglas, and James a. Warren. Atomic motion during the migration of general [001] tilt grain boundaries in Ni. *Acta Materialia*, 55(13):4527–4533, aug 2007.

[33] D.L. Olmsted, S.M. Foiles, and E.A. Holm. Survey of computed grain boundary properties in face-centered cubic metals: I. Grain boundary energy. *Acta Materialia*, 57(13):3694–3703, aug 2009.

[34] D.L. Olmsted, E.A. Holm, and S.M. Foiles. Survey of computed grain boundary properties in face-centered cubic metalsâĂŤII: Grain boundary mobility. *Acta Materialia*, 57(13):3704–3713, aug 2009.

[35] V.I. Razumovskiy, a.Y. Lozovoi, and I.M. Razumovskii. First-principles-aided design of a new Ni-base superalloy: Influence of transition metal alloying elements on grain boundary and bulk cohesion. *Acta Materialia*, 82:369–377, jan 2015.

[36] J.D. Tucker, R. Najafabadi, T.R. Allen, and D. Morgan. Ab initio-based diffusion theory and tracer diffusion in Ni-Cr and Ni-Fe alloys. *Journal of Nuclear Materials*, 405(3):216–234, oct 2010.

[37] F. Christien and a. Barbu. Modelling of copper precipitation in iron during thermal aging and irradiation. *Journal of Nuclear Materials*, 324:90–96, 2004.

REFERENCES

[1] U.S. DOE: Office of Nuclear Energy. 2015. Light Water Reactor Sustainability Program: Intergrated Program Plan, INL/EXT-11-23452. Tech. Rep. April, U.S. DOE: Office of Nuclear Energy.

[2] OECD Nuclear Energy Agency. 2014. Technology Roadmap Update for Generation IV Nuclear Energy Systems. Tech. Rep., OECD Nuclear Energy Agency.

[3] Gauntt, R., D. Kalinich, J. Cardoni, J. Phillips, A. Goldmann, S. Pickering, M. Francis, K. Robb, L. Ott, D. Wang, C. Smith, S. St.Germain, D. Schwieder, and C. Phelan. 2012. Fukushima Daiichi accident study (Status as of April 2012) SAND2012-6173. Tech. Rep. August, Sandia National Laboratories, Albuquerque, NM.

[4] Carmack, J., F. Goldner, B.-S. Shannon M, and L.L. Snead. 2013. Overview of the U.S. DOE accident tolerant fuel development program, INL/CON-13-29288. In *Lwr fuel performance meeting: Top fuel 2013*, 734–739. Idaho National Laboratory.

[5] Pint, B.A., K.A. Terrani, M.P. Brady, T. Cheng, and J.R. Keiser. 2013. High temperature oxidation of fuel cladding candidate materials in steam-hydrogen environments. *Journal of Nuclear Materials* 440(1-3):420–427.

[6] Terrani, K.A., S.J. Zinkle, and L.L. Snead. 2013. Advanced oxidation-resistant iron-based alloys for LWR fuel cladding. *Journal of Nuclear Materials* 448(1-3): 420–435.

[7] Zinkle, S.J., and G.S. Was. 2013. Materials challenges in nuclear energy. *Acta Materialia* 61(3):735–758.

[8] Little, E.A. 1979. Void-swelling in irons and ferritic steels. I. Mechanisms of swelling suppression. *Journal of Nuclear Materials* 87(1):11–24.

[9] Raj, B., and M. Vijayalakshmi. 2012. 4.03 - Ferritic steels and advanced ferritic-martensitic steels. In *Comprehensive nuclear materials*, 97–121. Elsevier.

[10] Terrani, K.A., B.A. Pint, Y.J. Kim, K.A. Unocic, Y. Yang, C.M. Silva, H.M. Meyer III, and R. Rebak. 2016. Uniform corrosion of FeCrAl alloys in LWR coolant environments. *Journal of Nuclear Materials* Manuscript.

[11] Yamamoto, Y., B.A. Pint, K.A. Terrani, K.G. Field, Y. Yang, and L.L. Snead. 2015. Development and property evaluation of nuclear grade wrought FeCrAl fuel cladding for light water reactors. *Journal of Nuclear Materials* 467:703–716.

[12] Ejenstam, J., M. Thuvander, P. Olsson, F. Rave, and P. Szakalos. 2015. Microstructural stability of Fe-Cr-Al alloys at 450-550°C. *Journal of Nuclear Materials* 457: 291–297.

[13] Field, K.G., S.A. Briggs, K. Sridharan, R.H. Howard, and Y. Yamamoto. 2016. Tensile properties of neutron irradiated model and commercial FeCrAl alloys. *Journal of Nuclear Materials*.

[14] Field, K.G., M.N. Gussev, Y. Yamamoto, and L.L. Snead. 2014. Deformation behavior of laser welds in high temperature oxidation resistant Fe-Cr-Al alloys for fuel cladding applications. *Journal of Nuclear Materials* 454(1-3):352–358.

[15] Chen, J., P. Jung, W. Hoffelner, and H. Ullmaier. 2008. Dislocation loops and bubbles in oxide dispersion strengthened ferritic steel after helium implantation under stress. *Acta Materialia* 56:250–258.

[16] Field, K.G., X. Hu, K.C. Littrell, Y. Yamamoto, and L.L. Snead. 2015. Radiation tolerance of neutron-irradiated model Fe-Cr-Al alloys. *Journal of Nuclear Materials* 465:746–755.

[17] George, N.M., K. Terrani, J. Powers, A. Worrall, and I. Maldonado. 2015. Neutronic analysis of candidate accident-tolerant cladding concepts in pressurized water reactors. *Annals of Nuclear Energy* 75:703–712.

[18] Bonny, G., D. Terentyev, and L. Malerba. 2008. On the α-α' miscibility gap of Fe-Cr alloys. *Scripta Materialia* 59(11):1193–1196.

[19] Bley, F. 1992. Neutron small-angle scattering study of unmixing in Fe-Cr alloys. *Acta Metallurgica et Materialia* 40(7):1505–1517.

[20] Mathon, M.H., Y. de Carlan, G. Geoffroy, X. Averty, A. Alamo, and C.H. de Novion. 2003. A SANS investigation of the irradiation-enhanced α-α' phase separation in 7-12 Cr martensitic steels. *Journal of Nuclear Materials* 312(2-3):236–248.

[21] Novy, S., P. Pareige, and C. Pareige. 2009. Atomic scale analysis and phase separation understanding in a thermally aged Fe-20 at.%Cr alloy. *Journal of Nuclear Materials* 384(2):96–102.

[22] Bachhav, M., G.R. Odette, and E.A. Marquis. 2014. α' precipitation in neutron-irradiated Fe-Cr alloys. *Scripta Materialia* 74:48–51.

[23] Bergner, F., a. Ulbricht, and C. Heintze. 2009. Estimation of the solubility limit of Cr in Fe at 300°C from small-angle neutron scattering in neutron-irradiated Fe-Cr alloys. *Scripta Materialia* 61(11):1060–1063.

[24] Chen, W., Y. Miao, Y. Wu, C.A. Tomchik, K. Mo, J. Gan, M.A. Okuniewski, S.A. Maloy, and J.F. Stubbins. 2015. Atom probe study of irradiation-enhanced α' precipitation in neutron-irradiated Fe-Cr model alloys. *Journal of Nuclear Materials* 462:242–249.

[25] Messoloras, S., B.C. Pike, R.J. Stewart, and C.G. Windsor. 1984. Precipitation in iron-chromium-aluminum alloys. *Metal Science* 18(June).

[26] Kobayashi, Satoru, and Takayuki Takasugi. 2010. Mapping of 475°C embrittlement in ferritic Fe-Cr-Al alloys. *Scripta Materialia* 63(11):1104–1107.

[27] Capdevila, C., M.M. Aranda, R. Rementeria, R. Domínguez-Reyes, E. Urones-Garrote, and M.K. Miller. 2015. Influence of nanovoids on α-α' phase separation in FeCrAl oxide dispersion strengthened alloy. *Scripta Materialia* 2–5.

[28] Gulbransen, Earl a., and Kenneth F. Andrew. 1959. Oxidation Studies on the Iron-Chromium-Aluminum Heater Alloys. *Journal of The Electrochemical Society* 106(4):294.

[29] Schneider, H. 1960. Foundry Trade Journal. *Foundry Trade Journal* 108:562–564.

[30] Lee, S., C.Y. Lee, and Y.K. Lee. 2015. Schaeffler diagram for high Mn steels. *Journal of Alloys and Compounds* 628:46–49.

[31] Little, E.A., and D.A. Stow. 1979. Void-swelling in irons and ferritic steels: II. An experimental survey of materials irradiated in a fast reactor. *Journal of Nuclear Materials* 87:25–39.

[32] Little, E.A. 2006. Development of radiation resistant materials for advanced nuclear power plant. *Materials Science and Technology* 22(5):491–518.

[33] Chubb, W., S. Alfant, A.A. Bauer, E.J. Jablonowski, F.R. Shober, and R.F. Dickerson. 1958. Constitution, metallurgy, and oxidation resistance of iron-chromium-aluminum alloys: BMI-1298. Tech. Rep., Battelle Memorial Institute, Columbus, OH.

[34] Hsieh, Chih-Chun, and Weite Wu. 2012. Overview of Intermetallic Sigma Phase Precipitation in Stainless Steels. *ISRN Metallurgy* 2012(4):1–16.

[35] Okamoto, H. 1990. Cr Binary Alloy Phase Diagrams. In *Asm handbook volume 3: Alloy phase diagrams*, 2152–2162. ASM International.

[36] Wukusick, C.S., and J.F. Collins. 1964. An iron-chromium-aluminum alloy containing yttrium. *Materials Research & Standards* December:637–646.

[37] Pint, B. A., K. A. Unocic, and K. A. Terrani. 2015. Effect of steam on high temperature oxidation behaviour of alumina-forming alloys. *Materials at High Temperatures* 32(1-2):28–35.

[38] Was, G.S. 2007. *Fundamentals of Radiation Materials Science*. New York: Springer.

[39] Was, G.S., and T.R. Allen. 1993. Intercomparison of microchemical evolution under various types of particle irradiation. *Journal of Nuclear Materials* 205:332–338.

[40] Certain, A., S. Kuchibhatla, V. Shutthanandan, D. T. Hoelzer, and T. R. Allen. 2013. Radiation stability of nanoclusters in nano-structured oxide dispersion strengthened (ODS) steels. *Journal of Nuclear Materials* 434(1-3):311–321.

[41] Bruno, J., D. Bosbach, D. Kulik, and A. Navrotsky. 2007. Chemical Thermodynamics of Solid Solutions of Interest in Nuclear Waste Management: A State-of-the-art Report. Tech. Rep., OECD Nuclear Energy Agency, Paris, France.

[42] Gaskell, D.R. 1996. Metallurgical Thermodynamics. In *Physical metallurgy, volume 1*, ed. R.W. Cahn and P. Haasen, 4th ed., chap. 5, 414–469. Amsterdam, Netherlands: Elsevier Science B.V.

[43] Bishop, R.J., and R.E. Smallman. 1999. *Modern Physical Metallurgy & Materials Engineering*. 6th ed. Oxford, UK: Butterworth & Heinemann.

[44] Fisher, R.M., E.J. Dulis, and K.G. Carroll. 1953. Identification of the Precipitate Accompanying 885°F Embrittlement in Chromium Steels. *Transactions of the Metallurgical Society of AIME* 197:690–695.

[45] Dubuisson, P., D. Gilbon, and J.L. Séran. 1993. Microstructural evolution of ferritic-martensitic steels irradiated in the fast breeder reactor Phénix. *Journal of Nuclear Materials* 205:178–189.

[46] Konobeev, Yu.V., A.M. Dvoriashin, S.I. Porollo, and F.A. Garner. 2006. Swelling and microstructure of pure Fe and Fe-Cr alloys after neutron irradiation to 26 dpa at 400°C. *Journal of Nuclear Materials* 355(1-3):124–130.

[47] Capdevila, C., M.K. Miller, K.F. Russell, J. Chao, and J.L. González-Carrasco. 2008. Phase separation in PM 2000™Fe-base ODS alloy: Experimental study at the atomic level. *Materials Science and Engineering A* 490(1-2):277–288.

[48] Ribis, J., and S. Lozano-Perez. 2012. Orientation relationships and interface structure of α-Cr nanoclusters embedded in α-Fe matrix after α-α' demixing in neutron irradiated Oxide Dispersion Strengthened material. *Materials Letters* 74:143–146.

[49] Kuksenko, V., C. Pareige, and P. Pareige. 2013. Cr precipitation in neutron irradiated industrial purity Fe-Cr model alloys. *Journal of Nuclear Materials* 432: 160–165.

[50] Heintze, C. 2013. Einfluss der Bestrahlung mit energiereichen Teilchen auf die Härte von Fe-Cr-Legierungen. Ph.D. thesis, Dresden University of Technology.

[51] Westraadt, J.E., E.J. Olivier, J.H. Neethling, P. Hedström, J. Odqvist, X. Xu, and A. Steuwer. 2015. A high-resolution analytical scanning transmission electron microscopy study of the early stages of spinodal decomposition in binary Fe-Cr. *Materials Characterization*.

[52] Han, Wentuo, Kiyohiro Yabuuchi, Akihiko Kimura, Shigeharu Ukai, Naoko Oono, Takeji Kaito, Tadahiko Torimaru, and Shigenari Hayashi. 2016. Effect of Cr/Al contents on the 475ºC age-hardening in oxide dispersion strengthened ferritic steels. *Nuclear Materials and Energy* 0:1–6.

[53] Tissot, O., C. Pareige, E. Meslin, B. Decamps, and J. Henry. 2016. Kinetics of α' precipitation in an electron-irradiated Fe15Cr alloy. *Scripta Materialia* 122:31–35.

[54] Li, W., S. Lu, Q.-M. Hu, H. Mao, B. Johansson, and L. Vitos. 2013. The effect of Al on the 475°C embrittlement of Fe-Cr alloys. *Computational Materials Science* 74: 101–106.

[55] Capdevila, C., M.K. Miller, and J. Chao. 2012. Phase separation kinetics in a Fe-Cr-Al alloy. *Acta Materialia* 60(12):4673–4684.

[56] Kattner, Ursula R. 1997. The thermodynamic modeling of multicomponent phase equilibria. *JOM* 49(12):14–19.

[57] Furusaka, M., Y. Ishikawa, S. Yamaguchi, and S. Fujino. 1986. Phase Separation Process in FeCr Alloys Studies by Neutron Small Angle Scattering. *Journal of the Physical Society of Japan* 55(7):2253–2269.

[58] Porollo, S.I, A.M Dvoriashin, A.N Vorobyev, and Yu.V Konobeev. 1998. The microstructure and tensile properties of Fe-Cr alloys after neutron irradiation at 400°C to 5.5-7.1 dpa. *Journal of Nuclear Materials* 256(February):247–253.

[59] Chen, Y., P.H. Chou, and E.A. Marquis. 2014. Quantitative atom probe tomography characterization of microstructures in a proton irradiated 304 stainless steel. *Journal of Nuclear Materials* 451(1-3):130–136.

[60] Capdevila, C., M.K. Miller, and K.F. Russell. 2008. Aluminum partitioning during phase separation in Fe-20%Cr-6%Al ODS alloy. *Journal of Materials Science* 43(11): 3889–3893.

[61] Capdevila, C., M K Miller, G Pimentel, and J Chao. 2012. Influence of recrystallization on phase separation kinetics of oxide dispersion strengthened Fe-Cr-Al alloy. *Scripta Materialia* 66(5):254–257.

[62] General Electric. 1967. Sixth Annual Report - High-Temperature Materials Program Part A. Tech. Rep., General Electric.

[63] ———. 1967. Sixth Annual Report - High-Temperature Materials Program Part B. Tech. Rep., General Electric.

[64] ———. 1968. Seventh annual report - AEC Fuels and Materials Development Program, GEMP-1004. Tech. Rep., General Electric.

[65] Larson, D.J., T.J. Prosa, R.M. Ulfig, B.P. Geiser, and T.F. Kelly. 2013. *Local Electrode Atom Probe Tomography: A User's Guide*. Springer.

[66] Gault, B., M.P. Moody, J.M. Cairney, and S.P. Ringer. 2012. *Atom Probe Microscopy*. Springer.

[67] Marquis, E.A., and J.M. Hyde. 2010. Applications of atom-probe tomography to the characterisation of solute behaviours. *Materials Science and Engineering R: Reports* 69(4-5):37–62.

[68] Auger, P., A. Menand, and D. Blavette. 1988. Statistical Analysis of Atom-Probe Data (II) : Theoretical Frequency Distributions for Periodic Fluctuations and Some Applications. *Journal de Physique* 49:439–444.

[69] Danoix, F., P. Auger, and D. Blavette. 1992. An atom-probe investigation of some correlated phase transformations in Cr, Ni, Mo containing supersaturated ferrites. *Surface Science* 266(1-3):364–369.

[70] Hetherington, M.G., J.M. Hyde, M.K. Miller, and G.D.W. Smith. 1991. Measurement of the amplitude of a spinodal. *Surface Science* 246(1-3):304–314.

[71] De Geuser, F., W. Lefebvre, and D. Blavette. 2006. 3D atom probe study of solute atoms clustering during natural ageing and pre-ageing of an Al-Mg-Si alloy. *Philosophical Magazine Letters* 86(4):227–234.

[72] Geiser, B.P., T.F. Kelly, D.J. Larson, J. Schneir, and J.P. Roberts. 2007. Spatial distribution maps for atom probe tomography. *Microsc. Microanal.* 13:437–447.

[73] Hyde, J.M., A. Cerezo, and T.J. Williams. 2009. Statistical analysis of atom probe data: Detecting the early stages of solute clustering and/or co-segregation. *Ultramicroscopy* 109(5):502–509.

[74] Vurpillot, F., F. De Geuser, G. Da Costa, and D. Blavette. 2004. Application of Fourier transform and autocorrelation to cluster identification in the three-dimensional atom probe. *Journal of Microscopy* 216(3):234–240.

[75] Heinrich, A., T. Al-Kassab, and R. Kirchheim. 2003. Investigation of the early stages of decomposition of Cu-0.7at.% Fe with the tomographic atom probe. *Materials Science and Engineering A* 353:92–98.

[76] Vaumousse, D., A. Cerezo, and P. J. Warren. 2003. A procedure for quantification of precipitate microstructures from three-dimensional atom probe data. *Ultramicroscopy* 95(SUPPL.):215–221.

[77] Hyde, J.M., E.A. Marquis, K. B. Wilford, and T. J. Williams. 2011. A sensitivity analysis of the maximum separation method for the characterisation of solute clusters. *Ultramicroscopy* 111(6):440–447.

[78] Stephenson, L.T., M.P. Moody, P.V. Liddicoat, and S.P. Ringer. 2007. New techniques for the analysis of fine-scaled clustering phenomena within atom probe tomography (APT) data. *Microscopy and microanalysis* 13(6):448–463.

[79] Lefebvre, W., T. Philippe, and F. Vurpillot. 2011. Application of Delaunay tessellation for the characterization of solute-rich clusters in atom probe tomography. *Ultramicroscopy* 111(3):200–206.

[80] Felfer, P., A. V. Ceguerra, S. P. Ringer, and J. M. Cairney. 2015. Detecting and extracting clusters in atom probe data: A simple, automated method using Voronoi cells. *Ultramicroscopy* 150:30–36.

[81] Cerezo, A., and L. Davin. 2007. Aspects of the observation of clusters in the 3-dimensional atom probe. *Surface and Interface Analysis* 39(2-3):184–188.

[82] Rose, D.J. 1956. On the magnification and resolution of the field emission electron microscope. *Journal of Applied Physics* 27(3):215–220.

[83] Birdseye, P.J., D.A. Smith, and G.D.W. Smith. 1974. Analogue investigations of electric field distribution and ion trajectories in the field ion microscope. *Journal of Physics D: Applied Physics* 7(12):1642–1651.

[84] Vurpillot, F., A. Bostel, and D. Blavette. 2000. Trajectory overlaps and local magnification in three-dimensional atom probe. *Applied Physics Letters* 76(21):3127.

[85] Jackson, A.J. 2008. Introduction to Small-Angle Neutron Scattering and Neutron Reflectometry. Tech. Rep. May, NIST Center for Neutron Research.

[86] Windsor, C.G. 1988. An introduction to small-angle neutron scattering. *Journal of Applied Crystallography* 21(6):582–588.

[87] Pedersen, J.S. 1997. Analysis of small-angle scattering data from colloids and polymer solutions: modeling and least-squares fitting. *Advances in Colloid and Interface Science* 70:171–210.

[88] Williams, D.B., and C.B. Carter. 2009. *Transmission Electron Microscopy: A Textbook for Materials Science*. 2nd ed. New York: Springer.

[89] Parish, C.M., and Luke N. Brewer. 2010. Multivariate statistics applications in phase analysis of STEM-EDS spectrum images. *Ultramicroscopy* 110(2):134–143.

[90] Parish, C.M., K.G. Field, A G Certain, and J P Wharry. 2015. Application of STEM characterization for investigating radiation effects in BCC Fe-based alloys. *Journal of Materials Research* 30(9):1246–1274.

[91] Hyde, J.M., M. G. Burke, G. D W Smith, P. Styman, H. Swan, and K. Wilford. 2014. Uncertainties and assumptions associated with APT and SANS characterisation of irradiation damage in RPV steels. *Journal of Nuclear Materials* 449(1-3):308–314.

[92] CAMECA. 2016. IVAS: CAMECA Integrated Visualization & Analysis Software for LEAP Atom Probes.

[93] Ludwig, S. B., and J. P. Renier. 1989. Standard- and Extended-Burnup PWR and BWR Reactor Models for the ORIGEN2 Computer Code, ORNL/TM-11018. Tech. Rep., Oak Ridge National Laboratory, Oak Ridge, TN.

[94] Hellman, O.C., J.A. Vandenbroucke, J. Rüsing, D. Isheim, and D.N. Seidman. 2000. Analysis of Three-dimensional Atom-probe Data by the Proximity Histogram. *Microscopy and Microanalysis* 6:437–444.

[95] Edmondson, P.D., S.A. Briggs, Y. Yamamoto, R.H. Howard, K. Sridharan, K.A. Terrani, and K.G. Field. 2016. Irradiation-Enhanced α' Precipitation in Model FeCrAl Alloys. *Scripta Materialia* 116:112–116.

[96] Muche, Lutz. 1996. Distributional properties of the three-dimensional Poisson Delaunay cell. *Journal of Statistical Physics* 84(1-2):147–167.

[97] Edmondson, P.D., M.K. Miller, K.A. Powers, and R.K. Nanstad. 2016. Atom probe tomography characterization of neutron irradiated surveillance samples from the R. E. Ginna reactor pressure vessel. *Journal of Nuclear Materials* 470:145–154.

[98] Miller, M.K., K.A. Powers, R.K. Nanstad, and P. Efsing. 2013. Atom probe tomography characterization of high nickel, low copper surveillance RPV welds irradiated to high fluences. *Journal of Nuclear Materials* 437:107–115.

[99] Styman, P.D., J.M. Hyde, D. Parfitt, K. Wilford, M.G. Burke, C.A. English, and P. Efsing. 2015. Post-irradiation annealing of Ni-Mn-Si-enriched clusters in a neutron-irradiated RPV steel weld using atom probe tomography. *Journal of Nuclear Materials* 459:127–134.

[100] Miller, M.K., A.A. Chernobaeva, Y.I. Shtrombakh, K.F. Russell, R.K. Nanstad, D.Y. Erak, and O.O. Zabusov. 2009. Evolution of the nanostructure of VVER-1000 RPV materials under neutron irradiation and post irradiation annealing. *Journal of Nuclear Materials* 385:615–622.

[101] Miller, M.K., K.F. Russell, J. Kocik, and E. Keilova. 2000. Embrittlement of low copper VVER-440 RPV surveillance samples neutron-irradiated to high fluences. *Journal of Nuclear Materials* 282:83–88.

[102] Kocik, J., E. Keilova, J. Cizek, and I. Prochazka. 2002. TEM and PAS study of neutron irradiated VVER-type RPV steels. *Journal of Nuclear Materials* 303:52–64.

[103] Bergner, F., A. Ulbricht, P. Lindner, U. Keiderling, and L. Malerba. 2014. Post-irradiation annealing behavior of neutron-irradiated FeCu, FeMnNi and FeMnNiCu model alloys investigated by means of small-angle neutron scattering. *Journal of Nuclear Materials* 454:22–27.

[104] Wells, P.B., T. Yamamoto, B. Miller, T. Milot, J. Cole, Y. Wu, and G.R. Odette. 2014. Evolution of manganese-nickel-silicon-dominated phases in highly irradiated reactor pressure vessel steels. *Acta Materialia* 80:205–219.

[105] Edmondson, P.D., C.M. Parish, and R.K. Nanstad. Forthcoming, 2017. Using complimentary microscopy methods to examine Ni-Mn-Si-precipitates in highly-irradiated reactor pressure vessel steels. *Acta Materialia*.

[106] Pint, B.A. 1996. Experimental observations in support of the dynamic-segregation theory to explain the reactive-element effect. *Oxidation of Metals* 45:1–37.

[107] Field, K.G., S.A. Briggs, P.D. Edmondson, X. Hu, K.C. Littrell, R. Howard, C.M. Parish, and Y. Yamamoto. 2015. Evaluation of the Effect of Composition on Radiation Hardening and Embrittlement in Model FeCrAl Alloys, ORNL/TM-2015/518. Tech. Rep., Oak Ridge National Laboratory.

[108] Campbell, A.A., W.D. Porter, Y. Katoh, and L.L. Snead. 2016. Method for analyzing passive SiC thermometry with a continuous dilatometer to determine irradiation temperature. *Nuclear Instruments and Methods in Physics Research B* 370:49–58.

[109] Field, K.G., S.A. Briggs, K. Sridharan, R.H. Howard, and Y. Yamamoto. Forthcoming, 2017. Mechanical properties of neutron-irradiated model and commercial FeCrAl alloys. *Journal of Nuclear Materials*.

[110] Miller, M.K., and K.F. Russell. 2007. Atom probe specimen preparation with a dual beam SEM/FIB miller. *Ultramicroscopy* 107(2007):761–766.

[111] Parish, C.M., N.A.P.K. Kumar, L.L. Snead, P.D. Edmondson, K.G. Field, C. Silva, A.M. Williams, K. Linton, and K.J. Leonard. 2015. LAMDA: Irradiated-materials microscopy at Oak Ridge National Laboratory. *Microscopy and Microanalysis* 21: 1003–1004.

[112] Wignall, G.D., K.C. Littrell, W.T. Heller, Y.B. Melnichenko, K.M. Bailey, G.W. Lynn, D.A. Myles, V.S. Urban, M.V. Buchanan, D.L. Selby, and P.D. Butler. 2012. The 40 m general purpose small-angle neutron scattering instrument at Oak Ridge National Laboratory. *Journal Of Applied Crystallography* 45(5):990–998.

[113] Ulbricht, A., C. Heintze, F. Bergner, and H. Eckerlebe. 2010. SANS investigation of a neutron-irradiated Fe-9 at%Cr alloy. *Journal of Nuclear Materials* 407(1):29–33.

[114] Száraz, Z., Gy. Török, V. Kršjak, and P. Hähner. 2013. SANS investigation of microstructure evolution in high chromium ODS steels after thermal ageing. *Journal of Nuclear Materials* 435(1-3):56–62.

[115] Meslin, E., M. Lambrecht, M. Hernández-Mayoral, F. Bergner, L. Malerba, P. Pareige, B. Radiguet, A. Barbu, D. Gómez-Briceño, A. Ulbricht, and A. Almazouzi. 2010. Characterization of neutron-irradiated ferritic model alloys and a RPV steel from combined APT, SANS, TEM and PAS analyses. *Journal of Nuclear Materials* 406(1):73–83.

[116] Bachhav, M., G.R. Odette, and E.A. Marquis. 2014. Microstructural changes in a neutron-irradiated Fe-15at.%Cr alloy. *Journal of Nuclear Materials* 454(1-3):381–386.

[117] Bachhav, M., L. Yao, G.R. Odette, and E.A. Marquis. 2014. Microstructural changes in a neutron-irradiated Fe-6at.%Cr alloy. *Journal of Nuclear Materials* 453(1-3): 334–339.

[118] Jaquet, V. 2000. Effet de l'irradiation sur la démixtion des alliages modèles FeCr autour de 15% de chrome. Ph.D. thesis, École polytechnique.

[119] Chen, W. 2014. Irradiation damage in neutron-irradiated Fe-Cr model alloys. Ph.D. thesis, University of Illinois at Urbana-Champaign.

[120] Korchuganova, O.A., M. Thuvander, A.A. Aleev, S.V. Rogozhkin, T. Boll, and T.V. Kulevoy. 2016. Microstructural evolution of Fe-22%Cr model alloy under thermal ageing and ion irradiation conditions studied by atom probe tomography. *Journal of Nuclear Materials* 477:172–177.

[121] Seeger, A., J. Diehl, S. Mader, and H. Rebstock. 1957. Work-hardening and work-softening of face-centred cubic metal crystals. *Philosophical Magazine* 2(15):323–350.

[122] Busby, J.T., M.C. Hash, and G.S. Was. 2005. The relationship between hardness and yield stress in irradiated austenitic and ferritic steels. *Journal of Nuclear Materials* 336(2-3):267–278.

[123] Umantsev, A., and G.B. Olson. 1993. Ostwald ripening in multicomponent alloys. *Scripta Metallurgica et Materialia* 29(8):1135–1140.

[124] Kuehmann, C.J., and P.W. Voorhess. 1996. Ostwald Ripening in Ternary Alloys. *Metallurgical and Materials Transactions A* 27(April):937–943.

[125] Lifshitz, I.M., and V.V. Slyozov. 1961. The kinetics of precipitation from supersaturated solid solutions. *Journal of Physics and Chemistry of Solids* 19(1):35–50. `arXiv:1011.1669v3`.

[126] Wagner, C. 1961. Theorie der alterung von niederschlägen durch umlösen. *Zeitschrift für Elektrochemie* 65:581.

[127] Wagner, R., R. Kampmann, and P.W. Voorhees. 2001. Homogeneous second-phase precipitation. In *Phase transformations in materials*, 309–407. Wiley-VCH.

[128] Ratke, L., and P.W. Voorhees. 2002. *Growth and Coarsening: Ripening in Material Processing*. New York: Springer. `arXiv:1011.1669v3`.

[129] Grobner, P.J. 1973. The 885°F (475°C) embrittlement of ferritic stainless steels. *Metallurgical Transactions* 4:251–260.

[130] Courtnall, M., and F.B. Pickering. 1976. The effect of alloying on 485°C embrittlement. *Metal Science* 10(8):273–276.

[131] Briggs, S.A., C.M. Barr, J. Pakarinen, M. Mahmivand, D.D. Morgan, M.L. Taheri, and K. Sridharan. 2016. Observations of defect structure evolution in proton and Ni ion irradiated Ni-Cr binary alloys. *Journal of Nuclear Materials* 479:48–58.